Universiteit
Leiden
The Netherlands

Quantifying functional phenotypes in human pluripotent stem cell derived cardiomyocytes for disease modelling and drug discovery

Meer, B.J. van

Citation
Meer, B. J. van. (2020, November 3). *Quantifying functional phenotypes in human pluripotent stem cell derived cardiomyocytes for disease modelling and drug discovery*. Retrieved from https://hdl.handle.net/1887/138008

Version:	Publisher's Version
License:	Licence agreement concerning inclusion of doctoral thesis in the Institutional Repository of the University of Leiden
Downloaded from:	https://hdl.handle.net/1887/138008

Note: To cite this publication please use the final published version (if applicable).

Cover Page

Universiteit Leiden

The handle http://hdl.handle.net/1887/138008 holds various files of this Leiden University dissertation.

Author: Meer, B.J. van
Title: Quantifying functional phenotypes in human pluripotent stem cell derived cardiomyocytes for disease modelling and drug discovery
Issue date: 2020-11-03

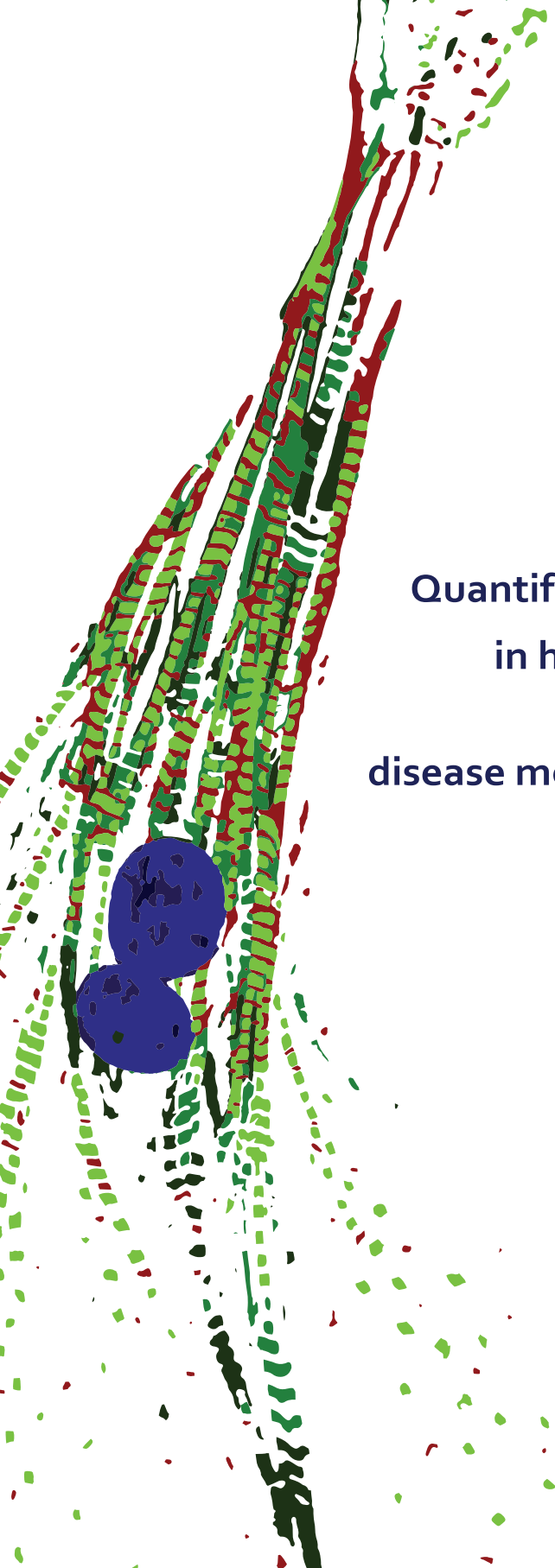

Quantifying functional phenotypes in human pluripotent stem cell derived cardiomyocytes for disease modelling and drug discovery

Berend van Meer

Quantifying functional phenotypes in human pluripotent stem cell derived cardiomyocytes for disease modelling and drug discovery

Berend van Meer

Colophon

Quantifying functional phenotypes in human pluripotent stem cell derived cardiomyocytes for disease modelling and drug discovery

Berend Jan van Meer
Thesis Leiden University Medical Center

Cover illustration & design by Mariëtte Kooren
ISBN 978-94-6423-022-2

Copyright: © Berend van Meer, Haarlem, the Netherlands
All rights reserved. No part of this publication may be reproduced or transmitted in any form or by any means without permission of the author, or, when applicable, of the publishers of the scientific papers.

Quantifying functional phenotypes in human pluripotent stem cell derived cardiomyocytes for disease modelling and drug discovery

Proefschrift

ter verkrijging van
de graad van Doctor aan de Universiteit Leiden,
op gezag van Rector Magnificus prof.mr. C.J.J.M. Stolker,
volgens besluit van het College voor Promoties
te verdedigen op dinsdag 3 november 2020
klokke 16.15 uur

door

Berend Jan van Meer
geboren te Bloemendaal
in 1988

Promotor	Prof. dr. C.L. Mummery
Co-promotor	Dr. L.G.J. Tertoolen
Promotiecommissie	Prof. dr. M.J.T.H. Goumans Prof. dr. D.E. Atsma Prof. dr. A.P. IJzerman Prof. dr. ir. R. Dekker Prof. dr. J. Bakkers

This research was conducted at the Department of Embryology & Anatomy of the Leiden University Medical Center, the Netherlands. It was supported by research grants from the European Research Council, the National Centre for the Replacement, Refinement and Reduction of Animals in Research and the Dutch Research Council.

Publication of this thesis was financally supported by Stichting Proefdiervrij, the Dutch Heart Foundation and the Willy van Heumenfonds.

Aan mijn ouders,
voor oneindig veel vertrouwen

Table of contents

1 General introduction 8

2 Measuring physiological responses of human pluripotent stem cell derived cardiomyocytes to drugs and disease 20

3 MUSCLEMOTION: a versatile open software tool to quantify cardiomyocyte and cardiac muscle contraction *in vitro* and *in vivo* 40

4 Quantification of muscle contraction *in vitro* and *in vivo* using MUSCLEMOTION software: from stem cell-derived cardiomyocytes to zebrafish and human hearts 74

5 Simultaneous measurement of excitation-contraction coupling parameters identifies mechanisms underlying contractile responses of hiPSC-derived cardiomyocytes 104

6 Blinded, multi-centre evaluation of drug-induced changes in contractility using human induced pluripotent stem cell-derived cardiomyocytes 138

7 Cytostretch, an Organ-on-Chip platform 200

8 Small molecule absorption by PDMS in the context of drug response bioassays 224

9 General discussion and future perspectives 240

Summary 250
Nederlandse samenvatting 254
Curriculum vitae 258
List of publications 260
Dankwoord 262

Abstract

Human pluripotent stem cell derived cardiomyocytes are a promising alternative to current preclinical models for cardiac disease modelling and drug screening. Currently, their predictive power is limited by their immature state and the lack of scalable clinical relevant readouts. In this thesis, new measurement methods are described. These methods allow quantification of human pluripotent stem cell derived cardiomyocyte maturity and their response to drugs and disease.

Chapter 1

General introduction

Models to study heart failure

Arguably, the heart is the most important organ of the human body. Cardiac failure remains a leading cause of death in the (Western) world[1] despite high investments in cardiac healthcare[2]. Although unhealthy lifestyle and diet are still major causes of heart failure (HF), the role of genetic defects resulting in metabolic diseases, high propensity for arrhythmias or high risk to develop congestive heart failure (CHF) should not be underestimated[3]. Consequently, secondary effects of CHF such as limited oxygen supply to tissue have also become more important to study and resolve. Apart from inherited susceptibility to HF, unexpected drug induced cardiotoxicity might trigger cardiac failure. For example, on September 30, 2004 the pharmaceutical company Merck voluntarily withdrew the drug rofecoxib from the market after it was found to induce myocardial infarction[4]. Rofecoxib was approved by the Food and Drug Administration in 1999 for treatment of arthritis, acute pain and menstrual cramps and used daily by 2 million patients. Such unexpected cardiovascular related toxicity is accountable for 45% of drug withdrawals from the market[5] and is still an important side effect of widely used chemotherapeutic drugs like doxorubicin[6] and trastuzumab[7]. Finding ways to prevent detrimental effects on the heart or alternative drugs without these effects is therefore still highly relevant in drug discovery and development.

To study cardiotoxicity and cardiac disease, *in vitro* models are used to mitigate the high risks, limited throughput and costs associated with *in* vivo testing. Animal models are used as well as non-cardiac human cells genetically modified to express critical cardiac features mediating toxicity. Examples of such features include the human Ether-à-go-go-Related Gene (hERG) ion channels to model risk of arrhythmia[8]. However, both type of models lack accuracy[9]. A critical reason underlying the lack of predictivity for both positive and negative drug- and disease effects in current models of the heart becomes clear by comparing their functional parameters to those of human cardiac tissue. Ventricular cardiomyocytes are functionally defined by the excitation-contraction coupling (EC-coupling) which key events are (i) the action potential (AP), which leads to (ii) an increase of free cytosolic calcium (Ca^{2+}) that in turn triggers (iii) the contraction through shortening of the cell's sarcomeres. This tightly orchestrated cascade is present in both animal and human cardiomyocytes, but the timing and shapes of these transient parameters exhibit high interspecies variation mainly due to different ion currents underlying the action potential[10]. It is thus no surprise that animal models often do not provide mechanistic insight in human cardiac function. Moreover, since most drugs and disease states affect ion channels or structural proteins of which animals and humans often express different isoforms, responses to them are highly species dependent. Non-cardiac cell based models transiently transfected with ion channels exhibit the correct currents, but are devoid of the complexity of the complete EC-coupling cascade which again leads to a lack of predictive power especially due to false-positives[11].

Stem cell derived cardiomyocytes

An emerging alternative class of *in vitro* models recapitulating both the complexity of EC-coupling and the accuracy of correct ion channel expression are based on human pluripotent stem cell derived cardiomyocytes (hPSC-CMs). Pluripotent stem cells

(PSCs) can divide indefinitely and are capable of differentiating to any cell type of the human body[12]. They are typically characterized by the expression of pluripotency associated genes Sox2, Oct-4 and Nanog[13], cell surface proteins recognized by TRA-1-60 and TRA-1-81 antibodies[14], and a high nuclear to cytoplasmic ratio. By inhibiting signalling pathways associated with pluripotency and activating pathways associated with lineage commitment during embryonic development it has become possible over the last decade to direct differentiation of PSCs to many specific tissue cell types with high efficiency[15–18]. The first human PSCs were isolated in 1998 from late blastocyst stage embryos generally donated for research after becoming surplus to requirements for treating infertility. Since this raises ethical issues because the embryo is destroyed during the procedure, many efforts were made to identify alternative sources for these embryonic. The greatest and most significant breakthrough in this context was the discovery of induced PSCs (iPSCs) in 2007 by Takahashi and Yamanaka[19]. iPSCs are derived from somatic cells from healthy or diseased individuals by reprogramming with the pluripotency associated transcription factors (e.g. Sox2, Oct-4, cMyc and Klf4) originally identified as characteristic of embryonic stem cells. Somatic cells from many different sources have been used including blood[20], skin[21] and urine[22]. This makes them widely available and moreover, they have a genotype of which the adult (disease or healthy) phenotype is known which theoretically enables personalized medicine.

In vitro differentiation of embryonic or induced hPSCs towards cardiomyocytes starts by inducing nascent mesoderm formation then cardiac mesoderm development which is regulated by three families of growth factors: bone morphogenetic proteins, wingless/INT proteins (WNTs) and fibroblast growth factors[23]. Next, WNT is inhibited to derive cardiac progenitors which develop towards ventricular-like cardiomyocytes[24] after removing the WNT inhibitor protein. Recently, different protocols have been established to derive different cardiac subtypes such as atrial-like cardiomyocytes using retinoic acid[25] and cardiac endothelial cells using vascular endothelial growth factor[26].

Characteristics of cardiomyocytes

Adult human cardiomyocytes are rod-shaped, often bi- or poly-nuclear cells highly optimized for cyclic contraction. The EC-coupling cascade of AP, increase of cytosolic Ca^{2+} and contraction is facilitated by a large number of cardiomyocyte specific processes, ion channels and structural proteins. The AP arises from an interplay of various passive and active ion transporters (i.e. channels, pumps and exchangers) that regulate the traffic of Na^{+}, Ca^{2+} and K^{+} across the membrane. The most important ion transporters for the AP of ventricular cardiomyocytes are encoded by the genes SCN5A, CACN1C, KCND2/3/4, KCNH2 (hERG), KCNQ1, KCNJ2/12/4 and a splice variant of SLC8A1 and produce the currents I_{Na}, $I_{Ca,L}$, I_{to}, I_{Kr}, I_{Ks}, I_{K1} and I_{NCX}, respectively[27]. $I_{Ca,L}$ and I_{NCX} increase the free cytosolic Ca^{2+} in the second phase of the AP mainly by triggering the fast release of stored Ca^{2+} in the sarcoplasmic reticulum (SR) via the ryanodine (RYR2) receptors. Finally, the contractile apparatus is activated which is made up of myofilaments, sarcomeres and their regulatory components[28]. Among the most important proteins involved in the assembly of the contractile apparatus are myosin light chain (MYL), myosin heavy chain (MYH), cardiac actin (ACTC1), tropomyosin (TPM), troponin (TNN), titin (TTN), cardiac α-actinin (ACTN2) and myosin binding protein-C3 (MYBPC3). Many

steps involved in EC-coupling have a high energy demand which is met by a large ratio of mitochondria to cell volume[29].

During embryonic development, the protein isoforms that are expressed in the human heart change in many cases. For example, ratios of MYL2/MYL7, MYH7/MYH6 and TNNI3/TTNI1 are higher than 1 in adult myocardium, while they are below 1 in prenatal myocardium[30]. Specific isoform transition of such structural proteins in adult myocardium is associated with sarcomeric dysfunction[31]. In general, mutations in genes encoding proteins involved in cardiomyocyte function are highly associated with cardiac diseases such as Brugada syndrome (mutation in SCN5A[32]), Long QT syndrome (mutation in KCNQ1[33], KCNH2[34], etc.; different types exist and are dependent on the specific mutation[35]), catecholaminergic polymorphic ventricular tachycardia 1 (CPVT1; mutation in RYR2)[36] and hypertrophic cardiomyopathy (mutation in MYBPC3)[37]. Cardiomyocytes originating from iPSC cells derived from patients with such mutations can be used to model the diseased phenotype *in vitro*[38–40].

hPSC-CM maturation

hPSC-CMs do not exhibit the same characteristics as adult cardiomyocytes. Instead, their state is more comparable to late embryonic or, at most, neonatal stages of development[30,41–43]. This lack of maturation is very likely to be limiting to the predictive power of hPSC-CMs as presently available since expected drug and disease responses might not be revealed if the cells do not recapitulate the adult state. For example, it has been shown that maturation is key in revealing the expected decrease in force of contraction in hiPSC-CMs derived from a patient with a mutation in MYPC3 leading to hypertrophic cardiomyopathy[44]. Since it limits the applicability of such models, improving hPSC-CM maturity is one of the major priorities in the field. Typically, this is pursued through biochemical stimulation with growth factors or hormones (e.g. triiodothyronine hormone, insulin-like growth factor 1 and dexamethasone[44]) or through the development of more complex heart models by introducing other cardiac cell types and organizing them in 3D geometries[43,45,46].

hPSC-CM immaturity is evident from looking at genomic, structural and functional level. The expression of certain cardiac specific genes remains rather low while genes associated with embryonic stages are upregulated (e.g. MYH7/MYH6 and TNNI3/TTNI1 ratios are typically below 1 [reference]). On a structural level, many signs of immaturity are present such as a low amount of bi-nucleated hPSC-CMs, a round shape and disorganized sarcomeres. Perhaps most importantly, many functional parameters of hPSC-CMs do not have similar levels. For example, the upstroke velocity of the AP in adult cardiomyocytes ranges from 150-350 V/s versus 10-50 V/s in hPSC-CMs, the resting membrane potential is reported to be around -85 mV versus -60 mV and the force of contraction is ranges from 40-80 mN/mm^2 versus 0.08-4 mN/mm^2, respectively [reference]. This issue of maturity and how to address it are considered more extensively in this thesis.

Functional phenotyping of cardiomyocytes

To gain insight in hPSC-CM performance, maturation and response to drugs and disease, accurate measurement methods are indispensable. Electrical activity is typically assessed using patch clamp, but this laborious method is limited by its low throughput and requires highly specialized operators. For higher throughput applications, multi electrode arrays can be used to measure the field potential of cardiomyocytes[47,48]. More recently, voltage sensitive fluorescent sensors originally developed for measuring neurons have been optimized and used for optical AP assessment[49]. Calcium flux is typically quantified using calcium sensitive fluorescent sensors[50]. For contraction, a wide range of measurement techniques exist[41], all varying in complexity and highly dependent on the configuration of the cellular model (e.g. single cells or monolayer of cells) which limits reproducibility across models and laboratories. The development of tools that can be applied in a wide range of cellular configurations is most important. Ideally, these measurement techniques would allow for measuring parameters not only *in vitro* but also *in vivo.* This would enable translational studies, which currently is a major challenge. For example, one important clinically used readout of contractility is ejection fraction output, which is impossible to measure *in vitro* since most hPSC-CM models are not configured to have cavities that pump out liquid, but are merely a planar monolayer cells exhibiting contractility.

Many of the current measurement methods are not suitable to assess hPSC-CM based models for pharmaceutical development applications, since they are limited by their throughput, operator dependency and number of readouts (i.e. only electrical activity, calcium or contraction). High-throughput assays that accurately quantify the complete EC-coupling are required to use hPSC-CMs for early cardiotoxicity screening in drug developmental pathways.

Increasing model complexity for the heart

Most differentiation protocols for deriving hPSC-CMs lead to heterogeneous cell populations with a high percentage of ventricular-like cells[24]. In recent years, biologists started to focus on more defined hPSC-CM cultures by increasing differentiation efficiency towards one cell type[25], purifying the cell type of interest[51] or culturing defined mixtures of purified cell types by putting them together in specific ratios[26], mimicking native myocardium. In the human heart, atrial and ventricular cardiomyocytes are the main cells responsible for the heart's contraction, but they rely on cell-cell interactions with, among others, nodal cardiomyocytes, cardiac endothelial cells[52] and cardiac fibroblasts[53] for their performance, including growth, electrical activity and contraction. It has therefore been hypothesized that cardiomyocyte maturation is dependent on biochemical or biophysical cues from these surrounding cell types. Besides co-culture of different cell types, researchers are increasingly adding biophysical complexity by developing 3D tissues[26,45,46,54] and including physical cues such as stretch[55,56] or flow using microfluidic channels[57]. Recapitulating the physiological environment of cardiomyocytes might not only induce maturation, but is likely to enable studying indirect cardiomyocyte failure due to affected endothelial cells or fibroblasts.

Organs-on-Chips

To be able to mimic the native environment of cells even more closely, Organ-on-Chip (OoC) devices have been developed using soft materials with tuneable properties such as stiffness and viscoelasticity. Huh et al. cultured a alveolar-capillary interface in a Lung-on-Chip device fabricated from polydimethylsiloxane (PDMS) using primary alveolar epithelial cells and microvascular endothelial cells[58]. Even though being notorious for small molecule absorption which is a challenge for use in drug development trajectories, PDMS has been widely used by others as well, for example by Parker et al. to develop thin film membranes coated with isolated neonatal rat cardiomyocytes which were the first Heart-on-Chip devices[59]. More recently, multiple organs have been coupled together to form more complex models, including a model consisting of multiple organs to replicate the 28-day menstrual cycle of females[60].

By combining microfabrication technologies originally used in integrated chip fabrication with hiPSC biotechnology, OoCs might both increase cell maturity and enable high throughput readouts. Microfabrication enables creation of chips in the shape of vessels, flexible membranes, or other structures that recapitulate the native environment of the cellular niche while hiPSCs can be used to derive cell types of interest from healthy or diseased individuals. For hPSC-CMs, it is known that substrate stiffness highly determines the force of contraction[61], but cardiomyocyte shape induced by micropatterning also determines sarcomeric organization and functional output[62,63]. Additionally, by including sensors such as electrodes or force transducers in the substrate these devices can integrate readout systems that allow upscaling and high-throughput cellular measurements, making these models suitable for the early toxicity testing and drug screening.

Aim and scope of this thesis

The future of hPSC-CM applications in pharma for drug discovery will depend on their predictive power and their ability to recapitulate human disease states. In order to investigate this predictivity, several chapters in this thesis describe different aspects of the application of hPSC-CM in the context of drug and disease modelling. To understand the limitations of current measurement, methods for physiological responses of hPSC-CMs are described in Chapter 2. In addition, current multiplexed measurements of AP, Ca^{2+} flux and contraction and the application of biophysical stimuli are explored. In Chapter 3 a new software (MUSLCEMOTION) tool for measuring contraction is described that overcomes limitations of current techniques such as the cell configuration dependency. Instead, MUSCLEMOTION is used to quantify contraction in a wide range of cellular configurations *in vitro, in situ* in complex devices and even *in vivo*, enabling clinical translational studies. In addition, contractile response to drug and diseases in the different models is quantified. In Chapter 4 a detailed protocol for using MUSCLEMOTION is presented to enable every biologist and research group not specialized in measuring contraction to quantify contractility using standard equipment. MUSCLEMOTION is used in Chapter 5 in combination with fluorescent voltage and calcium sensitive sensors to develop a novel scalable non-invasive "Triple Transient Measurement System" for simultaneous high-speed assessment of cardiac

action potential, calcium handling and contraction. To demonstrate its potential for cardiotoxicity screening, disease modelling and drug discovery, hPSC-CM response to drugs and diseases is measured and quantified with automated analysis software. Next, the Triple Transient Measurement System is one of three platforms used in Chapter 6 for a blinded, multi-centre study to evaluate drug-induced contractility changes in hPSC-CMs. In Chapter 7, to integrate methods for maturation and hPSC-CM phenotyping, microfabrication methods are described to develop a modular OoC device (Cytostretch) based on PDMS. Cytostretch recapitulates the native environment of the heart by cell alignment on a soft substrate which can be periodically stretched to model the changing heart volume during a heartbeat. Furthermore, Cytostretch includes electrodes to measure the electrical activity of hPSC-CMs plated on the device. Chapter 8 elaborates on the notorious problem of the absorption of drugs by PDMS, which requires a solution before it can be used in drug response assays. The absorption of four cardioactive drugs is quantified and reduced by applying cell membrane-like lipid layers to the surface of PDMS. Finally, in Chapter 9, results and conclusions presented in the previous chapters are discussed, accompanied by a general outlook and future implications on the field.

References

1. Benjamin, E. J. *et al. Heart Disease and Stroke Statistics'2017 Update: A Report from the American Heart Association*. *Circulation* **135,** (2017).
2. Cook, C., Cole, G., Asaria, P., Jabbour, R. & Francis, D. P. The annual global economic burden of heart failure. *Int. J. Cardiol.* **171,** 368–376 (2014).
3. Akhirome, E., Walton, N. A., Nogee, J. M. & Jay, P. Y. The Complex Genetic Basis of Congenital Heart Defects. *Circ. J.* **81,** 629–634 (2017).
4. Sibbald, B. Rofecoxib (Vioxx) voluntarily withdrawn from market. *Can. Med. Assoc. J.* **171,** 1027–1028 (2004).
5. Stevens, J. L. & Baker, T. K. The future of drug safety testing: expanding the view and narrowing the focus. *Drug Discov. Today* **14,** 162–167 (2009).
6. Chatterjee, K., Zhang, J., Honbo, N. & Karliner, J. S. Doxorubicin cardiomyopathy. *Cardiology* **115,** 155–162 (2010).
7. Seidman, B. A. *et al.* Cardiac Dysfunction in the Trastuzumab Clinical Trials Experience. **20,** 1215–1221 (2014).
8. Jones, D. K. *et al.* hERG 1b is critical for human cardiac repolarization. *Proc. Natl. Acad. Sci.* **111,** 18073–18077 (2014).
9. Braam, S. R., Passier, R. & Mummery, C. L. Cardiomyocytes from human pluripotent stem cells in regenerative medicine and drug discovery. *Trends Pharmacol. Sci.* **30,** 536–545 (2009).
10. Nerbonne, J. M., Nichols, C. G., Schwarz, T. L. & Escande, D. Genetic Manipulation of Cardiac K+ Channel Function in Mice: What Have We Learned, and Where Do We Go From Here? *Circ. Res.* **89,** 944–956 (2001).
11. Redfern, W. S. *et al.* Relationships between preclinical cardiac electrophysiology, clinical QT interval prolongation and torsade de pointes for a broad range of drugs: Evidence for a provisional safety margin in drug development. *Cardiovasc. Res.* **58,** 32–45 (2003).
12. Thomson, J. A. *et al.* Embryonic Stem Cell Lines Derived from Human Blastocysts. *Science (80-.).* **1145,** 1145–1148 (2009).
13. Boyer, L. a L. a. *et al.* Core Transcriptional Regulatory Circuitry in Human Embryonic Stem Cells. *Cell* **122,** 947–956 (2005).
14. Gerecht-Nir, S. & Itskovitz-Eldor, J. Human embryonic stem cells: a potential source for cellular therapy. *Am J Transpl.* **4 Suppl 6,** 51–57 (2004).
15. van den Berg, C. W., Elliott, D. A., Braam, S. R., Mummery, C. L. & Davis, R. P. Differentiation of Human Pluripotent Stem Cells to Cardiomyocytes Under Defined Conditions. in *Patient-Specific Induced Pluripotent Stem Cell Models: Generation and Characterization* (eds. Nagy, A. & Turksen, K.) 163–180 (Springer New York, 2016).
16. Orlova, V. V. *et al.* Generation, expansion and functional analysis of endothelial cells and pericytes derived from human pluripotent stem cells. *Nat. Protoc.* **9,** 1514–1531 (2014).
17. Dhara, S. & Stice, S. Neural differentiation of human embryonic stem cells. *J. Cell. Biochem.* **105,** 633–640 (2008).
18. Lam, A. Q., Freedman, B. S. & Bonventre, J. V. Directed Differentiation of Pluripotent Stem Cells to Kidney Cells. *Semin. Nephrol.* **34,** 445–461 (2014).
19. Takahashi, K. *et al.* Induction of

Pluripotent Stem Cells from Adult Human Fibroblasts by Defined Factors. *Cell* **131,** 861–872 (2007).

20. Zhang, X. B. Cellular Reprogramming of Human Peripheral Blood Cells. *Genomics, Proteomics Bioinforma.* **11,** 264–274 (2013).

21. Yu, J. *et al.* Induced pluripotent stem cell lines derived from human somatic cells. *Science* **318,** 1917–20 (2007).

22. Zhou, T. *et al.* Generation of human induced pluripotent stem cells from urine samples. *Nat. Protoc.* **7,** 2080–2089 (2012).

23. Mummery, C. *et al.* Differentiation of human embryonic stem cells to cardiomyocytes: role of coculture with visceral endoderm-like cells. *Circulation* **107,** 2733–2740 (2003).

24. Mummery, C. L. *et al.* Differentiation of Human Embryonic Stem Cells and Induced Pluripotent Stem Cells to Cardiomyocytes: A Methods Overview. *Circ. Res.* **111,** 344–358 (2012).

25. Devalla, H. D. *et al.* Atrial-like cardiomyocytes from human pluripotent stem cells are a robust preclinical model for assessing atrial-selective pharmacology. *EMBO Mol. Med.* **7,** 394–410 (2015).

26. Giacomelli, E. *et al.* Three-dimensional cardiac microtissues composed of cardiomyocytes and endothelial cells co-differentiated from human pluripotent stem cells. *Development* dev.143438 (2017).

27. Liu, J., Laksman, Z. & Backx, P. H. The electrophysiological development of cardiomyocytes. *Adv. Drug Deliv. Rev.* **96,** 253–273 (2016).

28. Bers, D. M. Cardiac excitation-contraction coupling. *Nature* **415,** 198–205 (2002).

29. Ventura-Clapier, R., Garnier, A., Veksler, V. & Joubert, F. Bioenergetics of the failing heart. *Biochim. Biophys. Acta - Mol. Cell Res.* **1813,** 1360–1372 (2011).

30. Denning, C. *et al.* Cardiomyocytes from human pluripotent stem cells: From laboratory curiosity to industrial biomedical platform. *Biochim. Biophys. Acta - Mol. Cell Res.* **1863,** 1728–1748 (2016).

31. Hinson, J. T. *et al.* Titin mutations in iPS cells define sarcomere insufficiency as a cause of dilated cardiomyopathy. **349,** 982–987 (2015).

32. Antzelevitch, C. Brugada syndrome. *Pacing Clin. Electrophysiol.* **29,** 1130–1159 (2006).

33. Crotti, L., Celano, G., Dagradi, F. & Schwartz, P. J. Congenital long QT syndrome. *Orphanet J. Rare Dis.* **3,** 1–16 (2008).

34. Keller, D. I. *et al.* Characterization of novel KCNH2 mutations in type 2 long QT syndrome manifesting as seizures. *Can. J. Cardiol.* **25,** 455–462 (2009).

35. Brandão, K. O., Tabel, V. A., Atsma, D. E., Mummery, C. L. & Davis, R. P. Human pluripotent stem cell models of cardiac disease: from mechanisms to therapies. *Dis. Model. Mech.* **10,** 1039–1059 (2017).

36. Priori, S. G. *et al.* Clinical and molecular characterization of patients with catecholaminergic polymorphic ventricular tachycardia. *Circulation* **106,** 69–74 (2002).

37. Carrier, L., Mearini, G., Stathopoulou, K. & Cuello, F. Cardiac myosin-binding protein C (MYBPC3) in cardiac pathophysiology. *Gene* **573,** 188–197 (2015).

38. Davis, R. P. *et al.* Cardiomyocytes Derived From Pluripotent Stem Cells Recapitulate Electrophysiological Characteristics of an Overlap Syndrome of Cardiac Sodium Channel Disease. *Circulation* **125,** 3079–3091 (2012).

39. Wang, Y. *et al.* Genome editing of isogenic human induced pluripotent stem cells recapitulates long QT phenotype for drug testing. *J. Am. Coll. Cardiol.* **64,** 451–459 (2014).

40. Bellin, M. *et al.* Isogenic human pluripotent stem cell pairs reveal the role of a KCNH2 mutation in long-QT syndrome. *EMBO J.* **32,** 3161–3175 (2013).

41. van Meer, B. J., Tertoolen, L. G. J. & Mummery, C. L. Concise Review: Measuring Physiological Responses of Human Pluripotent Stem Cell Derived Cardiomyocytes to Drugs and Disease. *Stem Cells* **34,** 2008–2015 (2016).

42. Robertson, C., Tran, D. D. & George, S. C. Concise review: Maturation phases of human pluripotent stem cell-derived cardiomyocytes. *Stem Cells* **31,** 829–837 (2013).

43. Godier-Furnémont, A. F. G. *et al.* Physiologic force-frequency response in engineered heart muscle by electromechanical stimulation. *Biomaterials* **60,** 82–91 (2015).

44. Birket, M. J. *et al.* Contractile Defect Caused by Mutation in MYBPC3 Revealed under Conditions Optimized for Human PSC-Cardiomyocyte Function. *Cell Rep.* **13,** 733–745 (2015).

45. Tiburcy, M. *et al.* Defined Engineered Human Myocardium with Advanced Maturation for Applications in Heart Failure Modelling and Repair. *Circulation* CIRCULATIONAHA.116.024145 (2017).

46. Lemoine, M. D. *et al.* Human iPSC-derived cardiomyocytes cultured in 3D engineered heart tissue show physiological upstroke velocity and sodium current density. *Sci. Rep.* **7,** 5464 (2017).

47. Tertoolen, L. G. J., Braam, S. R., van Meer, B. J., Passier, R. & Mummery, C. L. Interpretation of field potentials measured on a multi electrode array in pharmacological toxicity screening on primary and human pluripotent stem cell-derived cardiomyocytes. *Biochem. Biophys. Res. Commun.* 1–7 (2017).

48. Braam, S. R. *et al.* Prediction of drug-induced cardiotoxicity using human embryonic stem cell-derived cardiomyocytes. *Stem Cell Res.* **4,** 107–16 (2010).

49. Zhuge, Y. *et al.* Human pluripotent stem cell tools for cardiac optogenetics. *Conf Proc IEEE Eng Med Biol Soc* **2014,** 6171–6174 (2014).

50. Takahashi, a, Camacho, P., Lechleiter, J. D. & Herman, B. Measurement of intracellular calcium. *Physiol. Rev.* **79,** 1089–125 (1999).

51. Huber, I. *et al.* Identification and selection of cardiomyocytes during human embryonic stem cell differentiation. *FASEB J.* **21,** 2551–2563 (2007).

52. Brutsaert, D. L. Cardiac Endothelial-Myocardial Signaling: Its Role in Cardiac Growth, Contractile Performance, and Rhythmicity. *Physiol. Rev.* **83,** 59–115 (2003).

53. Souders, C. A., Bowers, S. L. K. & Baudino, T. A. Cardiac fibroblast: The renaissance cell. *Circ. Res.* **105,** 1164–1176 (2009).

54. Ronaldson-Bouchard, K. *et al.* Advanced maturation of human cardiac tissue grown from pluripotent stem cells. *Nature* **556,** 239–243 (2018).

55. Salameh, A. & Dhein, S. Effects of mechanical forces and stretch on intercellular gap junction coupling. *Biochim. Biophys. Acta - Biomembr.* **1828,** 147–156 (2013).

56. Yang, X., Pabon, L. & Murry, C. E. Engineering adolescence: Maturation of human pluripotent stem cell-derived cardiomyocytes. *Circ. Res.* **114,** 511–523 (2014).

57. Annabi, N. *et al.* Hydrogel-coated microfluidic channels for cardiomyocyte culture. *Lab Chip* **13,** 3569 (2013).

58. Huh, D. *et al.* Reconstituting organ-level lung functions on a chip. *Science* **328,** 1662–8 (2010).

59. Feinberg, A. W. *et al.* Muscular thin films for building actuators and powering devices. *Science* **317,** 1366–70 (2007).

60. Xiao, S. *et al.* A microfluidic culture model of the human reproductive tract and 28-day menstrual cycle. *Nat. Commun.* **8,** 1–13 (2017).

61. Hersch, N. *et al.* The constant beat: cardiomyocytes adapt their forces by equal contraction upon environmental stiffening. *Biol. Open* **2,** 351–361 (2013).

62. Bray, M.-A., Sheehy, S. P. & Parker, K. K. Sarcomere alignment is regulated by myocyte shape. *Cell Motil. Cytoskeleton* **65,** 641–651 (2008).

63. Ribeiro, A. J. S. *et al.* Contractility of single cardiomyocytes differentiated from pluripotent stem cells depends on physiological shape and substrate stiffness. *Proc. Natl. Acad. Sci.* **112,** 201508073 (2015).

Abstract

Cardiomyocytes from human pluripotent stem cells (hPSC) are of growing interest as models to understand mechanisms underlying genetic disease, identify potential drug targets and for safety pharmacology since they may predict human relevant effects more accurately and inexpensively than animals or other cell models. Crucial to their optimal use are accurate methods to quantify cardiomyocyte phenotypes accurately and reproducibly. Here we review current methods for determining biophysical parameters of hPSC-derived cardiomyocytes (hPSC-CMs) that recapitulate disease and drug responses. Even though hPSC-CMs as currently available are immature, various biophysical methods are nevertheless already providing useful insights into the biology of the human heart and its maladies. Advantages and limitations of assays currently available looking towards applications of hPSC-CMs are described with examples of how they have been used to date. This will help guide the choice of biophysical method to characterize healthy cardiomyocytes and their pathologies *in vitro*.

Chapter 2

Measuring physiological responses of human pluripotent stem cell derived cardiomyocytes to drugs and disease

Modified after Stem Cells 34, 2008-2015 (2016)

Berend van Meer, Leon Tertoolen, Christine Mummery

Introduction

Almost one in three drugs are not used clinically because of side-effects on the heart[1]. Cardiotoxic drugs are often not detected in animal models or cultured cell lines expressing selected cardiac genes because their physiology differs from that of the human heart. In rodents, for example, heart rates are almost ten times faster than in humans and ion channels, most importantly the $K_v7.1$ and hERG channels, are differentially expressed[2]. Mutations in the KCNQ1 or KCNH2 genes that encode these channels and cause severe cardiac disease in humans thus have little effect in mice. It is therefore not surprising that human relevance for drug responses and modelling cardiac disease is limited.

An emerging method to model the human heart and cardiac disease is using human pluripotent stem cells (hPSCs). hPSCs can be induced to differentiate to various types of cardiomyocytes (hPSC-CMs) with high efficiency (reviewed in[3]), although most protocols to date yield hPSC-CM with a ventricular phenotype. As a result, most data reported concerns drug responses or the effect of mutations in ventricular-like cardiomyocytes. hPSCs may be either embryonic (hESCs) or 'genetically reprogrammed' adult cells called induced pluripotent stem cells (hiPSCs)[3]. hPSC-CMs are relatively immature compared with cardiomyocytes from adult heart[4] (Table 1) but nevertheless can show drug-related cardiac responses that reflect QT-prolongation and arrhythmia evident in electrocardiograms from patients[29]. hiPSC-CMs generated from patients with mutations in cardiac-relevant genes are already proving useful for understanding mechanisms of disease since they often show expected disease phenotypes[30–33]. Gene targeting is also being used to introduce cardiac disease mutations into hPSC and hiPSC from patients with mutations are being genetically "repaired" to create isogenic pairs that differ only in the genomic region of interest. This allows control over the genetic background used for study[34].

Improving the maturity of hPSC-CMs is one of the main priorities in the field. In order to assess the state of maturation as well as effects of drugs and disease, improved biophysical methods for cardiomyocyte analysis are still needed. These should be able to measure dynamic parameters such as force of contraction, calcium handling and electrical activity and preferably, should not require specialist electrophysiology or mechanobiology facilities so that they can easily be used in many laboratories. Of note though, physical stimuli, such as mechanical stress and electrical pacing, might also be necessary for cardiomyocyte maturation[35] so some specialist expertise may be required. Here, we review measurement techniques currently available for phenotyping and stimulating contractile dynamics of hPSC-CMs *in vitro* and discuss ways to modulate the physical environment to best mimic human physiological and pathological states. Cardiomyocytes resulting from different differentiation protocols can vary in their stage of maturation but in general ion currents, sarcomeric structure and calcium handling stabilize 20 to 30 days after initiation of differentiation. The methods described in this review have generally been used once this stability has been established. We provide examples of how these approaches have been used on healthy and diseased hPSC-CMs.

Table 1: Biophysical parameters of human stem cell derived ventricular cardiomyocytes during development and primary cardiomyocytes.

	hPSC-CM				hPSC-EHT		Primary cardiomyocytes	
	early		late		late		adult	
Biophysical parameter	**value**	**ref**	**value**	**ref**	**value**	**ref**	**value**	**ref**
Force of contraction (mN/mm2)[a]	0.3	5	0.5	6	4.4	7	51	8
Cell aspect ratio (length-to-width)	01:02	9	01:04	9	unknown		01:07	10
Sarcomeric organization	disorganized	9	organized	9	highly organized	11	highly organized	
Sarcomeric distance (µm)	1.65	12	1.81	12	unknown		2.15	8
Conduction velocity (cm/s)	< 2	13	< 20	14	<26	14	100	15
Multinucleated cells (%)	5	16	20	16	25	17	26	18
Mitochondria-to-cell volume ratio	0.06	19	0.09	19	unknown		0.3	20
Resting membrane potential (mV)	-50	21	-73.5	22	- 50[b]	11	-81.8	23
Voltage upstroke velocity (V/s)	< 9	21	26.2	22	8[b]	11	215	23
Calcium Transient Duration (ms)	unknown		< 370 (CaDT90)	24	< 375 (CaDT80)	25	~ 300 (CaDT90)	15
Calcium Transient Rise time (ms) (80%)	unknown		> 10	26	< 100	25	unknown	
Calcium Transient Decay (ms) (80%)	unknown		> 50	26	< 150	25	unknown	
ATP level	<2000[c] (lum/#cell)	27	<3000[c] (lum/#cell)	27	unknown		5.69 (mmol/kg weight)	28

[a] Some differences may be explained by a difference in measured contraction phase (isotonic vs. isometric) or method (beads vs. posts).
[b] Measured on dissociated cardiomyocytes from EHTs.
[c] Relative values.
Abbreviations: ATP, Adenosine triphosphate; EHT, engineered heart tissue; hPSC, human pluripotent stem cells; hPSC-CM,human pluripotent stem cell-derived cardiomyocytes.

Finally, assuming limitations with respect to maturity of hPSC-CM *in vitro* and assay methods are overcome, we look forward towards future use of these human models in drug discovery and clinical translation.

Characterizing dynamics of hPSC-CMs

Action potential

The cardiac action potential (AP) is shaped by tightly regulated ion currents, most importantly the Na^+, Ca^{2+} and K^+ current. hPSC-CMs are considered electrically immature: in contrast to their adult counterparts ventricular hPSC-CMs show spontaneous beating and more depolarized resting membrane potentials (Table 1) caused by high pacemaker current (I_f) and low inwardly rectifying K^+ current (I_{K1}), respectively. Low expression of Na^+ channels causes slow upstroke velocity in the AP (Table 1) compared to adult ventricular cardiomyocytes; recent *in silico* analysis based on previously published hiPSC-CM electrophysiological data shows an increased sensitivity to L-type Ca^{2+} block due to overexpression of the Na^+/Ca^{2+} exchanger[36]. For a complete overview of ion current differences between hPSC derived and adult cardiac cells, we refer the reader to[22]. AP characteristics are distinct for each cardiomyocyte subtype. The subtype formed during differentiation can be directed by timed addition of cytokines and hormones: retinoic acid for example directs formation of atrial-like cardiomyocytes[37] and a Smoothened Agonist (SAG) in combination with insulin-like growth factor-1 (IGF-1) induces pacemaker-like cardiomyocytes[6]. Three experimental approaches are available to measure ion currents and APs in hPSC-CMs: patch clamp electrophysiology, voltage sensitive sensors and multi electrode arrays (MEAs). Each has its own advantages and disadvantages.

Patch-clamp electrophysiology allows precise measurements of ion currents and membrane potentials by voltage- and current clamping, respectively. It can be used to determine the identity of the cardiac subtype and specific drug responses. For example, atrial and ventricular cells from hPSC and their differential responses to the atrial specific drugs vernakalant and XEN-D0101 27 to 30 days after initiation of differentiation were evident in patch clamp assays[37]. Since every cardiomyocyte is "clamped" individually and a well-sealed pipette-membrane interface is essential, the procedure is labour intensive and dependent on operator skills. To address this, Scheel et al. used automated whole-cell patch clamp (CytoPatch 2) and measured responses to nifedipine, cisapride and TTX in commercially-supplied ventricular hiPSC-CMs that would be expected from clinical data and conventional patch clamp[38]. Similarly, using the IonWorks Barracuda system, a group of 353 compounds that included known hERG channel blockers, largely gave predicted pharmacological responses in HEK293 and CHO-K1 cells expressing hERG channels[39]. However, these automated whole-cell patch clamp systems measure APs by patching the cardiomyocytes whilst they are in suspension and not attached to a substrate. Under these conditions, cardiomyocyte lifespan is limited so that experiments need to be complete within a short time window. Automated patch clamp is designed for high throughput phenotyping of many cells under different conditions but manual patch clamp is at present more accurate.

A less invasive and labour intensive method is based on electrochromic fluorescent voltage-sensitive dyes (VSDs)[24], such as di-4-ANEPPS. VSDs are fast-response fluorescent probes that intercalate between lipid bilayers; they respond to changes in electrical field by fluctuations in fluorescence intensity that can be recorded optically. In standard (low-speed) optical systems the major limitation is the sampling frequency of the optical recorder. The upstroke velocity, the fastest kinetic parameter of the AP, is about 285 V/s in adult ventricular cardiomyocytes[23,40] causing a positive change in the membrane potential of about 130 mV. The minimum sample frequency of this near linear transient is around 8.8 kHz.hPSC-CMs have smaller upstroke velocities (10-100V/s) so that such high frequencies might not be required. Genetically encoded fluorescent voltage sensors, first used to map neural signalling pathways[41], are also potentially useful optical alternatives. Although they have improved since first introduced and have been stably expressed in hPSC-CMs, they have longer response times than VSDs, limiting their utility (Supplementary Table 1).

Microelectrode arrays (MEAs) are medium throughput, non-invasive alternatives that requires less operator training and specialized equipment compared to patch clamp. These are glass culture substrates containing electrodes that measure external electrical activity by transducing the extracellular ion flux into an electrical current readout of field potential. Several studies have shown that near-equivalents of QT-prolongation and changes in upstroke velocities can be measured as external field potentials. hESC-CMs exposed to compounds affecting AP duration[29] for example, or hiPSC-CMs from long QT patients with KCNQ1 mutations showed significant responses in MEA-recordings 20 to 30 days after initiation of differentiation[42]. Spira et al. recently manufactured MEAs with sharp electrodes that can penetrate the cell membrane and directly access the cytosol, much like patch-clamp[43]; however, variation in access resistance of the electrode and poor seal formation, as in the automated systems, limited their use as an alternative to conventional patch-clamp.

VSDs and MEAs have an additional advantage: cardiac conduction velocities can be measured as the wave propagation velocity in hPSC-CM monolayer cultures; this can reveal defective electrical conduction in the heart. Thompson et al. for example used VSDs to show improved AP conduction after engrafting ventricular-like hESC-CMs in a neonatal rat ventricular-cell model of arrhythmogenic cardiac tissue[44].

Calcium flux

The inflow of Ca^{2+} ions during the cardiac AP affects the AP itself and the shape of the contraction transient in hPSC-CMs. The kinetics of the Ca^{2+} flux provide information on calcium handling which is carefully orchestrated by the L-type channels, RYR2-channels and sarco/endoplasmic reticulum Ca^{2+}-ATPase (SERCA); this is of utmost importance in revealing disease phenotypes[32] and in predicting drug responses, toxicity and cardiac safety[45,46]. Fluorescent probes that bind Ca^{2+} are the method of choice for calcium transient measurements (reviewed in[47]). Gepstein et al. for example used Fluo-4 to investigate calcium handling by hESC-CMs. He showed an increase in sarcoplasmic reticulum calcium load as a function of time *in vitro* and predicted Ca^{2+} storage release in response to caffeine and ryanodine[26].

In general, fluorescent calcium sensitive detectors (CSDs) are categorized as ratiometric or non-ratiometric, the most important difference being their ability to measure absolute versus relative concentrations of Ca^{2+}. Ratiometric dyes allow bound and unbound dye molecules to be determined; from these values the absolute concentration of Ca^{2+} can be calculated[47]. This ratio of bound- to unbound dye molecules is not known when using non-ratiometric CSDs; whilst changes in fluorescence intensity reflect transient changes in cytosolic Ca^{2+} concentration these values cannot be translated to the absolute Ca^{2+} concentration without calibration. Additionally, there is inter-assay variability since the intracellular dye concentration is dependent on loading time, temperature, cell permeability and cell access (e.g. cell cluster size) rather than the loading concentration[47]. This makes keeping the intracellular dye concentration constant between experiments very difficult. The change in Ca^{2+} concentration is often calculated as a pseudo-ratio dF/F[48]. Although this pseudo-ratio adequately relates the change in signal to the change in Ca^{2+} concentration, it is sometimes incorrectly interpreted since the maximum value depends on loading conditions. Relative changes are best calculated and compared within a zero-to-one scale defined by the baseline conditions, eliminating confusing values for the maximum amplitude.

In hPSC-CMs, the relative change in Ca^{2+} response resulting from disease mutations or drugs is often more important than absolute levels. For example, Kosmidis et al. recently showed Ca^{2+} handling increased relatively in response to the synthetic glucocorticoid dexamethasone in ventricular hESC-CMs 28 to 30 days after initiation of differentiation[21]. It has also been shown that reduced caffeine-induced NCX currents in hiPSC-CMs from patients with catecholaminergic polymorphic ventricular tachycardia (CPVT) were evident as similar decreases of fluorescence intensity of the CSD[49]. A recent review on calcium signalling in hPSC-CMs[50] concluded that well-characterized hPSC-CMs are often reliable models for human cardiomyocyte calcium handling, since all calcium parameters of cardiac signalling are present and functional: calcium current induced Ca^{2+} release, Ca^{2+} sparks, NCX currents, SERCA2a and ß-adrenergic regulation. We would like to add that although CSDs are among the most valuable tools for evaluating hPSC-CMs, caution is needed in interpreting data since not all calcium regulating organelles are necessarily fully developed *in vitro* (e.g. t-tubules) possibly impacting conclusions.

Genetically encoded CSDs are relatively new; they were initially developed for neuroscience applications *in vivo* and have outperformed synthetic Ca^{2+} dyes in their sensitivity[51]. However, as for the genetically-encoded VSDs, slow on-and-off kinetics currently limit their use for cardiac mapping[52]. Both ratiometric and non-ratiometric detectors can easily be transduced and stably expressed in hPSC-CMs but variability in expression levels introduces similar inter-assay variation as the loading conditions of dyes.

Force of contraction

Heart failure is associated with decreased contraction force or a change in its kinetics[53]. Bray et al. showed that myocyte geometry dictates sarcomeric alignment[54]; in ventricular hPSC-CMs this was optimal at width-to-length (or "aspect") ratios of 1:7 and that it determined the net force of contraction[55]. The maximum contraction

Table 2: Qualitative comparison of measurement methods for hPSC-CMs phenotyping.

Relative scores of the pros and cons in measuring important features of hPSC-CM. The resolution, speed, ability to multiplex with other techniques, (non)-invasiveness of the technique , its accuracy (how close the output value is to the actual value), precision (how great the spread in values) and the ease of setting up the technique are given relative values (++ high to - low) to guide the choice made for phenotyping.

Measurement parameter	Methods	Tissue type	Resolution	Speed	Multiplexing	Non-invasiveness	Accuracy	Precision	Easy to set up	High throughput
Force of contraction	Beads	Single cell	+	+	++	++	+	++	--	+
Force of contraction	Flexible poles	EHT; single cell	+/-	+	-	++	+	+	--	++
Force of contraction	Skinned myocyte measurement	Single cell	++	++	+/-	--	++	++	+/-	--
Calcium transient	Non-Ratiometric dye	Any	++	+	+	+/-	+	++	++	+
Calcium transient	Ratiometric dye	Any	++	+	-	+/-	++	++	+	+
Calcium transient	Non-ratiometric protein construct	Any	++	--	+	+/-	--	-	-	++
Action potential	Voltage sensitive dye	Any	++	+	++	+	+/-	++	+	+
Action potential	Voltage sensitive protein construct	Any	++	--	++	+	--	-	-	++
Action potential	Patch clamp	Single Cell	++	++	-	--	++	++	-	--
Field potential	MEA	Monolayer; aggregates	++	++	++	+/-	++	+	+	+
Conduction velocity	MEA	Monolayer	++	++	++	+/-	++	+	+	+
Conduction velocity	Voltage sensitive dye	Any	++	+	++	+	+/-	++	+	+
ATP level	ATP fluorescent sensor*	Any	++	-	+/-	+	+	++	+/-	+
ATP level	Extracellular flux analyser	Monolayer	++	-	+	--	+	++	+/-	++
Sarcomeric organization	Protein expression construct	Any	+/-	+/-	++	++	+/-	+/-	-	+

* This technique has not yet been used on hPSC-CMs.

forces reported for hPSC-CMs are always an order of magnitude lower than for adult cardiomyocytes (see Table 1). Contraction of cardiac muscle is characterized by isotonic and isometric phases, where tension is developed with- and without the cell being able to shorten, respectively e.g. in free space or attached. Generally, the isotonic phase of hPSC-CM contraction has been assessed most often[5] and although techniques have been developed that assess the isometric phase of single cardiomyocytes[56], they have not yet been used on hPSC-CMs.

Measurements of isotonic tension on hPSC-CMs have been done on single cells, or on 2D and 3D multicellular cultures. Rape et al. developed polyacrylamide (PA)-coated coverslips containing fluorescent beads, with 20 μm wide microcontact-printed gelatine lines to guide orientation and elongation of single cells[57]. We used this technique (Figure 1A and D) recently to show that a commercially available culture medium for cardiomyocyte maturation increased contraction force of ventricular hESC-CM 33 days after initiation of differentiation compared to human fetal ventricular cardiomyocytes[5]. Another study by Rodriguez et al. using an array of small polydimethylsiloxane (PDMS) microposts showed higher contractile velocities in single ventricular hiPSC-CMs on a surface coated with laminin compared to fibronectin and collagen IV[17]. Of note though, the position in the z-axis of the post to which the cardiomyocyte attached affected its deflection so that correction for this underestimation is needed. Also, since the stiffness of the substrate on which hPSC-CMs are plated influences the force they generate[58], direct comparison of absolute values from different assays (i.e. with different substrates) is not meaningful.

Muscular thin films (MTFs) or bio-hybrid films are 2D constructs first developed for use with neonatal rat ventricular cardiomyocytes by Feinberg et al. (Figure 1B). They showed that greater tissue alignment resulted in a higher peak systolic stress[59]. Since then, MTFs have been proposed as *in vitro* contractility assays for drug screening and disease modelling[60]. However, Hinson et al. recently showed that 2D constructs do not recapitulate the structured architecture of native cardiac tissue well enough to capture the diseased phenotype in MTFs from patient hiPSC-CMs with a mutation in the sarcomeric protein titin. In contrast, 3D cardiac tissues generated from the same patient-derived iPSC line clearly showed reduced contraction[61].

Other approaches for measuring force of contraction include Engineered Heart Tissue (EHTs), cardiac microtissues (CMTs) and cardiac microwires (CMWs). These are millimetre-sized biomaterial 3D structures seeded with cardiomyocytes *in vitro,* which mimic cardiac myobundles (Figure 1C). EHTs are attached to PDMS posts and their deflection is directly related to the force exerted by the cell. hPSC-CMs incorporated in EHTs have been reported to be more mature than conventional 2D cultures, exhibiting highly organized sarcomeres, myocyte elongation and multinucleation (Table 1). For this reason and because of cell population heterogeneity that includes many fibroblasts, EHTs are strong candidates as models of mature functional myocardium. EHTs induce clinically relevant drug responses, such as the positive inotropic effects of isoprenaline, in ventricular hiPSC-CMs from day 25 on after initiation of differentiation[25]. Despite their exceptional myocardial maturity, the immediate utility of hPSC-CM-EHTs in high-throughput screening is limited by the large numbers of cells they require, drug

penetration and challenges with imaging. However, they are particularly amenable to analysis using classical physiology techniques such as "skinning" often used on explanted primary heart tissue, in which cytoplasm and membranes are removed leaving just the sarcomeric structures intact for force measurement[8].

Apart from measuring mechanical displacement, the kinetics of contraction force can also be determined from sarcomere movement, motion vector analysis and (as a surrogate) impedance measurements. During contraction, the sarcomere shortens and the distance between Z-disks is reduced. This can be measured in hiPSC-CMs as a change in sarcomeric distance which can be monitored using genetically encoded fluorescent alpha-actinin reporters built into hiPSC or live staining to visualize sarcomeres directly[55]. However, imaging systems with high spatial (~200 nm) and temporal (~30 ms) resolution are required to assess kinetics accurately. Motion vector analysis by contrast does not require such high spatial resolution, ectopic reporters or staining methods. It uses transmitted light microscopy to calculate the kinetics of contraction through, for example, edge detection algorithms or, more recently, an algorithm evaluating frame-to-frame similarities[62]. After taking substrate mechanics into account, this technique compares well with other measurement techniques, illustrating its utility[62]. Impedance measurements have also been used as readouts of contractile kinetics[63], but to date these have not been compared quantitatively with established technologies. Impedance measurement detects alterations in resistance of cardiomyocytes as a function of shape changes during contraction. xCELLigence and CardioExcyte96 are among the most widely used devices for measuring impedance. Results are encouraging[64] but require further validation.

Multiplexed measurements

More valuable are attempts to measure multiple dynamic parameters in hPSC-CMs simultaneously, since their temporal correlation can provide crucial insights into drug responses or disease mechanisms. For example: diseased hiPSC-CMs might have a genetically defective contractile apparatus, which delays the interval between the calcium flux and the contraction transient and/or alters drug response (Figure 1G).

The integration of multiple standard optical assays is an approach now being developed commercially for hPSC-CMs. Q-State Biosciences (Cambridge, Massachusetts) for example is offering a platform to analyse calcium flux and electrical activity simultaneously, although initially on neural cells. Relatively slow genetically-encoded dyes may limit use for hPSC-CMs at present but this will undoubtedly improve (Table 2). Clyde Biosciences (Glasgow) measure calcium, contraction and AP in the same cells sequentially as a service but at present without temporal correlation. Drawbacks of these multiplexed measurements include their invasiveness, light-induced generation of reactive oxygen species[65] and chemical interactions of the surface of the substrate with the cardiomyocytes. As an example of invasiveness, the chemical interaction of the calcium indicator with free cytosolic calcium ions will reduce the number of free calcium ions available for the contractile apparatus. When the force of contraction is measured in the presence of a calcium indicator, the reduction in free cytosolic Ca^{2+} will cause a significantly lower outcome in force. Since interactions between the techniques

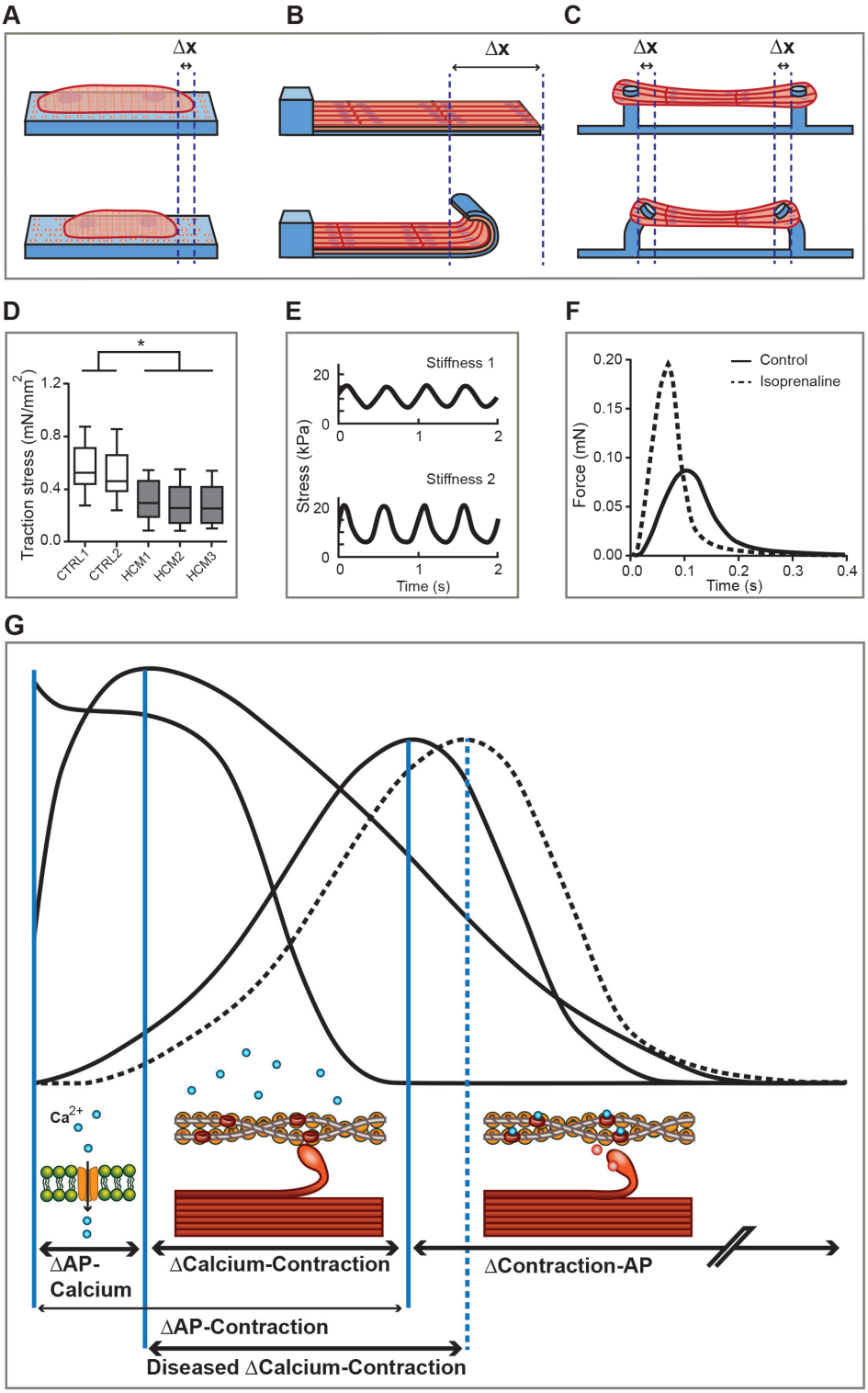
A
B
C
Δx
Δx
Δx
Δx
D
E
F
*
Traction stress (mN/mm²)
1.2
0.8
0.4
0.0
CTRL1
CTRL2
HCM1
HCM2
HCM3
Stiffness 1
Stiffness 2
Stress (kPa)
20
0
0
1
2
Time (s)
Force (mN)
0.20
0.15
0.10
0.05
0.00
0.0
0.1
0.2
0.3
0.4
Time (s)
Control
Isoprenaline
G
Ca2+
ΔAP-
Calcium
ΔCalcium-Contraction
ΔContraction-AP
ΔAP-Contraction
Diseased ΔCalcium-Contraction

used for measurement can impact their outcome, Table 3 summarizes and compares the most important features of dynamic measurement techniques qualitatively and scores their applicability in multiplexed systems. This table can be used as a starting point to select combinations of bioassays for hPSC-CMs that are compatible because they do not show mutual interference.

Table 3: State of the art response times of fluorescent calcium and voltage sensors.

Sensor	Response time	Ref
VSDs (ANNINE-6plus)	~ 10 fs	77
CSDs (Fluo-4)	~ 1 ms	78
Genetically encoded voltage probe (Ace1Q-mNeon)	< 1 ms	79
Genetically encoded calcium probe (GCaMP6f)	> 10 ms	51

Figure 1: Methods for measuring contraction force in hPSC-CMs in single cell, 2D and 3D constructs.

hPSC-CM cultured as single cells, 2D muscular thin film (MTF) or 3D engineered heart tissue (EHT) and corresponding methods for contraction force measurements. In (A) fluorescent beads are present in the elastic substrate, their displacement caused by the contraction of a single hPSC-CM is measured and used to calculate the resulting stress. In (D) this method is used to show a difference in maximum force of contraction in hiPSC-CMs with MYBPC3 mutations (HCM1, HCM2 and HCM3) compared to control (CTRL1, CTRL2) (adapted from75). Similarly, the deflection of MTFs can be used to calculate the force (B). The stress generated on different substrates with varying elasticity (E) (adapted from76) can be used to calculate the actual force of contraction. EHTs are fabricated around silicon rubber posts that deflect during contraction (C) and can be related to the force of contraction. This has been used to show the change in force of contraction in response to isoprenaline (F) (adapted from25).

In (G) the solid traces show an example of simultaneous measurement of action potential (AP), calcium flux (Ca2+) and contraction, which allows correlation between these biophysical parameters in time (vertical blue lines) to gain mechanistic insights in diseases and drug responses. Aspects of disease or drug responses reflected in the traces that might be compromised in hPSC-CMs are shown below: influx of calcium ions (blue circles) to the cytosol, binding of the myosin head to the actin filament and the release of the myosin head by binding of calcium to the filament. The dotted trace indicates an example of a diseased phenotype: if the calcium binding site on the filament is compromised in a diseased hPSC-CM one would expect the delay between Ca2+ and contraction to be longer, while the delay between AP and Ca2+ remains unaffected.

Applying biophysical stimuli

hPSC-CMs not only exert stress, and strain during contraction but they can also respond to imposed biophysical stimuli.

Mechanical stimulation

Kensah et al. showed that increased static stress enhances sarcomere alignment, cell-to-cell coupling and force of contraction in ventricular hPSC-CMs[7]. Salameh et al. reported on using "cyclic mechanical stretch" (CMS) to induce alignment[66]; CMS has also been shown to increase intercellular coupling between cardiomyocytes[67]. In addition, manipulating the magnitude or frequency of mechanical stress might also be used to reveal disease phenotypes *in vitro* that would not otherwise be evident; an example would be hypertrophic cardiomyopathy which *in vivo* can manifest as sudden death during exercise. Force transducers (as in the Flexcell Tension FX-series) or an oscillating vacuum underneath a thin film substrate[68] can be used to induce (uniaxial) stress on substrates. Although PDMS is often the material of choice we, and others[69], have encountered cell detachment during stretching due to the hydrophobic character of the material. Special coatings are currently being developed to solve this problem.

Electrical field and optical stimulation

Mature ventricular cardiomyocytes do not generate spontaneous APs but rely on pacemaker activity for contraction that is regulated by the sinus atrial node (SAN). Since hPSC-CMs are often cultured as isolated ventricular cell populations without SAN cells, electrical stimulation might be key to inducing maturation *in vitro*[70]. In addition, congestive heart failure (CHF) can be induced *in vivo* by forcibly "pacing" the heart at increased frequencies (reviewed by Moe et al.[71]) and may also be induced in (diseased) hiPSC-CMs *in vitro*. Such frequency-dependent behaviour emphasizes the importance of absolute beating frequency control in ventricular hPSC-CMs, either to exclude inter-assay variation or to investigate pacing-induced effects.

Exposing cardiomyocytes to short electric fields of 0.5 to 10 ms, causes the membrane to depolarize and initiates an AP. Long-term pacing experiments have however been limited by electrolysis at the culture medium-electrode interface. This can be reduced by perfusion or frequently refreshing medium but the issue is circumvented using optogenetics.

One optogenetic approach is based on channelrhodopsin-2 (ChR2), a light gated sodium ion channel originally found in algae to enable light induced movement. Nagel et al. showed that, when expressed in mammalian cells, the influx of Na^+ initiates the action potential cascade directly[72]. Zhuge et al. demonstrated that ChR2 can be used to depolarize hESC-CMs *in vitro*[73]. However, hPSC-CM cultures *in vitro* often lack adequate concentrations of retinal – essential for the conformational change under the influence of blue light – so that ChR2 channels do not respond; this can be solved by adding retinal to the medium[74].

Outlook

Rapid technological advances in human pluripotent stem cell biology over the past 5 years are poised to transform disease modelling and drug discovery for the heart. hPSC-CMs capture genetic variation among healthy individuals and patients with cardiac disease. The development of CRISPR/CAS9 for efficient genetic modification of hPSC now allows the generation of isogenic pairs – or even series – of diseased and healthy hPSC-CMs, differing only in the gene of interest[42]. Shortcomings remain, the most significant being hPSC-CM maturity: they are not yet adult cardiomyocyte mimics. Improved and defined culture conditions, heterogeneous cell populations and 3D tissue engineering are, however, contributing to finding solutions and in at least two cases – hypertrophic myopathy caused by mutations in MYBC3[75] and titin[61] – these have been crucial in revealing the disease phenotype. Further improvements in (bio) physical conditions may be expected to allow more cardiac phenotypes in hPSC-CMs to be revealed with greater differences in experimental and control values.

Improved methods to assess responses and drivers of physiological changes in hPSC-CMs are still essential to derive full benefit from the opportunities presented by patient cells. New multiplexed systems will soon allow temporal correlation between multiple cardiac features in various contexts of cell population composition, tissue architecture and culture media so that these models accurately mimic physiological and/or pathological characteristics of cardiac tissue. As these models become more complex, they are likely to require more sophisticated measurement techniques as readouts. For example, all cell types in the heart, not just those that are contractile, could be assessed separately by introducing different genetically encoded fluorescent probes into cell type specific loci. Combined with multiplexed optical systems it would then be possible to assess and correlate the different cell type responses, providing insight into their interactions and identifying the major cellular culprit in cardiac disease. The whole range of single cell and multicellular heterogeneous cell population assays will likely be necessary depending on specific requirements for research on underlying disease mechanisms to drug discovery and repurposing.

In order for Pharma to adopt hPSC-CM models in their drug development trajectory, these integrated measurement techniques will have to be scalable and high-throughput. This will reduce the costs and make the "price per data point" acceptable in a business model. Multidisciplinary collaboration between engineers, stem cell biologists, physicists, materials scientists is the way forward in implementing hPSC in the next generation of cardiac drug discovery and disease research.

Acknowledgements

We apologize to those authors whose many papers we have not cited due to length constraints. We thank Bas Blankevoort for figure design. Work in the Mummery lab is supported by the European Research Council (ERCAdG 323182 STEMCARDIOVASC) and the GSK-NC3R CrackIt programme INPULSE.

References

1. Laverty, H. G. *et al.* How can we improve our understanding of cardiovascular safety liabilities to develop safer medicines? *Br. J. Pharmacol.* **163,** 675–693 (2011).

2. Redfern, W. S. *et al.* Relationships between preclinical cardiac electrophysiology, clinical QT interval prolongation and torsade de pointes for a broad range of drugs: Evidence for a provisional safety margin in drug development. *Cardiovasc. Res.* **58,** 32–45 (2003).

3. Mummery, C. L. *et al.* Differentiation of Human Embryonic Stem Cells and Induced Pluripotent Stem Cells to Cardiomyocytes: A Methods Overview. *Circ. Res.* **111,** 344–358 (2012).

4. Veerman, C. C. *et al.* Immaturity of Human Stem-Cell-Derived Cardiomyocytes in Culture: Fatal Flaw or Soluble Problem? *Stem Cells Dev.* **24,** 1035–1052 (2015).

5. Ribeiro, M. C. *et al.* Functional maturation of human pluripotent stem cell derived cardiomyocytes *in vitro* - Correlation between contraction force and electrophysiology. *Biomaterials* **51,** 138–150 (2015).

6. Birket, M. J. *et al.* Expansion and patterning of cardiovascular progenitors derived from human pluripotent stem cells. *Nat. Biotechnol.* **33,** 970–979 (2015).

7. Kensah, G. *et al.* Murine and human pluripotent stem cell-derived cardiac bodies form contractile myocardial tissue *in vitro*. *Eur. Heart J.* **34,** 1134–1146 (2013).

8. van der Velden, J. *et al.* Force production in mechanically isolated cardiac myocytes from human ventricular muscle tissue. *Cardiovasc. Res.* **38,** 414–423 (1998).

9. Snir, M. *et al.* Assessment of the ultrastructural and proliferative properties of human embryonic stem cell-derived cardiomyocytes. *Am. J. Physiol. Heart Circ. Physiol.* **285,** H2355–H2363 (2003).

10. McCain, M. L. & Parker, K. K. Mechanotransduction: The role of mechanical stress, myocyte shape, and cytoskeletal architecture on cardiac function. *Pflugers Arch. Eur. J. Physiol.* **462,** 89–104 (2011).

11. Schaaf, S. *et al.* Human Engineered Heart Tissue as a Versatile Tool in Basic Research and Preclinical Toxicology. *PLoS One* **6,** e26397 (2011).

12. Lundy, S. D., Zhu, W.-Z., Regnier, M. & Laflamme, M. a. Structural and functional maturation of cardiomyocytes derived from human pluripotent stem cells. *Stem Cells Dev.* **22,** 1991–2002 (2013).

13. Mehta, A. *et al.* Pharmacological response of human cardiomyocytes derived from virus-free induced pluripotent stem cells. *Cardiovasc. Res.* **91,** 577–586 (2011).

14. Zhang, D. *et al.* Tissue-engineered cardiac patch for advanced functional maturation of human ESC-derived cardiomyocytes. *Biomaterials* **34,** 5813–5820 (2013).

15. Boron, W. F. *Medical Physiology*. (Elsevier - Health Sciences Division, 2009).

16. Klug, M. G., Soonpaa, M. H. & Field, L. J. DNA synthesis and multinucleation in embryonic stem cell-derived cardiomyocytes. *Am. J. Physiol.* **269,** H1913–H1921 (1995).

17. Rodriguez, M. L. *et al.* Measuring

the contractile forces of human induced pluripotent stem cell-derived cardiomyocytes with arrays of microposts. *J. Biomech. Eng.* **136,** 51005 (2014).

18. Olivetti, G. *et al.* Aging, cardiac hypertrophy and ischemic cardiomyopathy do not affect the proportion of mononucleated and multinucleated myocytes in the human heart. *J. Mol. Cell. Cardiol.* **28,** 1463–1477 (1996).

19. Birket, M. J. *et al.* PGC-1α and reactive oxygen species regulate human embryonic stem cell-derived cardiomyocyte function. *Stem Cell Reports* **1,** 560–574 (2013).

20. Piquereau, J. *et al.* Mitochondrial dynamics in the adult cardiomyocytes: which roles for a highly specialized cell? *Front. Physiol.* **4,** 1–12 (2013).

21. Mummery, C. *et al.* Differentiation of human embryonic stem cells to cardiomyocytes: role of coculture with visceral endoderm-like cells. *Circulation* **107,** 2733–2740 (2003).

22. Ma, J. *et al.* High purity human-induced pluripotent stem cell-derived cardiomyocytes: electrophysiological properties of action potentials and ionic currents. *AJP: Heart and Circulatory Physiology* **301,** H2006–H2017 (2011).

23. Magyar, J. *et al.* Effects of endothelin-1 on calcium and potassium currents in undiseased human ventricular myocytes. *Pflugers Arch. Eur. J. Physiol.* **441,** 144–149 (2000).

24. Lee, P. *et al.* Simultaneous Voltage and Calcium Mapping of Genetically Purified Human Induced Pluripotent Stem Cell-Derived Cardiac Myocyte Monolayers. *Circ. Res.* **110,** 1556–1563 (2012).

25. Stoehr, A. *et al.* Automated analysis of contractile force and Ca2+ transients in engineered heart tissue. *AJP Hear. Circ. Physiol.* **306,** H1353–H1363 (2014).

26. Satin, J. *et al.* Calcium handling in human embryonic stem cell-derived cardiomyocytes. *Stem Cells* **26,** 1961–1972 (2008).

27. Rana, P., Anson, B., Engle, S. & Will, Y. Characterization of human-induced pluripotent stem cell-derived cardiomyocytes: Bioenergetics and utilization in safety screening. *Toxicol. Sci.* **130,** 117–131 (2012).

28. Beer, M. *et al.* Absolute concentrations of high-energy phosphate metabolites in normal, hypertrophied, and failing human myocardium measured noninvasively with 31P-SLOOP magnetic resonance spectroscopy. *J. Am. Coll. Cardiol.* **40,** 1267–1274 (2002).

29. Braam, S. R. *et al.* Prediction of drug-induced cardiotoxicity using human embryonic stem cell-derived cardiomyocytes. *Stem Cell Res.* **4,** 107–16 (2010).

30. Bellin, M. *et al.* Isogenic human pluripotent stem cell pairs reveal the role of a KCNH2 mutation in long-QT syndrome. *EMBO J.* **32,** 3161–3175 (2013).

31. Liang, P. *et al.* Drug Screening Using a Library of Human Induced Pluripotent Stem Cell-Derived Cardiomyocytes Reveals Disease-Specific Patterns of Cardiotoxicity. *Circulation* **127,** 1677–1691 (2013).

32. Lin, B. *et al.* Modeling and study of the mechanism of dilated cardiomyopathy using induced pluripotent stem cells derived from individuals with Duchenne muscular dystrophy. *Dis. Model. Mech.* **8,** 457–466 (2015).

33. Bellin, M., Marchetto, M. C., Gage, F. H. & Mummery, C. L. Induced pluripotent

stem cells: the new patient? *Nat. Rev. Mol. Cell Biol.* **13,** 713–26 (2012).

34. Soldner, F. *et al.* Generation of isogenic pluripotent stem cells differing exclusively at two early onset Parkinson point mutations. *Cell* **146,** 318–331 (2012).

35. Ruan, J.-L. *et al.* Mechanical Stress Promotes Maturation of Human Myocardium From Pluripotent Stem Cell-Derived Progenitors. *Stem Cells* **33,** 2148–2157 (2015).

36. Paci, M., Hyttinen, J., Rodriguez, B. & Severi, S. Human induced pluripotent stem cell-derived versus adult cardiomyocytes: An *in silico* electrophysiological study on effects of ionic current block. *Br. J. Pharmacol.* **172,** 5147–5160 (2015).

37. Devalla, H. D. *et al.* Atrial-like cardiomyocytes from human pluripotent stem cells are a robust preclinical model for assessing atrial-selective pharmacology. *EMBO Mol. Med.* **7,** 394–410 (2015).

38. Scheel, O. *et al.* Action Potential Characterization of Human Induced Pluripotent Stem Cell–Derived Cardiomyocytes Using Automated Patch-Clamp Technology. *Assay Drug Dev. Technol.* **12,** 457–469 (2014).

39. Gillie, D. J., Novick, S. J., Donovan, B. T., Payne, L. a. & Townsend, C. Development of a high-throughput electrophysiological assay for the human ether-à-go-go related potassium channel hERG. *J. Pharmacol. Toxicol. Methods* **67,** 33–44 (2013).

40. Dangman, K. H. *et al.* Electrophysiologic characteristics of human ventricular and Purkinje fibers. *Circulation* **65,** 362–8 (1982).

41. Siegel, M. S. & Isacoff, E. Y. A genetically encoded optical probe of membrane voltage. *Neuron* **19,** 735–741 (1997).

42. Zhang, M. *et al.* Recessive cardiac phenotypes in induced pluripotent stem cell models of Jervell and Lange-Nielsen syndrome: Disease mechanisms and pharmacological rescue. *Proc. Natl. Acad. Sci.* **111,** E5383–E5392 (2014).

43. Spira, M. E. & Hai, A. Multi-electrode array technologies for neuroscience and cardiology. *Nat. Nanotechnol.* **8,** 83–94 (2013).

44. Thompson, S. a. *et al.* Engraftment of human embryonic stem cell derived cardiomyocytes improves conduction in an arrhythmogenic *in vitro* model. *J. Mol. Cell. Cardiol.* **53,** 15–23 (2012).

45. Kim, J. J. *et al.* Mechanism of automaticity in cardiomyocytes derived from human induced pluripotent stem cells. *J. Mol. Cell. Cardiol.* **81,** 81–93 (2015).

46. Braam, S. R. *et al.* Repolarization reserve determines drug responses in human pluripotent stem cell derived cardiomyocytes. *Stem Cell Res.* **10,** 48–56 (2013).

47. Silei, V. *et al.* Measurement of intracellular calcium levels by the fluorescent Ca2+ indicator Calcium-Green. *Brain Res. Protoc.* **5,** 132–134 (2000).

48. Svoboda, K., Denk, W., Kleinfeld, D. & Tank, D. W. In vivo dendritic calcium dynamics in neocortical pyramidal neurons. *Nature* **385,** 161–165 (1997).

49. Zhang, X.-H. *et al.* Ca2+ signaling in human induced pluripotent stem cell-derived cardiomyocytes (iPS-CM) from normal and catecholaminergic polymorphic ventricular tachycardia (CPVT)-afflicted subjects. *Cell Calcium* **54,** 57–70 (2013).

50. Zhang, X.-H. & Morad, M. Calcium signaling in human stem cell-derived cardiomyocytes: Evidence from normal subjects and CPVT afflicted patients. *Cell Calcium* **59,** 98-107 (2016).

51. Chen, T.-W. *et al.* Ultrasensitive fluorescent proteins for imaging neuronal activity. *Nature* **499,** 295–300 (2013).

52. Herron, T. J., Lee, P. & Jalife, J. Optical Imaging of Voltage and Calcium in Cardiac Cells & Tissues. *Circ. Res.* **110,** 609–623 (2012).

53. Davies, C. H. *et al.* Reduced contraction and altered frequency response of isolated ventricular myocytes from patients with heart failure. *Circulation* **92,** 2540–2549 (1995).

54. Bray, M.-A. A., Sheehy, S. P. & Parker, K. K. Sarcomere alignment is regulated by myocyte shape. *Cell Motil. Cytoskeleton* **65,** 641–651 (2008).

55. Ribeiro, A. J. S. *et al.* Contractility of single cardiomyocytes differentiated from pluripotent stem cells depends on physiological shape and substrate stiffness. *Proc. Natl. Acad. Sci.* **112,** 12705–12710 (2015).

56. Nishimura, S. *et al.* Single cell mechanics of rat cardiomyocytes under isometric, unloaded, and physiologically loaded conditions. *Am. J. Physiol. Heart Circ. Physiol.* **287,** H196–H202 (2004).

57. Rape, A. D., Guo, W.-H. H. & Wang, Y.-L. L. The regulation of traction force in relation to cell shape and focal adhesions. *Biomaterials* **32,** 2043–2051 (2011).

58. Hersch, N. *et al.* The constant beat: cardiomyocytes adapt their forces by equal contraction upon environmental stiffening. *Biol. Open* **2,** 351–361 (2013).

59. Feinberg, A. W. *et al.* Controlling the contractile strength of engineered cardiac muscle by hierarchal tissue architecture. *Biomaterials* **33,** 5732–5741 (2012).

60. Grosberg, A. *et al.* Muscle on a chip: *In vitro* contractility assays for smooth and striated muscle. *J. Pharmacol. Toxicol. Methods* **65,** 126–135 (2012).

61. Hinson, J. T. *et al.* Titin mutations in iPS cells define sarcomere insufficiency as a cause of dilated cardiomyopathy. *Science* **349,** 982–986 (2015).

62. Kijlstra, J. D. *et al.* Integrated Analysis of Contractile Kinetics, Force Generation, and Electrical Activity in Single Human Stem Cell-Derived Cardiomyocytes. *Stem Cell Reports* **5,** 1226–1238 (2015).

63. Hayakawa, T. *et al.* Image-based evaluation of contraction–relaxation kinetics of human-induced pluripotent stem cell-derived cardiomyocytes: Correlation and complementarity with extracellular electrophysiology. *J. Mol. Cell. Cardiol.* **77,** 178–191 (2014).

64. Scott, C. W. *et al.* An impedance-based cellular assay using human iPSC-derived cardiomyocytes to quantify modulators of cardiac contractility. *Toxicol. Sci.* **142,** 331–338 (2014).

65. Lavi, R. *et al.* Low Energy Visible Light Induces Reactive Oxygen Species Generation and Stimulates an Increase of Intracellular Calcium Concentration in Cardiac Cells. *J. Biol. Chem.* **278,** 40917–40922 (2003).

66. Salameh, A. *et al.* Cyclic mechanical stretch induces cardiomyocyte orientation and polarization of the gap junction protein connexin43. *Circ. Res.* **106,** 1592–1602 (2010).

67. Salameh, A. & Dhein, S. Effects of mechanical forces and stretch on

intercellular gap junction coupling. *Biochim. Biophys. Acta - Biomembr.* **1828,** 147–156 (2013).

68. Dekker, R. *et al.* Living Chips and Chips for the living. in *2012 IEEE Bipolar/ BiCMOS Circuits and Technology Meeting (BCTM)* 1–9 (IEEE, 2012).

69. Wipff, P.-J. *et al.* The covalent attachment of adhesion molecules to silicone membranes for cell stretching applications. *Biomaterials* **30,** 1781–1789 (2009).

70. Radisic, M. *et al.* Functional assembly of engineered myocardium by electrical stimulation of cardiac myocytes cultured on scaffolds. *Proc. Natl. Acad. Sci. U. S. A.* **101,** 18129–18134 (2004).

71. Moe, G. W. & Armstrong, P. Pacing-induced heart failure: a model to study the mechanism of disease progression and novel therapy in heart failure. *Cardiovasc. Res.* **42,** 591–599 (1999).

72. Nagel, G. *et al.* Channelrhodopsin-2, a directly light-gated cation-selective membrane channel. *Proc. Natl. Acad. Sci. U. S. A.* **100,** 13940–13945 (2003).

73. Zhuge, Y. *et al.* Human pluripotent stem cell tools for cardiac optogenetics. *Conf Proc IEEE Eng Med Biol Soc* **2014,** 6171–6174 (2014).

74. Ullrich, S., Gueta, R., Nagel, G., Ullrich, S. & Gueta, R. Degradation of channelopsin-2 in the absence of retinal and degradation resistance in certain mutants. *Biol. Chem.* **394,** 271–280 (2013).

75. Birket, M. J. *et al.* Contractile Defect Caused by Mutation in MYBPC3 Revealed under Conditions Optimized for Human PSC-Cardiomyocyte Function. *Cell Rep.* **13,** 733–745 (2015).

76. Grosberg, A., Alford, P. W., McCain, M. L. & Parker, K. K. Ensembles of engineered cardiac tissues for physiological and pharmacological study: Heart on a chip. *Lab Chip* **11,** 4165 (2011).

77. Miller EW, Lin JY, Frady EP, et al. Optically monitoring voltage in neurons by photo-induced electron transfer through molecular wires. *Proc. Natl. Acad. Sci* **109,** 2114–2119 (2012).

78. Takahashi A, Camacho P, Lechleiter JD, et al. Measurement of intracellular calcium. *Physiol. Rev* **79,** 1089–1125 (1999).

79. Gong Y, Huang C, Li JZ, et al. High-speed recording of neural spikes in awake mice and flies with a fluorescent voltage sensor. *Science* **350,** 1361–1366 (2015).

Abstract

There are several methods to measure cardiomyocyte (CM) and muscle contraction but these require customized hardware, expensive apparatus and advanced informatics or can only be used in single experimental models. Consequently, data and techniques have been difficult to reproduce across models and laboratories, analysis is time consuming and only specialist researchers can quantify data. Here we describe and validate an automated, open source software tool (MUSCLEMOTION) adaptable for use with standard laboratory- and clinical imaging equipment that enables quantitative analysis of normal cardiac contraction, disease phenotypes and pharmacological responses. MUSCLEMOTION allowed rapid and easy measurement of movement from high-speed movies in: (i) 1-dimensional *in vitro* models such as isolated adult and human pluripotent stem cell-derived CMs (hPSC-CMs); (ii) 2-dimensional *in vitro* models, such as beating CM monolayers or small clusters of hPSC-CMs; (iii) 3-dimensional multicellular *in vitro* or *in vivo* contractile tissues such as cardiac "organoids", engineered heart tissues (EHT), zebrafish- and human hearts. MUSCLEMOTION was effective under different recording conditions (bright field microscopy with simultaneous patch clamp recording, phase contrast microscopy and traction force microscopy). Outcomes were virtually identical to the current gold standards for contraction measurement such as optical flow, pole deflection, edge-detection systems or manual analyses. Finally, we used the algorithm to quantify contraction in *in vitro* and *in vivo* arrhythmia models and to measure pharmacological responses. Using a single open source method for processing video recordings, we obtained reliable pharmacological data and measures of cardiac disease phenotype in experimental cell-, animal- and human models.

Chapter 3

MUSCLEMOTION: a versatile open software tool to quantify cardiomyocyte and cardiac muscle contraction *in vitro* and *in vivo*

Modified after Circulation Research 122, e5-e16 (2018)

Berend van Meer#, Luca Sala#, Leon Tertoolen, Jeroen Bakkers, Milena Bellin, Richard Davis, Chris Denning, Michel Dieben, Thomas Eschenhagen, Elisa Giacomelli, Catarina Grandela, Arne Hansen, Eduard Holman, Monique Jongbloed, Sarah Kamel, Lotte Koopman, Quintin Lachaud, Ingra Mannhardt, Mervyn Mol, Diego Mosqueira, Valeria Orlova, Robert Passier, Marcelo Ribeiro, Umber Saleem, Godfrey Smith*, Francis Burton*, Christine Mummery*

# these authors contributed equally to this work
* these authors contributed equally to this work

Introduction

The salient feature of cardiomyocytes (CMs) is their ability to undergo cyclic contraction and relaxation, a feature critical for cardiac function. In many research laboratories and clinical settings it is therefore essential that cardiac contraction can be quantified at multiple levels, from single cells to multicellular or intact cardiac tissues. Measurement of contractility is relevant for analysis of disease phenotypes, cardiac safety pharmacology, and longitudinal measures of cardiac function over time, both *in vitro* and *in vivo*. In addition, human genotype-phenotype correlations, investigation of cardiac disease mechanisms and the assessment of cardiotoxicity are increasingly performed on human induced pluripotent stem cells (hiPSCs) derived from patients[1-3]. Many of these studies are carried out in non-specialist laboratories so that it is important that analysis methods are simplified such that they can be used anywhere with access to just standard imaging equipment. Here, we describe a single method with high versatility that can be applied to most imaging outputs of cardiac contraction likely to be encountered in the laboratory or clinic.

Electrical and calcium signals are usually quantified *in vitro* using established technologies such as patch clamp electrophysiology, multi electrode arrays (MEAs), cation-sensitive dyes or cation-sensitive genetic reporters[4]. Although experimental details differ among laboratories, the values for these parameters are with some approximations comparable across laboratories, cardiomyocyte source and cell culture configuration (e.g. single cells, multicellular 2-Dimensional (2D) CM monolayers, 3-Dimensional (3D) cultures)[5,6]. However, there is no comparable method for measuring cardiac contraction across multiple platforms, despite this being a crucial functional parameter affected by many diseases or drugs[7]. We have developed a method to address this that is built on existing algorithms and is fully automated, but most importantly can be used on videos, image stacks or image sequences loaded in the open source image processing program ImageJ[8]. Moreover, it is an open source, dynamic platform that can be expanded, improved and integrated for customized applications. The method, called MUSCLEMOTION, determines dynamic changes in pixel intensity between image frames and expresses the output as a relative measure of movement during muscle contraction and relaxation. We applied the concept to a range of biomedical- and pharmacologically relevant experimental models that included single hPSC-CMs, patterned- or 2D cultures of hPSC-CMs, cardiac organoids, engineered heart tissues (EHTs) and isolated adult rabbit CMs. Results were validated by comparing outputs of the tool with those from three established methods for measuring contraction: optical flow, post deflection and fractional shortening of sarcomere length. These methods have been tailored to (or only work on) specific cell configurations. Traction force microscopy, fractional shortening of sarcomere length and microposts are predominantly suitable for single cells[8,9]. Cardiomyocyte edge or perimeter detection is suitable for adult CMs but challenging for immature hPSC-CMs due to poorly defined plasma membrane borders and concentric contraction[10], while large post deflection is suitable for EHTs or small cardiac bundles[11] but less so for single cells. Our MUSCLEMOTION software by contrast can be used for all of these applications without significant adaptions. Furthermore, it can be used for multi-parameter recording conditions and experimental settings using transmitted light microscopy, fluorescent membrane labeling, fluorescent beads

embedded in soft substrates or patch clamp video recordings. Drug responses to positive and negative inotropic agents were evaluated across four different laboratories in multiple cell configurations using MUSCLEMOTION with reliable predictions of drug effects from all laboratories. Furthermore, MUSCLEMOTION was also applicable to optical recordings of zebrafish hearts *in vivo*, where it represented a significant time-saving in analysis, and in human echocardiograms. This versatile tool thus provides a rapid and straightforward way to detect disease phenotypes and pharmacological responses *in vitro* and *in vivo.*

Results

Algorithm development

The principle underlying the algorithm of MUSCLEMOTION is the assessment of contraction using an intuitive approach quantifying absolute changes in pixel intensity between a reference frame and the frame of interest, which can be described as

$$|img_i - img_{ref}| = img_{result}$$

where is the frame of interest, is the reference frame and is the resulting image. For every pixel in the frame, each reference pixel is subtracted from the corresponding pixel of interest and the difference is presented in absolute numbers. Unchanged pixels result in low (black) values, while pixels that are highly changed result in high (white) values (Figure 1a). Next, the mean pixel intensity of the resulting image is measured. This is a quantitative measure of how much the pixels have moved compared to the reference frame: more white pixels indicate more changing pixels and, thus, more displacement. When a series of images is analysed relative to the same reference image, the output describes the accumulated displacement over time (measure of displacement, Figure 1b).

However, if a series of images is analysed with a reference frame that depends on the frame of interest (e.g. $img_{ref} = img_{i-1}$), this results in a measure of the relative displacement per interframe interval. We defined this parameter as contraction velocity (measure of velocity, Figure 1b).

Since velocity is the first derivative of displacement in time, the first derivative of the measure of displacement should resemble the measure of velocity derived from image calculations. To test the linearity of the method, three movies of moving blocks were analysed. The block moved back and forth at two different speeds in each direction (where): i) along the x-axis, ii) along the y-axis and iii) along both axes (Supplementary Movie 1). As expected, the measure of displacement and velocity showed a linear correlation (Supplementary Figure 1). This does not hold when the position of the block in does not overlap the position of the block in , with a consequent saturation in the measure of displacement (i.e. max pixel white value, Supplementary Figure 2). Therefore, comparison of the differentially derived velocities should approximately overlap in the absence of pixel saturation. This was used as a qualitative parameter to determine whether the algorithm outputs were reliable.

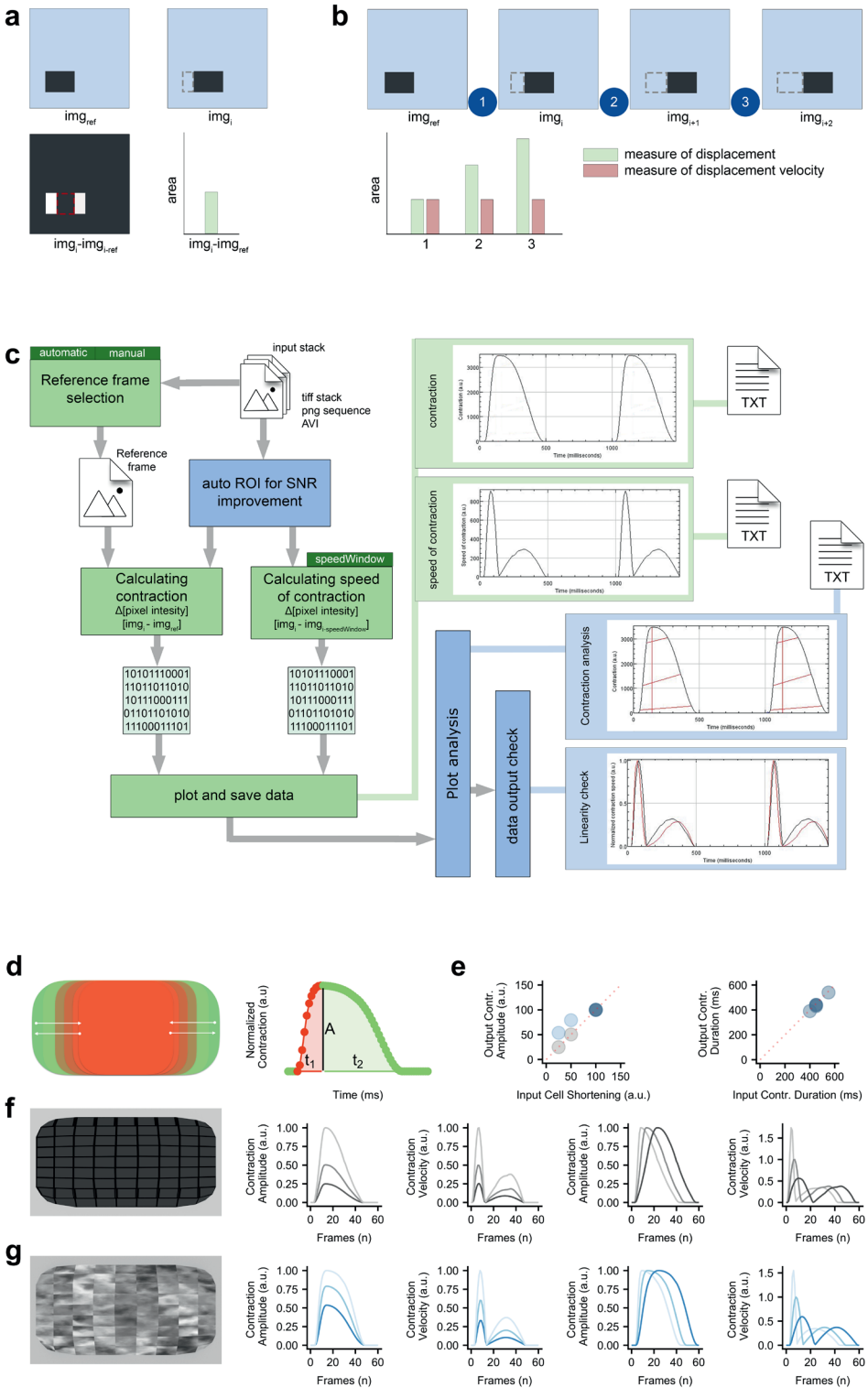
a
b
c
d
e
f
g
automatic
manual
Reference frame selection
input stack
tiff stack
png sequence
AVI
Reference frame
auto ROI for SNR improvement
speedWindow
Calculating contraction
Δ[pixel intesity]
Calculating speed of contraction
Δ[pixel intesity]
plot and save data
Plot analysis
data output check
contraction
speed of contraction
Contraction analysis
Linearity check
TXT
measure of displacement
measure of displacement velocity
area
Normalized Contraction (a.u)
Time (ms)
Output Contr. Amplitude (a.u.)
Input Cell Shortening (a.u.)
Output Contr. Duration (ms)
Input Contr. Duration (ms)
Contraction Amplitude (a.u.)
Contraction Velocity (a.u.)
Frames (n)

Algorithm implementation

MUSCLEMOTION was then modified to handle typical experimental recordings by (i) improving the signal-to-noise ratio (SNR), (ii) automating reference frame selection and (iii) programming built-in checks to validate the generated output data (Figure 1c). The SNR was increased by isolating the pixels of interest in a three-step process: i) maximum projection of pixel intensity in the complete contraction stack, ii) creation of a binary image of this maximum projection with a threshold level equal to the mean grey value plus standard deviation and iii) multiplication of the pixel values in this image by the original contraction and speed of the contraction image stack (Supplementary Figure 3). This process allowed the algorithm to work on a region of interest with movement above the noise level only.

Next, a method was developed to identify the correct from the speed of contraction image stack by comparing values obtained from the frame-to-frame calculation with their direct neighbouring values, while also checking for the lowest absolute value (Supplementary Figure 4).

The reliability of MUSCLEMOTION for structures with complex movements was validated using a custom-made contracting 3D "synthetic CM" model (Figure 1d,f,g) that was adapted to produce contractions with known amplitude and duration. Linearity was preserved during the analysis of the contraction and velocity; other output parameters of the analysis matched the input parameters (Figure 1e). A second 3D model (Figure 1g), with a repetitive pattern aimed to create out-of-bounds problems was also generated. As expected, contraction amplitude information here was not linear (Figure 1e), although contraction velocity and temporal parameters did remain linear (Figure 1e,g). To mitigate this problem, we implemented an option for a 10-sigma

Figure 1: Algorithm construction and validation.

a) Principle of pixel intensity difference by subtraction of imgref of imgi and measurement of the non-zero area after image subtraction. b) Principle of using pixel intensity difference as a measure of displacement and as a measure of displacement velocity. c) Schematic overview of MUSCLEMOTION. Green blocks indicate basic steps of the algorithm. Dark green blocks indicate important user input choices. Plots within light green blocks indicate results. Optional steps are shown in blue blocks, with graphical representation of the analysed parameters indicated by red lines. Three result files are generated containing the raw data: "contraction.txt", "speed-of-contraction.txt" and "overview-results.txt". Furthermore, three images showing relevant traces and a log file are generated and saved (not shown in schematic). d) Schematic of the contractile pattern of the artificial cell and relative parameters corresponding to amplitude of contraction (A), time-to-peak (t1) and relaxation time (t2). e) Correlation between input (x axis) and output (y axis) parameters used to validate MUSCLEMOTION with two artificial cells. f-g) Frame representing the two artificial cells built for MUSCLEMOTION validation and their relative output parameters.

Gaussian blur filter that can be applied on demand to biological samples that presented highly repetitive patterns (e.g. sarcomeres in adult CMs).

Algorithm application to multiple cell configurations and correlation with existing gold standards

This set of experiments aimed to investigate the versatility of MUSCLEMOTION and examine how its performance compared with standard measures used in each system: i) optical flow for isolated hPSC-CMs, monolayers and organoids; ii) post deflection for EHT; iii) sarcomere length fractional shortening for adult CMs. Remarkably, standard methods currently used measure only contraction or contraction velocity. Linearity was preserved in all cases during the analyses, demonstrating the reliability of the results (Supplementary Figure 5).

First, single hPSC-CMs (Figure 2a, Supplementary Movie 2) exhibited concentric contraction (Figure 2a ii) and contraction velocity amplitudes correlated well with the amplitudes obtained by optical flow analysis ($R^2 = 0.916$) (Figure 2a v). In contrast to single cells, the area of contraction for hPSC-CM monolayers was distributed heterogeneously throughout the whole field (Figure 2b ii, Supplementary Movie 3). Optical flow analysis was compared with our measure of velocity (Figure 2b iv); this showed a good linear correlation ($R^2 = 0.803$) (Figure 2b v). Complex (mixed, multicellular) 3D configurations were also investigated by analyzing hPSC-derived cardiac organoids[18] (Supplementary Movie 4) and EHTs[15] (Supplementary Movie 5). Cardiac organoids showed moderate levels of contraction throughout the tissue (Figure 2c ii), while the EHTs showed high deflection throughout the bundle (Figure 2d ii). The contraction velocity of the organoids correlated well with the output of optical flow analysis ($R^2 = 0.747$, Figure 2c v). Similarly, contraction amplitudes in EHTs showed high linear correlation ($R^2 = 0.879$) with the absolute force values derived from measurement of pole deflection (Figure 2d v). Finally, single adult rabbit ventricular CMs were analyzed (Figure 2e, Supplementary Movie 6). Large movement was evident around the long edges of the CM (Figure 2e ii). These cells were analyzed with a 10-sigma Gaussian blur filter, which also minimized (unwanted) effects of transverse movements on contraction patterns. Linearity was preserved (Supplementary Figure 5) despite the repetitive pattern of the sarcomeres and this resulted in accurate measures of both contraction (Figure 2e iii) and speed of contraction (Figure 2e iv). The contraction amplitude of the adult CMs stimulated at 1 Hz correlated well with the output of sarcomeric shortening using fast Fourier transform analysis[23] ($R^2 = 0.871$, Figure 2e v). Thus, the MUSCLEMOTION algorithm yielded data in these initial studies comparable with methods of analysis tailored for the individual platforms.

Application of MUSCLEMOTION to multiple imaging and recording platforms

To examine whether MUSCLEMOTION could potentially be used in applications that measure other aspects of CMs functionality in parallel, we first determined the electrophysiological properties of hPSC-CMs using patch clamp whilst recording their contractile properties through video imaging. This allowed simultaneous quantitative measurement of action potentials (APs) and contraction (Figure 3a), for in-depth investigation of their interdependence. We observed a typical[24] profile of AP followed by its delayed contraction.

To measure contractile force in combination with contractile velocity in single CMs, we integrated fluorescent beads into polyacrylamide substrates patterned with gelatin (Figure 3b), where the displacement of the beads is a measure of CM contractile force[20] (Supplementary Movie 7). Additionally, field potentials and contraction profiles of hPSC-CMs were analyzed from simultaneous electrical and video recordings of monolayers plated on MEAs (Figure 3c, Supplementary Movie 8).

Similarly, effective quantification of contraction profiles was obtained for fluorescently labeled hPSC-CM monolayer cultures (Figure 3d, Supplementary Movie 9), allowing MUSCLEMOTION to be integrated on high speed fluorescent microscope systems for automated data analysis.

Application of MUSCLEMOTION to drug responses in different cell models in different laboratories

Having shown that MUSCLEMOTION was fit-for-purpose in analyzing contraction over a variety of platforms, we next sought to demonstrate its ability to detect the effects of positive and negative inotropes. This is essential for ensuring the scalability of the tool over multiple platforms, particularly in the context of hiPSC-CMs where regulatory authorities and pharmaceutical companies are interested in using these cells as human heart models for drug discovery, target validation or safety pharmacology[25]. For isoprenaline (ISO) and nifedipine (NIFE) the main parameters of interest are: contraction amplitude (ISO, NIFE), relaxation time (ISO) and contraction duration (NIFE).

The relaxation time of spontaneously beating isolated hPSC-CMs on gelatin patterned polyacrylamide substrates treated with ISO significantly decreased as expected at doses higher than 1 nM. Similar to what has been reported[27], contraction amplitude decreased at doses higher than 1 nM. NIFE treatment decreased both contraction amplitude and duration starting from 3 nM, respectively (Figure 4a). In paced (1.5 Hz) hPSC-CMs monolayers, no significant effects were measured after addition of ISO on either relaxation time or contraction amplitude. NIFE caused a progressive decrease in contraction duration and amplitude in a concentration-dependent manner starting at 100 nM (Figure 4b). Similarly, cardiac organoids paced at 1.5 Hz showed no significant effects on both relaxation time and contraction amplitude with ISO, while both parameters decreased after NIFE, starting from 100 nM and 300 nM, respectively (Figure 4c). EHTs paced at 1.5 times baseline frequency and analyzed with MUSCLEMOTION showed a positive inotropic effect starting from 1 nM ISO and a negative inotropic effect starting at 30 nM NIFE as previously reported[15] (Figure 4d).

Paced (1 Hz) adult rabbit CMs exhibited no significant increase in relaxation time and contraction amplitude at any ISO concentration. At concentrations higher than 3 nM, adult CMs exhibited after-contractions and triggered activity during diastole, which hampered their ability to be paced at a fixed frequency. No significant effects were observed on contraction duration with NIFE, while contraction amplitude significantly decreased in a dose-dependent manner starting from 100 nM (Figure 4e). Data generated by post deflection and sarcomere fractional shortening are available for comparison purposes in Supplementary Figure 6.

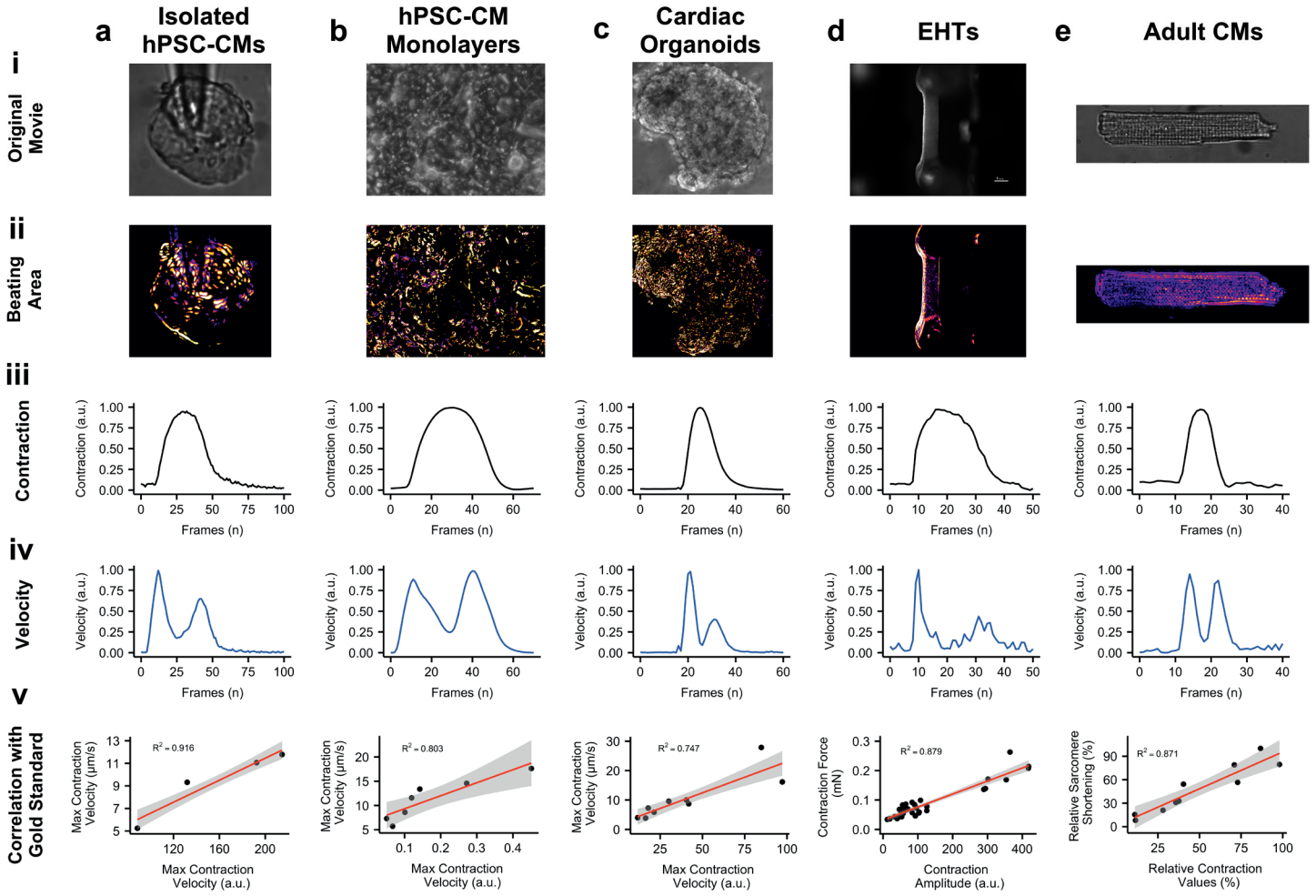
a Isolated hPSC-CMs
b hPSC-CM Monolayers
c Cardiac Organoids
d EHTs
e Adult CMs
i Original Movie
ii Beating Area
iii Contraction
iv Velocity
v Correlation with Gold Standard
Contraction (a.u.)
Velocity (a.u.)
Frames (n)
Max Contraction Velocity (µm/s)
Max Contraction Velocity (a.u.)
Contraction Force (mN)
Contraction Amplitude (a.u.)
Relative Sarcomere Shortening (%)
Relative Contraction Values (%)
R² = 0.916
R² = 0.803
R² = 0.747
R² = 0.879
R² = 0.871

Analysis of disease phenotypes *in vitro*

Contractility of hiPSC-CMs carrying mutations associated with Long QT Syndrome Type 1 (LQT1)[26] and hypertrophic cardiomyopathy (HCM) were characterized in distinct cell configurations: monolayers plated on MEAs and EHTs, respectively. As demonstrated previously, LQT1 phenotype was captured as a prolongation of the QT interval of the field potential[17,26]. As expected, contraction duration measured with MUSCLEMOTION was also prolonged (Figure 5a,b). EHTs were fabricated from an isogenic triplet carrying the $MYH7^{R453C}$ mutation either in homozygosity or heterozygosity and showed a gene dosage effect on the contractility recapitulating disease severity.

Analysis of disease phenotypes *in vivo*

To extend analysis to hearts *in vivo*, we took advantage of the transparency of zebrafish, which allows recording of contracting cardiac tissue *in vivo* (Figure 6a, Supplementary Movie 10). It was previously shown that mutations in G protein β subunit 5 (GNB5) are associated with a multisystem syndrome in human, with severe bradycardia at rest. Zebrafish with loss of function mutations in gnb5a and gnb5b were generated. Consistent with the syndrome manifestation in patients, zebrafish gnb5a/gnb5b double mutant embryos showed severe bradycardia in response to parasympathetic activation[22]. Irregularities in heart rate were visually evident and were clearly

Figure 2: Correlation of results with gold standards.

a) Brightfield image of isolated hPSC-CMs (i), with maximum projection step visually enhanced with a fire Look Up Table (ii), contraction (iii) and velocity (iv) profiles of each individual beat have been generated by MUSCLEMOTION and temporally aligned; linear regression analysis between MUSCLEMOTION results (x-axis) and optical flow results (y-axis) (v). b) Phase contrast image of hPSC-CM monolayers (i), with maximum projection step visually enhanced with a fire Look Up Table (ii), contraction (iii) and velocity (iv) profiles of each individual beat have been generated by MUSCLEMOTION and temporally aligned; linear regression analysis between MUSCLEMOTION results (x-axis) and those obtained with optical flow results (y-axis) (v). c) Phase contrast image of cardiac organoids (i), with maximum projection step visually enhanced with a fire Look Up Table (ii), contraction (iii) and velocity (iv) profiles of each individual beat have been generated by MUSCLEMOTION and temporally aligned; linear regression analysis between MUSCLEMOTION results (x-axis) and those obtained with optical flow results (y-axis) (v). d) Live view of an EHT during contraction analysis. Scale bar = 1 mm. (i), with maximum projection step visually enhanced with a fire Look Up Table (ii), contraction (iii) and velocity (iv) profiles of each individual beat have been generated by MUSCLEMOTION and temporally aligned; linear regression analysis between MUSCLEMOTION results (x-axis) and those obtained with post deflection (y-axis) (v). e) Brightfield image of adult rabbit CMs (i), with maximum projection step visually enhanced with a fire Look Up Table (ii); contraction (iii) and velocity (iv) profiles of each individual beat have been generated by MUSCLEMOTION and temporally aligned; linear regression analysis between MUSCLEMOTION results (x-axis) and those obtained from sarcomere fractional shortening calculation with Fast Fourier Transform (y-axis) (v).

For details on cell sources and cell lines please refer to the Supplementary Table 1.

distinguishable from the wild type counterpart after analysis with MUSCLEMOTION (Figure 6b). Quantification of the heart rate of these zebrafishes with MUSCLEMOTION highly correlated (R^2 = 0.98) with the results of the published manual analyses[22] (Figure 6c). There was however, a striking time-saving for operators in carrying out the analysis using the algorithm (5-10 times faster than manual analysis; 150 recordings were analysed in 5 hours versus 4 days) without compromising accuracy of the outcome. Qualitative analysis of contraction patterns allowed rapid discrimination between arrhythmic vs non-arrhythmic responses to carbachol treatment (Figure 6c).

Finally, we examined human echocardiograms from five healthy and cardiomyopathic individuals (Figure 6d, Supplementary Movie 11). To assess ventricular function, videos were cropped to exclude movement contributions of the atria and valves. MUSCLEMOTION enabled rapid quantification of temporal parameters from standard ultrasound echography (Figure 6e) such as time-to-peak, relaxation time, RR interval and the contraction duration (Figure 6f).

Discussion

A reliable and easy-to-use method to quantify cardiac muscle contraction would be of significant benefit to many basic and clinical science laboratories to characterize cardiac disease phenotypes, understand underlying disease mechanisms and predicting cardiotoxic effects of drugs[15,27]. Quantification of frame-to-frame differences in pixel intensity has been used in recent reports with success[10]; however, the full spectrum of applications for which these algorithms are relevant, how their output data correlates with gold standards in each system and software performance, specifications, license and software availability, have remained unclear.

Here we developed and tested a user-friendly, inexpensive, open source software platform that serves this purpose in a variety of biological systems of heart tissue. Its integration into current research practices would benefit data sharing, reproducibility, comparison and translation in many clinically relevant contexts[28].

The linearity and reliability of MUSCLEMOTION were validated using a 3D reconstructed artificial CM which gave the expected linear correlations between known inputs and the outputs (Figure 1d-f). When random repetitive patterns were applied, amplitude outputs differed from inputs, suggesting a potential limitation to measuring contraction amplitudes in highly repetitive biological samples (such as when sarcomere patterns are well-organized), while temporal parameters remained valid (Figure 1d,e,g). However, conditions such as these would be unlikely in standard biological samples, where camera noise significantly reduces the possibility of saturating pixel movement. We partially attenuated this problem by applying, on user demand, a 10-sigma Gaussian blur filter which significantly increased the accuracy of MUSCLEMOTION with highly repetitive structures. Also, to increase reliability, we built in additional controls to detect any mismatches and errors. MUSCLEMOTION can automatically identify and select the reference frame and increase the signal-to-noise-ratio, features which were particularly relevant in reducing user bias and interaction while improving user experience. MUSCLEMOTION is valid in a wide range of illumination conditions without changing

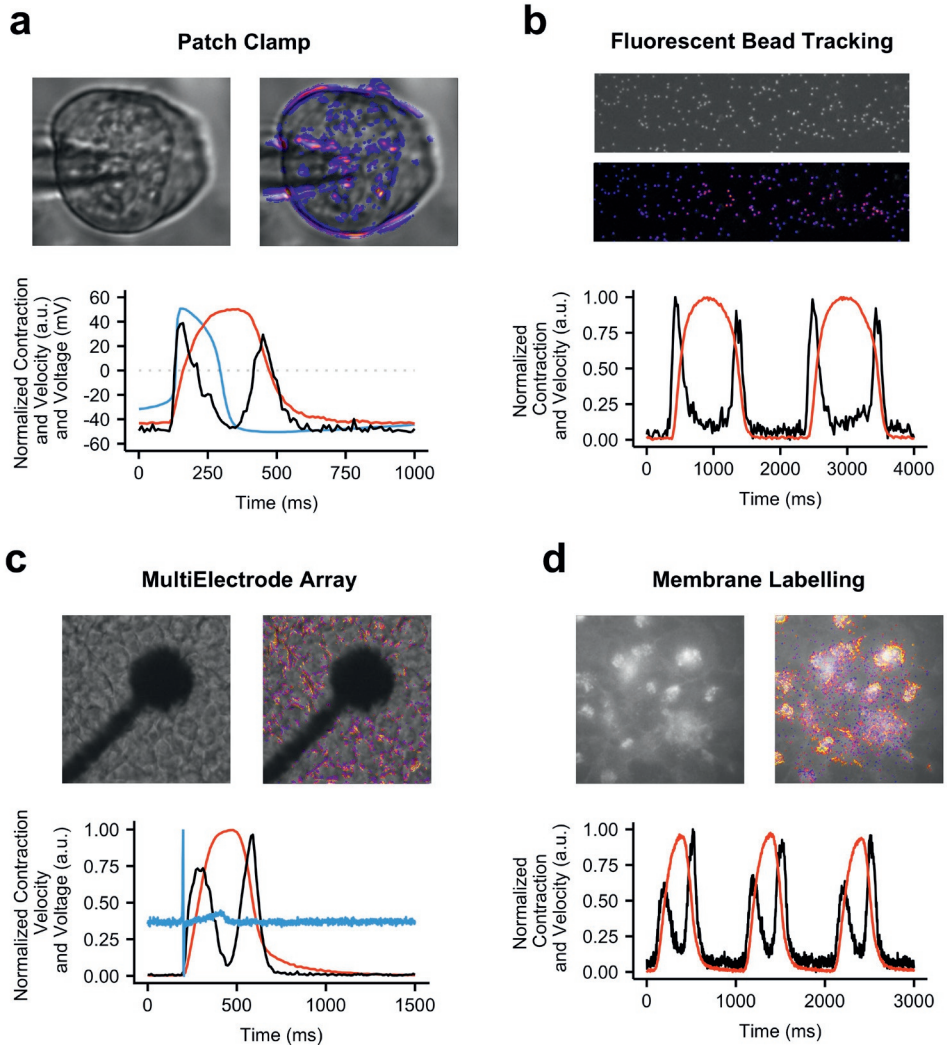

Figure 3: Application of contraction tool to multiple biological situations.

Representative examples with enhancement of moving pixels (top) and profiles (bottom) of contraction (a-d, red), velocity (a-d, black) and voltage (a, c, blue) respectively obtained from high speed movies of patched hPSC-CMs (a), aligned hPSC-CMs on polyacrylamide gels with fluorescent beads (b), monolayers of hiPSC-CMs seeded on MEAs (c) and hPSC-CMs whose membranes have been labelled with CellMask Deep Red (d).

For details on cell sources and cell lines please refer to the Supplementary Table 1.

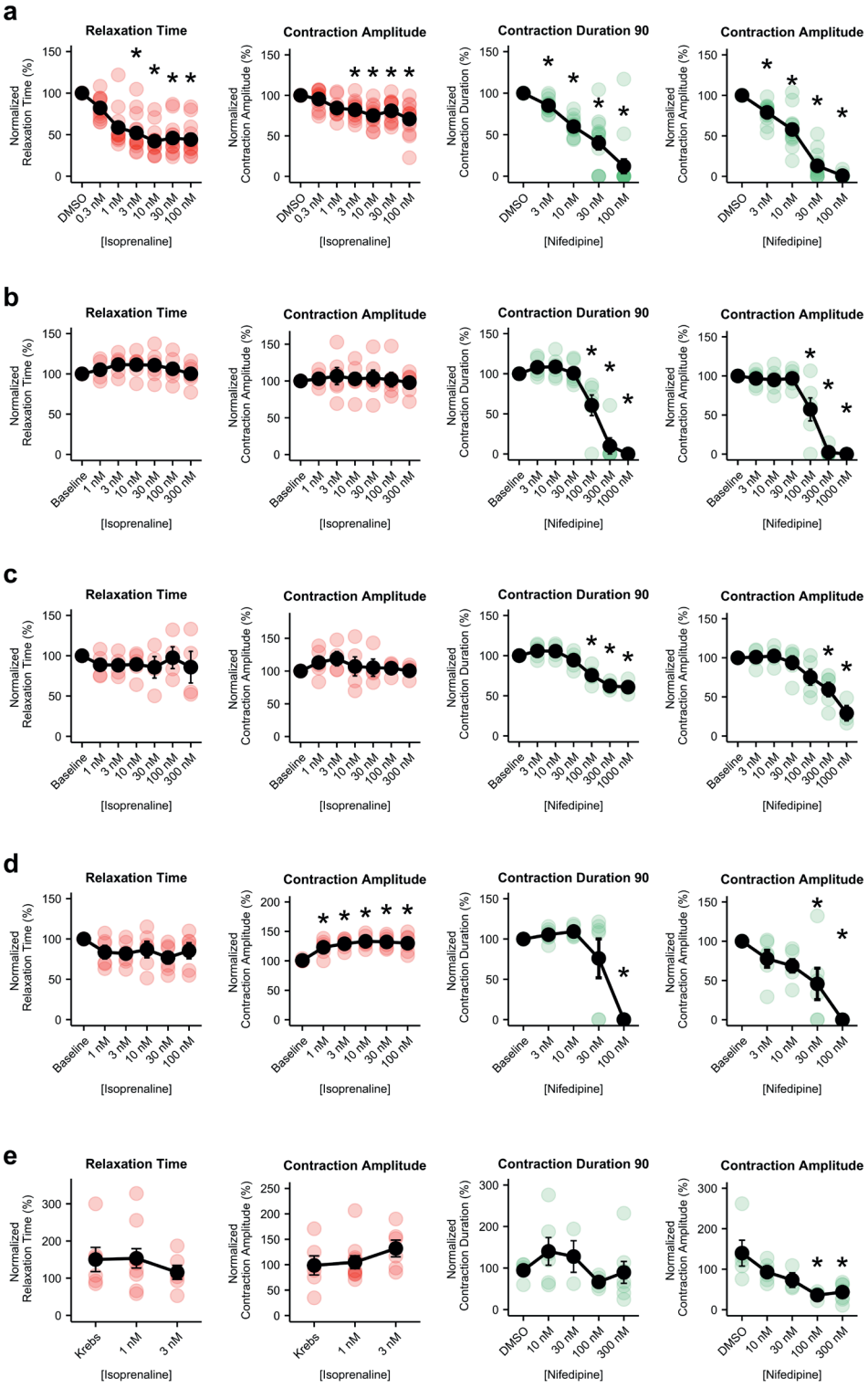
a
Relaxation Time
Normalized Relaxation Time (%)
DMSO 0.3 nM 1 nM 3 nM 10 nM 30 nM 100 nM
[Isoprenaline]
Contraction Amplitude
Normalized Contraction Amplitude (%)
DMSO 0.3 nM 1 nM 3 nM 10 nM 30 nM 100 nM
[Isoprenaline]
Contraction Duration 90
Normalized Contraction Duration (%)
DMSO 3 nM 10 nM 30 nM 100 nM
[Nifedipine]
Contraction Amplitude
Normalized Contraction Amplitude (%)
DMSO 3 nM 10 nM 30 nM 100 nM
[Nifedipine]
b
Relaxation Time
Normalized Relaxation Time (%)
Baseline 1 nM 3 nM 10 nM 30 nM 100 nM 300 nM
[Isoprenaline]
Contraction Amplitude
Normalized Contraction Amplitude (%)
Baseline 1 nM 3 nM 10 nM 30 nM 100 nM 300 nM
[Isoprenaline]
Contraction Duration 90
Normalized Contraction Duration (%)
Baseline 3 nM 10 nM 30 nM 100 nM 300 nM 1000 nM
[Nifedipine]
Contraction Amplitude
Normalized Contraction Amplitude (%)
Baseline 3 nM 10 nM 30 nM 100 nM 300 nM 1000 nM
[Nifedipine]
c
Relaxation Time
Normalized Relaxation Time (%)
Baseline 1 nM 3 nM 10 nM 30 nM 100 nM 300 nM
[Isoprenaline]
Contraction Amplitude
Normalized Contraction Amplitude (%)
Baseline 1 nM 3 nM 10 nM 30 nM 100 nM 300 nM
[Isoprenaline]
Contraction Duration 90
Normalized Contraction Duration (%)
Baseline 3 nM 10 nM 30 nM 100 nM 300 nM 1000 nM
[Nifedipine]
Contraction Amplitude
Normalized Contraction Amplitude (%)
Baseline 3 nM 10 nM 30 nM 100 nM 300 nM 1000 nM
[Nifedipine]
d
Relaxation Time
Normalized Relaxation Time (%)
Baseline 1 nM 3 nM 10 nM 30 nM 100 nM
[Isoprenaline]
Contraction Amplitude
Normalized Contraction Amplitude (%)
Baseline 1 nM 3 nM 10 nM 30 nM 100 nM
[Isoprenaline]
Contraction Duration 90
Normalized Contraction Duration (%)
Baseline 3 nM 10 nM 30 nM 100 nM
[Nifedipine]
Contraction Amplitude
Normalized Contraction Amplitude (%)
Baseline 3 nM 10 nM 30 nM 100 nM
[Nifedipine]
e
Relaxation Time
Normalized Relaxation Time (%)
Krebs 1 nM 3 nM
[Isoprenaline]
Contraction Amplitude
Normalized Contraction Amplitude (%)
Krebs 1 nM 3 nM
[Isoprenaline]
Contraction Duration 90
Normalized Contraction Duration (%)
DMSO 10 nM 30 nM 100 nM 300 nM
[Nifedipine]
Contraction Amplitude
Normalized Contraction Amplitude (%)
DMSO 10 nM 30 nM 100 nM 300 nM
[Nifedipine]

temporal parameters; however, exposure time was linearly correlated with contraction amplitude (Supplementary Figure 7). Furthermore, a series of conditions in which there is no contraction has been used as a negative control (Supplementary Figure 8). Batch mode analyses and data storage in custom folders were also incorporated to support overnight automated analyses. For accurate quantification of amplitude, time-to-peak and relaxation time, an appropriate sampling rate should be chosen. For applications similar to those described here, we recommend recording rates higher than 70 frames per second to sample correctly the fast upstroke of the time-to-peak typical of cardiac tissue. This recording rate is easily achievable even using smartphone slow motion

Figure 4: Pharmacological challenge with positive and negative inotropic compounds.

a) Average dose-response curves (black traces) and single measurements for several parameters obtained in isolated, spontaneously beating, aligned hPSC-CMs treated with isoprenaline (left, red) and nifedipine (right, green). b) Average dose-response curves (black traces) and single measurements for several parameters obtained from monolayers of hPSC-CMs treated with isoprenaline (left, red) and nifedipine (right, green). c) Average dose-response curves (black traces) and single measurements for several parameters obtained in cardiac organoids treated with isoprenaline (left, red) and nifedipine (right, green). d) Average dose-response curves (black traces) and single measurements for several parameters obtained in EHTs treated with isoprenaline (left, red) and nifedipine (right, green). e) Average dose-response curves (black traces) and single measurements for several parameters obtained in adult rabbit CMs treated with isoprenaline (left, red) and verapamil (right, green).

Average data points (black) represent mean ± standard error of mean. For details on cell sources and cell lines please refer to the Supplementary Table 1.

Data information: P-values DMSO versus dose. Panel a i) 0.3 nM: 0.2897; 1 nM: $3.4{\cdot}10^{-6}$; 3 nM: $3.8{\cdot}10^{-8}$; 10 nM: $7{\cdot}10^{-11}$; 30 nM: $7.3{\cdot}10^{-10}$; 100 nM: $2.4{\cdot}10^{-10}$. Panel a ii) 0.3 nM: 1; 1 nM: 0.0645; 3 nM: 0.0136; 10 nM: $8.2{\cdot}10^{-5}$; 30 nM: 0.0063; 100 nM: $2.4{\cdot}10^{-6}$. (N=14; 14; 14; 14; 14; 14; 14) Panel a iii) 3 nM: 0.6533; 10 nM: $4{\cdot}10^{-5}$; 30 nM: $2{\cdot}10^{-9}$; 100 nM: $1.5{\cdot}10^{-15}$. Panel a iv) 3 nM: 0.00054; 10 nM: $1.9{\cdot}10^{-11}$; 30 nM: $< 2{\cdot}10^{-16}$; 100 nM: $< 2{\cdot}10^{-16}$. (N=14; 14; 14; 14; 14) P-values baseline versus dose. Panel b i) 1 nM: 1; 3 nM: 1; 10 nM: 1; 30 nM: 1; 100 nM: 1; 300 nM: 1. Panel b ii) 1 nM: 1; 3 nM: 1; 10 nM: 1; 30 nM: 1; 100 nM: 1; 300 nM: 1. (N=6; 5; 6; 6; 6; 6; 6) Panel b iii) 3 nM: 1; 10 nM: 1; 30 nM: 1; 100 nM: 0.00801; 300 nM: $2.7{\cdot}10^{-9}$; 1000 nM: $1.8{\cdot}10^{-10}$. Panel b iv) 3 nM: 1; 10 nM: 1; 30 nM: 1; 100 nM: 0.00084; 300 nM: $2.9{\cdot}10^{-11}$; 1000 nM: $1.5{\cdot}10^{-11}$. (N=6; 6; 6; 6; 6; 6) P-values baseline versus dose. Panel c i) 1 nM: 1; 3 nM: 1; 10 nM: 1; 30 nM: 1; 100 nM: 1; 300 nM: 1. Panel c ii) 1 nM: 1; 3 nM: 1; 10 nM: 1; 30 nM: 1; 100 nM: 1; 300 nM: 1. (N=5; 5; 4; 5; 4; 4; 4) Panel c iii) 3 nM: 1; 10 nM: 1; 30 nM: 1; 100 nM: 0.00181; 300 nM: $2.9{\cdot}10^{-6}$; 1000 nM: $1.7{\cdot}10^{-5}$. Panel c iv) 3 nM: 1; 10 nM: 1; 30 nM: 1; 100 nM: 0.54836; 300 nM: 0.01392; 1000 nM: $8.2{\cdot}10^{-5}$. (N=5; 5; 4; 5; 5; 5; 3) P-values baseline versus dose. Panel d i) 1 nM: 1; 3 nM: 1; 10 nM: 1; 30 nM: 0.47; 100 nM: 1. Panel d ii) 1 nM: 0.02318; 3 nM: 0.00170; 10 nM: 0.00028; 30 nM: 0.00044; 100 nM: 0.00113. (N=5; 5; 5; 5; 5; 5). Panel d iii) 3 nM: 1; 10 nM: 1; 30 nM: 1; 100 nM: $3{\cdot}10^{-5}$. Panel d iv) 3 nM: 1; 10 nM: 0.49856; 30 nM: 0.01473; 100 nM: $7{\cdot}10^{-6}$. (N=6; 6; 6; 6; 6) P-values Krebs versus dose. Panel e i) 1 nM: 1; 3 nM: 1. Panel e ii) 1 nM: 1; 3 nM: 0.54. (N=6; 10; 7) P-values DMSO versus dose. Panel e iii) 10 nM: 1; 30 nM: 1; 100 nM: 1; 300 nM: 1. Panel e iv) 10 nM: 0.5298; 30 nM: 0.2470; 100 nM: 0.0054; 300 nM: 0.0029. (N=7; 8; 4; 5; 7).

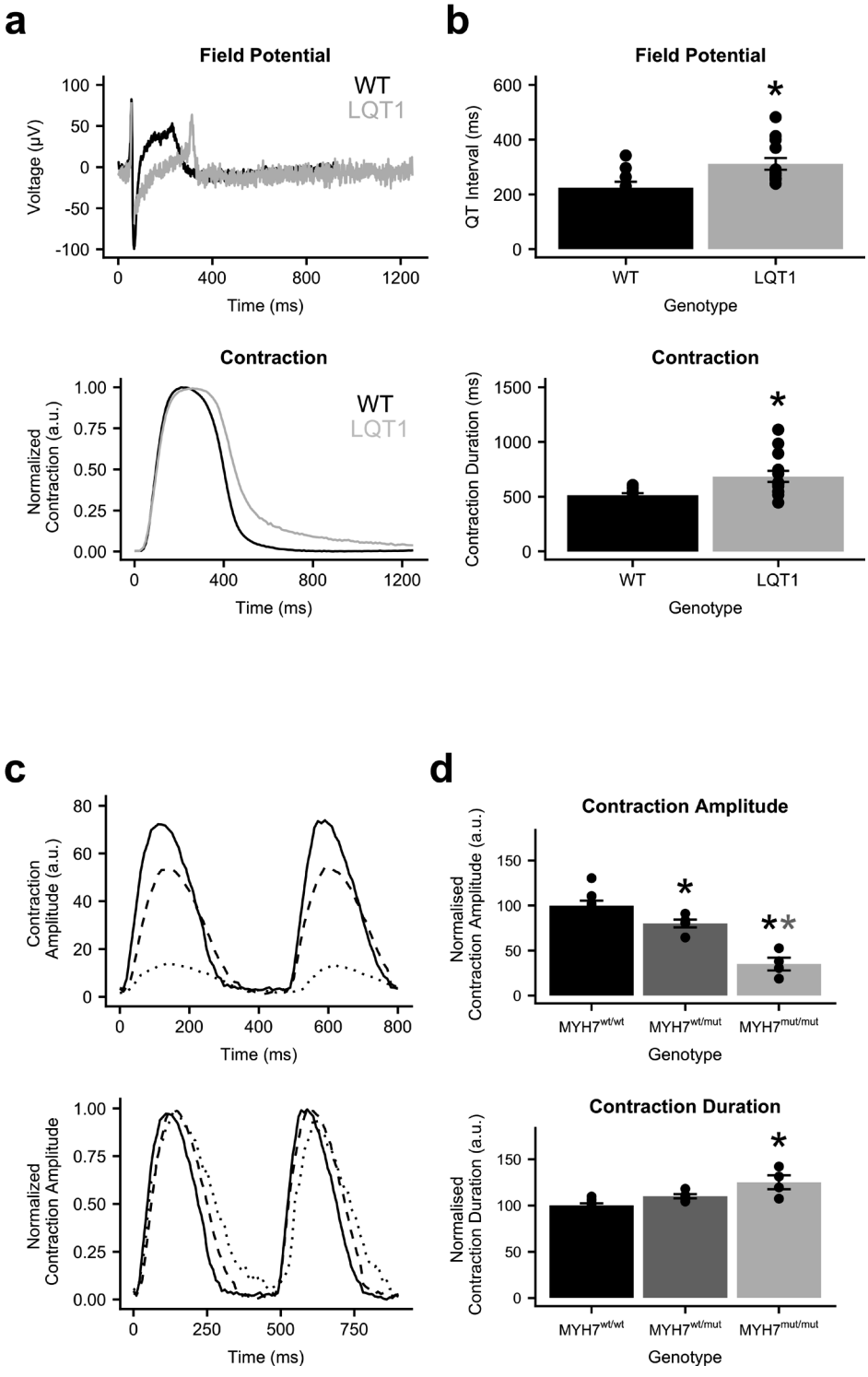
a
Field Potential
WT
LQT1
Voltage (μV)
100
50
0
-50
-100
0
400
800
1200
Time (ms)
b
Field Potential
QT Interval (ms)
600
400
200
0
*
WT
LQT1
Genotype
Contraction
Normalized Contraction (a.u.)
1.00
0.75
0.50
0.25
0.00
WT
LQT1
Time (ms)
Contraction
Contraction Duration (ms)
1500
1000
500
0
*
WT
LQT1
Genotype
c
Contraction Amplitude (a.u.)
80
60
40
20
0
Time (ms)
Normalized Contraction Amplitude
1.00
0.75
0.50
0.25
0.00
0
250
500
750
Time (ms)
d
Contraction Amplitude
Normalised Contraction Amplitude (a.u.)
150
100
50
0
*
**
MYH7wt/wt
MYH7wt/mut
MYH7mut/mut
Genotype
Contraction Duration
Normalised Contraction Duration (a.u.)
150
100
50
0
*
MYH7wt/wt
MYH7wt/mut
MYH7mut/mut
Genotype

video options (~120/240 frames per second), obviating the need for dedicated cameras and recording equipment if necessary.

We demonstrated excellent linear correlations between our software tool and multiple other standard methods independent of substrate, cell configuration and technology platform and showed that MUSCLEMOTION is able to capture contraction in a wide range of *in vivo* and *in vitro* applications (Figure 2 and Figure 3). Specifically, we identified several advantages compared to optical flow algorithms in terms of speed and the absence of arbitrary binning factors or thresholds which, when modified, profoundly affect the results. One limitation compared to optical flow or EHT standard algorithm is that the tool lacks qualitative vector orientation, making it more difficult to assess contraction direction. Particularly important was the correlation with force data calculated from the displacement of flexible posts by EHTs. This indicates that when the mechanical properties of substrates are known[29], MUSCLEMOTION allows absolute quantification of contractile force. Technical limitations of the EHT recording system allowed us to analyze only movies with JPEG compression; this resulted in loss of pixel information that might have negatively influenced the correlation shown. For better and more accurate results on contraction quantification, non-lossy/uncompressed video formats should be used for recordings since individual pixel information is lost upon compression and therefore not available for analysis by MUSCLEMOTION.

We proposed and validated practical application in pharmacological challenges using multiple biological preparations recorded in different laboratories; this means that immediate use in multiple independent high-throughput drug-screening pipelines is possible without further software development being required, as recently applied for a drug screening protocol on cardiac organoids from hPSCs[18]. Intuitively, the possibility of having inter-assay comparisons will also be of particular relevance where comparisons of contraction data across multiple platforms are required by regulatory agencies or consortia (e.g. CiPA, CSAHi)[5,6,25,30]. Moreover, this might offer a quantitative approach

Figure 5: *In vitro* disease phenotypes.

a) Field potential and contraction profile of wildtype (black) and LQT1 (gray) hPSC-CM monolayers on MEAs. b) Quantitative analysis of the QT interval and the contraction duration. c) Raw (top) and normalized (bottom) contraction profiles of HCM-EHTs from $MYH7^{wt/wt}$ (solid), $MYH7^{wt/mut}$ (dashed), $MYH7^{mut/mut}$ (dotted) cell lines. d) Quantitative analysis of contraction amplitude and contraction duration.

Data information: P-values QT-interval: WT versus LQT1: 0.012. P-values contraction duration: WT versus LQT1: 0.012. P-values contraction amplitude: $MYH7^{wt/wt}$ versus $MYH7^{wt/mut}$: 0.026; $MYH7^{wt/wt}$ versus $MYH7^{mut/mut}$: $6{\cdot}10^{-6}$; $MYH7^{wt/mut}$ versus $MYH7^{mut/mut}$: 0.00065. P-values contraction duration: $MYH7^{wt/wt}$ versus $MYH7^{wt/mut}$: 0.062; $MYH7^{wt/wt}$ versus $MYH7^{mut/mut}$: 0.00085; $MYH7^{wt/mut}$ versus $MYH7^{mut/mut}$: 0.0046.

to investigating how genetic or acquired diseases of the heart (e.g. cardiomyopathies[7], Long QT Syndrome[31]), heart failure resulting from anticancer treatments[32,33] or maturation strategies[20,34,35] affect cardiac contraction. The possibility of linking *in vitro* with *in vivo* assays, with low cost technologies applicable with existing hardware certainly represents an advantage as demonstrated by automatic quantification of zebrafish heartbeats and human echocardiograms (Figure 6). Overall, these results clearly demonstrated that contraction profiles could be derived and quantified in a wide variety of commonly used experimental and clinical settings. MUSCLEMOTION might represent a starting point for a swift screening method to provide clinically relevant insights into regions of limited contractility in the hearts of patients. We encourage further development of this open source platform to fit specific needs; future areas of application could include skeletal or smooth muscle in the same range of formats described here.

MUSCLEMOTION allows the use of a single, transparent method of analysis of cardiac contraction in many modalities for rapid and reliable identification of disease phenotypes, potential cardiotoxic effects in drug screening pipelines and translational comparison of contractile behaviour.

Limitations

Saturation of pixel movements may affect contraction amplitudes. However, as demonstrated with the artificial CM, contraction velocity and all temporal parameters remained valid. We also minimized the impact of highly repetitive structures on the

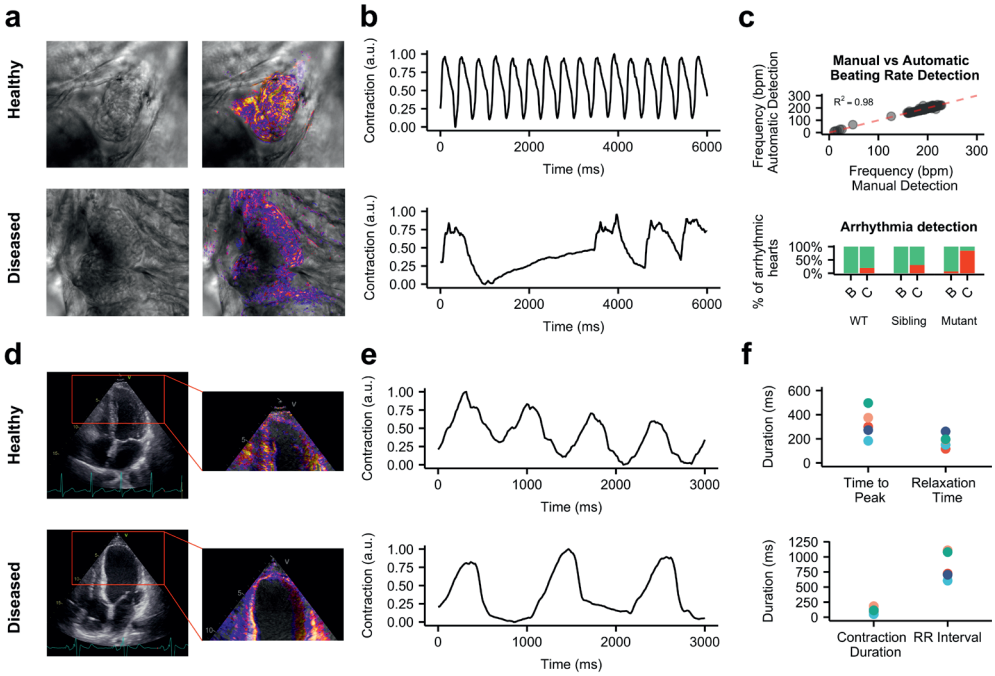

output of MUSCLEMOTION by applying a Gaussian filter, which also helped in reducing the impact of transverse movements on contraction profiles. High frequency contraction might complicate baseline detection, especially if the duration of the contracted state is similar to that of the relaxed (e.g. approaching sinusoidal). We have implemented a "fast mode" option that captures reliable baseline values even at high contraction rates. MUSCLEMOTION does not measure absolute values of cell shortening or force of contraction. However, as demonstrated by correlations with these physical quantities (Figure 2d,e v), specific setups can be calibrated to obtain such readout.

Adult CMs contract dominantly along the longitudinal axis. However, hPSC-CMs are highly variable in shape, often showing concentric contractions, so that effects of transverse movement are usually intrinsic to the experimental model and they should be considered in the global contraction analysis. Indirect transverse movements originating from uncontrolled experimental conditions or moving objects other than those of interest (e.g. vibrations, sample shift, floating debris, air bubbles) should be avoided since they might lead to overestimation of the cardiomyocyte contraction.

Methods

Extended methods are in the Supplementary Information. The datasets generated and/or analyzed during the current study are available from the corresponding authors on reasonable request.

Figure 6: *In vivo* disease phenotypes.

a) Representative examples of wild type (top) and gnb5a/gnb5b mutant (bottom) zebrafishes and relative enhancement of moving pixels. b) Representative qualitative analyses of normal (top) and arrhythmic (bottom) contraction profiles from wild type and gnb5a/gnb5b mutant zebrafishes treated with carbachol. c) Correlation of results obtained from manual (x-axis) vs automatic (y-axis) detection of beating frequency (top); distribution of normal (green) and arrhythmic (red) contraction patterns in baseline condition (B) and after treatment with carbachol (C) in wild type and gnb5a/gnb5b mutant zebrafishes (bottom). d) Representative echocardiograms of healthy (top) and cardiomyopathic (bottom) human individuals. Ventricles have been manually cropped and the enhancement of moving pixels is overlaid. e) Representative qualitative analyses of normal (top) and poor (bottom) ventricular functions. f) Quantitative data collected from echocardiogram in 5 individuals. Each colour represents one individual.

Code Availability
MUSCLEMOTION source code has been written in the ImageJ Macro Language and is available for use and further development.

Model Cell
The *in silico* cardiomyocyte-like model (Figure 1d,f,g) was created using Blender v2.77.

Optical Flow analysis
Optical flow analysis was implemented in LabVIEW as described by Hayakawa et al.[12,13].

Generation of hiPSC-HCM isogenic triplet using CRISPR/Cas9
Dual guide RNA/Cas9-Nickase strategy was designed to introduce the MYH7-C9123T SNP (encoding the R453C-β-MHC modification) in ReBL-PAT hiPSC line, as previously described[14].

hPSC Culture and Differentiation
hPSCs from multiple independent cell lines (Supplementary Table 1) were differentiated to CMs as previously described[15-18], or with the Pluricyte® Cardiomyocyte Differentiation Kit (Pluriomics b.v.) according to the manufacturer's protocol. Experiments were performed at 18-30 days after initiation of differentiation, depending on the cell source and configuration. Pluricytes® were kindly provided by Pluriomics b.v.

Patch Clamp Recordings on hPSC-CMs
Electrophysiological recordings of isolated hPSC-CMs were performed as previously described[17].

MEA Recordings of hPSC-CMs
Field potentials from MEAs were recorded and analyzed as previously published[19].

Movement of embedded beads
Gelatin-patterned polyacrylamide gels containing fluorescent beads were generated and analyzed as described previously[20].

Monolayers of hPSC-CMs
25k-40k cells were plated per Matrigel-coated glass ø10 mm coverslip.

Cardiac Organoids
Cardiac organoids composed of hPSC-CMs and hPSC-derived endothelial cells, were generated as previously described[18].

Adult cardiomyocytes
CMs were isolated from New Zealand White male rabbits as previously described[21].

Membrane labelling
hPSC-CMs were plated on Matrigel-coated glass-bottom 24-well plates and labelled with CellMask Deep Red according to the manufacturer's instructions.

Engineered heart tissues
EHTs were generated and analyzed as previously described[15].

Zebrafish hearts
Zebrafish hearts were recorded, treated and analysed as previously described[22].

Echocardiograms
Anonymized ultrasounds of 5 adult patients were selected from the echocardiography database of the Leiden University Medical Center.

Statistics
One-way ANOVA for paired or unpaired measurements was applied to test the differences in means on normalized drug effects. P-values obtained from two-tailed pairwise comparisons were corrected for multiple testing using Bonferroni's method. Statistical analyses were performed with R v3.3.3. P-values lower than 0.05 were considered statistically significant and indicated with an asterisk (*). N-values represent biological repeats.

Sources of Funding
This work was initiated in the context of the National Centre for the Replacement, Refinement, and Reduction of Animals in Research CRACK IT InPulse project code 35911 to 259146, with support from GlaxoSmithKline. It was supported by the following grants: ERC-AdG (European Research Council - Advanced Grant) STEMCARDIOVASC (C.L. Mummery, B.J. van Meer, E. Giacomelli, M. Bellin, and L.G.J. Tertoolen), ZonMW (ZorgOnderzoek Nederland - Medische wetenschappen) MKMD (Meer Kennis met Minder Dieren) Applications of Innovations 2015 to 2016 (C.L. Mummery, M. Bellin, and L. Sala), BHF (British Heart Foundation) grants SP/15/9/31605 and PG/14/59/31000 and BIRAX 04BX14CDLG grants (C. Denning), ERC-AdG IndivuHeart (T. Eschenhagen), DZHK (German Centre for Cardiovascular Research; T. Eschenhagen, U. Saleem, A. Hansen, and I. Mannhardt), ERC-StG (European Research Council - Starting Grant) StemCardioRisk (R.P. Davis and M.P.H. Mol), and the Netherlands Organisation for Scientific Research grant VIDI-917.15.303 (R.P. Davis and C. Grandela). The Dutch Heart Foundation: CVON (Cardiovasculair Onderzoek Nederland) 2012–10 Predict project (C.D. Koopman), E-Rare–CoHeart project (S.M. Kamel), and CVON–HUSTCARE 2013 to 2018 (C.L. Mummery and L. Sala).

References

1. Laverty, H. G. *et al*. How can we improve our understanding of cardiovascular safety liabilities to develop safer medicines? *Br J Pharmacol*. **163,** 675–693 (2011).

2. Passier, R., Orlova, V. V. & Mummery, C. L. Complex Tissue and Disease Modeling using hiPSCs. *Cell Stem Cell*. **18,** 309–321 (2016).

3. Bellin, M., Marchetto, M. C., Gage, F. H. & Mummery, C. L. Induced pluripotent stem cells: the new patient? *Nat Rev Mol Cell Biol*. **13,** 713–726 (2012).

4. van Meer, B. J., Tertoolen, L. G. J. & Mummery, C. L. Concise Review: Measuring Physiological Responses of Human Pluripotent Stem Cell Derived Cardiomyocytes to Drugs and Disease. *Stem Cells*. **34,** 2008–2015 (2016).

5. Kitaguchi, T. *et al*. CSAHi study: Evaluation of multi-electrode array in combination with human iPS cell-derived cardiomyocytes to predict drug-induced QT prolongation and arrhythmia - Effects of 7 reference compounds at 10 facilities. *J Pharmacol Toxicol Methods*. **78,** 93–102 (2016).

6. Hwang, H. S. *et al.* Comparable calcium handling of human iPSC-derived cardiomyocytes generated by multiple laboratories. *J Mol Cell Cardiol*. **85,** 79–88 (2015).

7. Birket, M. J. *et al.* Contractile Defect Caused by Mutation in MYBPC3 Revealed under Conditions Optimized for Human PSC-Cardiomyocyte Function. *Cell Rep*. **13,** 733–745 (2015).

8. Ribeiro, A. J. S. *et al.* Contractility of single cardiomyocytes differentiated from pluripotent stem cells depends on physiological shape and substrate stiffness. *Proc Natl Acad Sci USA*. **112,** 12705–12710 (2015).

9. Ribeiro, A. J. S. *et al.* Multi-Imaging Method to Assay the Contractile Mechanical Output of Micropatterned Human iPSC-Derived Cardiac Myocytes. *Circ Res*. **120,** 1572–1583 (2017).

10. Kijlstra, J. D. *et al.* Integrated Analysis of Contractile Kinetics, Force Generation, and Electrical Activity in Single Human Stem Cell-Derived Cardiomyocytes. *Stem Cell Reports*. **5,** 1226–1238 (2015).

11. Stoehr, A. *et al.* Automated analysis of contractile force and Ca2+ transients in engineered heart tissue. *Am J Physiol Heart Circ Physiol*. **306,** H1353–63 (2014).

12. Hayakawa, T. *et al.* Image-based evaluation of contraction–relaxation kinetics of human-induced pluripotent stem cell-derived cardiomyocytes: Correlation and complementarity with extracellular electrophysiology. *J Mol Cell Cardiol*. **77,** 178–191 (2014).

13. Hayakawa, T. *et al.* Noninvasive evaluation of contractile behavior of cardiomyocyte monolayers based on motion vector analysis. *Tissue Eng Part C Methods*. **18,** 21–32 (2012).

14. Ran, F. A. *et al.* Genome engineering using the CRISPR-Cas9 system. *Nat Protoc*. **8,** 2281–2308 (2013).

15. Mannhardt, I. *et al.* Human Engineered Heart Tissue: Analysis of Contractile Force. *Stem Cell Reports*. **7,** 29–42 (2016).

16. van den Berg, C. W., Elliott, D. A., Braam, S. R., Mummery, C. L. & Davis, R. P. Differentiation of Human Pluripotent Stem Cells to Cardiomyocytes Under Defined Conditions. *Methods Mol Biol*. **1353,** 163–180 (2016).

17. Sala, L. *et al.* A new hERG allosteric modulator rescues genetic and drug-

induced long-QT syndrome phenotypes in cardiomyocytes from isogenic pairs of patient induced pluripotent stem cells. *EMBO Mol Med*. **8,** 1065–1081 (2016).

18. Giacomelli, E. *et al.* Three-dimensional cardiac microtissues composed of cardiomyocytes and endothelial cells co-differentiated from human pluripotent stem cells. *Development* **144,** dev.143438–1017 (2017).

19. Sala, L., Ward-van Oostwaard, D., Tertoolen, L. G. J., Mummery, C. L. & Bellin, M. Electrophysiological Analysis of human Pluripotent Stem Cell-derived Cardiomyocytes (hPSC-CMs) Using Multi-electrode Arrays (MEAs). *J Vis Exp*. (2017)

20. Ribeiro, M. C. *et al.* Functional maturation of human pluripotent stem cell derived cardiomyocytes *in vitro*-correlation between contraction force and electrophysiology. *Biomaterials*. **51,** 138–150 (2015).

21. MacQuaide, N., Ramay, H. R., Sobie, E. A. & Smith, G. L. Differential sensitivity of Ca^{2+} wave and Ca^{2+} spark events to ruthenium red in isolated permeabilised rabbit cardiomyocytes. *J Physiol (Lond)*. **588,** 4731–4742 (2010).

22. Lodder, E. M. *et al.* GNB5 Mutations Cause an Autosomal-Recessive Multisystem Syndrome with Sinus Bradycardia and Cognitive Disability. *Am J Hum Genet*. **99,** 704–710 (2016).

23. Rocchetti, M. *et al.* Ranolazine prevents INaL enhancement and blunts myocardial remodelling in a model of pulmonary hypertension. *Cardiovasc Res*. **104,** 37–48 (2014).

24. Bers, D. M. Cardiac excitation-contraction coupling. *Nature* **415,** 198–205 (2002).

25. Sala, L., Bellin, M. & Mummery, C. L. Integrating cardiomyocytes from human pluripotent stem cells in safety pharmacology: has the time come? *Br J Pharmacol*. **97,** 2684 (2016).

26. Zhang, M. *et al.* Recessive cardiac phenotypes in induced pluripotent stem cell models of Jervell and Lange-Nielsen syndrome: disease mechanisms and pharmacological rescue. *Proc Natl Acad Sci USA*. **111,** E5383–92, (2014).

27. Rodriguez, M. L. *et al.* Measuring the contractile forces of human induced pluripotent stem cell-derived cardiomyocytes with arrays of microposts. *J Biomech Eng*. **136,** 051005 (2014).

28. Bullen, A. Microscopic imaging techniques for drug discovery. *Nat Rev Drug Discov*. **7,** 54–67 (2008).

29. Vandenburgh, H. *et al.* Drug-screening platform based on the contractility of tissue-engineered muscle. *Muscle Nerve*. **37,** 438–447 (2008).

30. Cavero, I. & Holzgrefe, H. Comprehensive *in vitro* Proarrhythmia Assay, a novel *in vitro*/*in silico* paradigm to detect ventricular proarrhythmic liability: a visionary 21st century initiative. *Expert Opin Drug Saf*. **13,** 745–758 (2014).

31. Rocchetti, M. *et al.* Elucidating arrhythmogenic mechanisms of long-QT syndrome CALM1-F142L mutation in patient-specific induced pluripotent stem cell-derived cardiomyocytes. *Cardiovasc Res*. **113,** 531–541 (2017).

32. Burridge, P. W. *et al.* Human induced pluripotent stem cell-derived cardiomyocytes recapitulate the predilection of breast cancer patients to doxorubicin-induced cardiotoxicity. *Nat Med*. **22,** 547–556 (2016).

33. Bellin, M. & Mummery, C.L. Stem

cells: The cancer's gone, but did chemotherapy damage your heart? *Nat Rev Cardiol*. **13,** 383–384 (2016).

34. Nunes, S. S. *et al.* Biowire: a platform for maturation of human pluripotent stem cell-derived cardiomyocytes. *Nat Meth*. **10,** 781–787 (2013).

35. Chan, Y-C. *et al.* Electrical stimulation promotes maturation of cardiomyocytes derived from human embryonic stem cells. *J Cardiovasc Transl Res*. **6,** 989–999 (2013).

Supplementary information

Supplementary Methods

Model cell

To establish and test the algorithm of MUSCLEMOTION we first created an *in silico* CM-like shape (Figure 1d,f,g) using Blender v2.77 (Stichting Blender Foundation). This three-dimensional squared sphere had an aspect ratio of 1:1:0.26 (XYZ) when contracted and 2:1:0.26 (XYZ) when relaxed. A diffuse "shader" with a foggy, patterned texture was then applied to the object to simulate extremely repetitive phase contrast image features. Temporal input parameters were then imposed: 100 ms for time-to-peak (t_1) and 350 ms for relaxation time (t_2). A beating frequency of 1 Hz and sampling rate of 100 frames per second were simulated. Modifications of cell shortening (25% and 50% of baseline) and time-to-peak (50% and 200% of baseline) were generated to validate the algorithm linearity.

Patch clamp recordings on hPSC-CMs

Electrophysiological recordings of isolated hPSC-CMs were performed using the perforated patch clamp technique as previously described[1]. Briefly, cells were paced at 1 Hz through the glass capillary and were perfused with warm (37 °C) Tyrode's solution containing (mM): 154 NaCl, 5.4 KCl, 1.8 $CaCl_2$, 1 $MgCl_2$, 5 HEPES-NaOH, 5.5 D-Glucose; pH was adjusted to 7.35 with NaOH. Pipette solution contained (mM): 125 K-Gluconate, 20 KCl, 10 NaCl, 10 HEPES; pH was adjusted to 7.2 with KOH. Amphotericin-B was dissolved in DMSO right before each experiment and added to the pipette solution to reach a final concentration of 0.22 mM.

Movement of embedded beads

Fabrication of gelatin-patterned polyacrylamide gels containing fluorescent beads and contraction force measurements were performed as described previously2, with an increased recording frame rate to 56 frames per second. For nifedipine experiments, cells were paced through an external stimulator to ensure a constant and triggered beating rate. Experiments with isoprenaline were performed in spontaneously beating aligned hPSC-CMs to investigated the pharmacological effect on beat rate. hPSC-CMs on patterned polyacrylamide gels were measured in Pluricyte® medium (Pluriomics b.v.). Drug treatment was performed with additive doses which were compared to baseline.

Monolayers of hPSC-CMs

Pluricytes® (Pluriomics b.v.) were cultured following the manufacturer's instructions. Cells were plated at a density of 25k-40k cells/coverslip on Matrigel-coated glass ø10 mm coverslips for 7 days before measurements of contraction. Monolayers were paced by an external field stimulator (bipolar square pulse of ~15 V for 5 ms) and superfused with a warm (37 °C) Tyrode's solution (described above). Drug treatment was performed with additive doses which were compared to baseline.

Cardiac organoids

Cardiac organoids composed of hPSC-CMs and hPSC-derived endothelial cells were generated as previously described[3]. Cardiac organoids were paced through an external field stimulator (bipolar square pulse of ~15 V for 5 ms) and superfused with a warm

(37 °C) Tyrode's solution (described above). Drug treatment was performed with additive doses which were normalized to baseline.

Adult cardiomyocytes

CMs were isolated from New Zealand White male rabbits as previously described[4]. Animal experiments complied with the ARRIVE guideline for animal studies. The procedures used complied with current regulations and were approved by the Research Committee of the University of Glasgow. In total, 3 animals were used for these experiments. Sarcomere shortening was estimated using an ImageJ macro that calculates, for each image in a stack, the spatial frequency of the pixel intensity profile along a fixed, elongated rectangular region of interest placed inside the cell boundary and on a part of the cell showing clear banding. At each time point, mean sarcomere length corresponded to the location of the peak frequency value of the power spectrum obtained by taking the Fourier Transform of the intensity profile. Drug treatment was performed with single dose additions which were normalized to their pre-treatment baseline.

Membrane labelling

hPSC-CMs were plated on Matrigel-coated glass-bottom 24-well plates in either BPEL[5] or Differentiation Medium C (Pluriomics b.v.) at a density between 20k-70k cells per well. Live cells were labelled with Cell Mask Deep Red (Thermo Fisher Scientific Inc.) and imaged with on a Nikon Ti-U Eclipse with a CamRecord CR600x2 monochromatic camera (Optronis GmbH) at 333 Hz after amplification of the image with an intensifier tube (Photonis b.v.).

Engineered heart tissues

EHTs were generated and analyzed as previously described[6]. In brief, hiPSC were differentiated into CMs with a growth factor based protocol in suspension culture using spinner flasks. Following dissociation with collagenase, fibrin-based EHTs were generated with $1x10^6$ cells per 100 µL EHT construct[7]. Contraction analysis based on a video-optical figure recognition algorithm (100 frames per second) was performed under electrical stimulation in serum-free Tyrode's solution in a humidified gas (40% O_2, 7% CO_2) and temperature (37 °C) controlled incubation chamber[8]. Drug treatment was performed with additive doses which were compared to baseline.

Zebrafish hearts

All experiments were conducted in accordance to the ARRIVE guidelines and approved by the local ethics committee of the Koninklijke Nederlandse Akademie van Wetenschappen (KNAW). Wild-type, sibling and *gnb5a/gnb5b* double mutant embryos (5 days post fertilization) were embedded in 0.3% agarose (Ultra Pure agarose, Invitrogen) prepared in E3 medium containing 16 mg/ml tricaine and mounted on glass bottom dishes. Recordings were performed at 28 °C using an inverted light microscope with climate chamber. Recordings were performed at 150 frames per second for 10-30 seconds using a C9300-221 high-speed CCD camera (Hamamatsu Photonics K.K). Basal heart rates were recorded first. Subsequently 400 µM carbachol (CCh; Sigma-Aldrich) was added and incubated for 30 min before heart rates were measured a second time.

Echocardiograms
Anonymized ultrasounds of 5 adult patients who had undergone transthoracic echocardiography between 2012 and 2017 on clinical indication, were selected from the echocardiography database of the Leiden University Medical Center. Transthoracic echocardiography was performed using a GE Vivid7 or E9 (GE-Vingmed, Horten, Norway) ultrasound machine with standard views from the parasternal, subcostal, suprasternal and apical window. For MUSCLEMOTION analysis, 4 chamber views were used. The images were converted to avi-format, preferably containing multiple beats. For this analysis of clinically acquired data, the Institutional Review Board waived the need for patient written informed consent.

Supplementary references

1. Sala, L. et al. A new hERG allosteric modulator rescues genetic and drug-induced long-QT syndrome phenotypes in cardiomyocytes from isogenic pairs of patient induced pluripotent stem cells. *EMBO Mol Med.* **8,** 1065–1081 (2016).

2. Ribeiro, M.C. et al. Functional maturation of human pluripotent stem cell derived cardiomyocytes *in vitro*--correlation between contraction force and electrophysiology. *Biomaterials* **51,** 138–150 (2015).

3. Giacomelli, E. et al. Three-dimensional cardiac microtissues composed of cardiomyocytes and endothelial cells co-differentiated from human pluripotent stem cells. *Development* **144,** dev.143438–1017 (2017).

4. MacQuaide, N., Ramay, H.R., Sobie, E.A., Smith, G.L.. Differential sensitivity of Ca^{2+} wave and Ca^{2+} spark events to ruthenium red in isolated permeabilised rabbit cardiomyocytes. *J. Physiol. (Lond)* **588,** 4731–4742 (2010).

5. van den Berg CW, Elliott DA, Braam SR, Mummery CL, Davis RP. Differentiation of Human Pluripotent Stem Cells to Cardiomyocytes Under Defined Conditions. *Methods. Mol. Biol.* **1353,** 163–180 (2016).

6. Mannhardt I, Breckwoldt K, Letuffe-Brenière D, et al. Human Engineered Heart Tissue: Analysis of Contractile Force. *Stem Cell Reports* **7,** 29–42 (2016).

7. Mannhardt I, Saleem U, Benzin A, Schulze T, Klampe B, Eschenhagen T, Hansen A. Automated Contraction Analysis of Human Engineered Heart Tissue for Cardiac Drug Safety Screening. *J Vis Exp.* **122,** 55461 (2017).

8. Hansen A, Eder A, Bonstrup M, Flato M, Mewe M, Schaaf S, Aksehirlioglu B, Schworer A, Uebeler J, Eschenhagen T. Development of a Drug Screening Platform Based on Engineered Heart Tissue. *Circ Res*. **107,** 35–44 (2010).

Supplementary movie legends

Supplementary Movies are available at:
https://doi.org/10.1161/CIRCRESAHA.117.312067

Supplementary Movie 1: test bench of block displacements.

Supplementary Movie 2: single human stem cell derived cardiomyocyte during a patch clamp experiment.

Supplementary Movie 3: human stem cell derived cardiomyocyte monolayer culture.

Supplementary Movie 4: human stem cell derived cardiac organoid.

Supplementary Movie 5: Engineered heart tissue from human stem cell derived cardiomyocytes.

Supplementary Movie 6: isolated adult rabbit cardiomyocyte.

Supplementary Movie 7: Fluorescent bead displacement by a single hPSC-CM aligned on a gelatin patterned polyacrylamide substrate.

Supplementary Movie 8: hPSC-CMs monolayer culture plated on a Multi Electrode Array.

Supplementary Movie 9: Fluorescently labelled hPSC-CMs monolayer.

Supplementary Movie 10: Optical recording of a zebrafish heart (wildtype) *in vivo*.

Supplementary Movie 11: Human echocardiogram from healthy individual.

Supplementary Figures

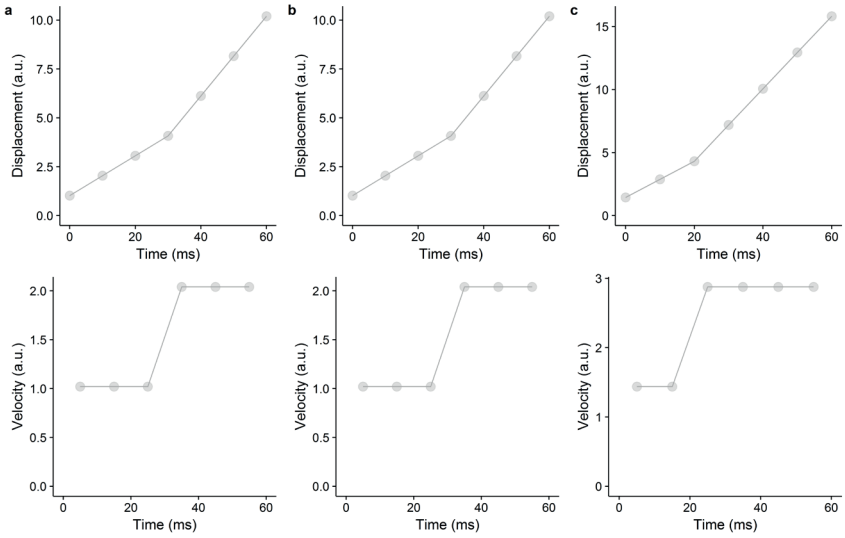

Supplementary Figure 1: Linearity of the contraction tool.

a) Profiles of displacement (top) and velocity (bottom) when the block is moving along the x-axis; b) Profiles of displacement (top) and velocity (bottom) when the block is moving along the y-axis; c) Profiles of displacement (top) and velocity (bottom) when the block is moving along both axes. In all figures, the linearity between displacement and velocity is clearly preserved.

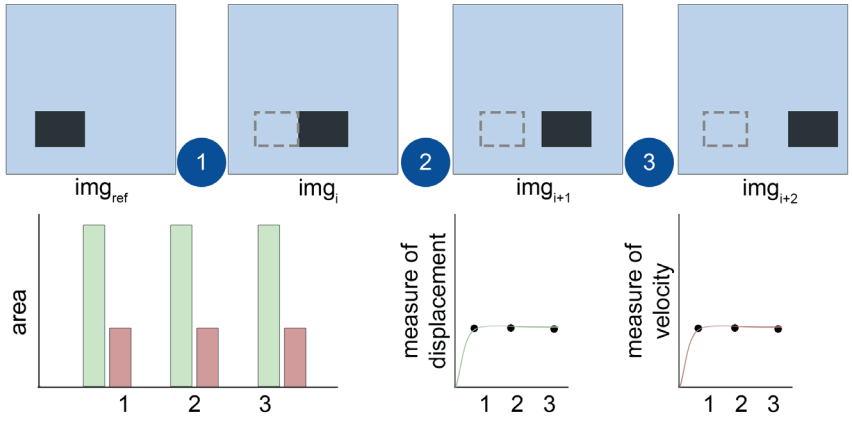

Supplementary Figure 2: Out-of-bounds limitation of the contraction tool.

Demonstration of the out-of-bounds limitation occurring when the differences of moving areas in img_i an img_{i-1} relative to img_{ref} reached the maximum level. This is clearly visible in the clipping of the contraction plot. However, the velocity plot is still valid, since it calculates the difference between img_i and img_{i-1}.

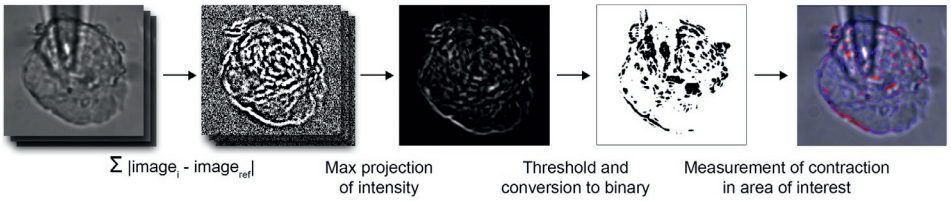

Supplementary Figure 3: Automatic region of interest selection using maximum projection.

First the difference from img_i to img_{ref} is calculated. Next, the projection of the maximum intensity of the resulting image stack is generated. This projection is subjected to a threshold (standard set to the mean intensity of the projection image plus one standard deviation) and made binary. Next, this mask is used to analyze only the moving (contracting) areas.

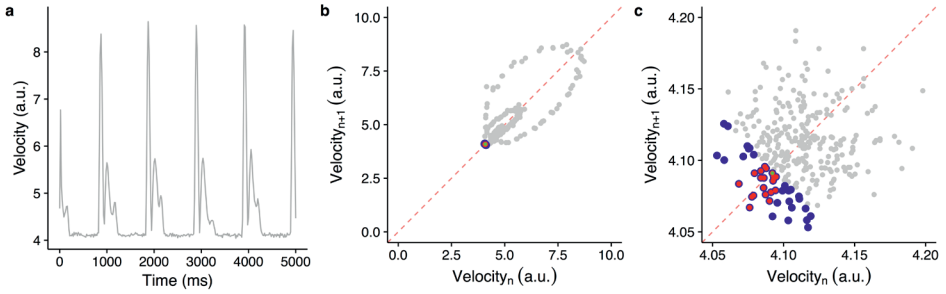

Supplementary Figure 4: Automatic reference frame detection.

a) Example of measured velocity profile; b) Velocity$_n$ values are plotted against velocity$_{n+1}$ values. In order to select the point that has both low velocity and neighbour with similar values (two characteristics of a flat diastolic period, where the derivative is ideally zero) a number of points (in this example 50, blue) are selected that have the smallest distance to the origin; c) Magnification of a region in b). For each of the selected points, a number of points (in this example 20, red) that are closet to the unity line (dotted red) is selected. Finally, of those points, one point (green) is selected as the smallest combination of values and distance from unity line.

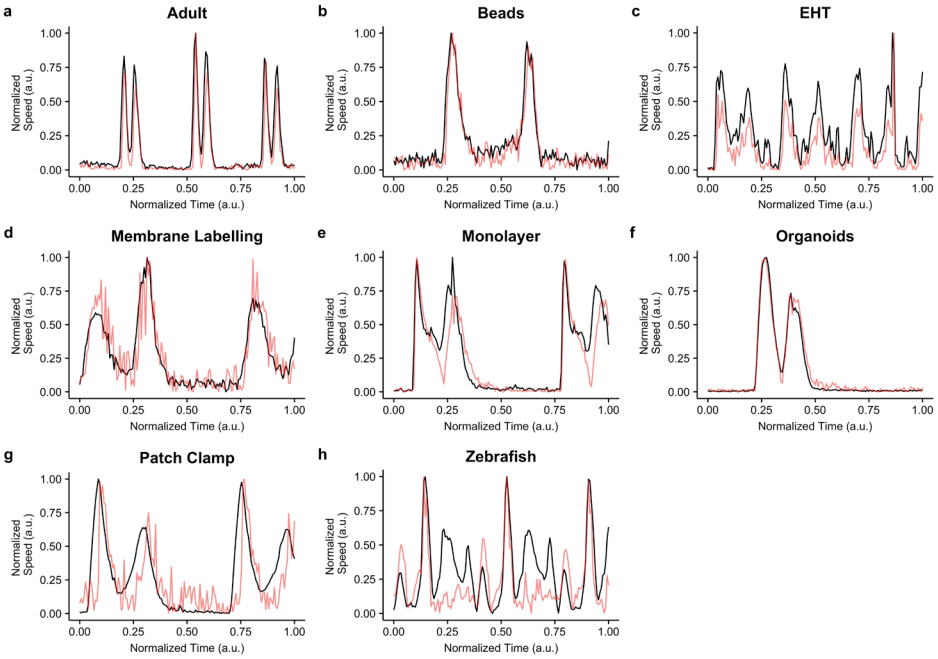

Supplementary Figure 5: Examples of linearity checks for various cardiac models.

The measured speed by frame-to-frame analysis (black) and calculated speed from the frame to reference frame analysis (red) of a) isolated adult rabbit cardiomyocyte contraction; b) fluorescent bead displacement by hPSC-CM on gelatin patterned polyacrylamide; c) engineered heart tissue contraction; d) contraction of fluorescently labelled monolayer; e) hPSC-CM monolayer contraction; f) hPSC-CM organoid contraction; g) single hPSC-CM contraction during patch clamp; h) zebrafish heart *in vivo*.

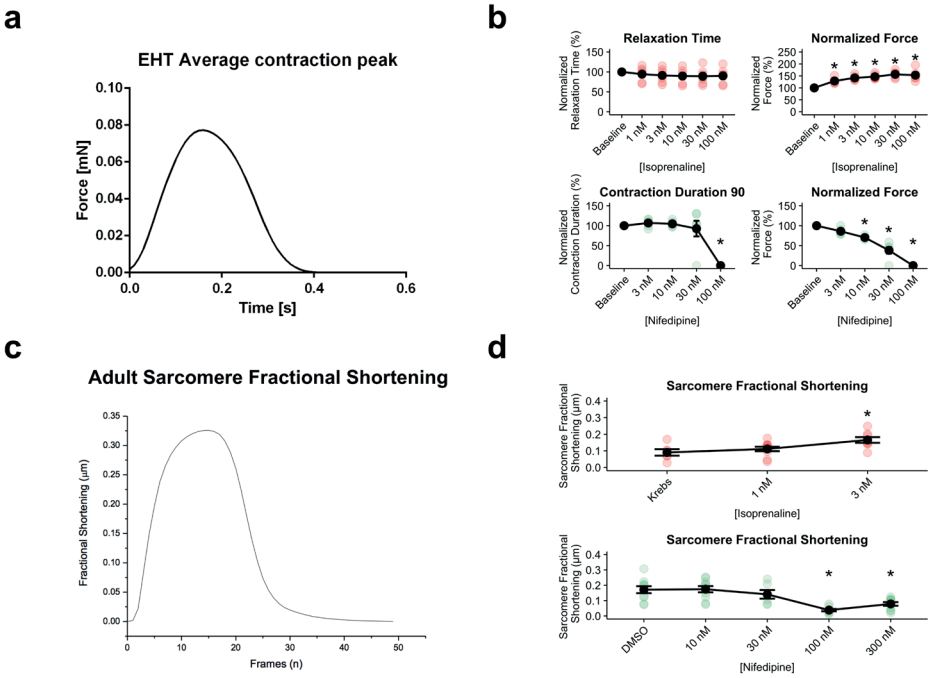

Supplementary Figure 6: Results from EHT and Adult gold standards

a) Representative average contraction profile obtained by pole deflection analysis of a single EHT during the recording period; b) average dose-response curves (black traces) and single measurements for several parameters obtained in EHTs treated with isoprenaline (top, red) and nifedipine (bottom, green) by pole deflection analysis; c) representative contraction profile obtained by sarcomere fractional shortening analysis of an adult rabbit CM; d) average dose-response curves (black traces) and single measurements for sarcomere fractional shortening obtained in adult CMs treated with isoprenaline (top, red) and nifedipine (bottom, green).

P-values baseline versus dose. Panel b i) 1 nM: 1; 3 nM: 1; 10 nM: 1; 30 nM: 1; 100 nM: 1. Panel b ii) 1 nM: 0.01517; 3 nM: 0.00016; 10 nM: $2.8 \cdot 10^{-5}$; 30 nM: $8.8 \cdot 10^{-7}$; 100 nM: $2.9 \cdot 10^{-6}$. (N=6; 6; 6; 6; 6; 6). Panel b iii) 3 nM: 1; 10 nM: 1; 30 nM: 1; 100 nM: $3.8 \cdot 10^{-7}$. Panel b iv) 3 nM: 0.2095; 10 nM: 0.0002; 30 nM: $5.2 \cdot 10^{-10}$; 100 nM: $1.2 \cdot 10^{-14}$. (N=6; 6; 6; 6; 6). Panel d i) 1 nM: 1; 3 nM: 0.018. Panel d ii) 10 nM: 1; 30 nM: 1; 100 nM: 0.00013; 300 nM: 0.00676.

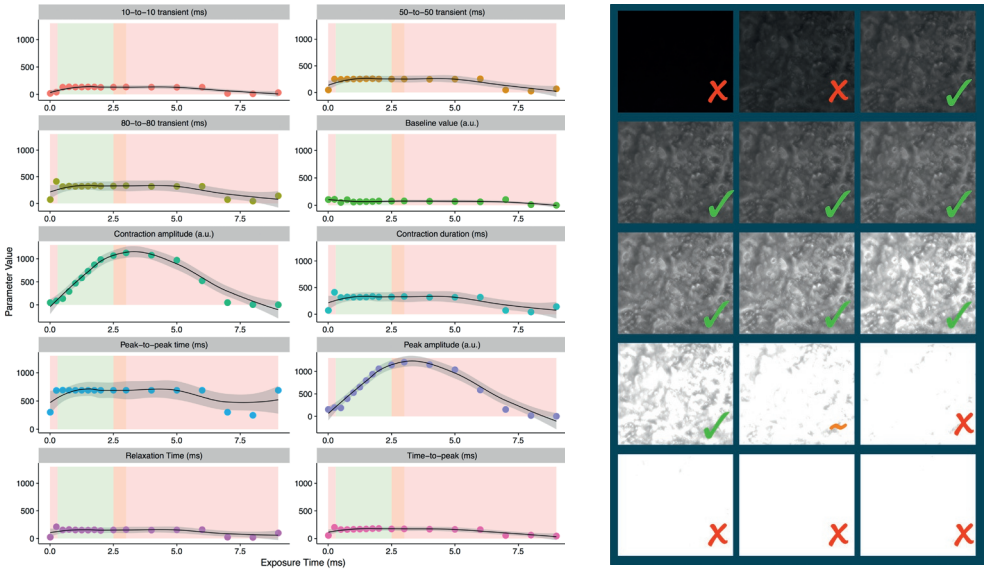

Supplementary Figure 7: MUSCLEMOTION behaviour with different camera exposures.

The output parameters of MUSCLEMOTION are shown for the same monolayer sample recordings with different exposure times. The contraction amplitude output increases linearly with increased exposure time while all temporal output parameters are independent of the lighting conditions within a reasonable range (i.e. the image should not be dark and it should not be saturated completely).

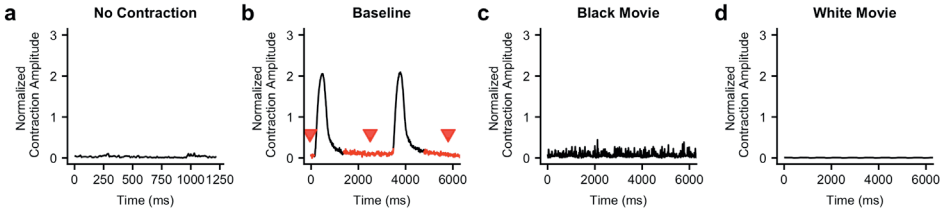

Supplementary Figure 8: Negative controls of MUSCLEMOTION.

The response of MUSCLEMOTION to a) a video of a single cell hPSC-CM that does not contract; b) a video of a contracting single cell hPSC-CM with baseline (i.e. diastolic period without contraction) indicated; c) a movie with extremely low exposure (i.e. black frames) and d) extremely high exposure (i.e. white frames).

Abstract

Quantification of contraction is essential to study cardiac diseases, injury and responses to drugs. While there are many techniques to assess contractility, most rely on costly, dedicated hardware, advanced informatics and can only be used in specific experimental models. We have developed an automated open-source software tool (MUSCLEMOTION), for use with standard imaging equipment, to assess contractility *in vitro* and *in vivo* and quantify responses to drugs and diseases. We describe high-speed and disturbance-free acquisition of images from both electrically paced or non-paced human pluripotent stem cell-derived cardiomyocytes, isolated adult cardiomyocytes, zebrafish hearts and human echocardiograms. Recordings are then used as input for automated batch analysis by the MUSCLEMOTION software tool configured with specific settings and parameters tailored to the recording technique. Details on accuracy, interpretation and troubleshooting are discussed. Acquisition duration depends on the experimental setup and aim, but quantification of drug or disease responses in an *in vitro* muscle model can typically be completed within a few hours.

Chapter 4

Quantification of muscle contraction *in vitro* and *in vivo* using MUSCLEMOTION software: from stem cell-derived cardiomyocytes to zebrafish and human hearts

Modified after Current Protocols in Human Genetics 99, e67 (2018)

Berend van Meer#, Luca Sala#, Leon Tertoolen, Godfrey Smith*, Francis Burton*, Christine Mummery*

# these authors contributed equally to this work
* these authors contributed equally to this work

Introduction

Many basic and clinical research laboratories as well as pharmaceutical companies are investigating factors that affect cardiac contraction in various *in vitro* and *in vivo* models with view to screening for new therapeutic targets, modelling human cardiac diseases *in vitro* or investigating cardiotoxicity, the most common reason for drug withdrawal[1]. However, in contrast to typical features of the heart, such as electrical activity, methods for measuring contraction are not standardized; this has led to a wide range of laboratory- or experimental model-specific setups being developed, often with outputs only relevant to individual techniques[2]; this significantly hampers cross comparison of data, its reproducibility and data validation. In addition, implementation of these methods often requires dedicated hardware and software expertise, which is not commonly present in biological laboratories. The improvement of preclinical cardiac models and, equally importantly, the development of easy-to-use, widely applicable quantitative methods of phenotype analysis that are independent of the experimental model, is essential to translate laboratory results into meaningful clinical conclusions.

We have recently developed and used a software tool we called MUSCLEMOTION[3] to quantify cardiac contraction noninvasively both *in vitro* and *in vivo* (Figure 1). We have (i) validated MUSCLEMOTION in *in silico* contraction models, (ii) compared it with current gold standards in six different experimental cell configurations and found correlations that were sufficiently high that these standards could be replaced and (iii) used the method to quantify drug- and disease responses across a wide range of human pluripotent stem cell derived (hPSC) cardiomyocyte (hPSC-CM) models, adult CMs and hearts *in situ* in zebrafish and humans. The tool is an ImageJ macro which runs on standard desktop operating system, is open source, scalable and customizable to individual experimental settings and, importantly, was refined such that it can be used by non-specialist labs, clinics and non-experienced users. MUSCLEMOTION can be used in both electrically paced or non-paced cells and tissues.

In this protocol, we describe the experimental design and step-by-step procedure to assess contraction in cardiac models using MUSCLEMOTION (Figure 2). To simplify the instructions for use, the procedure primarily describes how to analyse contraction in hPSC-CM monolayer cultures but additionally provides the exact settings and parameters that allow use of MUSCLEMOTION in each cellular configuration (isolated CMs, complex cultures in 2D or 3D, hearts *in vivo*) previously reported. Moreover, this protocol serves as a guide to use MUSCLEMOTION to set up contraction recording and analysis for any cellular setup of interest to the researcher.

Basic Protocol 1

Data recording and data analysis with MUSCLEMOTION

This protocol describes the necessary steps used for sample preparation and data recording. We used monolayers of hPSC-CMs as a representative biological platform on which we evaluated the effect of a drug at different concentrations.

Materials

Reagents

- hPSC-CMs - human pluripotent stem cell-derived cardiomyocytes
- NaCl (Sigma-Aldrich, cat. no. S7653-1KG)
- KCl (Sigma-Aldrich, cat. no. P9541-500G)
- $MgCl_2$ (Sigma-Aldrich, cat. no. M8266-100G)
- $CaCl_2$ (Sigma-Aldrich, cat. no. C3306-250G)
- HEPES (Sigma-Aldrich, cat. no. H3375-100G)
- NaOH (Sigma-Aldrich, cat. no. S5881-500G-M)
- Dimethyl sulfoxide (DMSO) (Sigma-Aldrich, cat. no. 276855-100ML)
- Ethanol (Sigma-Aldrich, cat. no. 51976-500ML-F)
- Matrigel Growth Factor Reduced Basement Membrane Matrix (Corning, cat. no. 354230)
- PBS minus (Thermo Fisher Scientific, cat. no. 14190-169)
- TrypLE Select Enzyme (1 X), no phenol red 100 mL (GIBCO, cat. no. 12563011)
- RevitaCell Supplement (100X) (GIBCO, cat. no. A2644501)
- Nifedipine (Sigma-Aldrich, cat. no. N7634-5G)
- Distilled Water (Thermo Fisher Scientific, cat. no. 15230-089)
- IMDM (Thermo Fisher Scientific, cat. no. 21056-023)

Equipment

- A personal computer (PC) with minimally 4 GB of RAM (16 GB recommended) for analysis with MUSCLEMOTION.
- A PC with Windows 7 (32, 64-bit) or higher, USB3.0, minimally 4 GB of RAM (8 GB or more is recommended) for video acquisition with the ThorLabs USB3.0 CMOS Camera.
- Depending on the number and size of the recorded data, the appropriate size of local storage on the PC must be selected. The output files of MUSCLEMOTION are very small compared to the recorded data, so they should not impose any limitation regarding the local storage. Please be aware that any movie conversion towards 'raw' quality will increase the file size substantially.
- USB 3.0 CMOS Camera (ThorLabs, cat. no. DCC3240M, or equivalent commercially available device)
- Electric field stimulator (homemade or equivalent commercially available device, e.g. IonOptix myopacer cell stimulator)
- Temperature Controller (Cell MicroControls, cat. no. Analog TC2BIP 2/3Ch Bipolar Temp controller or equivalent commercially available device)
- Chamber (Cell MicroControls, cat. no. BT-1-13B/BT-1-13B45 [-SY] or equivalent commercially available)
- 8 channel perfusion System (Cell MicroControls, cat. no. cFlow 8Ch Perfusion controller or equivalent commercially available device)
- Tubing (Smiths Medical, cat. no. 12665497)
- Inverted microscope (Nikon, cat. no. Eclipse T1 or equivalent commercially available device with 20x or 40x objectives, preferably for phase contrast microscopy)
- Stainless-steel tweezers (Dumont, cat. no. 0101-0-PO-1)
- Single- or multichannel 10-, 20-, 200-, 1000-µL micropipettes

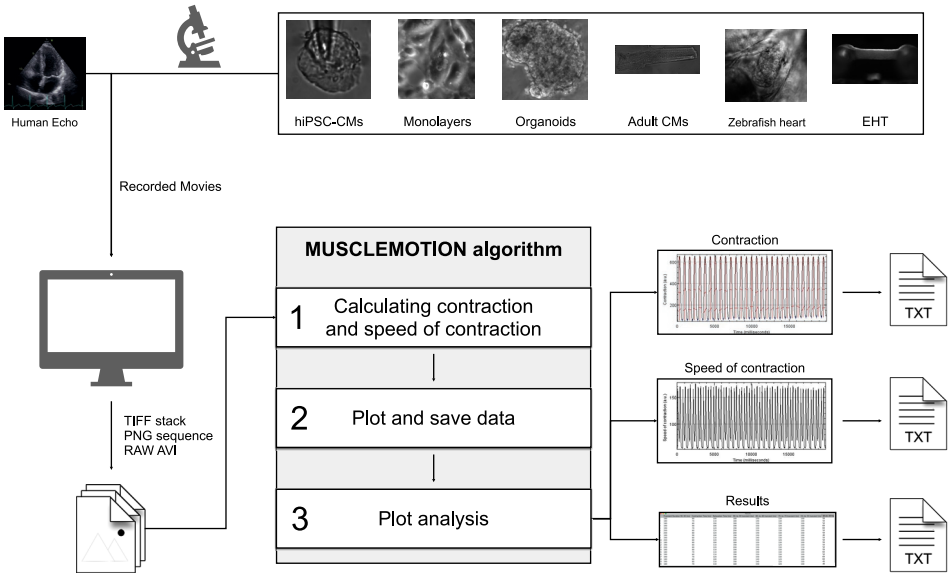

Figure 1. Overview of the method.

Human echography recordings or movies of human induced pluripotent stem cell derived cardiomyocytes (hiPSC-CMs), hiPSC-CM monolayers, hiPSC-CM organoids, adult rabbit cardiomyocytes, zebrafish hearts and hiPSC-CM engineered heart tissues (EHTs) acquired through microscopy can be are transferred to the computer. If necessary, the data is pre-processed to generate the appropriate input for the MUSCLEMOTION software. Next, the software will calculate the contraction and speed of contraction, save the data and perform plot analysis. Plots and text files will be generated for further processing. Movies from hPSC-CMs monolayers (in red) have been used in this article as examples.

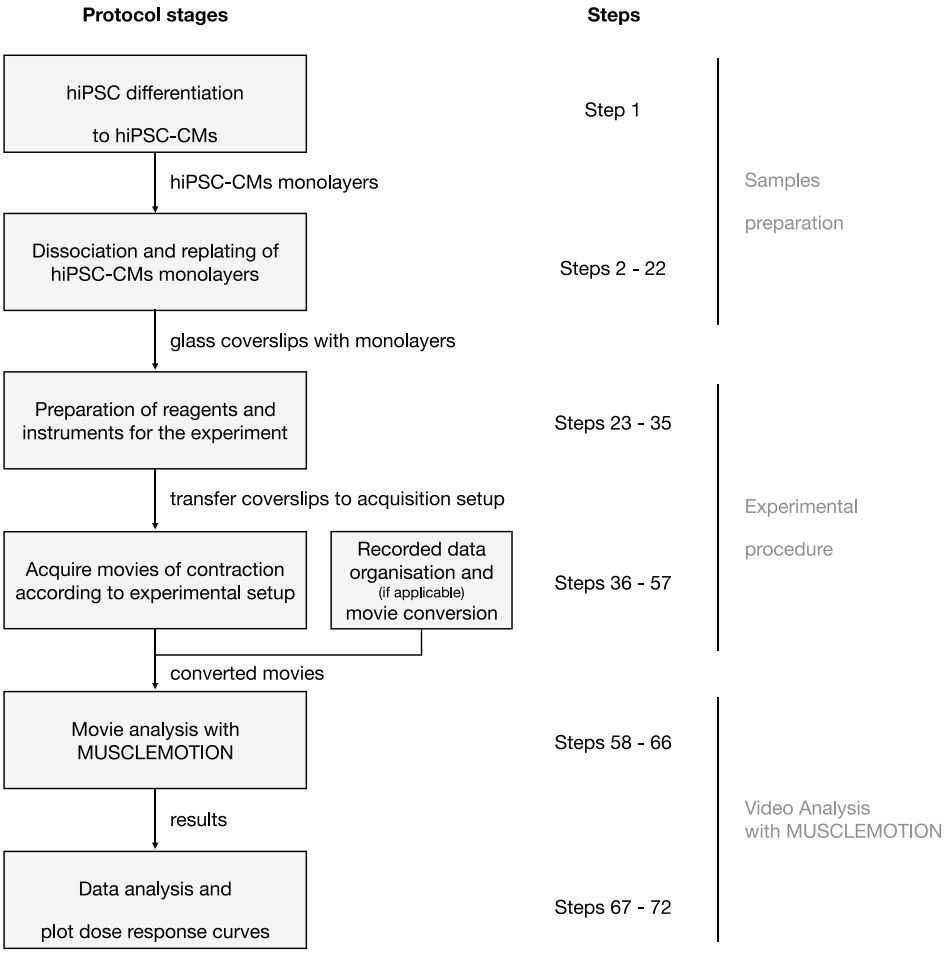

Figure 2. Flowchart of the protocol.

- 12 mm round Glass coverslips (Harvard Apparatus, cat. no. 64-0732)
- 13 mm Thermanox Plastic Coverslip, Round (Thermo Fisher Scientific, cat. no., 174950)
- 6-wells Not Treated Multiple Well Plates (Corning Costar®, cat. no. 3736)
- 12-wells Not Treated Multiple Well Plates (Corning Costar®, cat. no. 3737)
- 24-wells Not Treated Multiple Well Plates (Corning Costar®, cat. no. 3738)
- Borosilicate glass Pasteur pipette (Fisher Scientific, cat. no. 13-678-20B)
- 50 mL syringes (Merck Millipore, cat. no. XX1105005)
- Biological safety cabinet/laminar flow hood (Cleanair)
- Bunsen burner (Wld Tec™, cat. no. 8.201.000)
- Vacuum system
- CO_2 cell culture incubator (Sanyo, cat. no. MCO-15A)
- Centrifuge (Hitachi, cat. no. himac-CT6EL)
- Leica stereomicroscope (Leica Microsystems, cat. no. MS5 or equivalent commercially available device)
- Filter tips (Corning, cat. no. 4807 (10 µL), 4810 (200µL), 4809 (1000µL))
- Disposable bottle top filter (0.22 µm pore size) (Millipore, cat. no. SCGVU02RE)
- Sterile plastic pipette (Greiner Bio-One, cat. no. 606180 (5 mL), 607180 (10 mL), 760180 (25 mL))

Tools, Software, Databases
FFmpeg is available for multiple operating systems and must be installed. Download- and installation instructions can be found at https://www.ffmpeg.org/.
ImageJ or Fiji (recommended) is available for multiple operating systems and must be installed. Download- and installation instructions can be found at https://imagej.nih.gov/ij/ or https://fiji.sc/.

uc480 Version 4.20 for Compact USB Cameras is available for Window 7 (32, 64-bit) and higher and must be installed for video acquisition with the ThorLabs USB3.0 CMOS Camera. Download- and installation instructions can be found under the 'Archive' section at https://www.thorlabs.com/software_pages/ViewSoftwarePage.cfm?Code=ThorCam Microsoft Excel or any other type of data processing software is required for further analysis of the MUSCLEMOTION macro output.

Strategic planning

Some experimental systems may allow absolute quantification of contraction parameters. Special preparations in advance might be required in order to calibrate the system for such quantifications. Please refer to Support Protocol 1 for detailed instructions.

Protocol steps

Sample preparation
The following steps must be carried out under aseptic conditions.
Timing: Step 1: 17-21 days; Step 2-21: 3 h; Step 22+23: 7 days

1. Differentiate hPSCs to cardiomyocytes in a 6-well plate using the preferred cell line and protocol[4–6] and culture until day 17 - 21 (Note: older cell cultures can be used with slight modifications in the TrypLE timing or in the pipetting strength described in step 9 and step 11, respectively).
2. Transfer 10 sterile glass or plastic coverslips (diameter ~10 to 12 mm) to the wells of a 24-well plate using sterilized tweezers.
3. Coat the coverslips with a 60 µL drop of Matrigel (1:100 in PBS Ca^{2+} and Mg^{2+} free) and leave to polymerize > 2 hours at room temperature (19 °C).
4. Prepare BPEL (See Reagents and Solutions).
5. Warm Bovine Serum Albumin Polyvinylalchohol Essential Lipids (BPEL), TrypLE Select 1X and PBS^- to room temperature.
6. Remove the hPSC-CM culture from the incubator and place in the sterile hood.
7. Aspirate the culture medium from 1 well of hPSC-CM culture with a glass Pasteur pipette connected to a vacuum system and add 2 mL of PBS- to the well
8. Aspirate the PBS- and add 1 mL TrypLE Select 1 X
9. Remove the plate from the hood and place in the incubator at 37 °C for 10 minutes.
10. Return the plate to the sterile hood.
11. Pipet up and down and gently scrape cells from the sides with a P1000 tip.
12. Add 3 mL of BPEL and transfer the content to a 15 mL tube.
13. Wash the well with 2 mL of BPEL and transfer remaining cells into the same 15 mL tube.
14. Put the 15 mL tube in a centrifuge (300×*g* for 3 min at room temperature).
15. Remove the tube from the centrifuge and return it to the sterile hood.
16. Aspirate the supernatant and resuspend the pellet in 1 mL BPEL.
17. Gently pipet up and down to mix the solution.
18. Use your preferred method to count the cells and calculate the dilution factors[7].
19. Put the 24-well plate with Matrigel under the sterile hood and aspirate the drops of Matrigel.
20. Plate $25*10^3$ hPSC-CMs /coverslip in 500 µL of BPEL.
21. Add 1:100 RevitaCell™ Supplement to reduce cell death.
22. Refresh the BPEL after 24 h (dissociation day plus 1 day).
23. Refresh every 72 h (dissociation day plus 4 days and 7 days).

Experimental preparation
These steps do not require sterile conditions.
Timing: 1 h

24. Prepare Tyrode's solution (See Reagents and Solutions).
25. Connect the gravity perfusion system, with multiple syringes (one for each drug concentration), and temperature control to the chamber.
26. Weigh nifedipine powder and dissolve it in DMSO to generate a 10 mM stock solution.

CRITICAL STEP*: protect nifedipine solution from light exposure, prepare the stock solution fresh before each experiment and store it according to the instructions of the manufacturer*

27. Dilute 10 mM nifedipine stock in Tyrode's to prepare solutions at different

concentrations.

CRITICAL STEP*: protect nifedipine solution from light exposure. Ensure that the DMSO concentration is equal in all the solutions and keep it as low as possible. It is advised to stay below 0.1% DMSO. Adjust the DMSO concentration in vehicle accordingly*

28. Load solutions in the perfusion setup and protect the syringes from light.
29. Start the flow of the vehicle solution and set the temperature to 37 °C.
30. Make sure that the camera is connected with the computer via a USB 3.0 interface.

CRITICAL STEP: *otherwise the camera will not be able to reach the required frame rate*

31. Turn on the computer and start the camera software (Thorlabs uc480).
32. Turn on the microscope light and confirm that it is visible through the camera.
33. In the camera software: select the menu 'uc480' > 'properties' > 'camera' and set the clock frequency to 86 MHz, the frame rate to 100 fps (this will be automatically adjusted to 99.93 fps) (For other cellular models see Table 1) and exposure time to 1.5 ms. Lock the frame rate and exposure time by ticking the 'hold' boxes to prevent automatic adaptations issued by the software. Finally, click 'Close'. For defining the correct frame rate in alternative measurements, see Support Protocol 2.
34. In the camera software: select the menu 'uc480' > 'set new AOI' and select an area of approximately 600 by 600 pixels.

CRITICAL STEP: *The size of the crop area will affect the camera frame rate. To achieve higher frame rates, reduce the width and/or height of the cropped region*

35. Check in the bottom bar whether the recording speed is between 99 and 101 frames per second (fps). Detailed information for a correct sample speed selection is present in Support Protocol 2.

Experimental procedure
The following steps must be carried out in aseptic conditions.
Timing: 45 min per sample.

36. In the sterile hood, sterilize two tweezers using the Bunsen burner flame or ethanol.
37. Use two sterile tweezers to transfer a coverslip from the 24-well plate to a 35 mm Petri dish previously filled with warm BPEL or warm Tyrode's solution.

These steps do not require sterile conditions.

38. Gently transfer the coverslip to the chamber of the perfusion setup using two tweezers.
39. Wait 4 minutes to allow the hPSC-CM monolayer to adapt to Tyrode's solution. the incubation time of the drug will be identical (for other cellular models see Table 1).
40. Focus with 20X or 40X objectives on an area that is suitable for contraction measurement (for other cellular models see Table 1). A suitable area for contraction measurement is a frame filling representative area of the sample. Be sure to focus

Table 1: Detailed settings for different types of cellular configurations.

Cell model	Recording speed (fps)	Incubation time (min)	Objective	Pacing parameters (frequency)	Speed window	Gaussian blur	Signal-to-noise reduction	Automatic transient detection	Automatic reference frame detection
hPSC-CM monolayer	100	5	20x	1.5 Hz	2	OFF	ON	ON	ON
hPSC-CM single cells	100	5	40x	1.5 Hz	2	OFF	ON	ON	ON
hPSC-CM organoids	100	10	20X	1.5 Hz	1	OFF	ON	ON	ON
hPSC-CM engineered heart tissues	100	30	1.25X	1.5 times spontaneous beat rate	2	ON	ON	ON	ON
Adult rabbit CMs	100	10	40X	1 Hz	1	ON	ON	ON	ON
Zebrafish	150	30	20X	Spontaneous	1	OFF	ON	ON	ON
Human echoscopic recordings	18	n.a.	n.a.	Spontaneous	1	OFF	ON	ON	ON

every sample in a similar way (i.e. for hPSC-CM monolayers: focus on the cell borders of the CMs).

CRITICAL STEP: *Do not change the area, lighting conditions or focus during the experiment as this might mask or be mistaken for drug induced changes.* ***TROUBLESHOOTING***

41. Submerse the electrodes in the bath solution and start the electric field stimulation (1.5 Hz; 5 ms pulse duration; 3 V/mm bipolar pulse voltage) by switching on the electrical stimulator (for other cellular models see Table 1). **NOTE:** pulse duration and pulse voltage parameters may vary depending on the stimulator, electrode and cellular model.
42. Check whether the cells are following the pacing frequency after 20 seconds. If the cells are steadily contracting, proceed to Step 44.
43. If the cells are not contracting at the imposed frequency, increase the pulse duration with steps of 2 ms or the pulse voltage with steps of 2 V and retry again from Step 42 until the maximum pulse duration (15 ms) and pulse voltage (7 V/mm) is reached. If the maximum is reached, discard this sample.

CRITICAL STEP: *be aware that by increasing either stimulation time and/or voltage, as a consequence of electrolysis, bubbles might form on the edges of the stimulator. Depending on the intensity of the stimulation and the size of the bubbles, significant disruptive effects can be visible on the illumination and focus. Avoid such situations and clean the stimulator if necessary.*

44. Allow the cells to adapt to the stimulation frequency for 1 minute (last minute of incubation time).
45. Record the sample for 20 seconds to ensure registration of minimally three beats.
46. Stop the stimulation.
47. Stop the current flow and start the flow of next drug concentration.
48. Wait for 4 minutes (incubation time minus 1 minute) (for other cellular models see Table 1).
49. Start stimulation with same parameters as previously.

CRITICAL STEP: *do not change the stimulation parameters since this might mask or be mistaken for drug effects.*

50. Allow the cells to adapt to the stimulation frequency for 1 minute (last minute of incubation time).
51. Record the sample for 20 seconds to ensure registration of minimally three beats.
52. Stop stimulation.
53. Repeat Step 47 to Step 52 for the remainder of the drug doses.
54. Repeat Step 34 to Step 53 for the remainder of the samples.

Data organization

Timing: 10-20 min per sample depending on the computer speed.

55. Start the PC equipped with ImageJ/Fiji, MUSCLEMOTION and FFmpeg (see Materials for installation instructions).

56. Move all videos to one directory on the PC.
57. Check the format of the videos. If this is uncompressed AVI, a TIFF image sequence or TIFF image stack, go to Step 59. Otherwise, follow the next step. An easy way to check whether the AVI is uncompressed is to try to open it using ImageJ/Fiji (see Materials for installation instructions).
58. Browse the directory that contains all movies and

- **MacOS/Linux**
  open the Terminal and paste the following command:
  *for i in *.*; do ffmpeg -i "$i" -pix_fmt nv12 -f avi -c:v rawvideo "${i%.*}.avi "; done*

- **Windows**
  run the following command on the Command Prompt:
  for %A IN ("sourcefolder.*") DO ffmpeg -i "%A" -f avi -c:v rawvideo "sourcefolder/%~nA.avi"*

59. If spatially related differences in the recorded data are needed, for example in the case of echography recordings, see Support Protocol 4 for image segmentation and before proceeding (optional).

Video analysis using MUSCLEMOTION
Timing: 30 min per sample depending on the computer speed. Video files for demonstration purposes can be found at:
https://gitlab.com/bjvanmeer/MUSCLEMOTION/tree/master/demoFiles.

60. Start ImageJ/Fiji and run the MUSCLEMOTION macro (see Support Protocol 3 for installation instructions).
61. Before starting batch analysis, it is important to check whether the automated settings are appropriate or whether a customization of the settings is required (Support Protocol 5).
62. Select 'Yes' for batch analysis, select the other settings according to the result of the previous step and click 'OK' (Figure 4, 5).
63. Select the destination folder for the results of the MUSCLEMOTION analysis and click 'OK' (Figure 6).
64. Select the source folder (i.e. where the recordings in the right format are stored) and click 'OK' (Figure 6).

CRITICAL STEP: *Do not use the computer until MUSCLEMOTION has finished since it is possible that foreground windows other than MUSCLEMOTION will interfere with the automated analysis. This will lead to an error in the script which will terminate the batch analysis.* ***TROUBLESHOOTING***

65. Once the analysis of MUSCLEMOTION is finished and the log file of the last measurement is shown (Figure 6), it is necessary to check the outcome of MUSCLEMOTION by inspecting the .jpg files that are generated in the results

folder(s). Locate the result folder. **TROUBLESHOOTING**

66. Open 'Contraction.jpg' and confirm that the reference frame is correct (Figure 7). If in doubt, use the original movie to confirm the correct timing of the contracted state versus the relaxed state. **TROUBLESHOOTING**
67. In addition, check whether the automated analysis identified the points at the correct location (blue dot/line at baseline, vertical red line indicates the amplitude and horizontal red lines to indicate durations at different levels) (Figure 8). **TROUBLESHOOTING**
68. Open 'Comparison calculated (red) and measured (black) speed.jpg' and confirm whether the calculated and measured speed are overlapping and thus indicating linearity. "Proper overlapping" means that the timing of the peaks and valleys is overlapping (Figure 9A). When the peaks and/or valleys are desynchronized (Figure 9Biv., Figure 9C) there is a linearity problem. **TROUBLESHOOTING**

Data analysis

Timing: 30 min per sample.

69. Open the 'Overview-results.txt' file in Excel or any other data processing software to calculate the means of the columns shown in the file (see 'Collected results.xlsx' in the demoFiles folder in the online MUSCLEMOTION repository).
70. Copy the means to designated tables in Excel.
71. Repeat this for all samples and concentrations.
72. Normalize all means of the different concentrations to the mean of the baseline of that specific sample (see 'Collected results.xlsx' in the demoFiles folder in the online MUSCLEMOTION repository).
73. Calculate the mean and standard error of the mean (SEM) of the different samples per concentration. The formula for calculating the SEM is:

$$\mathrm{SE}M = \frac{SD(samples)}{\sqrt{(n\ of\ samples)}}$$

74. Some experimental systems may allow absolute quantification of contraction parameters. Please refer to Support Protocol 1 for detailed instructions.
75. Plot the mean ± SEM per concentration to visualise the dose-response curve. You may want to display the concentrations on the x-axis in log scale.

Support Protocol 1

Correlating and calibrating MUSCLEMOTION for use with specific systems

MUSCLEMOTION quantifies contraction in arbitrary units based on pixel intensity changes but is linearly correlated to certain physical quantities such as force of contraction and displacement [3]. This linearity can be exploited to use MUSCLEMOTION in specific measurement setups to quantify absolute values of physical quantities by 'calibrating' MUSCLEMOTION. To do this, an alternate measurement (AM) technique with which the researcher is familiar is required (e.g. edge detection, force

measurements, optical flow). Furthermore, the following steps need to be followed.

1. Make at least 10 recordings of the cardiac model under study. It is important that the recording allows optimal analysis for both the AM and MUSCLEMOTION. If the AM is an optical assessment similar to MUSCLEMOTION, the same input video can be used for both approaches. If the AM is based on other recordings, (e.g. force transducers, bead tracking) it is necessary to capture this recording simultaneously with the video acquired for MUSCLEMOTION since it is crucial to analyse precisely the same contractions with the two different approaches.
2. Analyse the recordings using both MUSCLEMOTION (as described previously) and the AM.
3. Plot the output of interest of the AM (e.g. displacement, force of contraction, speed of contraction) against the output of interest of MUSCLEMOTION (i.e. in most cases /contraction amplitude) using the user's data analysis software of choice.
4. Use the data analysis software to fit a linear correlation and output the coefficient of determination (R^2) and the formula of the linear fit ($y=ax+b$ where a and b are given by the linear model).
5. If the two datasets have a positive linear correlation and in case the coefficient of determination is high enough for these purposes (typically > 0.7 but may vary depending on the number of measurements and type of applications) the formula describes the relation to be used for absolute quantifications:

   [physical quantity AM] = a • [output MUSCELMOTION]+b

Support Protocol 2

Selecting the appropriate sample speed for applications.

To ensure accurate analysis by MUSCLEMOTION it is essential to record the events of interest (i.e. contraction cycles) at a frame rate that is high enough to correctly reconstruct the information in the event. This is related to the speed of change (e.g. contraction speed or relaxation speed) of the event of interest. This guide will enable users of MUSCLEMOTION to estimate the absolute minimum frame rate required for their own application based on the Nyquist-Shannon sampling theory. As an example, the cardiomyocyte monolayer is described below.

1. Estimate or derive the fastest component of the contraction under baseline conditions from previous experiments or literature.

   For monolayer hPSC-CMs we derived a contraction time of ~170 to ~260 ms from our previous optical flow measurements.

2. Use the following equation to estimate the absolute minimum frame rate under baseline conditions:

$$frame\ rate_{min} = \frac{4}{time_{estimated}}$$

   For monolayer hPSC-CMs we calculated:

$$frame\ rate_{min} = \frac{4}{170 \cdot 10^{-3}} = 23.53\ fps$$

3. To increase the dynamic range and remain accurate should drugs increase the speed of change of the event of interest, it is advised to increase the minimum frame rate with a factor 3.

   For monolayer hPSC-CMs we calculated:

$$23.53 \cdot 3 = 70.59\ fps$$

Support Protocol 3

MUSCLEMOTION macro setup

This protocol provides installation instructions to run the MUSCLEMOTION macro.

1. Download the latest version of the MUSCLEMOTION macro (.ijm) from the online MUSCLEMOTION repository at https://gitlab.com/bjvanmeer/MUSCLEMOTION.
2. Start ImageJ/Fiji and install the macro by clicking 'Plugins' > 'Macros' > 'Install' and selecting the downloaded MUSCLEMOTION macro (.ijm) file. An icon displaying 'MM' will now appear in the toolbar of ImageJ/Fiji (Figure 3).
3. Increase the maximum memory size of ImageJ/Fiji by clicking 'Edit' > 'Options' > 'Memory & Threads…' and setting it to the maximum size of your RAM memory. In the example shown in Figure 3, we had 16 GB of RAM.
4. Start MUSCLEMOTION by clicking the 'MM' icon in the toolbar of ImageJ/Fiji.

Support Protocol 4

Manual segmentation of recordings (optional)

To measure spatially related differences such as contraction wave propagation in acquired videos, it is possible to segment the videos in order to identify the delay between different points. This approach is recommended when analysing movies from echoscopic recordings to capture temporal differences in contraction of heart chambers.

1. Start ImageJ/Fiji and run the MUSCLEMOTION macro (see Support Protocol 3 for installation instructions).
2. Open the video of interest.
3. Select the rectangle tool and select the first area of interest.
4. Select 'Image' > 'Duplicate' and tick 'Duplicate stack' in the pop-up window.
5. Save this image by selecting 'File' > 'Save as' > 'Tiff…' with an appropriate name.
6. Repeat steps 3 to Step 5 for all areas of interest.
7. Repeat steps 2 to Step 6 for all videos of interest.

Support Protocol 5

Choosing appropriate MUSCLEMOTION settings

To make optimal use of MUSCLEMOTION, we recommend using the batch processing function. This allows a batch of recorded movies to be analysed without user interaction. For successful analysis, it is important to identify the appropriate settings for the recordings of interest. To check whether the settings work properly, test the analysis on a single recording before selecting batch mode. Using the parameter wizard that initiates after starting the MUSCLEMOTION macro, a step-by-step guide for selecting the appropriate MUSCLEMOTION settings is described below.

1. Select 'No' for setting (A) to analyse single recordings (Figure 4).
2. Select 'Yes' (in case of TIFF image sequence) or 'No' (in case of TIFF stack, AVI, etc.) for setting (B) depending on the format used for the recordings.
3. Select 'Yes' or 'No' in setting (C) will introduce a Gaussian blur (low-pass filter) in every frame of the recording to decrease the change of 'out-of-bounds' errors due to repetitive patterns such as sarcomeres[3]. It is advised to start without Gaussian blur.
4. In setting (D) select the frame rate used to record the videos.
5. The speed window (setting E) determines the frame-to-frame interval used for calculating the contraction velocity and identifying the reference frame. One to five percent of the frame rate is recommended. For high noise levels, this might need to be increased. High levels might affect timing and amplitude levels.
6. For the first run, select 'Yes, but keep it simple' in setting (F) (Figure 5).
7. For the first run, select 'Yes, but keep it simple' in setting (G).
8. For the first run, select 'Yes, but keep it simple' in setting (H).
9. Click 'OK' and select the requested locations to run the algorithm.
10. Evaluate output (see Basic Protocol 1, step 65).
11. If the results, linearity checks and graphs are in order, these settings are appropriate and can be used for batch processing. If not, please continue with the steps below.
12. If the macro displays an error, retry the analysis and make relevant changes. **TROUBLESHOOTING**
13. If the reference frame is incorrect, retry the analysis and make relevant changes; **TROUBLESHOOTING**
14. If the linearity plots do not overlap, retry the analysis and make relevant changes. **TROUBLESHOOTING**

Reagents and Solutions

- **Tyrode's solution:** mix (in mM): 140 NaCl, 5.4 KCl, 1.8 $CaCl_2$, 1.0 $MgCl_2$, 5.5 glucose, 5.0 HEPES. Set the pH to 7.35 using NaOH[8].
- **BPEL:** prepare BPEL medium as described previously[9].

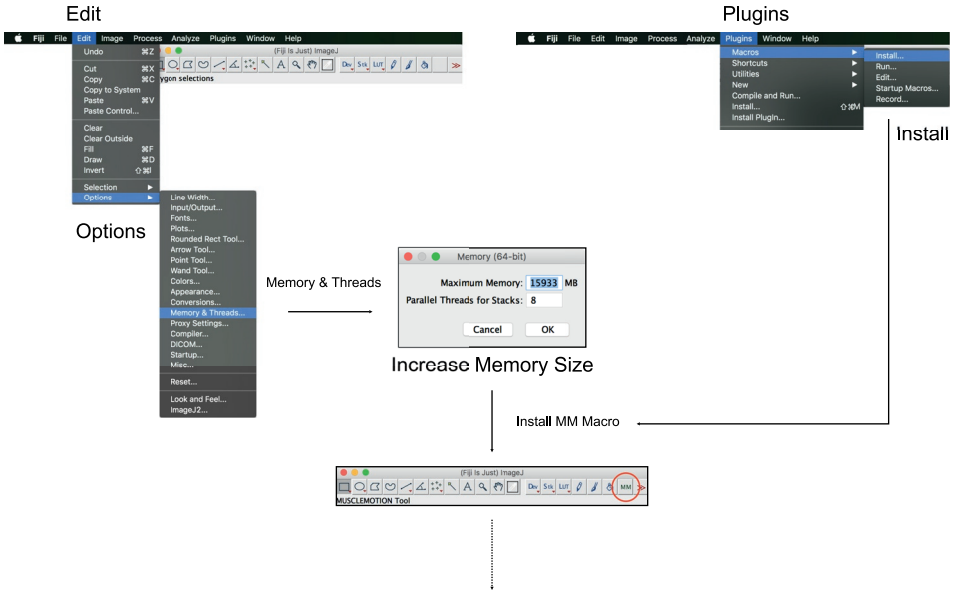

Figure 3. Installation of MUSCLEMOTION.

Increasing the processing memory of ImageJ/Fiji is recommended before using MUSCLEMOTION. After installation of MUSCLEMOTION a button 'MM' will appear on the toolbar.

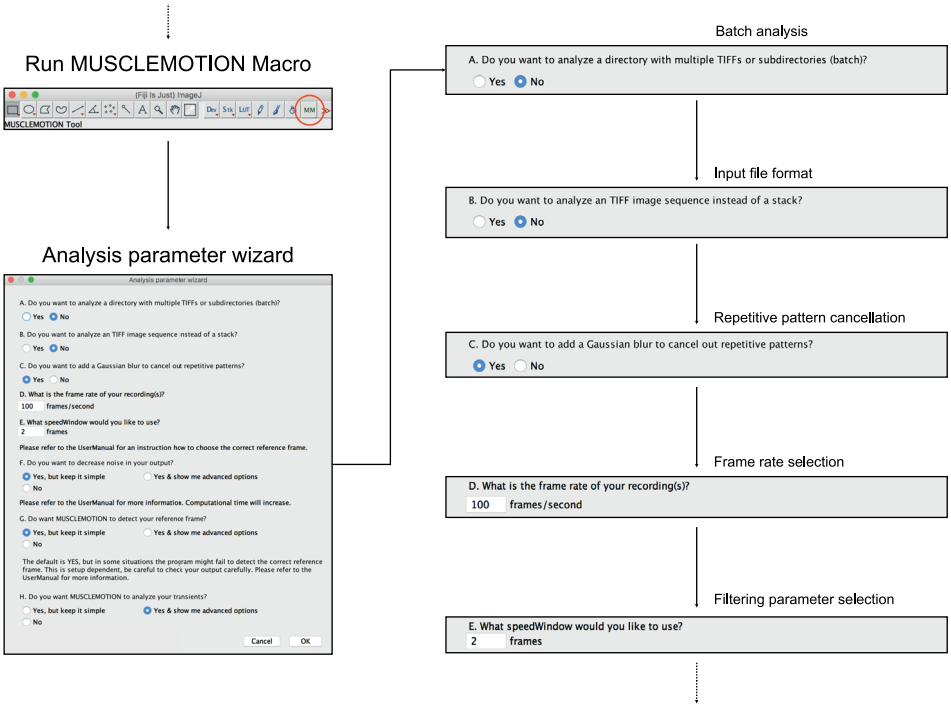

Figure 4. Running MUSCLEMOTION with the analysis parameter wizard.

The analysis parameter wizard of MUSCLEMOTION enables users to select analysis parameters without having to change (parts of) the macro code. The wizard remembers the last used settings and will recall them automatically in the next run. See Support Protocol 5 for defining the appropriate settings for custom applications.

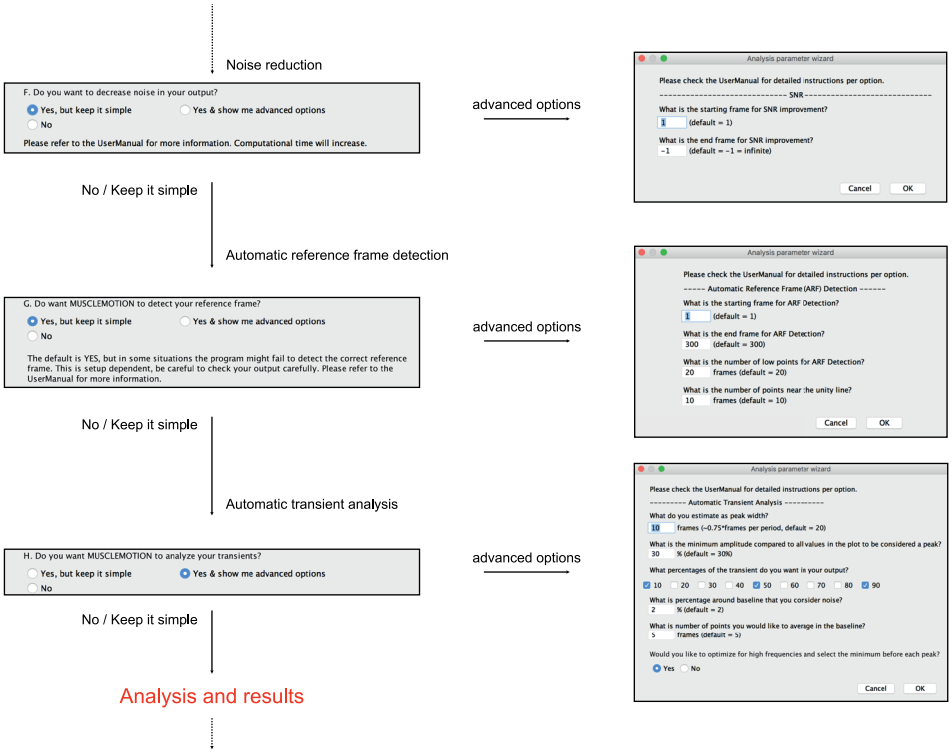

Figure 5. Advanced functions in the analysis parameter wizard.

More advanced users are enabled to customize MUSCLEMOTION using the advanced settings in the wizard. See Support Protocol 5 for defining the appropriate settings for custom applications.

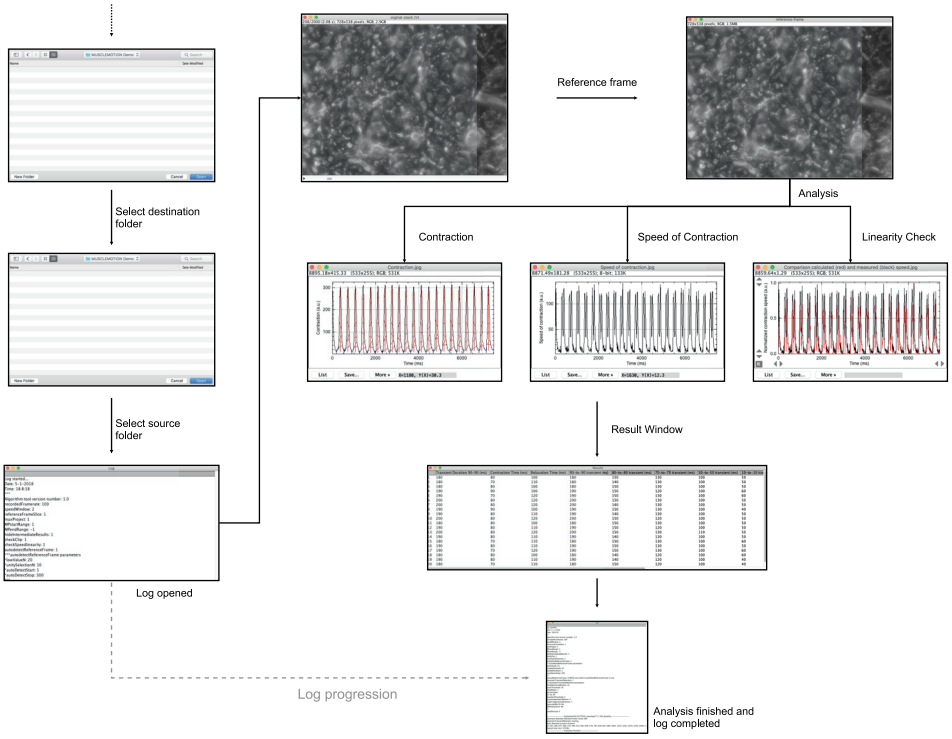

Figure 6. Input/output selection and result windows of MUSCLEMOTION.

After going through the analysis parameter wizard users are requested to indicate the destination folder for the results and the source folder (or file if not operating in batch mode). Next, a log window starts and during analysis multiple windows will be opened, among which the result windows of contraction, speed of contraction, the comparison plot (linearity check) and the result window. When the analysis is finished, the log window will appear up front again and displays 'Evaluation finished'.

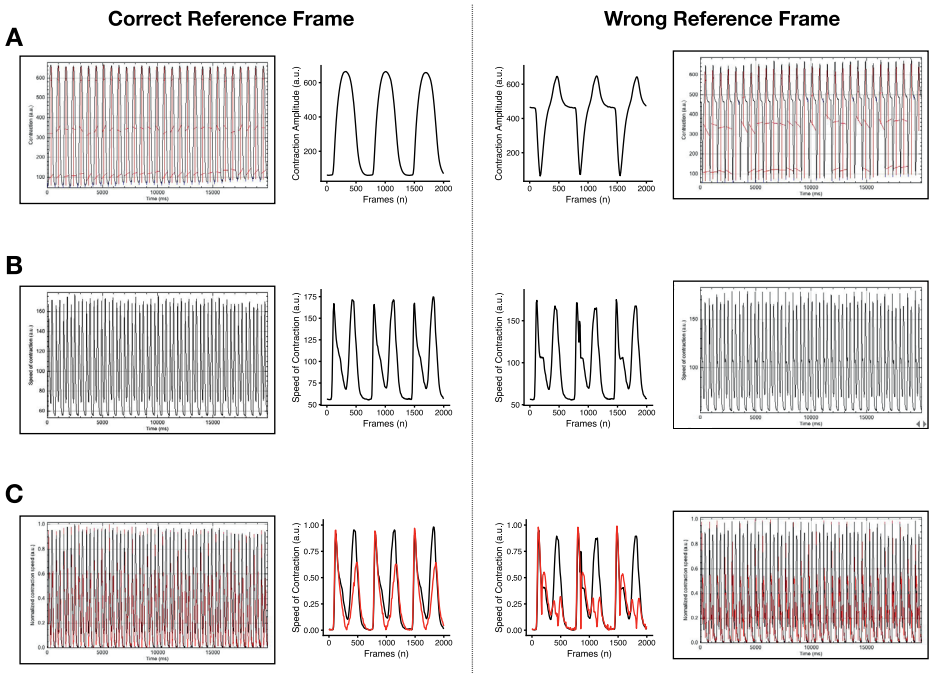

Figure 7. Example of correct and incorrect detected reference frame.

The analysis of movie in which a correct reference frame was detected versus analysis of movie in which an incorrect reference frame was detected. A) Contraction analysis, B) speed of contraction analysis and C) comparison calculated (red) and measured (black) speed of contraction.

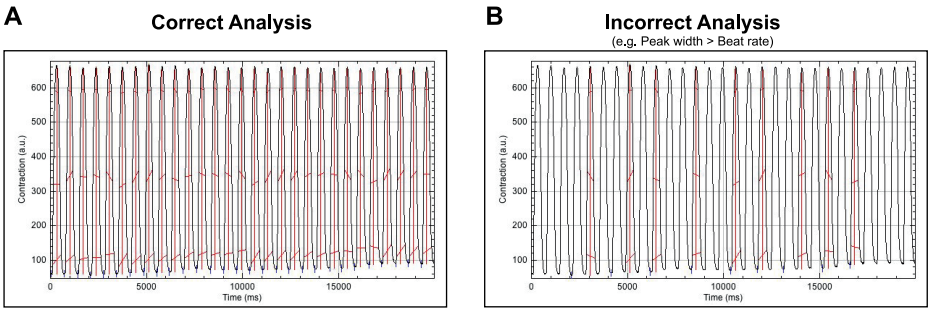

Figure 8. Example of correct and incorrect contraction transient analysis.

A) Example of correct analysis, with contraction transients properly identified by a vertical red line centred on each transient peak. B) Example of incorrect analysis, where only a few contraction transients (overall nine transients in the example) could be automatically identified.

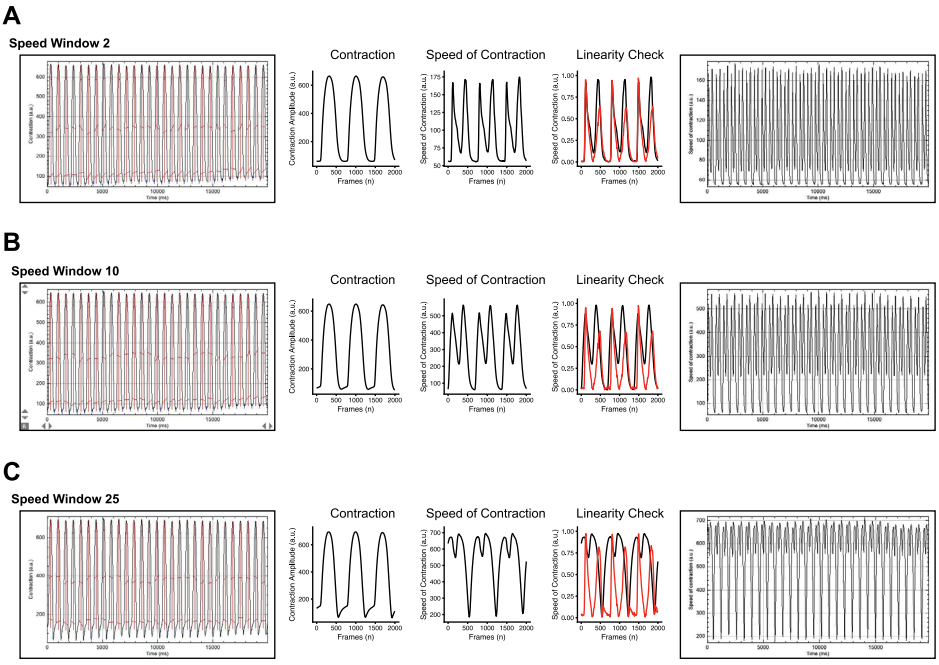

Figure 9. Contraction analysis for increasing speed windows to demonstrate decreased linearity.

A) Contraction analysis with a speed window of 2. B) Contraction analysis with a speed window of 10. C) Contraction analysis with a speed window 25.

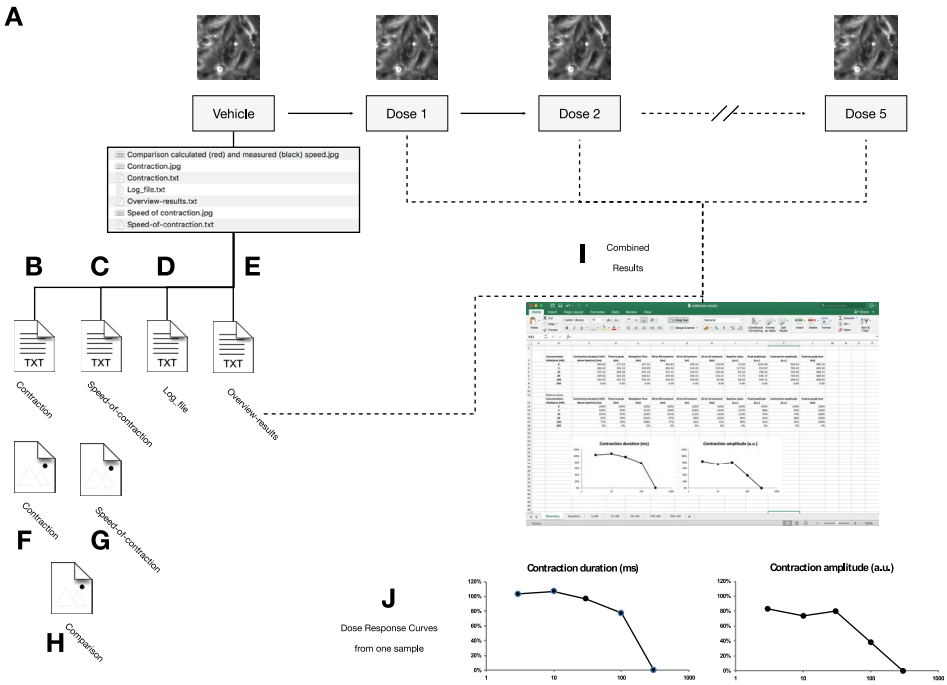

Figure 10. Overview of the anticipated results.

A) Area for contraction measurements of the monolayer on the coverslip. B-H) Contraction analysis files generated by MUSCLEMOTION. I-J) Overview-results file and relative dose-response plots loaded as spreadsheet.

Commentary

Background Information

We previously demonstrated that MUSCLEMOTION can be used to analyse movies of contracting cells or tissues obtained by any platform. In our original publication[3], we showed that the output of MUSCLEMOTION correlated well with outputs from gold standards used in different cell configurations. We compared MUSCLEMOTION to Optical Flow algorithms, demonstrating that, although information on directionality was lost, significant improvements in the linearity of results were achieved; this is extremely important for disease modelling as the effect of a disease on contraction can be predicted more precisely. Fast Fourier Transform analysis to assess sarcomere fractional shortening on adult rabbit CMs correlated well with results from MUSCLEMOTION, expanding the applicability of this method to multiple cell types. Furthermore, MUSCLEMOTION outputs correlated well with force values obtained from post deflection by Engineered Heart Tissues, indicating that absolute force values can be generated upon initial calibration and that MUSCLEMOTION works well with 3D tissues.

Troubleshooting

Troubleshooting for data collection and analysis is extensively discussed in Table 2.

Statistical Analyses

In the reported example, one-way Repeated Measures ANOVA should be used to compare means among different doses. Tailored pairwise comparisons can be made to further investigate the significance among groups. In the case of multiple groups, e.g. a comparison between healthy and diseased cell lines at different drug doses, use of two-ways Repeated Measures ANOVA is required.

Understanding Results

This protocol describes the preparation of samples, experimental procedures and data analysis using MUSCLEMOTION for contraction measurements in hPSC-CM monolayer cultures. Moreover, it provides guidance and detailed additional information to enable contractility measurements to be carried out in a wide range of other contractile cell configurations including custom applications. Following this protocol, the differentiation of hPSCs into hPSC-CM monolayers is the first stage. Next, hPSC-CMs are attached to the substrate and show regular cyclic contraction in a dense monolayer on coverslips (Figure 10A). The experiments carried out according to the protocol result in a series of movies of each sample after drug incubation over a range of concentrations (see movies in the demoFiles folder in the online MUSCLEMOTION repository). MUSCLEMOTION quantifies data from these movies and generates a folder for each movie containing (i) a file describing the contraction (Figure 10B, see result folders in the demoFiles folder in the online MUSCLEMOTION repository), (ii) a file describing the speed of contraction (Figure 10C), (iii) a log file containing information regarding the analysis settings and parameters (Figure 10D) and (iv) a file summarizing the quantification of the contraction (Figure 10E). In addition, three .jpg files are generated for quick data checks (Figure 10F-H).

After all movies have been analysed using MUSCLEMOTION and the data collected, averaged and normalized as described (Figure 10I), a dose-response curve is created that depicts the effect of the drug on contractility in the particular cellular setup of study (Figure 10J). In this protocol, nifedipine is used as an example as it shows a clear decrease of contraction amplitude and contraction duration compared to vehicle, as expected (Figure 10G, H).

Time considerations

Sample preparation
Step 1: 17-21 days.
Step 2-21: 3 h.
Step 22+23: 7 days.

Experimental preparation
1 h.

Experimental procedure
45 min per sample.

Data organization
10-20 min per sample depending on the computer speed.

Video analysis using MUSCLEMOTION
30 min per sample depending on the computer speed.

Data analysis
30 min per sample.

Acknowledgements

We thank Umber Saleem, Ingra Mannhardt, Arne Hansen and Thomas Eschenhagen (Hamburg) for movies of hPSC-CM engineered heart tissues, Charlotte Koopman, Sarah Kamel and Jeroen Bakkers (Hubrecht Institute, Utrecht) for movies of zebrafish, Eduard Holman and Monique Jongbloed (LUMC) for echography recordings, and Elisa Giacomelli, Valeria Orlova and Milena Bellin (LUMC) for movies of cardiac microtissues in the original paper. We are also grateful for funding from: the National Centre for the Replacement, Refinement and Reduction of Animals in Research (NC3Rs) CRACK IT InPulse project code 35911-259146; ERC-AdG STEMCARDIOVASC to CLM (CLM, BJM, LGJT); ZonMW MKMD Applications of Innovations 2015-2016 (CLM, LS), CVON – HUSTCARE 2013-2018 (CLM). The authors declare competing financial interests (see the HTML version of this article for details). CLM is co-founder of Pluriomics (now Ncardia) b.v., GLS and FB are co-founders of Clyde Biosciences Ltd. BJM and LS designed the study, developed the protocol, carried out the experiments, carried out the data analysis and drafted the manuscript. LGJT designed the study, co-developed the protocol and revised the manuscript critically. FLB, GLS and CLM designed the study and revised the manuscript critically.

Key reference

The development, validation and head-to-head comparison of MUSCLEMOTION was carried out in the following publication:
Sala, L., van Meer, B. J., Tertoolen, L. T., Bakkers, J., Bellin, M., Davis, R. P., Denning, C. N., Dieben, M. A., Eschenhagen, T., Giacomelli, E., et al. 2017. MUSCLEMOTION: A Versatile Open Software Tool to Quantify Cardiomyocyte and Cardiac Muscle Contraction *In Vitro* and *In Vivo*. *Circulation Research.* CIRCRESAHA.117.312067.

Internet resources

Open git repository with source files, demo files and guide: https://gitlab.com/bjvanmeer/MUSCLEMOTION.git

Table 2: Troubleshooting

Step	Problem	Possible reason	Solution
65	"no images open" error	A wrong file or file format is selected	(i) Check whether all files are correct and if not, convert with FFmpeg. (ii) Check whether the selected option regarding TIFF image sequence and batch mode is selected in the macro wizard.
66	Incorrect reference frame		(i) Change the speed window. (ii) Change the advanced settings of automatic reference frame detection by selecting 'Yes & show me advanced options' in the macro wizard. Make sure that the interval (starting frame to end frame) is set to include at least three full events (i.e. contractions). In addition, increasing the number of low points and points near unity line might help, especially when evaluating movies with high frame rates. (iii) Select 'No' in setting (G) and you will be asked to select the reference frame manually for each recording. NOTE: this requires manual interaction in every movie of the batched analysis and is only advised when analysing a small number of movies or when all above steps did not help in resolving issues with automatic reference frame detection.
66	Plots are too noisy	(i) Sampling rate is too high (ii) Excessive noise in the movie (iii) Not enough movement	(i) Increase the speed window. (ii) Ensure that the experimental conditions and the lighting are free from debris, oscillations or flickering. (iii) Manually check whether the movie has movement.
66	Large spikes in the plot	(i) Undesired movement influenced the measurement	(i) Check the original movie for undesired debris or vibrations.
66	Baseline drift	(i) The field of view has changed (ii) Incomplete cell/ tissue relaxation	(i) Check the original movie for frame shifts. (ii) Evaluate whether this effect is desired (e.g. as a consequence of a drug) or whether is due to an incorrect adaptation to the stimulation.
68	Linearity plots do not overlap	(i) filtering due to the running difference might be too high (ii) Repetitive patterns might lead to out-of-bounds situations	(i) Decrease the speed window. (ii) Switch on Gaussian blur in the macro wizard.

References

1. Chi, K. R. Revolution dawning in cardiotoxicity testing. *Nat. Rev. Drug Discov.* **12,** 565–567 (2013).

2. van Meer, B. J., Tertoolen, L. G. J. & Mummery, C. L. Concise Review: Measuring Physiological Responses of Human Pluripotent Stem Cell Derived Cardiomyocytes to Drugs and Disease. *Stem Cells* **34,** 2008–2015 (2016).

3. Sala, L. et al. MUSCLEMOTION: A Versatile Open Software Tool to Quantify Cardiomyocyte and Cardiac Muscle Contraction *In Vitro* and *In Vivo*. Circ.Res. 122, e5–e16 (2018).

4. van den Berg, C. W., Elliott, D. A., Braam, S. R., Mummery, C. L. & Davis, R. P. Differentiation of Human Pluripotent Stem Cells to Cardiomyocytes Under Defined Conditions. in *Patient-Specific Induced Pluripotent Stem Cell Models: Generation and Characterization* (eds. Nagy, A. & Turksen, K.) 163–180 (Springer New York, 2016).

5. Breckwoldt, K. et al. Differentiation of cardiomyocytes and generation of human engineered heart tissue. *Nat. Protoc.* **12,** 1177–1197 (2017).

6. Burridge, P. W., Holmström, A. & Wu, J. C. Chemically Defined Culture and Cardiomyocyte Differentiation of Human Pluripotent Stem Cells. *Curr. Protoc. Hum. Genet.* **87,** 21.3.1-21.3.15 (2015).

7. Phelan, M. C. Techniques for Mammalian Cell Tissue Culture. in *Current Protocols in Cytometry* 1–19 (John Wiley & Sons, Inc., 2006).

8. Sala, L. et al. A new hERG allosteric modulator rescues genetic and drug-induced long-QT syndrome phenotypes in cardiomyocytes from isogenic pairs of patient induced pluripotent stem cells. *EMBO Mol. Med.* **8,** 1065–1081 (2016).

9. Ng, E. S., Davis, R., Stanley, E. G. & Elefanty, A. G. A protocol describing the use of a recombinant protein-based, animal product-free medium (APEL) for human embryonic stem cell differentiation as spin embryoid bodies. *Nat. Protoc.* **3,** 768–76 (2008).

Abstract

Cardiomyocytes from human induced pluripotent stem cells (hiPSC-CMs) are increasingly recognized as valuable for determining the effects of drugs on ion channels but they do not always accurately predict contractile responses of the human heart. This is in part attributable to their immaturity but the sensitivity of measurement tools may also be limiting. Measuring action potential, calcium flux or contraction individually misses critical information that is captured when interrogating the complete excitation-contraction coupling cascade simultaneously. Here, we develop an hypothesis-based statistical algorithm that identifies mechanisms of action. We design and build a high-speed optical system to measure action potential, cytosolic calcium and contraction simultaneously using fluorescent sensors. These measurements are automatically processed, quantified and then assessed by the algorithm. Multiplexing these three critical physical features of hiPSC-CMs allows identification of all major drug classes affecting contractility with detection sensitivities higher than individual measurement of action potential, cytosolic calcium or contraction.

Chapter 5

Simultaneous measurement of excitation-contraction coupling parameters identifies mechanisms underlying contractile responses of hiPSC-derived cardiomyocytes

Modified after Nature Communications 10, article number 4325 (2019)

Berend van Meer, Ana Krotenberg, Luca Sala, Richard Davis, Thomas Eschenhagen, Chris Denning, Leon Tertoolen, Christine Mummery

Introduction

Human induced pluripotent stem cell derived cardiomyocytes (hiPSC-CM) are increasingly used to study mechanisms underlying drug responses and disease *in vitro*, with action- or field potential measurements by microelectrode arrays translating well to clinically relevant arrhythmia or cardiotoxicity classification[1-4]. Pharma and regulatory authorities are thus already implementing such approaches in early drug discovery and cardiotoxicology assessment. However, analytical methods that relate these electrophysiological parameters to contraction and cytosolic calcium transients, also salient features of cardiomyocyte physiology, are still limited. This makes clinically relevant interpretation of drug responses affecting cardiomyocyte contractility challenging[5].

Under normal conditions, contraction is the result of excitation-contraction coupling (EC coupling). This is a complex cascade of ion channel activities, internal calcium storage and contractile filament availability with the action potential (AP), cytosolic calcium flux (Ca) and the actual contraction (Co) being the most important physical transients[6]. The mechanisms of action (MOAs) through which cardioactive drugs affect contraction typically target ion channels or -pumps, adenosine-, muscarinic- and adrenergic receptors, phosphodiesterases (PDE), myosin or elements of thin filaments such as troponin C. The effect of some of these cardioactive drugs would not be expected in hiPSC-CM cultures (for example, antagonists of adrenergic and adenosine receptors require the presence of respective agonists in the culture medium) while often the effect of other drugs would be expected but is undetectable because of hiPSC-CM immaturity[7]. Improving hiPSC-CM maturity, either by altering cellular configuration (e.g. 2D or 3D and cell alignment, which is highly correlated with

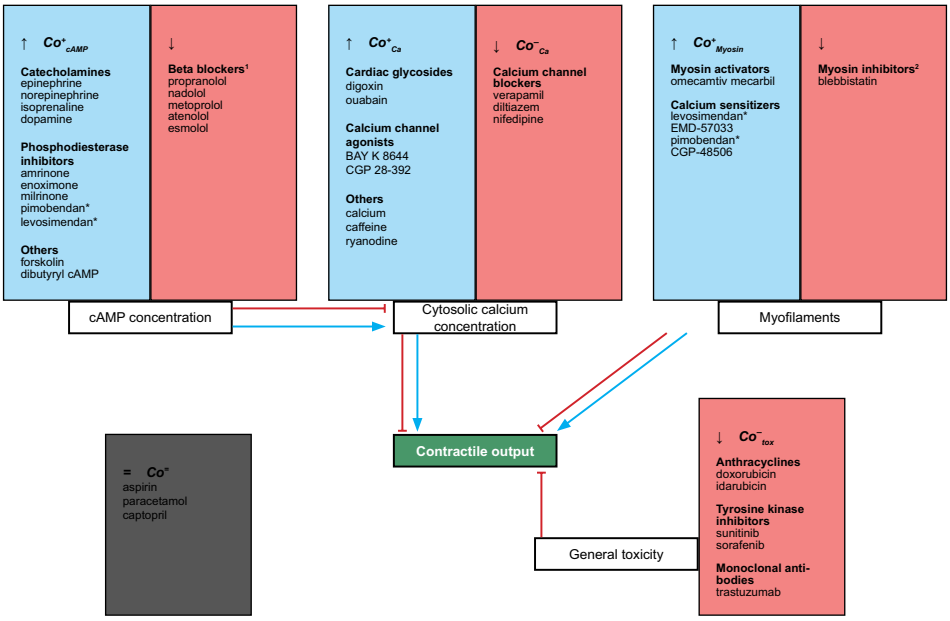

maturity)[8-10] or refined measurement methods[11] are factors reported to overcome the lack of response in such cases, but are still limited in providing mechanistic insight into hiPSC-CM pharmacological responses. Measurement methods that give insight into AP, Ca and Co simultaneously are needed and they would allow assessment of the complete EC coupling of a single cardiomyocyte beat cycle and thereby reducing data variability and experimental bias compared to asynchronous measurements. We therefore hypothesize that simultaneous quantification of the changes of AP, Ca and Co in response to drugs will provide insight into the contractile MOA affected, higher detection sensitivity of those mechanisms and allow proper contractile risk classification of drugs.

We thus report the development of tools to gain the necessary mechanistic insight into hiPSC-CM physiology. First, building on literature, we develop a hypothesis-based statistical analysis algorithm to test the likelihood of occurrence for each of the most important mechanisms via which drugs affect cardiomyocyte contractility. Next, we engineer a high-speed system capable of measuring and quantifying AP, Ca and Co simultaneously by means of fluorescent sensors ANNINE-6plus, Rhod-3 and CellMask Deep Red in combination with our recently developed optical contraction software tool MUSCLEMOTION[12]. Using this Triple Transient Measurement (TTM) system we measure and quantify the response of commercial hiPSC-CMs to a set of drugs that covers the complete range of potentially affected contractile mechanisms.

We find that simultaneous TTM in combination with our algorithm allows automatic and unbiased identification of the MOAs affected by the test set of compounds and increased the sensitivity of detecting contractile MOAs compared to separate assessment of AP, Ca and Co.

Figure 1: Schematic of most critical mechanisms affecting cardiomyocyte contraction targeted by drugs.

Most therapeutics that target the heart or have off-target effects on the heart fall within the mechanisms shown. 1: Since no beta-adrenergic agonists are present in *in vitro* cultures with defined medium, this category is not relevant in this study. 2: This group is small and the mechanisms are not specific. For example, while blebbistatin reduces contractility, it also affects cardiomyocyte electrophysiology. Therefore, this category is not included in this study. *: These compounds exhibit both PDE inhibiting and myofilament Ca2+ sensitizing properties, with the dominant mechanism typically depending on the concentration.

Results

Hypothesis table

To develop an algorithm capable of identifying contractile MOAs affected in response to drugs, we first inventoried potential effects on the kinetics of cardiomyocyte AP, Ca and Co. A schematic is shown in Figure 1. Three general possibilities defined the first set of categories: enhanced contraction (Co^{+}), reduced contraction (Co^{-}) and no effect on contraction ($Co^{=}$). The most important contractile MOAs underlying Co^{+} in cardiomyocytes are (i) Co^{+}_{Ca}: increased free cytosolic calcium concentration ($[Ca^{2+}]_i$) via for example calcium- and sodium channel agonists[13,14], cardiac glycosides[15] and human ether-a-go-go related gene (hERG) channel blockers[16]; (ii) Co^{+}_{Myosin}: direct thick- or thin myosin filament activation[17] or (iii) Co^{+}_{cAMP}: enhancement of the complete contractile cascade via higher levels of the second messenger 3',5'-cyclic adenosine monophosphate (cAMP) by beta-adrenergic stimulation[18] or PDE_3 inhibition[19].

Main mechanisms resulting in Co^{-} are (i) Co^{-}_{Ca}: reduction in $[Ca^{2+}]_i$ either via changes in the activity of the L-type calcium channel, sarcoplasmic reticulum calcium ATPase (SERCA) or ryanodine receptors type 2[20], or (ii) Co^{-}_{tox}: via general cardiotoxicity, often associated with mitochondrial dysfunction or more generally with increased mitochondrial Ca^{2+} buffering capacity, apoptosis and necrosis[21]. These Co^{-} mechanisms do not include contractile quiescence that occurs as a consequence of excessive AP duration (APD) prolongation, since these compounds are often Co^{+} before failing to repolarize in time to meet the imposed stimulation frequency.

Two general class of drugs have been excluded in the algorithm: beta blockers and myosin inhibitors. Since no beta-adrenergic agonists are present in *in vitro* cultures with defined medium, beta blockers are not relevant in this study. Regarding the myosin inhibitors, this group is small and the mechanisms are not specific. For example, while blebbistatin reduces contractility, it also affects cardiomyocyte electrophysiology[22].

The expected effects on AP, Ca and Co kinetics per MOA are listed in the hypotheses table (Table 1). Due to the heterogeneity of the drugs within each class, it is often possible for some compounds to have mixed or even diverse effects on the kinetic parameters although being grouped by their main effect on Co. For this reason, we indicated in these cases what the effects are that, from a theoretical point of view, we do not expect for each specific class of compound (i.e. NOT ↓; NOT ↑; NOT =). For example, digoxin and E-4031 are both part of Co^{+}_{Ca}, while they shorten[23] and prolong[24] the action potential, respectively. While most kinetic parameters in Table 1 are simple measurements of parts of the waveform, action potential triangulation is calculated as the difference between APD at 30% of repolarization and APD at 90% of repolarization[25]. Triangulation is instrumental in detecting proarrhythmic effects.

Experimental design and statistical analysis algorithm

Next, we developed an algorithm based on standard statistics to test whether a certain drug response is described by the effects summarized in the Hypotheses Table. The experimental design to test the concentration-dependent drug response in hiPSC-CMs is shown in Figure 2a. To eliminate variation and time-dependent response effects,

Table 1: Hypotheses Table.

Expected effects on kinetic measures of action potential (AP), cytosolic calcium transient (Ca) and contraction (Co) per contractile mechanism of action (MOA). ↓: decrease; ↑: increase; =: no difference. NOT [effect] means all other effects than [effect] might be expected, depending on the specific drug within the MOA category.

	$\overline{Co^{=}}$	$\overline{Co^{+}_{Ca}}$	$\overline{Co^{+}_{Myosin}}$	$\overline{Co^{+}_{cAMP}}$	$\overline{Co^{-}_{Ca}}$	$\overline{Co^{-}_{tox}}$	
	Typical compound	**Aspirin**	**Ouabain**	**Omecamtiv Mecarbil**	**β-adrenergic agonist**	**Verapamil**	**Doxorubicin (long term)**
Kinetic parameter	**References**	42–44	15,45,46	17,47,48	6,49,50	51–53	21,54,55
Action potential (AP)	amplitude	=	=	=	=	↓	↓
	t_{rise}	=	↓	=	↓	NOT ↓	↑
	t_{APD}	=	NOT =	=	↓	↓	NOT ↑
	triangulation	=	↓	=	↓	↓	↑
Calcium transient (Ca)	amplitude	=	↑	=	↑	↓	↓
	$t_{to\ peak}$	=	NOT ↓	NOT ↑	↓	↓	NOT ↑
	t_{decay}	=	NOT ↓	NOT ↑	↓	↓	NOT ↑
Contraction (Co)	amplitude	=	↑	↑	↑	↓	↓
	$t_{contraction}$	=	NOT ↓	↑	↓	↓	NOT ↑
	$t_{relaxation}$	=	NOT ↓	NOT ↓	↓	↓	NOT ↑

all concentrations are compared to the vehicle (0.01% DMSO) measurements in the resulting concentration-response plots (Figure 2b). These vehicle measurements are also the basis of our analysis algorithm since the probability of a kinetic parameter not changing ('=' in Table 1) is equal to the probability of it being part of the vehicle population, described by its probability density function (PDF). To determine the likelihood of a parameter to be increased, decreased or unchanged, the PDF was normalized to the mean and multiplied by 10 to have a range of 0–10. The resulting function was divided in three corresponding spaces (Figure 2c), which determine the Probability Scores (PS) for each possibility (↑, ↓ or =) using the following formulae:

$$PDF(x) = \frac{1}{\sqrt{2\pi \cdot sd_{mean}^2}} \cdot e^{-\frac{(x-mean_{vehicle})^2}{2 \cdot sd_{mean}^2}}$$

$$PS_{=}(x) = \frac{10 \cdot PDF(x)}{PDF(mean_{vehicle})}$$

$$PS_{\uparrow}(x) = \begin{cases} 0, & x < mean_{vehicle} \\ 10 - PS_{=}(x), & x \geq mean_{vehicle} \end{cases}$$

$$PS_{\downarrow}(x) = \begin{cases} 10 - PS_{=}(x), & x \leq mean_{vehicle} \\ 0, & x > mean_{vehicle} \end{cases}$$

where $sd_{vehicle}$ is the standard deviation of the vehicle measurements. Since we are interested in finding the most likely hypothesis rather than looking at absolute values resulting from these formulae and

$$PS_{=}(x) \gg PS_{\uparrow}(x)$$

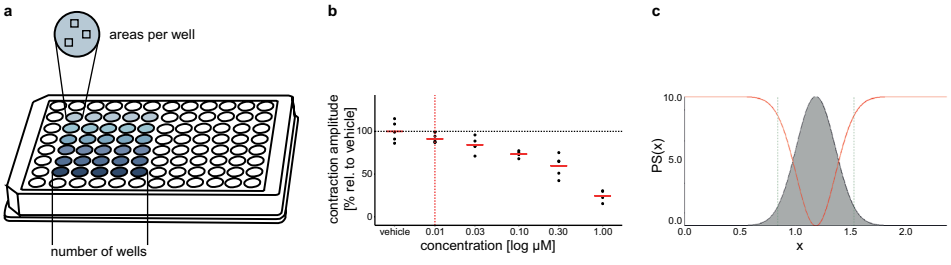

and

$$PS_{=}(x) \gg PS_{\downarrow}(x)$$

if $x \approx mean_{vehicle}$, it is reasonable to assume $PS_{\uparrow}(x) = 0$ and $PS_{\downarrow}(x) = 0$ if $x < mean_{vehicle}$ and $x > mean_{vehicle}$, respectively.

The process is repeated for the 10 kinetic parameters according to Table 1 and all PS values are added to reach a total PS between 0 and 100. The hypothesis with the highest total score is most likely to indicate the relevant MOA.

Development of the Triple Transient Measurement system

Although a wide range of tools is available to measure the transients separately or as combinations of two, we aimed to measure the three transients AP, Ca and Co simultaneously to decrease the measurement-to-measurement variation and enable multiplexing of all 10 parameters from a single biological sample at exactly the same time. Since most dedicated measurement systems have limited flexibility in the setup itself (e.g. measuring only impedance-based contractility or extracellular electrical field properties by multi electrode arrays; MEAs) or in the throughput or invasiveness (e.g. patch clamp electrophysiology requiring individual cell impalement) an optical system was designed that had a sampling speed >300 frames per second (fps) as required to capture all hiPSC-CM transient kinetics accurately. AP, Ca and Co can be measured optically using fluorescent voltage- and calcium sensitive dyes and fluorescent membrane labelling combined with the analysis algorithm MUSCLEMOTION[12], respectively.

Simultaneous fluorescent imaging can be done using wavelength separation in the emission pathway or by high-speed switching between wavelengths. Since wavelength separation decreases the light intensity and exposure times had to be low due to the sampling speed, high-speed switching was the method of choice in combination with a multiband filter to avoid slow mechanical switching. In turn, this limited the choice of dyes since they had to have no or minimal overlapping excitation wavelengths. ANNINE-6plus, Rhod 3 and CellMask Deep Red were selected together with the appropriate excitation LEDs emitting at 470 nm, 560 nm and 656 nm (Supplementary Figure 1). To investigate the extent to which the optical sensors affected baseline

Figure 2: Experimental setup and example output.

a) Schematic layout of the experimental setup; b) output example of contraction amplitude in a concentration-response plot in which individual points show averaged values of a well and the red dotted line indicates the known therapeutic concentration; c) corresponding probability density function (grey) and $PS_{\uparrow}$ and $PS_{\downarrow}$ (red lines) describing the three spaces for the three Probability Scores.

electrophysiological responses, hiPSC-CMs previously derived from patients with Jervell and Lange-Nielsen Syndrome (JLNS)[26] were plated on MEAs and the spontaneous electrophysiological response was measured before and after incubation with the dyes (Supplementary Figure 2). Inferential statistics with ANOVA was performed and no significant effect of the sensors was found. In addition, values found were similar to those previously reported[27]. Finally, the LEDs and camera where synchronized using a computer with data acquisition card and custom software to reach a sampling speed of 1000 fps, resulting in a sample speed of 333 fps per transient, which allowed us to reach an effective synchronisation among transients. Due to the high sampling speed required, the camera exposure time was limited which, in turn, limited the levels of fluorescent signal that could be detected in the camera; we therefore amplified the light using an image intensifier.

Our algorithm uses vehicle measurements to define the baseline population, so a fixed pacing frequency of 1.2 Hz was chosen for all measurements instead of an adaptive frequency. The latter would have required frequency correction for all parameters but the mathematical models for such correction are imperfect for action potentials and unavailable for calcium and contraction. hiPSC-CMs were stimulated using a method developed in-house to produce a block pulse that was chosen to be as short as possible (2–10 ms) and used a voltage as low as possible (10–18 V) while still activating the cells. The settings were kept consistent while measuring under baseline conditions and after drug addition. All wells were measured, and thus stimulated, only twice and no changes were seen in susceptibility of response to the field stimulation during the second measurement. A 50% medium change during drug addition minimized electrolysis effects. To test whether there was any crosstalk between the fluorescent signals of the different dyes, different wells of Pluricyte hiPSC-CMs where exclusively labelled with each of the three dyes and exposed to all three LED wavelengths individually (Supplementary Figure 3). Assessment of the fluorescence intensity revealed that ANNINE-6plus and Rhod 3 signals were only present in response to 470 and 560 nm wavelengths, respectively. CellMask Deep Red showed a modulating image intensity due to contraction usable for MUSCELMOTION analysis only at 656 nm. An overview of the setup is shown in Figure 3a.

Data extraction and processing

For each measurement point, 7 s of recording were made at 1000 fps using a spatial resolution of 720 × 720 pixels yielding a file size of 3.6 GB. This large amount of data is then handled using automated data processing algorithms. First, the total file is split into three separate stacks corresponding with the three transients AP, Ca and Co. Next, the image intensity plots are extracted from all three image stacks (Figure 3b). This yields the raw AP signal, Ca signal and the motion artefact (MA) signal. Since CellMask Deep Red (i.e. the fluorophore that is the origin of the MA signal) is colocalized with the VSD in the membrane of the hPSC-CMs and recorded simultaneously with the VSD signal, we could use the MA signal for ratiometric correction of the AP and Ca signal[28]. Meanwhile, the Co stack was also analysed using MUSCLEMOTION to quantify hiPSC-CM contraction.

Next, the data were cleaned by applying MA correction, the AP signal inverted (since

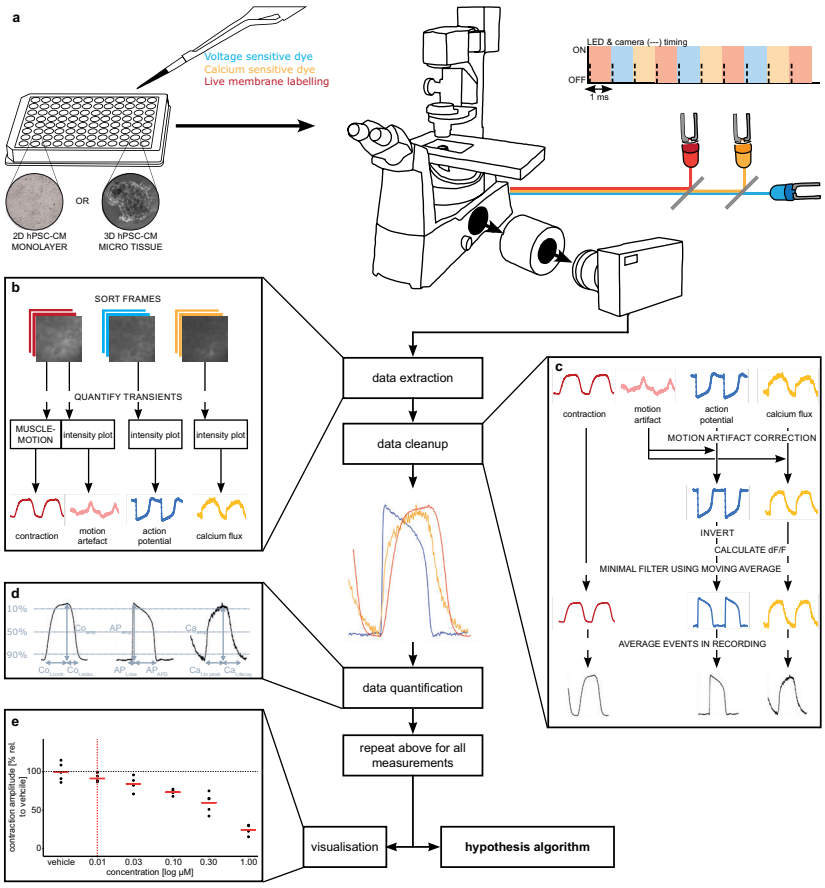

Figure 3: Triple Transient Measurement (TTM) system for determining AP, Ca and Co simultaneously.

a) Hardware setup: the hiPSC-CM model of interest (2D or 3D) is incubated with the voltage sensitive dye (ANNINE-6plus), calcium sensitive dye (Rhod 3) and cell membrane label (CellMask Deep Red) used for measuring contraction. The hiPSC-CMs are excited using three rapidly alternating LEDs which are synchronized with a high-speed camera. The camera receives the emitted signal from the hiPSC-CMs after photon amplification by the image intensifier. The data are then fed into the data processing pipeline. b) The video frames are split into three stacks that contain the information regarding the AP (blue), Ca (yellow) and Co (red). The information of each stack is extracted by either plotting the intensity changes and/or applying MUSCLEMOTION. c) The data are then "cleaned" to remove the motion artefacts, invert the signal when necessary, calculate ΔF/F , apply a minimal filter and/or average the events within one recording. d) The data are quantified by summarizing the kinetic parameters of interest determined in Table 1. e) Finally, the data are plotted and meanwhile fed into the hypothesis algorithm.

the signal intensity of ANNINE-6plus decreases with depolarization), the pseudo ratio

$$\frac{\Delta F}{F_{min}}$$

for AP and Ca calculated, a minimally moving average filter (2 frames) applied and finally five events in the recording averaged[29] after checking whether the interpeak distance corresponded to the pacing frequency (Figure 3c). The data were then summarized by the kinetic parameters described in Table 1 (Figure 3d). After these steps were repeated for all the measurements, concentration-response plots were generated per kinetic parameter for visual interpretation of the results (Figure 3e). Finally, the data were fed into the hypothesis algorithm.

hiPSC-CM drug response

To validate the setup and algorithm, a set of 12 drug responses was selected that comprised at least all MOA identified in Table 1 once. Briefly, commercial hiPSC-CM monolayers were cultured in glass-bottomed 96-well plates. Per drug, five concentrations and a vehicle (DMSO) were tested. These conditions were each tested in five different wells and three individual areas were measured per well (Figure 2a). The area was measured before and after drug- or vehicle incubation (30 min at 37 °C). Representative transients normalized to baseline of vehicle measurements and an illustrative concentration per drug are shown in Figure 4. The vast amount of data (±600 GB per drug) was then automatically evaluated and quantified.

Next, the analysis algorithm was applied to the data. For each drug at and each concentration, the hypothesis table was populated using the calculations of the probability scores and summarized (Supplementary Table 1). As described earlier, the highest summarized value identified the MOA. The resulting assignments per concentration are shown in Supplementary Table 2 (column 'ALL'). The algorithm accurately indicated the correct MOAs for 10 of the 12 drugs when analysing the response of AP, Ca and Co. A comparison with conventional statistical methods per parameter per drug per dose can be found in Supplementary Table 3. It is evident that the algorithm is typically not triggered by small changes that might not be physiologically relevant (e.g. captopril at 1 µM) while it does indicate a relevant change in certain cases although no statistical differences are evident in the individual parameters (e.g. omecamtiv mecarbil at 0.03 and 0.3 µM). In some cases, small 'significant' changes in single parameters might not be physiologically meaningful while a combined system of changes does more robustly indicate a relevant cell response.

Both PDE3-inhibiting drugs levosimendan and pimobendan had no effect assigned by the algorithm, whilst the opposite would be expected based on the literature, where the calcium sensitizing- and PDE3-inhibiting effects of the drugs should cause a positive inotropic effect[30,31]. Reviewing the data manually also did not show any changes compared to vehicle. This lack of effect is most likely due to by hiPSC-CM immaturity[32,33] or incubation time. Furthermore, one unexpected observation was made with atenolol, which binds to the β1-adrenoceptor and competes with endogenous neurostimulators.

Because neurostimulators are not present in serum-free hiPSC-CM cultures, no effect was expected, but a myosin-related increase in Co was seen at 0.3 µM. However, calcium current enhancement and inhibition have been reported previously in agonist-free conditions[34] which might explain the increase in $AP_{t,rise}$ at 0.3 µM. Therefore, while the assignment of a myosin related contractile increase is incorrect, the assignment of 'no effect' is also questionable. Since the dataset generated is too large to include in standard figures, an interactive online tool was developed to give readers access to all data and both qualitative and quantitative insight in the data and analysis. In addition, the tool allows comparison to traditional statistics. Baseline statistics and raw concentration-response curves are also available to demonstrate the high inter-measurement variation and time-dependent effects, respectively, which is the reason for normalization to the vehicle. The tool is available at https://bjvanmeer.shinyapps.io/TTM-algorithm/.

Comparison to AP, Ca or Co only

In addition, the assignments that resulted from only analysing Vo, Ca or Co are listed in Supplementary Table 2 (column 'AP-', 'Ca-' and 'Co only'). As expected, assignments of the individual parameters are not as accurate as analysis of all parameters together and this gives further strength to our combined analysis strategy. The individual parameters are often incorrect in identifying the MOA and more frequently show inconsistent responses throughout the different concentrations. Another issue, which can also be seen in Table 1, is that some parameters are unable to distinguish between certain MOAs (i.e. AP only is unable to distinguish between $Co^{=}$ and Co^{+}_{Myosin}; Co is unable to distinguish between Co^{+}_{Myosin} and Co^{+}_{Ca}).

Other platforms that use multi parameter assessments in hPSC-CMs exist but differ from the TTM system. The system developed by Klimas et al. relies on optogenetics and therefore requires cell lines in which the optogenetic actuators have been transfected or stably inserted, adding significant complexity and decreasing flexibility[35]. Furthermore while the channelrhodopsin2 enables the cells to be paced, it has to be controlled by light pulses which limits the time for fluorescence recording and therefore only allows simultaneous measurements of two parameters (voltage and calcium) rather than all three. While the CellOPTIQ system[36] (Clyde Biosciences) can record all three parameters, this can only be performed sequentially and not simultaneously like the TTM system. Additionally, the CellOPTIQ system has a lower frame rate which might limit the accuracy especially for the action potential. However, the resulting output is similar to that obtained with the TTM system, meaning that similar analysis using the hypothesis-based model for the classification of pharmacological effects might be possible. Similarly, Christoph et al. recently published a more complex method to perform accurate 3D voltage mapping[37]. While only suitable for 3D tissues and more focused on the spatiotemporal patterns during fibrillation, the output data from this system might be suitable for the hypothesis-based algorithm.

Automated evaluation of the output data generated by different systems using the hypothesis-based algorithm would enable comparable interpretation of the results. Since the algorithm is based on the vehicle population of the system it would not be limited by differences between absolute values or percentages of change which often

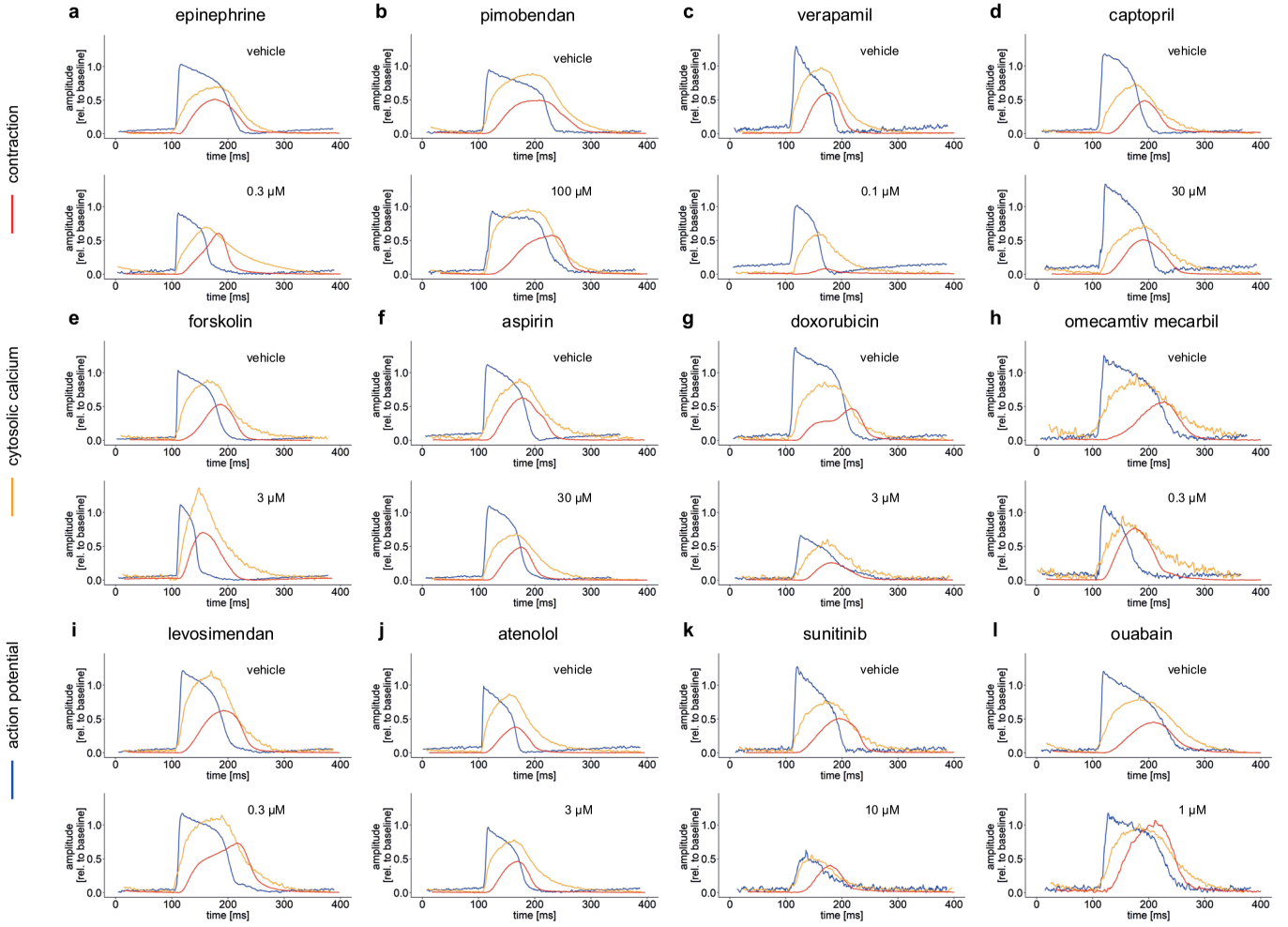
contraction
cytosolic calcium
action potential
a
epinephrine
vehicle
0.3 µM
b
pimobendan
vehicle
100 µM
c
verapamil
vehicle
0.1 µM
d
captopril
vehicle
30 µM
e
forskolin
vehicle
3 µM
f
aspirin
vehicle
30 µM
g
doxorubicin
vehicle
3 µM
h
omecamtiv mecarbil
vehicle
0.3 µM
i
levosimendan
vehicle
0.3 µM
j
atenolol
vehicle
3 µM
k
sunitinib
vehicle
10 µM
l
ouabain
vehicle
1 µM
amplitude [rel. to baseline]
time [ms]

make head to head comparison of different techniques difficult or impossible. More generally, user bias is greatly reduced using automated interpretation. However, currently all systems still rely on non-automated manual response interpretation.

In summary, it is now widely recognized that predicting clinical impact of drugs using *in vitro* and/or *in silico* models and obtaining more insight in the mechanisms underlying individual responses to drugs or disease mutations is crucial for developing new therapeutic compounds, treatments and strategies. The work here contributes to this by combining multiple functional readouts in one system with automatic quantitative assessment not subject to operator bias. We focussed specifically on contractile mechanisms in cardiac models while others have integrated qualification of other drug types such as chemotherapeutics[38]. Combining such scores might ultimately lead to an integrated cardiac safety score. The majority of hiPSC-CMs remain immature in most standard laboratory formats and are therefore associated with a high inter-sample variability. Whilst methods are emerging that can promote maturation[7,8,39,40], advanced multiplexed tools as described here can help identify immature features and suggest possible methods to address this and reduce inter-sample variability. The method was demonstrated here on monolayer cultures of hiPSC-CMs, but is equally applicable to more complex multicellular and 3D formats. Ultimately, multiplexing not only functional readouts but also those from genetics, metabolomics and proteomics could provide truly predictive models for insight into the cellular mechanisms underlying drug response and pathology in the human heart.

Methods

TTM system

An Eclipse Ti microscope (Nikon) was fitted with a 3 high-power LED system (Mightex; 470 nm, 560 nm and 656 nm) including collimators and excitation filters (Semrock; 470 ± 14 nm, 544 ± 12 nm, 650 ± 7.5 nm). The LEDs were controlled using a custom-made current source that was coupled to a 32 channel PCI DAQ Card (National Instruments). Furthermore, an image intensifier (Photonis, the Netherlands) was coupled to a high-speed camera (Optronis GmbH), which was triggered by the DAQ card using a custom Labview (National Instruments) program. The microscope was fitted with a custom-

Figure 4: Averaged representative transients of hiPSC-CMs in response to vehicle (DMSO) and drugs measured with the TTM system and normalized to their individual baseline measurements.

Cells were paced at 1.2 Hz. Simultaneous measurements show action potential (blue), cytosolic calcium (orange) and contraction (red) of Pluricytes under baseline conditions and in response to 0.3 µM epinephrine (a), 100 µM pimobendan (b), 0.1 µM verapamil (c), 30 µM captopril (d), 3 µM forskolin (e), 30 µM aspirin (f), 3 µM doxorubicin (g), 0.3 µM omecamtiv mecarbil (h), 0.3 µM levosimendan (i) and 3 µM atenolol (j), 10 µM sunitinib (k) and 1 µM ouabain (l).

built environmental chamber that allowed measurements to be performed at 37 °C and 5% CO_2. All analyses were performed using ImageJ (NIH) and R (R Foundation for Statistical Computing).

hiPSC-CM cell culture

Black glass-bottom 96-well plates (Greiner) were coated with 1:100 Matrigel (Sigma–Aldrich) in DMEM F12 (Sigma–Aldrich). Per drug, one vial of commercial hiPSC-CMs (Pluricytes; Ncardia, catalogue number PCK-1.5, kindly provided by Ncardia) was thawed according to manufacturer's instructions in Pluricyte medium (PCM; Ncardia, catalogue number PCK-1.5, kindly provided by Ncardia). To allow dye incubation and measurements in parallel, cells were distributed over two plates in 15–20 wells (40k cells per well in 100 µL). RevitaCell (1:100, ThermoFisher Scientific) was added to the culture medium to improve cell recovery. Empty wells around the wells with hiPSC-CMs were filled with 200µL of PBS−/− (Gibco) to minimize evaporation. Cells were refreshed with 200 µL PCM medium at day 1 and day 4 or 5 after plating. All measurements for each drug were always performed either on day 5 and 6 or day 6 and 7 after plating.

Dye and drug incubation

ANNINE 6-plus (Sensitive Farbstoffe GbR), Rhod-3 (Invitrogen) and CellMask Deep Red (Invitrogen) with stock concentrations 0.5 g per L, 10 mM and 5 mg per mL were mixed in 500 µL PCM in ratios of 1:833, 1:833 and 1:100, respectively. 50 µL of the mix was added to each well and incubated for 20 min at 37 °C. Before starting baseline measurements, wells were refreshed with 200 uL per well of PCM and left for 10 min at 37 °C to recover.

After baseline measurements 100 µL medium was removed and 100 µL of drug solution in PCM (200% of the final concentration) was added and the hiPSC-CMs incubated for 30 min at 37 °C. All drugs were reconstituted in DMSO (Sigma–Aldrich) with solutions prepared to ensure a final concentration of 0.1% DMSO in each well. Vehicle incubations were done similarly using PCM plus 0.1% DMSO. All drugs, apart from ouabain (Sigma–Aldrich), were kindly provided by GlaxoSmithKline (United Kingdom).

MEA Recordings of hiPSC-CMs

Extracellular field potentials from hiPSC-CMs plated on MEAs were recorded (recording duration 2 min) using a 96-well Multiwell MEA system (Multichannel Systems GmbH) at 37 °C running the Multiwell-Screen software. Beating monolayers of hiPSC-CMs were incubated with fluorescent reporters following the protocol developed for the TTM System, with DMSO concentrations balanced accordingly. After incubating the hiPSC-CMs with the dyes for 20 min, the beating monolayers were washed with warm BPEL and the electrophysiological properties of the monolayers assessed at two different time points after the washout (2–4 min and 13–15 min). Data were exported with Multiwell-Analyzer and visualised through a custom-made R script. The interpretation of QT and RR intervals was done using Clampfit (analysis module from Axon™ pCLAMP™ 11)[41].

Reporting summary

Further information on research design is available in the Nature Research Reporting Summary linked to this article.

Data availability

We have developed an interactive webtool to access the vast amount of data more easily and intuitively. The tool is available at https://bjvanmeer.shinyapps.io/TTM-algorithm/. The source data underlying Supplementary Table 2, Supplementary Table 3 and Supplementary Figure 2 are provided as a Source Data file. In addition, the source data of all measurements is provided as Source Data file. In addition, the data can be found at the Dryad Digital Repository under the following https://doi.org/10.5061/dryad.67c92vm.

Code availability

Source codes for the software are available on https://gitlab.com/bjvanmeer/ttm-algorithm/.

Acknowledgements

This work was supported by the National Centre for the Replacement, Refinement and Reduction of Animals in Research [grant number NC/K000225/1] through the NC3Rs CRACK-IT (full proposal code 35911–259146). We gratefully acknowledge support and input from all consortium members: G. Smith, F. Burton, K. McGlynn (Clyde Bioscience & University of Glasgow, United Kingdom); A. Hansen, I. Mannhardt, U. Saleem (EHT Technologies & University Medical Center Hamburg Eppendorf, Germany); R. Passier, M. Ribeiro (Twente University, the Netherlands); P. Katili, N. Mohd Yusof (University of Nottingham); S. Braam, T. de Korte (Ncardia, the Netherlands); A. Bahinsky, P. Clements, S. Turner (GlaxoSmithKline, United Kingdom); C. Vickers, S. Jackson (NC3Rs, United Kingdom). We are particularly grateful to GSK for contributing to defining and providing the test set of compounds used, and to Ncardia for providing hPSC-CMs and medium. We thank Sander van Berloo, Huybert van de Stadt and Bram de Visser for their indispensable craftsmanship and support in developing the TTM system. Finally, we would like to thank Mervyn Mol, Giulia Campostrini and Elisa Giacomelli for critical reviewing of the manuscript and providing hiPSC-CMs for preliminary testing with the TTM system. C.D. was supported by the British Heart Foundation [grant numbers SP/15/9/31605, RG/15/6/31436, PG/14/59/31000, RG/14/1/30588, P47352/Centre for Regenerative Medicine]; BIRAX [grant number 04BX14CDLG]; the Medical Research Council [grant number MR/M017354/1, G0801098]; and the Heart Research UK [grant number TRP01/12]. R.P.D. was supported by a H2020 European Research Council (ERC) Starting Grant (STEMCARDIORISK; grant agreement #638030), and a VIDI fellowship from the Netherlands Organisation for Scientific Research (Nederlandse Organisatie voor Wetenschappelijk Onderzoek; ILLUMINATE; #91715303). C.L.M. and B.J.M. were supported by the Netherlands Science Foundation (NWO) under the Gravitation Grant 'NOCI' (#024.003.001).

References

1. Braam, S. R. *et al.* Prediction of drug-induced cardiotoxicity using human embryonic stem cell-derived cardiomyocytes. *Stem Cell Res.* **4,** 107–16 (2010).

2. Blinova, K. *et al.* Comprehensive Translational Assessment of Human Induced Pluripotent Stem Cell Derived Cardiomyocytes for Evaluating Drug-Induced Arrhythmias. *Toxicol. Sci.* **155,** (2016).

3. Colatsky, T. *et al.* The Comprehensive *in Vitro* Proarrhythmia Assay (CiPA) initiative — Update on progress. *J. Pharmacol. Toxicol. Methods* **81,** 15–20 (2016).

4. Redfern, W. S. *et al.* Relationships between preclinical cardiac electrophysiology, clinical QT interval prolongation and torsade de pointes for a broad range of drugs: Evidence for a provisional safety margin in drug development. *Cardiovasc. Res.* **58,** 32–45 (2003).

5. Pointon, A. *et al.* Assessment of Cardiomyocyte Contraction in Human-Induced Pluripotent Stem Cell-Derived Cardiomyocytes. *Toxicol. Sci.* **144,** 227–237 (2014).

6. Bers, D. M. Cardiac excitation-contraction coupling. *Nature* **415,** 198–205 (2002).

7. Birket, M. J. *et al.* Contractile Defect Caused by Mutation in MYBPC3 Revealed under Conditions Optimized for Human PSC-Cardiomyocyte Function. *Cell Rep.* **13,** 733–745 (2015).

8. Giacomelli, E. *et al.* Three-dimensional cardiac microtissues composed of cardiomyocytes and endothelial cells co-differentiated from human pluripotent stem cells. *Development* **144,** 1008–1017 (2017).

9. Pointon, A. *et al.* High-Throughput Imaging of Cardiac Microtissues for the Assessment of Cardiac Contraction during Drug Discovery. *Toxicol. Sci.* (2016).

10. Mannhardt, I. *et al.* Human Engineered Heart Tissue: Analysis of Contractile Force. *Stem Cell Reports* **7,** 29–42 (2016).

11. van Meer, B. J., Tertoolen, L. G. J. & Mummery, C. L. Concise Review: Measuring Physiological Responses of Human Pluripotent Stem Cell Derived Cardiomyocytes to Drugs and Disease. *Stem Cells* **34,** 2008–2015 (2016).

12. Sala, L. *et al.* MUSCLEMOTION: A Versatile Open Software Tool to Quantify Cardiomyocyte and Cardiac Muscle Contraction *In Vitro* and *In Vivo*. *Circ. Res.* **122,** e5–e16 (2018).

13. Ravens, U., Wettwer, E., Pfeifer, T., Himmel, H. & Armah, B. Characterization of the effects of the new inotropic agent BDF 9148 in isolated papillary muscles and myocytes of the guinea-pig heart. *Br. J. Pharmacol.* **104,** 1019–1023 (1991).

14. Thomas, G., Chung, M. & Cohen, C. J. A dihydropyridine (Bay k 8644) that enhances calcium currents in guinea pig and calf myocardial cells. A new type of positive inotropic agent. *Circ. Res.* **56,** 87–96 (1985).

15. Fuerstenwerth, H. On the differences between ouabain and digitalis glycosides. *Am. J. Ther.* **21,** 35–42 (2014).

16. Cui, X.-L., Zhao, L.-Y. & Wu, B.-W. E-4031 enhanced Ca2+ transient and ventricular myocytes contraction via reverse mode Na+/Ca2+ exchange in normal and hypertrophic rats. *Acta Pharmacol. Sin.* **23,** 797–802 (2002).

17. Planelles-Herrero, V. J., Hartman, J. J., Robert-Paganin, J., Malik, F. I. & Houdusse, A. Mechanistic and structural basis for activation of cardiac myosin force production by omecamtiv mecarbil. *Nat. Commun.* **8,** 190 (2017).

18. Lohse, M. J., Engelhardt, S. & Eschenhagen, T. What is the role of beta-adrenergic signaling in heart failure? *Circ. Res.* **93,** 896–906 (2003).

19. Knight, W. & Yan, C. Therapeutic potential of PDE modulation in treating heart disease. *Future Med. Chem.* **5,** 1607–1620 (2013).

20. Itzhaki, I. *et al.* Calcium Handling in Human Induced Pluripotent Stem Cell Derived Cardiomyocytes. *PLoS One* **6,** e18037 (2011).

21. Zhao, L. & Zhang, B. Doxorubicin induces cardiotoxicity through upregulation of death receptors mediated apoptosis in cardiomyocytes. *Sci. Rep.* **7,** 1–11 (2017).

22. Brack, K. E., Narang, R., Winter, J. & Andr, G. The mechanical uncoupler blebbistatin is associated with significant electrophysiological effects in the isolated rabbit heart. **5,** 1009–1027 (2013).

23. Guo, L. *et al.* The Electrophysiological Effects of Cardiac Glycosides in Cardiomyocytes and in Guinea Pig Isolated Hearts. *Cell. Physiol. Biochem.* **27,** 453–462 (2011).

24. Abrahamsson, C., Duker, G., Lundberg, C. & Carlsson, L. Electrophysiological and inotropic effects of H 234/09 (almokalant) *in vitro*: a comparison with two other novel IK blocking drugs, UK-68,798 (dofetilide) and E-4031. *Cardiovasc. Res.* **27,** 861–7 (1993).

25. Cherry, E. M. & Fenton, F. H. Suppression of alternans and conduction blocks despite steep APD restitution: electrotonic, memory, and conduction velocity restitution effects. *Am. J. Physiol. Circ. Physiol.* **286,** H2332–H2341 (2004).

26. Zhang, M. *et al.* Recessive cardiac phenotypes in induced pluripotent stem cell models of Jervell and Lange-Nielsen syndrome: Disease mechanisms and pharmacological rescue. *Proc. Natl. Acad. Sci.* **111,** E5383–E5392 (2014).

27. Sala, L. *et al.* A new hERG allosteric modulator rescues genetic and drug-induced long-QT syndrome phenotypes in cardiomyocytes from isogenic pairs of patient induced pluripotent stem cells. *EMBO Mol. Med.* **8,** 1065–1081 (2016).

28. Knisley, S. B., Justice, R. K., Kong, W. & Johnson, P. L. Ratiometry of transmembrane voltage-sensitive fluorescent dye emission in hearts. *Am. J. Physiol. Circ. Physiol.* **279,** H1421–H1433 (2000).

29. Uzelac, I. & Fenton, F. H. Robust framework for quantitative analysis of optical mapping signals without filtering. in *2015 Computing in Cardiology Conference (CinC)* 461–464 (IEEE, 2015).

30. Bohm, M. *et al.* Contribution of cAMP-phosphodiesterase inhibition and sensitization of the contractile proteins for calcium to the inotropic effect of pimobendan in the failing human myocardium. *Circ. Res.* **68,** 689–701 (1991).

31. Abi-Gerges, N. *et al.* Preservation of cardiomyocytes from the adult heart. *J. Mol. Cell. Cardiol.* **64,** 108–119 (2013).

32. Watanabe, H., Honda, Y., Deguchi, J., Yamada, T. & Bando, K. Usefulness of cardiotoxicity assessment using calcium transient in human induced pluripotent stem cell-derived cardiomyocytes. *J.*

Toxicol. Sci. **42,** 519–527 (2017).

33. Mannhardt, I. *et al.* Blinded contractility analysis in hipsc-cardiomyocytes in engineered heart tissue format: Comparison with human atrial trabeculae. *Toxicol. Sci.* **158,** 164–175 (2017).

34. Mewes, T., Dutz, S., Ravens, U. & Jakobs, K. H. Activation of calcium currents in cardiac myocytes by empty β- adrenoceptors. *Circulation* **88,** 2916–2922 (1993).

35. Klimas, A. *et al.* Multimodal on-axis platform for all-optical electrophysiology with near-infrared probes in human stem-cell-derived cardiomyocytes. *bioRxiv* **10776,** 10767–10776 (2018).

36. Hortigon-Vinagre, M. P. *et al.* The Use of Ratiometric Fluorescence Measurements of the Voltage Sensitive Dye Di-4-ANEPPS to Examine Action Potential Characteristics and Drug Effects on Human Induced Pluripotent Stem Cell-Derived Cardiomyocytes. *Toxicol. Sci.* **154,** 320–331 (2016).

37. Christoph, J. *et al.* Electromechanical vortex filaments during cardiac fibrillation. *Nature* **555,** 667–672 (2018).

38. Sharma, A. *et al.* High-throughput screening of tyrosine kinase inhibitor cardiotoxicity with human induced pluripotent stem cells. *Sci. Transl. Med.* **9,** eaaf2584 (2017).

39. Ruan, J.-L. *et al.* Mechanical Stress Promotes Maturation of Human Myocardium From Pluripotent Stem Cell-Derived Progenitors. *Stem Cells* **33,** 2148–2157 (2015).

40. Lemoine, M. D. *et al.* Human iPSC-derived cardiomyocytes cultured in 3D engineered heart tissue show physiological upstroke velocity and sodium current density. *Sci. Rep.* **7,** 5464 (2017).

41. Sala, L., Ward-van Oostwaard, D., Tertoolen, L. G. J., Mummery, C. L. & Bellin, M. Electrophysiological Analysis of human Pluripotent Stem Cell-derived Cardiomyocytes (hPSC-CMs) Using Multi-electrode Arrays (MEAs). *J. Vis. Exp.* e55587 (2017).

42. Guo, L. *et al.* Estimating the Risk of Drug-Induced Proarrhythmia Using Human Induced Pluripotent Stem Cell–Derived Cardiomyocytes. *Toxicol. Sci.* **123,** 281–289 (2011).

43. Clements, M., Millar, V., Williams, A. S. & Kalinka, S. Bridging functional and structural cardiotoxicity assays using human embryonic stem cell-derived cardiomyocytes for a more comprehensive risk assessment. *Toxicol. Sci.* **148,** 241–260 (2015).

44. Maddah, M. *et al.* A non-invasive platform for functional characterization of stem-cell-derived cardiomyocytes with applications in cardiotoxicity testing. *Stem Cell Reports* **4,** 621–631 (2015).

45. Fürstenwerth, H. Ouabain - the insulin of the heart. *Int. J. Clin. Pract.* **64,** 1591–1594 (2010).

46. Shimoni, Y., Gotsman, M., Deutsch, J., Kachalsky, S. & Lichtstein, D. Endogenous ouabain-like compound increases heart muscle contractility. *Nature* **307,** 369–71 (1984).

47. Cleland, J. G. F. *et al.* The effects of the cardiac myosin activator, omecamtiv mecarbil, on cardiac function in systolic heart failure: A double-blind, placebo-controlled, crossover, dose-ranging phase 2 trial. *Lancet* **378,** 676–683 (2011).

48. Horváth, B. *et al.* Frequency-dependent effects of omecamtiv mecarbil on cell shortening of isolated canine

ventricular cardiomyocytes. *Naunyn. Schmiedebergs. Arch. Pharmacol.* **390,** 1239–1246 (2017).

49. Reyes, G., Schwartz, P. H., Newth, C. J. & Eldadah, M. K. The pharmacokinetics of isoproterenol in critically ill pediatric patients. *J. Clin. Pharmacol.* **33,** 29–34 (1993).

50. Molenaar, P. *et al.* (-)-Adrenaline elicits positive inotropic, lusitropic, and biochemical effects through β2-adrenoceptors in human atrial myocardium from nonfailing and failing hearts, consistent with Gs coupling but not with Gi coupling. *Naunyn. Schmiedebergs. Arch. Pharmacol.* **375,** 11–28 (2007).

51. Singh, B. N., Ellrodt, G. & Peter, C. T. Verapamil: A Review of its Pharmacological Properties and Therapeutic Use. *Drugs* **15,** 169–197 (1978).

52. Angus, J. A., Sarsero, D., Fujiwara, T., Molenaar, P. & Xi, Q. Quantitative analysis of vascular to cardiac selectivity of L- and T-type voltage-operated calcium channel antagonists in human tissues. *Clin. Exp. Pharmacol. Physiol.* **27,** 1019–21 (2000).

53. Giacomini, K. M., Massoud, N., Wong, F. M. & Giacomini, J. C. Decreased binding of verapamil to plasma proteins in patients with liver disease. *J. Cardiovasc. Pharmacol.* **6,** 924–8 (1984).

54. Hanna, A. D., Lam, A., Tham, S., Dulhunty, A. F. & Beard, N. A. Adverse Effects of Doxorubicin and Its Metabolic Product on Cardiac RyR2 and SERCA2A. *Mol. Pharmacol.* **86,** 438–449 (2014).

55. Temma, K. *et al.* Comparison of cardiac actions of doxorubicin, pirarubicin and aclarubicin in isolated guinea-pig heart. *Eur. J. Pharmacol.* **234,** 173–181 (1993).

Supplementary information

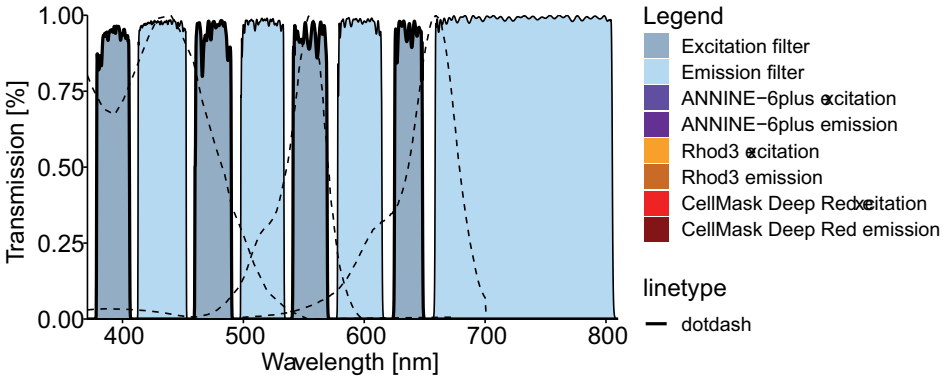

Supplementary Figure 1: Spectral overview of TTM system and dyes used.

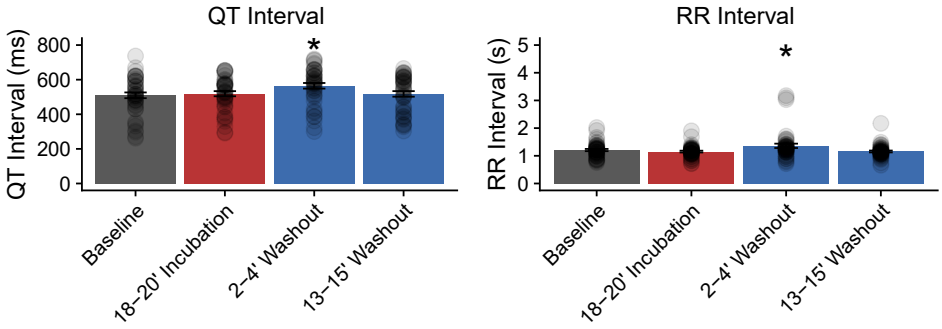

Supplementary Figure 2: Effect on the electrophysiological properties of hiPSC-CMs by combined loading of ANNINE-6plus, Rhod-3 and CellMask Deep Red.

QT and RR-interval are shown before addition (grey), after 18-20 minutes incubation (red) and 2-4 and 13-15 minutes after washout (blue). N=46 measurements. One-way ANOVA was used to test for differences in means between conditions but all p-values were larger than 0.05. The bars in the bar graph indicate the mean and the error bars indicate SEM.

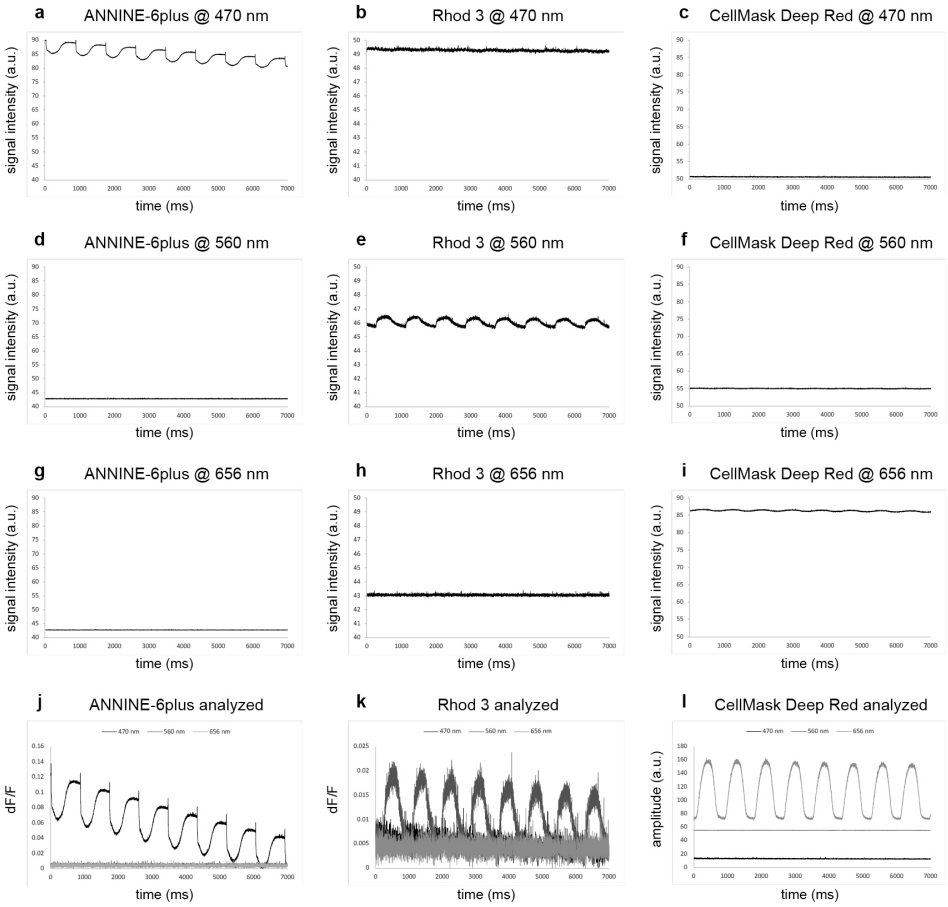

Supplementary Figure 3: Absence of crosstalk between the different channels.

Different wells of hiPSC-CMs were loaded with either ANNINE-6plus, Rhod 3 or CellMask Deep Red. These wells were then exposed to the three different LEDs of the system individually (470 nm, 560 nm and 656 nm) to investigate whether a measurable signal occurred in the different channels. Measurable signals where exclusively detected at 470 nm, 560 nm and 656 nm for ANNINE-6plus (a), Rhod 3 (e) and CellMask Deep Red (i), respectively. To confirm whether the raw signals were not contributing to the analysis of the transients we have performed the first steps of analysis for the dyes: dF/F calculation (ANNINE-6plus and Rhod 3) and MUSCLEMOTION analysis (CellMask Deep Red). Again, the only relevant contribution to the signal was originating from the 470 nm, 560 nm and 656 nm wavelength for ANNINE-6plus (j), Rhod 3 (k) and CellMask Deep Red (l), respectively.

Supplementary Table 1: Overview of all probability scores in the hypothesis table per drug per concentration.

	Concentration (µM)	Contractility+ (cAMP)	Contractility+ (calcium)	Contractility+ (myosin)	Contractility- (calcium)	Contractility- (toxicity)	No change
levosimendan	Vehicle	2.38	3.13	4.64	2.19	3.01	**5.85**
	0.01	1.86	3.31	3.73	1.9	3.18	**4.51**
	0.03	1.94	3.31	4.79	1.8	3.34	**5.47**
	0.1	2.82	3.59	4.53	2.12	2.85	5.21
	0.3	2.28	2.73	4	2.82	3.34	**4.9**
	1	1.97	3.29	3.48	2.44	3.38	**4.95**
omecamtiv mecarbil	Vehicle	2.88	3.04	3.9	2.52	2.64	**4.78**
	0.01	2.1	2.6	3.94	2.24	3.24	**4.4**
	0.03	2.4	2.76	**3.73**	2.18	2.49	3.68
	0.1	2.48	2.71	3.1	2.14	2.22	**3.4**
	0.3	4.12	3.46	**4.54**	3.27	2.63	4.18
	1	2.84	3.18	**4.25**	2.01	2.19	3.32
doxorubicin	Vehicle	2.54	3.15	4.29	2.48	3.12	**5.69**
	1	4.07	3.34	4.37	3.47	3.17	5.38
	3	3.42	3.37	3.9	2.3	2.52	**4.74**
	10	3.06	2.34	3.66	3.35	3.59	**4.94**
	30	2.09	2.17	2.31	3.62	**4.47**	3.76
	100	0.22	0.18	0.17	0.58	**0.87**	0.19

	Concentration (μM)	Contractility+ (cAMP)	Contractility+ (calcium)	Contractility+ (myosin)	Contractility- (calcium)	Contractility- (toxicity)	No change
verapamil	Vehicle	2.74	3.45	4.55	2.46	3.17	5.69
	0.01	3.06	2.99	4.16	4.09	4.01	**4.83**
	0.03	3.87	2.27	3.18	**5.66**	4.33	3.27
	0.1	3.63	1.77	2.41	**5.8**	3.7	1.82
	0.3	2.84	1.75	1.52	**4.56**	2.8	1.22
	1	1.42	1.07	0.67	**2.23**	1.17	0.67
aspirin	Vehicle	2.16	2.98	4.25	1.99	2.8	**5.67**
	10	2.09	3.17	4.78	2.35	3.3	**5.5**
	30	2.61	2.76	4.81	2.66	2.86	**5.3**
	100	2.57	3.03	4.95	2.09	2.62	**5.53**
	300	2.22	2.65	4.22	2.79	3.13	5.07
	1000	2.95	3.08	4.64	3.1	3.08	**5.27**
captopril	Vehicle	2.62	3.35	3.79	2.66	3.41	**4.86**
	1	2.1	3.26	3.44	1.57	2.82	**4.73**
	3	2.28	3.71	4.85	1.25	2.82	**5.84**
	10	2.3	3.25	3.55	1.83	3.11	4.81
	30	2.83	3.61	4	2.22	3.41	**4.77**
	100	2.29	3.31	4.48	1.67	2.93	**5.55**

sunitinib	Vehicle	2.56	3.15	4.18	2.3	3.03	**5.67**
	0.1	1.06	2.72	4.45	1.95	3.3	**4.72**
	0.3	1.15	2.49	3.81	1.87	3.01	4.13
	1	1.69	2.28	3.04	2.45	**3.74**	3.65
	3	1.88	1.99	2.62	3.17	**4.38**	3.29
	10	2.69	1.46	2.16	5.02	**5.43**	2.35
atenolol	Vehicle	3	3.45	4.66	2.64	3.1	**5.39**
	0.1	2.98	3.05	**5.12**	2.42	2.84	5.03
	0.3	2.86	2.77	3.97	2.99	3.5	**4.13**
	1	3.03	3.24	4.84	2.89	3.69	**5.06**
	3	3.61	3.31	3.84	3.07	3.31	**4.24**
	10	3.46	3.53	4.96	2.71	3.23	**5.07**
pimobendan	Vehicle	1.94	2.96	4.95	1.83	2.97	7.01
	1	2.16	2.89	4.2	1.45	2.68	**5.57**
	3	2.34	3.24	4.52	1.92	2.54	**6.35**
	10	1.95	3.1	4.31	1.48	2.54	**6.06**
	30	2.14	2.91	4.54	1.85	2.36	**4.7**
	100	1.92	2.98	3.29	1.26	1.96	**5.05**

	Concentration (μM)	Contractility+ (cAMP)	Contractility+ (calcium)	Contractility+ (myosin)	Contractility- (calcium)	Contractility- (toxicity)	No change
forskolin	Vehicle	2.22	2.89	4.39	2.33	3.08	**5.74**
	0.1	**5.04**	3.74	4.3	3.43	2.77	4.79
	0.3	6.05	3.95	3.11	4.33	2.69	3.15
	1	**6.61**	3.87	2.13	5.28	2.86	2.06
	3	**6.63**	3.77	2.45	4.8	2.89	2.51
	10	**6.61**	3.97	2.35	4.45	2.43	1.98
epinephrine	Vehicle	2.11	3.23	5.04	1.88	2.95	**6.7**
	0.01	3.45	3.51	3.3	2.85	3.29	**4.4**
	0.03	4.48	3.84	4.88	3.16	2.66	**5.12**
	0.1	**5.36**	4.17	3.99	4.2	2.74	4.42
	0.3	**4.56**	3.13	2.83	3.42	2.11	3
	1	**5.7**	3.98	3.85	4.48	2.86	4.21
ouabain	Vehicle	2.46	3.05	4.08	2.32	2.98	**5.19**
	0.03	2.66	3.34	4.3	3	2.81	**4.53**
	0.1	2.89	3.65	3.9	2.08	2.43	4.65
	0.3	2.45	3.13	4.01	2.34	3.25	**4.88**
	1	2.48	**3.07**	2.33	1.87	2.58	2.56
	3	1.63	**1.7**	0.88	1.4	1.47	0.83

Supplementary Table 2: Effects assigned by the hypothesis based model.

Drug	Epinephrine		MOA:	Co^{+}_{cAMP}
	ALL	AP only	Ca only	Co only
Vehicle	$Co^{=}$	$Co^{=}$ / Co^{+}_{Myosin}	$Co^{=}$	$Co^{=}$
0.01 µM	$Co^{=}$	Co^{+}_{cAMP}	$Co^{=}$	$Co^{=}$
0.03 µM	$Co^{=}$	$Co^{=}$ / Co^{+}_{Myosin}	$Co^{=}$	$Co^{=}$
0.1 µM	Co^{+}_{cAMP}	Co^{+}_{cAMP}	Co^{+}_{Myosin}	$Co^{=}$
0.3 µM	Co^{+}_{cAMP}	Co^{+}_{cAMP}	Co^{+}_{cAMP}	$Co^{=}$
1 µM	Co^{+}_{cAMP}	Co^{+}_{cAMP}	Co^{+}_{cAMP}	$Co^{=}$

Drug	Forskolin		MOA:	Co^{+}_{cAMP}
	ALL	AP only	Ca only	Co only
Vehicle	$Co^{=}$	$Co^{=}$ / Co^{+}_{Myosin}	$Co^{=}$	$Co^{=}$
0.1 µM	$Co^{=}$	$Co^{=}$ / Co^{+}_{Myosin}	$Co^{=}$	Co^{+}_{cAMP}
0.3 µM	Co^{+}_{cAMP}	Co^{+}_{cAMP}	Co^{+}_{cAMP}	Co^{+}_{cAMP}
1 µM	Co^{+}_{cAMP}	Co^{+}_{cAMP}	Co^{+}_{cAMP}	Co^{+}_{cAMP}
3 µM	Co^{+}_{cAMP}	Co^{+}_{cAMP}	Co^{+}_{cAMP}	Co^{+}_{cAMP}
10 µM	Co^{+}_{cAMP}	Co^{+}_{cAMP}	Co^{+}_{cAMP}	Co^{+}_{cAMP}

Drug	Pimobendan		MOA:	Co^{+}_{cAMP}
	ALL	AP only	Ca only	Co only
Vehicle	$Co^{=}$	$Co^{=}$ / Co^{+}_{Myosin}	$Co^{=}$	$Co^{=}$
1 µM	$Co^{=}$	$Co^{=}$ / Co^{+}_{Myosin}	$Co^{=}$	$Co^{=}$
3 µM	$Co^{=}$	$Co^{=}$ / Co^{+}_{Myosin}	$Co^{=}$	$Co^{=}$
10 µM	$Co^{=}$	$Co^{=}$ / Co^{+}_{Myosin}	$Co^{=}$	$Co^{=}$
30 µM	$Co^{=}$	$Co^{=}$ / Co^{+}_{Myosin}	$Co^{=}$	Co^{+}_{Myosin} / Co^{+}_{Ca}
100 µM	$Co^{=}$	$Co^{=}$ / Co^{+}_{Myosin}	$Co^{=}$	$Co^{=}$

Drug	Aspirin	MOA:	MOA:	$Co^{=}$
	ALL	AP only	Ca only	Co only
Vehicle	$Co^{=}$	$Co^{=}$ / Co^{+}_{Myosin}	$Co^{=}$	$Co^{=}$
10 µM	$Co^{=}$	$Co^{=}$ / Co^{+}_{Myosin}	$Co^{=}$	$Co^{=}$
30 µM	$Co^{=}$	$Co^{=}$ / Co^{+}_{Myosin}	$Co^{=}$	$Co^{=}$
100 µM	$Co^{=}$	$Co^{=}$ / Co^{+}_{Myosin}	$Co^{=}$	$Co^{=}$
300 µM	$Co^{=}$	$Co^{=}$ / Co^{+}_{Myosin}	Co^{-}_{Ca}	$Co^{=}$
1000 µM	$Co^{=}$	$Co^{=}$ / Co^{+}_{Myosin}	Co^{+}_{Myosin}	$Co^{=}$

Drug	Levosimendan		MOA:	Co^{+}_{cAMP}
	ALL	AP only	Ca only	Co only
Vehicle	$Co^{=}$	$Co^{=}$ / Co^{+}_{Myosin}	$Co^{=}$	$Co^{=}$
0.01 µM	$Co^{=}$	$Co^{=}$ / Co^{+}_{Myosin}	Co^{+}_{Ca}	$Co^{=}$
0.03 µM	$Co^{=}$	$Co^{=}$ / Co^{+}_{Myosin}	$Co^{=}$	$Co^{=}$
0.1 µM	$Co^{=}$	$Co^{=}$ / Co^{+}_{Myosin}	$Co^{=}$	$Co^{=}$
0.3 µM	$Co^{=}$	Co^{-}_{Tox}	$Co^{=}$	$Co^{=}$
1 µM	$Co^{=}$	$Co^{=}$ / Co^{+}_{Myosin}	$Co^{=}$	$Co^{=}$

Drug	Verapamil		MOA:	Co^{-}_{Ca}
	ALL	AP only	Ca only	Co only
Vehicle	$Co^{=}$	$Co^{=}$ / Co^{+}_{Myosin}	$Co^{=}$	$Co^{=}$
0.01 µM	$Co^{=}$	$Co^{=}$ / Co^{+}_{Myosin}	Co^{-}_{Ca}	Co^{-}_{Tox}
0.03 µM	Co^{-}_{Ca}	Co^{-}_{Ca}	Co^{-}_{Ca}	Co^{-}_{Ca}
0.1 µM	Co^{-}_{Ca}	Co^{-}_{Ca}	Co^{-}_{Ca}	Co^{-}_{Ca}
0.3 µM	Co^{-}_{Ca}	Co^{-}_{Ca}	Co^{-}_{Ca}	-
1 µM	Co^{-}_{Ca}	Co^{-}_{Ca}	Co^{-}_{Ca}	-

Drug	Atenolol		MOA:	$Co^{=}$
	ALL	AP only	Ca only	Co only
Vehicle	$Co^{=}$	$Co^{=}$ / Co^{+}_{Myosin}	$Co^{=}$	$Co^{=}$
0.1 µM	$Co^{=}$	$Co^{=}$ / Co^{+}_{Myosin}	$Co^{=}$	Co^{+}_{Myosin} / Co^{+}_{Ca}
0.3 µM	Co^{+}_{Myosin}	$Co^{=}$ / Co^{+}_{Myosin}	$Co^{=}$	Co^{+}_{Myosin} / Co^{+}_{Ca}
1 µM	$Co^{=}$	$Co^{=}$ / Co^{+}_{Myosin}	$Co^{=}$	Co^{+}_{Myosin} / Co^{+}_{Ca}
3 µM	$Co^{=}$	$Co^{=}$ / Co^{+}_{Myosin}	Co^{+}_{cAMP}	Co^{+}_{cAMP}
10 µM	$Co^{=}$	$Co^{=}$ / Co^{+}_{Myosin}	$Co^{=}$	$Co^{=}$

Drug	Captopril		MOA:	$Co^{=}$
	ALL	AP only	Ca only	Co only
Vehicle	$Co^{=}$	$Co^{=}$ / Co^{+}_{Myosin}	$Co^{=}$	$Co^{=}$
1 µM	$Co^{=}$	$Co^{=}$ / Co^{+}_{Myosin}	$Co^{=}$	$Co^{=}$
3 µM	$Co^{=}$	$Co^{=}$ / Co^{+}_{Myosin}	$Co^{=}$	$Co^{=}$
10 µM	$Co^{=}$	$Co^{=}$ / Co^{+}_{Myosin}	$Co^{=}$	$Co^{=}$
30 µM	$Co^{=}$	$Co^{=}$ / Co^{+}_{Myosin}	$Co^{=}$	$Co^{=}$
100 µM	$Co^{=}$	$Co^{=}$ / Co^{+}_{Myosin}	$Co^{=}$	$Co^{=}$

Drug	Doxorubicin		MOA:	Co^{-}_{Tox}
	ALL	AP only	Ca only	Co only
Vehicle	$Co^{=}$	$Co^{=}$ / Co^{+}_{Myosin}	$Co^{=}$	$Co^{=}$
1 µM	$Co^{=}$	$Co^{=}$ / Co^{+}_{Myosin}	Co^{+}_{Myosin}	$Co^{=}$
3 µM	$Co^{=}$	Co^{+}_{cAMP}	$Co^{=}$	$Co^{=}$
10 µM	$Co^{=}$	Co^{-}_{Ca}	Co^{+}_{Myosin}	$Co^{=}$
30 µM	Co^{-}_{Tox}	Co^{-}_{Tox}	Co^{-}_{Tox}	$Co^{=}$
100 µM	Co^{-}_{Tox}	Co^{-}_{Tox}	-	Co^{-}_{Ca}

Drug	Omecamtiv Mecarbil		MOA:	Co^{+}_{Myosin}
	ALL	AP only	Ca only	Co only
Vehicle	$Co^{=}$	$Co^{=}$ / Co^{+}_{Myosin}	$Co^{=}$	$Co^{=}$
0.01 µM	$Co^{=}$	$Co^{=}$ / Co^{+}_{Myosin}	$Co^{=}$	$Co^{=}$
0.03 µM	Co^{+}_{Myosin}	$Co^{=}$ / Co^{+}_{Myosin}	Co^{+}_{Myosin}	Co^{+}_{Myosin} / Co^{+}_{Ca}
0.1 µM	$Co^{=}$	$Co^{=}$ / Co^{+}_{Myosin}	Co^{+}_{Myosin}	$Co^{=}$
0.3 µM	Co^{+}_{Myosin}	Co^{+}_{cAMP}	Co^{+}_{Myosin}	Co^{+}_{Myosin} / Co^{+}_{Ca}
1 µM	Co^{+}_{Myosin}	$Co^{=}$ / Co^{+}_{Myosin}	Co^{+}_{Myosin}	Co^{+}_{Myosin} / Co^{+}_{Ca}

Drug	Sunitinib		MOA:	Co^{-}_{Tox}
	ALL	AP only	Ca only	Co only
Vehicle	$Co^{=}$	$Co^{=}$ / Co^{+}_{Myosin}	$Co^{=}$	$Co^{=}$
0.1 µM	$Co^{=}$	Co^{-}_{Tox}	$Co^{=}$	Co^{+}_{Myosin} / Co^{+}_{Ca}
0.3 µM	$Co^{=}$	Co^{-}_{Tox}	$Co^{=}$	Co^{+}_{Myosin} / Co^{+}_{Ca}
1 µM	$Co^{=}$	Co^{-}_{Tox}	$Co^{=}$	$Co^{=}$
3 µM	Co^{-}_{Tox}	Co^{-}_{Tox}	$Co^{=}$	Co^{-}_{Ca}
10 µM	Co^{-}_{Tox}	Co^{-}_{Tox}	Co^{-}_{Ca}	Co^{-}_{Ca}

Drug	Ouabain		MOA:	Co^{+}_{Ca}
	ALL	AP only	Ca only	Co only
Vehicle	$Co^{=}$	$Co^{=}$ / Co^{+}_{Myosin}	$Co^{=}$	$Co^{=}$
0.03 µM	$Co^{=}$	$Co^{=}$ / Co^{+}_{Myosin}	$Co^{=}$	$Co^{=}$
0.1 µM	$Co^{=}$	$Co^{=}$ / Co^{+}_{Myosin}	$Co^{=}$	$Co^{=}$
0.3 µM	$Co^{=}$	Co^{-}_{Tox}	$Co^{=}$	$Co^{=}$
1 µM	Co^{+}_{Ca}	Co^{+}_{Ca}	Co^{+}_{Ca}	$Co^{=}$
3 µM	Co^{+}_{Ca}	Co^{+}_{Ca}	Co^{-}_{Tox}	Co^{+}_{Ca}

Supplementary Table 3: A comparison of the outcome of the hypothesis-based algorithm and traditional statistics.

P-values were calculated using a Dunnett's test after one-way ANOVA.

	Concentration (μM)	Algorithm output	Contract. amplitude	Calcium amplitude	Contract. time	Relax. time	Calcium time to peak	Calcium decay time	APD90	Action potenial amplitude	Triangu-lation	AP[Trise]
levosimendan	Vehicle	No change	--	--	--	--	--	--	--	--	--	--
	0.01	No change	p<0.05									
	0.03	No change										
	0.1	No change	p<0.01									
	0.3	No change										
	1	No change										
omecamtiv mecarbil	Vehicle	No change	--	--	--	--	--	--	--	--	--	--
	0.01	No change										p<0.01
	0.03	Contractility+ (myosin)										
	0.1	No change										
	0.3	Contractility+ (myosin)										
	1	Contractility+ (myosin)	p<0.01		p<0.01							
doxorubicin	Vehicle	No change	--	--	--	--	--	--	--	--	--	--
	1	No change					p<0.05					
	3	No change					p<0.05					
	10	No change							p<0.001			
	30	Contractility- (toxicity)				p<0.01			p<0.0001	p<0.001		
	100	Contractility- (toxicity)				NA	NA	NA	p<0.0001	p<0.0001		

verapamil	Vehicle	No change	--	--	--	--	--	--	--	--	--	--
	0.01	No change	p<0.05								p<0.05	
	0.03	Contractility-(calcium)	p<0.01			p<0.0001			p<0.05	p<0.01	p<0.0001	
	0.1	Contractility-(calcium)	p<0.01		p<0.01	p<0.0001		p<0.0001	p<0.0001	p<0.0001	p<0.0001	
	0.3	Contractility-(calcium)	NA	NA	NA	p<0.0001		p<0.0001	p<0.0001	p<0.0001	p<0.0001	
	1	Contractility-(calcium)	NA	NA	NA	p<0.0001		p<0.001	p<0.0001	p<0.0001	p<0.0001	
aspirin	Vehicle	No change	--	--	--	--	--	--	--	--	--	--
	10	No change										
	30	No change										
	100	No change										
	300	No change										
	1000	No change										
captopril	Vehicle	No change	--	--	--	--	--	--	--	--	--	--
	1	No change	p<0.05			p<0.01			p<0.05			
	3	No change										
	10	No change										
	30	No change										
	100	No change										

	Concentration (μM)	Algorithm output	Contract. amplitude	Calcium amplitude	Contract. time	Relax. time	Calcium time to peak	Calcium decay time	APD90	Action potenial amplitude	Triangu-lation	AP[Trise]
sunitinib	Vehicle	No change	--	--	--	--	--	--	--	--	--	--
	0.1	No change										
	0.3	No change										
	1	Contractility-(toxicity)								p<0.01	p<0.05	
	3	Contractility-(toxicity)				p<0.01				p<0.0001	p<0.05	
	10	Contractility-(toxicity)				p<0.0001		p<0.0001	p<0.0001	p<0.01		
atenolol	Vehicle	No change	--	--	--	--	--	--	--	--	--	--
	0.1	Contractility+(myosin)									p<0.05	
	0.3	No change									p<0.05	p<0.01
	1	No change	p<0.01									p<0.05
	3	No change										
	10	No change										
pimobendan	Vehicle	No change	--	--	--	--	--	--	--	--	--	--
	1	No change										
	3	No change										
	10	No change										
	30	No change										
	100	No change										

forskolin	Vehicle	No change	--	--	--	--	--	--	--	--	--	--
	0.1	Contractility+ (cAMP)			p<0.01			p<0.01			p<0.01	
	0.3	Contractility+ (cAMP)			p<0.05	p<0.05		p<0.001			p<0.0001	p<0.01
	1	Contractility+ (cAMP)			p<0.001			p<0.0001		p<0.001	p<0.0001	p<0.001
	3	Contractility+ (cAMP)			p<0.0001			p<0.0001			p<0.0001	p<0.001
	10	Contractility+ (cAMP)	p<0.05		p<0.001	p<0.05	p<0.05	p<0.0001		p<0.01	p<0.0001	p<0.0001
epinephrine	Vehicle	No change	--	--	--	--	--	--	--	--	--	--
	0.01	No change										
	0.03	No change									p<0.05	
	0.1	Contractility+ (cAMP)			p<0.05			p<0.01		p<0.05	p<0.0001	
	0.3	Contractility+ (cAMP)			p<0.01			p<0.01			p<0.0001	
	1	Contractility+ (cAMP)			p<0.001			p<0.0001			p<0.0001	
ouabain	Vehicle	No change	--	--	--	--	--	--	--	--	--	--
	0.03	No change										
	0.1	No change										
	0.3	No change		p<0.05					p<0.05			
	1	Contractility+ (calcium)								p<0.05		p<0.01
	3	Contractility+ (calcium)		p<0.0001						p<0.001		p<0.01

Abstract

Animal models are 78% accurate in determining whether drugs will alter contractility of the human heart. To evaluate the suitability of human-induced pluripotent stem cell-derived cardiomyocytes (hiPSC-CMs) for predictive safety pharmacology, we quantified changes in contractility, voltage, and/or Ca^{2+} handling in 2D monolayers or 3D engineered heart tissues (EHTs). Protocols were unified via a drug training set, allowing subsequent blinded multicenter evaluation of drugs with known positive, negative, or neutral inotropic effects. Accuracy ranged from 44% to 85% across the platform-cell configurations, indicating the need to refine test conditions. This was achieved by adopting approaches to reduce signal-to-noise ratio, reduce spontaneous beat rate to ≤ 1 Hz or enable chronic testing, improving accuracy to 85% for monolayers and 93% for EHTs. Contraction amplitude was a good predictor of negative inotropes across all the platform-cell configurations and of positive inotropes in the 3D EHTs. Although contraction- and relaxation-time provided confirmatory readouts forpositive inotropes in 3D EHTs, these parameters typically served as the primary source of predictivity in 2D. The reliance of these "secondary" parameters to inotropy in the 2D systems was not automatically intuitive and may be a quirk of hiPSC-CMs, hence require adaptations in interpreting the data from this model system. Of the platform-cell configurations, responses in EHTs aligned most closely to the free therapeutic plasma concentration. This study adds to the notion that hiPSC-CMs could add value to drug safety evaluation.

Chapter 6

Blinded, multi-centre evaluation of drug-induced changes in contractility using human induced pluripotent stem cell-derived cardiomyocytes

Modified after Toxicological Sciences 176, 103-123 (2020)

Berend van Meer#, Umber Saleem#, Puspita Katili, Nurul Mohd Yusof, Ingra Mannhardt, Ana Krotenberg, Leon Tertoolen, Tessa de Korte, Maria Vlaming, Karen McGlynn, Jessica Nebel, Anthony Bahinski, Kate Harris, Eric Rossman, Xiaoping Xu, Francis Burton, Godfrey Smith, Peter Clements, Christine Mummery, Thomas Eschenhagen, Arne Hansen, Chris Denning

# these authors contributed equally to this work

Introduction

On average, 37 new drugs are launched to market each year but cost of development has increased from approximately $14M per drug in the 1960s to approximately $1.5Bn now, inflation adjusted[1,2]. Attrition rates remain high, with only approximately 2% of the drugs entering phase 1 clinical trials actually progressing to use in patients. A key concern is cardiovascular toxicity, where acute, chronic, and comorbidity effects account for 17% of the 462 drugs withdrawn from market[3] and for 41% of the top 200 prescribed drugs being labeled with adverse drug reaction or black box warnings[4].

Altered cardiac electrophysiology was implicated in the withdrawal of 13 drugs from market between 1990 and 2006[5]. Such events led to International Conference on Harmonization (ICH) S7B guidelines for proarrhythmic risk detection using simplified *in vitro* assays to measure blockade of the rapid repolarization IKr current, commonly known as hERG[6]. Combined with ICH E14[7]guidelines on electrocardiogram monitoring, drug withdrawal due to electrical dysfunction has reduced, with no reported incidences since 2007. These approaches have improved safety, but the relatively poor specificity for predicting human outcomes and overconservativism of the assays has raised concern that promising drug candidates may be abandoned too early due to false positives[8].

Greater predictivity during the early stages of the drug development pipeline will require certain attributes from the chosen assays. These include being of human origin, suitable longevity for acute and chronic studies, compatible with medium-throughput analysis, reflective of working cardiomyocyte physiology and function, and compliant with 3Rs polices. This reduces the attractiveness or relevance of many existing systems, such as those involving animal models. This is also true for human- and animal-derived primary cardiomyocytes, which rapidly dedifferentiate in culture, lose viability, or become overrun with fibroblasts.

Alternative technologies are now showing potential in cardiovascular safety evaluation, with human-induced pluripotent stem cell-derived cardiomyocytes (hiPSC-CMs) as a key modality[9]. This is evidenced by their use in disease modeling, drug discovery and cardiac safety studies, which culminated in the Comprehensive *in vitro* Proarrhythmia Assay (CiPA) and Japanese iPS cardiac safety assessment initiatives[10-12]. Using CiPA as an example, the approach proposed was to identify proarrhythmic risk based on several key modalities including: (1) assessment of several major ion channels in transfected cell lines; (2) *in silico* modeling of the ion channel effects; (3) proarrhythmic assessment in hiPSC-CMs; and (4) clinical assessment of electrocardiograms from phase I human studies. Data that emerged from CiPA show that optical- and multielectrode array-based platforms using commercially sourced hiPSC-CMs enable an 87% accuracy in predicting proarrhythmic liability across geographically diverse testing laboratories[13], with similar studies being reported by others[14].

In contrast, there have been relatively few studies that have used hiPSC-CM contractility in predictive safety assessment[15]. This is surprising because cardiovascular liability of drugs occurs commonly via altered function of the contractile myocardium. Also, monitoring contractility in hiPSC-CMs is currently being done at low throughput or by

using surrogate markers (eg, impedance) and, so far, there has been no detailed cross-site validation study to accurately assess the impact of drugs on hiPSC-CM contractility.

Within this context, a public-private partnership "InPulse CRACK-IT Challenge" was established between the pharmaceutical company, GlaxoSmithKline (GSK), and a U.K. funding agency, the National Centre for the Replacement, Refinement & Reduction of Animals in Research (NC3Rs). The aim was to develop medium-throughput technology platform that could measure contractility in hiPSC-CMs as a physiologically relevant functional output for use in preclinical drug safety evaluation. Parallel or simultaneous measures for Ca2+ handling and/or voltage, potentially with physiological loading, were requested as part of the challenge as optional parameters to multiplex mechanistically relevant endpoints and thereby inform integrated decision making.

To this end, we established a multinational consortium, comprising 4 academic teams in Germany, Holland, and the United Kingdom, along with 2 biotech companies (Clyde Biosciences; Ncardia), GSK and NC3Rs. We describe the process by which 36 drugs were selected, distributed, and formulated, allowing a training set of 8 drugs to be used to unify standard operating procedures (SOPs). This enabled a multicenter study to be undertaken for blinded evaluation of up to 28 drugs with known positive, negative, or neutral inotropic effects, and led to the creation of an interactive web tool to access datasets for contractility, voltage, and/or Ca2+ handling (https://bjvanmeer.shinyapps.io/crackit/). Overall, the different platform-cell combinations had an accuracy of 44%–85% in correctly predicting inotropy. With simple refinement of the test conditions, namely by adopting approaches to reduce signal-to-noise ratio, data variability, reduce spontaneous beat rate to ≤ 1 Hz, and/or enable chronic testing, accuracy could be increased to 85%–93%, comparing favorably with that currently possible with *in vivo* animal models.

Materials and methods

CellOPTIQ: adult rabbit ventricular cardiomyocytes

Rabbit hearts were excised via a thoracotomy and submerged in a modified Krebs-Henseleit (KH) solution of the following composition (mmol/L): NaCl (130), KCl (4.5), HEPES (5), NaH_2PO_4 (0.4), $MgCl_2$ (3.5), and Glucose (10), pH 7.25 at 37°C with NaOH. Hearts were removed and perfused retrogradely at 25 mL/min (37°C) with a modified KH solution containing 0.75 mmol/L [Ca^{2+}] for 5 min, followed by a nominally Ca^{2+}-free KH solution with 0.1 mmol/L EGTA for 5 min. Hearts were then perfused with KH solution containing 0.24 mmol/L [Ca^{2+}], 1 mg/mL collagenase (type I), and 0.06 mg/mL protease (type XIV). After approximately 4–5 min, enzyme was removed and the left ventricular free wall was then cut into strips in the recirculated enzyme solution containing 1% bovine serum albumin before being mixed to yield a single cell suspension. Cells were maintained in either Ca^{2+}-free KH solution or 1 mmol/L Ca^{2+} (via stepwise increments) until use. Intact cardiomyocytes in 1.8 mmol/L modified Ca^{2+} KH solution were loaded with FluoVolt (Thermo Fisher Scientific) at 1:3000 dilution for 10 min. The incubation medium was removed and the cells resuspended in a modified KH solution.

Cardiomyocytes were allowed to settle on a coverslip in a bath (35 mm petri-dish) at

37°C. Cells were field stimulated at a frequency of 2 Hz with 2 ms duration voltage pulses delivered to parallel graphite electrodes (stimulation voltage set to 1.5 times the threshold) for 2 min before sampling FluoVolt and cell video for 10 s. After repeating this for 10–12 cells/dish the drug was added to quiescent cells and left for 30 min before returning to the same myocytes and repeating the stimulus and data capture protocol. A parallel set of vehicle (DMSO) time control experiments were also performed FluoVolt fluorescence (490 nm excitation) was measured at a sampling rate of 10 KHz, whereas the image was recorded on a CCD camera at 100 Hz frame rate using > 700 nm light. Sarcomere length and fractional shortening of sarcomere length was subsequently extracted from the image using a FFT-based algorithm.

TTM system

The TTM system was developed and used as described previously[16]. Briefly, the all-optical fluorescent system consists of a microscope capable of recording sequential frames while switching exposure wavelengths within 1 ms. Using 3 LEDs at 470, 560, and 656 nm this results in an effective recording speed of 333 Hz per parameter. Baselines measurements (7- s recordings) were made by choosing 3 areas per well and saving the positions to measure the same areas after drug incubation. Data were analyzed with custom software offline and automatically to reduce used bias.

Black glass-bottom 96-well plates (Grenier) were coated with 1:100 Matrigel (Sigma-Aldrich) in DMEM F12 (Sigma-Aldrich). Pluricyte hiPSC-CMs were thawed and plated (40 000/well in 100 µL) according to manufacturer's instructions in Pluricyte Cardiomyocyte Medium. To help the recovery of the cells 1:100 RevitaCell (Sigma-Aldrich) was added to each well. Empty wells around the plated CM were filled with 200 µL of PBS to minimize evaporation. Cells were refreshed with 200 µL Pluricyte medium (PCM) at day 1 and day 4 or 5 after plating. All measurements for 1 drug were always performed on days 5 and 6 or days 6 and 7 after plating.

hiPSC-CMs were labeled with ANNINE 6-plus (Sensitive Farbstoffe GbR, Germany; stock concentration: 0.7 mM, dilution 1:833), Rhod 3 (Invitrogen; stock concentration 10 mM, dilution 1:833), and CellMask Deep Red (Thermo Fisher Scientific; stock concentration 5 mg/mL, dilution 1:1000) in 50 mL PCM for 20 min at 37°C, refreshed (200 mL PCM), and given 10 min to recover at 37°C before recording baseline measurements. Drug incubation took place just after baseline measurements by removing 100 µL medium and adding 100 µL drug solution (30 min at 37°C) prepared according to formulation instructions supplied by GSK.

CellOPTIQ: hiPSC-CMs

The hiPSC-CMs used were R-PAT (derived and differentiated in house as described previously)[17,18], and iCell2 and Pluricyte (purchased from Cellular Dynamics International and Ncardia). Manufacturer instructions were followed for the commercial hiPSC lines. For iCell2, seeding was at 25 000 cells into each well of 96-well plates (Nunclon Delta Surface; Thermo, 167008) and then maintained for 10 days before use in drug evaluation studies. The same plates were used for R-PAT hiPSC-CMs, which were seeded at 40 000 cells/well and maintained until days 20 and 21 of differentiation before use. For Pluricyte hiPSC-CMs, seeding was at 35 000 cells into each well of 96-well plates (Greiner Bio-

One; 655087) and then maintained for 8 days before use. Confluent monolayers of R-PAT and iCell2 hiPSC-CMs were changed into serum-free medium (SFM) (Dulbecco's Modified Eagle Medium [Gibco, 21969035] + 10 mM galactose [Sigma-Aldrich, G0750] and 1 mM sodium pyruvate [Sigma-Aldrich, P2256] 24 h before testing). Pluricyte hiPSC-CMs were changed into 50% SFM and 50% PCM (serum-free) 24 h before day of testing, and on the day of testing were changed into SFM. For the refined conditions described for R-PAT hiPSC-CMs, plating and maintenance were as before but cells were received fresh RPMI-B27 medium 24 h before testing instead of SFM.

hiPSC-CMs in 96-well plate were transiently loaded in 50 µL/well of SFM containing FluoVolt (1:200 part B, 1:2000 part A; Life Tech, F10488) for 20 min at 37°C and 5% CO_2. After incubation, the medium was replaced with 200 µL/well of SFM. Plates were then incubated at 37 °C and 5% CO_2 for 15 min before recording, which were made using a ×40 (NAO.6) objective at 10 kHz. To apply electric field stimulation, a custom-made 8 channel electrode StimStrip (Clyde Biosciences Ltd) was placed in a row of a 96-well plate and connected externally to a box (DC power supply; Lavota). hiPSC-CMs were paced at a frequency of 1.2–1.7 Hz (or 0.7–1 Hz in the refined conditions) with an amplitude of 8 V and a pulse width of 20 ms. Recordings of 10 s were made for each well (contractility was 100 frames/s, hence 1000 frames). Baselines and drug addition were as described for the TTM system. Electrophysiology data were analyzed using CellOPTIQ proprietary software of Clyde Biosciences and were normalized to a maximum amplitude of 1 and minimum of 0 to standardize height for comparison of traces created in OriginPro (OriginLab version 7.5). Contractility data were analyzed based on pixel displacement using an ImageJ plug-in. This plug-in uses a sum of absolute differences algorithm.

Engineered heart tissues

To generate EHTs, in-house hiPSC lines, R-PAT, and ERC18, were differentiated using 2D-monolayer- (R-PAT) or 3D-embryoid body- (ERC18) protocol and fabricated as recently described[19,17]. In brief, casting molds were generated in 24-well plates with 2% agarose (Invitrogen, 15510-019) and Polytetrafluorethylene (PTFE) spacers (EHT Technologies, C0002). PDMS racks (EHT Technologies, C0001) were placed in the 24-well plates so that pairs of PDMS posts reached into each agarose casting mold. A reconstitution mix was prepared consisting of: 1 × 106 hiPSC-CM; 81.9 µL cardiomyocyte medium; 10 µL Matrigel basement membrane matrix (BD 354234); 5.5 µL 2 × DMEM; 0.1 µL Y-27632 (10 mM; Biorbyt orb60104); 2.5 µL bovine fibrinogen (5 mg/mL; Sigma F4753). Reconstitution mix (97 µL) was mixed with prealiquoted 3 µL thrombin (100 U/mL; Biopur BP11-10-1104) and pipetted into the agarose casting mold. GCAMP6f-lentiviral particles (multiplicity of infection: 0.3, functional titer) were included in the EHT reconstitution mix for Ca^{2+} transient analysis. EHTs started to beat coherently after 10–14 days and were analyzed for contraction and Ca^{2+} transient at ≥ 20 days.

EHTs were transferred from culture medium into preequilibrated (37 °C, 40% O_2, 7% CO_2), modified Tyrode's solution (in mM, 120 NaCl; 22.6 $NaHCO_3$; 5.4 KCl; 5 glucose; 1 $MgCl_2$; 0.4 NaH_2PO_4; 0.6–1 $CaCl_2$; 0.05 Na_2EDTA; 25 HEPES) for R-PAT and into DMEM (Gibco 21068028; in mM, 110 NaCl; 44 $NaHCO_3$; 5 KCl; 25 glucose; 0.8 $MgSO_4$; 0.9 NaH_2PO_4, 0.6–1 $CaCl_2$; 25 HEPES, and vitamins and amino acids) for ERC18 EHTs 40 min before analysis to equilibrate to the testing medium. After equilibration, the cumulative

concentration response curve was started with baseline recording in preequilibrated medium with Ca^{2+} concentration of 0.6–1 mM.

For long-term contractility analysis of sunitinib, hiPSC-CM EHTs were equilibrated to regular cell culture medium without serum (DMEM, Biochrom F0415; penicillin/streptomycin 1% [volume/volume], Gibco 15140; aprotinin 5 µM, Sigma-Aldrich A1153; insulin 1.7 µM, Sigma-Aldrich I9278; glutamine 2000 µM, Gibco 25030-081; triiodothyronine 0.77 nM, European Commission-Joint Research Center IRMM-469; hydrocortisone 137 µM: Sigma-Aldrich H0888). Medium change, drug addition and video-optical contractility analysis was performed daily and contraction data was normalized to time control.

Contractility analysis was via automated video-optical contractility analysis was performed in 24-well cell culture plates (Nunc, 122475)[19]. Video files of EHT contractions were analyzed by automated EHT figure recognition software (EHT Technologies, A0001). Top and bottom ends of EHT contour were identified and followed during the course of recording. Force was calculated based on shortening during contraction, elastic propensity, and geometry of PDMS posts.

Ca^{2+} transient analysis was combined with contraction in 24-well cell imaging plates (Eppendorf, 030741005). Briefly, set up consisted of an inverted fluorescence microscope (Zeiss) with a custom-made, automated, light tight, CO_2- and temperature-controlled XY-stage with 24-well plate holder. A camera attached to front port of the microscope was used for contraction analysis (×1.25 objective) and a camera attached to side port of the microscope was used to adjust position of the tissue for fluorescence/Ca^{2+} transient measurement (×10 objective). A small predefined area (0.1 × 0.4 mm) in the center of EHT was used to record Ca^{2+} transients. Mercury lamp, GFP filter set, and photomultiplier tube were used to record change in fluorescence in EHTs expressing GCaMP6f (increase fluorescence during contraction phase). Predefined XYZ coordinates for contraction and Ca^{2+} transient were defined and saved in a bespoke software which controlled microscope settings, XYZ coordinates, and recorded automated-, sequential-contraction and Ca^{2+} transients. Cumulative concentration response curves were performed, similar to contractility analysis, for selective concentrations based on results of contractility analysis.

Data were normalized to a pool of time-matched controls (contractility analysis, ERC18: n = 22 EHTs/7.0 experiments; R-PAT: 16 EHTs/5.0 experiments; combined contractility- and Ca^{2+} transient-analysis: 21 EHTs/8.0 experiments) used for all contractility/combined contractility- and Ca^{2+} transient-measurements. Data are plotted as relative change to the mean baseline, normalized to pool time control. Statistical significance was evaluated by GraphPad Software, 1-way ANOVA with Dunnett's multiple comparisons test versus baseline.

Web tool

The web tool was build using the "Shiny" package in R Language and Environment for Statistical Computing. Data were analyzed and visualized using the packages "ggplot2," "reshape," "Rfast," "ggpubr," "RColorBrewer," "multcomp," and "tidyverse."

Results

Rationale for selection, handling, and distribution of training and blinded drug sets
Driven by the interests of the pharmaceutical industry, and specifically GSK, the 36 drugs in this study (Supplementary Table 1) were selected on basis of: (1) commercial availability; (2) approximate balance in numbers between positive inotropes (PIs), negative inotropes (NIs), and no effect drugs (NE), with respect to contractility; (3) inclusion of false positives or negatives; (4) availability of functional data on inotropic effect on cardiomyocyte and/or heart function from 1 or more species, including human, spanning use *in vitro*, *ex vivo*, preclinically, and clinically; (5) data on free therapeutic plasma concentrations (FTPCs); (6) solubility in DMSO to allow unified testing at a maximum concentration of 0.1% v/v, which does not cause toxicity in hiPSC-CMs; and (7) broad range of modes of action relevant to contractility and toxicity, including modulation of ion channels and pumps in the cell membrane (INaV1.5, IKr, IKATP, ICaL, If, NCX, Na^+/K^+-ATPase) or sarcoplasmic reticulum (SR) (RYR, SERCA), β1- and β2-adrenoceptors, Ca^{2+} sensitivity, signaling cascades (phosphodiesterase [PDE], adenylyl cyclase, cyclic AMP), energy production (ATP, mitochondrial stress), myofilament response, and myofilaments as well as less well-known mechanisms (eg, inhibition of tyrosine kinases).

All drugs were purchased, formulated and distributed under contractual material transfer agreement by GSK to ensure that the same lot numbers were used by the testing laboratories. Eight drugs were not blinded and used as a "training set" to establish the working parameters and protocols for the technology platforms (isoprenaline, nifedipine, digoxin, Bay K 8644, EMD-57033, ryanodine, thapsigargin, caffeine). The remaining 28 "test set" drugs were encoded and blinded by GSK's Sample Management Technology department, which dealt with handling and distribution as preweighed lots in coded brown glass vials. Samples were formulated according to prescribed, blinded instructions, and using single-shot vials of DMSO where possible to minimize absorption of water from the atmosphere, hence avoid inadvertent drug dilution. Powders and formulated drugs were stored at −80°C, with the solutions undergoing no more than 2 rounds of freeze-thaw and use within 2 weeks.

Refining and establishing working parameters with the drug "Training Set"
The training set of 8 drugs was used to unify the methods for testing, analysis, and presentation (Supplementary Figures 1–3). This helped to establish SOPs (Supplementary Table 2), which were used for subsequent blinded evaluation of the "test set" drugs. Three technology platforms were used, differing in configuration, format of wells, and approach to calculate contractility. These were the Triple Transient Measurement (TTM), CellOPTIQ (CO), and engineered heart tissue (EHT) platforms.

The TTM platform is bespoke and was the only system in this study that could simultaneously measure contractility, electrophysiology, and Ca^{2+} handling. Interlaced 1000 frame/s movies (i.e. sequential 1 ms/channel) were recorded from hiPSC-CMs cultured in 2D monolayers in 96-well plates loaded with appropriate dye[20,16]. The CO is a proprietary system that was used to measure contractility, via bright field images, and electrophysiology, via voltage-sensitive dyes[21]. Here, it was used on hiPSC-CMs

cultured in 2D monolayers in 96-well plates and isolated adult rabbit cardiomyocytes. Finally, the EHT system is commercially available, using 3D constructs fabricated from hiPSC-CMs using a fibrin hydrogel between 2 polydimethylsiloxane (PDMS) posts and multiplexed in 24-well plates[22]. Determining Ca^{2+} handling required viral transgenesis of a genetically encoded calcium indicator (GCAMP6f) during EHT fabrication. Whereas pixel displacement was used as a surrogate of contractility in the 2D systems (TTM and CO), 3D EHTs enable force of contraction to be calculated from the extent of deflection of PDMS posts upon each beat.

Action potential duration (APD30, APD90) and triangulation (APD90–APD30) were calculated from voltage waveforms to determine whether electrophysiology was altered, including the appearance of arrhythmias. For Ca2+ handling, amplitude, time to peak, and decay time were assessed, whereas similar parameters (contraction amplitude [CA], contraction time [CT], and relaxation time [RT]) were derived for contraction (Supplementary Figure 2). Contractility responses were further subdivided (Supplementary Figure 2), such that positive inotropy reflected an increase in CA, positive clinotropy a decrease in CT and positive lusitropy a decrease in RT. The opposite is true for negative responses.

The training set of 8 drugs was used to test and refine protocols. Representative data are shown for the PIs, digoxin/isoprenaline, and the NI, nifedipine (Supplementary Figure 3). For each parameter, the percentage change in drug-treated samples relative to their respective vehicle control was calculated using the formula ([drug/drug baseline]/[vehicle/vehicle baseline])*100–100. Consistent with the mode of action of these drugs, in all cases there was a trend or significant response for positive inotropy (increased CA) in hiPSC-CMs treated with digoxin/isoprenaline but negative inotropy (decreased CA) for those treated with nifedipine (Supplementary Figure 3). Digoxin tended to increase RT in 2D configuration, whereas isoprenaline decreased of both CT and RT in 3D EHTs (Supplementary Figure 3). These studies allowed unification of SOPs, although physical and technical constraints between the platforms meant that some unavoidable differences remained (Supplementary Table 2).

Blinded evaluation and assignment of drug "Test Set"

Using the SOPs established above, up to 28 blinded drugs were tested in a rank order that was predefined by GSK (Table 1). Contraction was the parameter common to all platforms because the primary aim of the study was to predict whether drugs were positive, negative, or neutral inotropes. Differentiation of the in-house hiPSC lines, R-PAT, and ERC18, provided sufficient hiPSC-CMs to test all available drugs on the CO and/or EHT platforms. Testing was restricted to 10 drugs in rabbit CMs (as a comparator) and in commercial hiPSC-CMs (Pluricyte and iCell2) due to cost, availability and timelines, whereas throughput was a limitation of the TTM system. Overall, 9 drugs were tested in common across all platform-cell combinations, which were later unblinded and identified as: PIs, epinephrine, forskolin, levosimendan, pimobendan; NIs, verapamil, sunitinib; NE, acetylsalicylic acid, atenolol, captopril.

All data for contraction, voltage, and Ca^{2+} handling across the various platform-cell combinations are accessible via an interactive web tool via https://bjvanmeer.shinyapps.

io/crackit/. Representative data for contractility illustrates the output format for 6 drugs where the response was generally predicted correctly or incorrectly, respectively. Thus, data are shown for the PIs, epinephrine, and levosimendan (Figure 1A), NIs, verapamil, and sunitinib (Figure 1B), and NE drugs, acetylsalicylic acid, and captopril (Figure 1C). In some instances, data from Ca^{2+} and, to a lesser extent, voltage analyses were used to assist in prediction of inotropic response, as was the case for the PI, epinephrine, and the NI, verapamil (Supplementary Figures 4A and 4B).

Prediction of inotropy involved a 2-day face-to-face meeting between all investigators, with colleagues from GSK overseeing the process as observers rather than contributors. Each platform-cell-drug combination was evaluated individually and a consensus between the research team on the outcome was established using the terminology defined in Supplementary Figure 2 (i.e. positive or negative inotropy [CA], clinotropy [CT], and lusitropy [RT]; altered electrophysiology ± arrhythmias [AE ± *]; altered Ca^{2+}). In some cases, decisions were based on trends rather than statistical significance. For example, this was true for TTM: Pluricyte evaluation of epinephrine (Figure 1A, see CA and CT). Once predictions were finalized, the document was "locked" and drugs were unblinded by GSK to allow comparison with their known effects (Tables 1 and 2).

Across the 9 drugs evaluated in common, all platforms mainly predicted NE drugs and NIs (Table 2). One exception was sunitinib, which was poorly detected by the EHT platform. This may be due to slower penetration, lower sensitivity, and greater cell community effect of 3D tissues protecting against short-term (30 min) exposure to this chronic toxicant. Poorest predictivity was for PIs, which ranged from 0% to 50% accuracy. Overall predictivity for the 9 drugs ranged from 44% to 78%. This range was similar across all drugs tested (50%–85%), with NE and NI being predicted most accurately (up to 100%; Table 2). The trend was for the EHT:hiPSC-CM combination to be more predictive of PIs (75%) than CO: hiPSC-CM (0%–25%). Together, these data implied that continuous measurements from 3D preparations of hiPSC-CMs yielded more predictive contractility data than cell motion sampled from a 2D culture.

We looked for trends in the data that might point toward ways to improve the process of predicting response. The drug concentration at which the maximum responses were recorded were broadly similar across the TTM, CO, and EHT platforms, irrespective of whether prediction was correct (Table 1). However, we noted that the response range was wider in 2D relative to 3D platforms. Whereas mean maximum measurable percentage changes in CA for the TTM and CO platforms ranged from –100% to +196%, it was –100 to +53% for the EHT platform (Table 1). Where there was an increase in CA, the standard deviation of these mean values was 41.5 versus 12.1 for the 2D versus 3D platforms. A similar pattern was observed for NIs, and for changes in CT and RT. This was corroborated by the wider distribution of data points in the 2D platforms relative to the 3D platform (Figures 1A-C, Supplementary Figures 4A and 4B, web tool). This likely relates in part to the cumulative concentration response protocol used for EHTs (Supplementary Table 2).

These observations prompted us to examine sensitivity of the different platforms. Where platform-cell combinations correctly predicted inotropy, data were converted

A

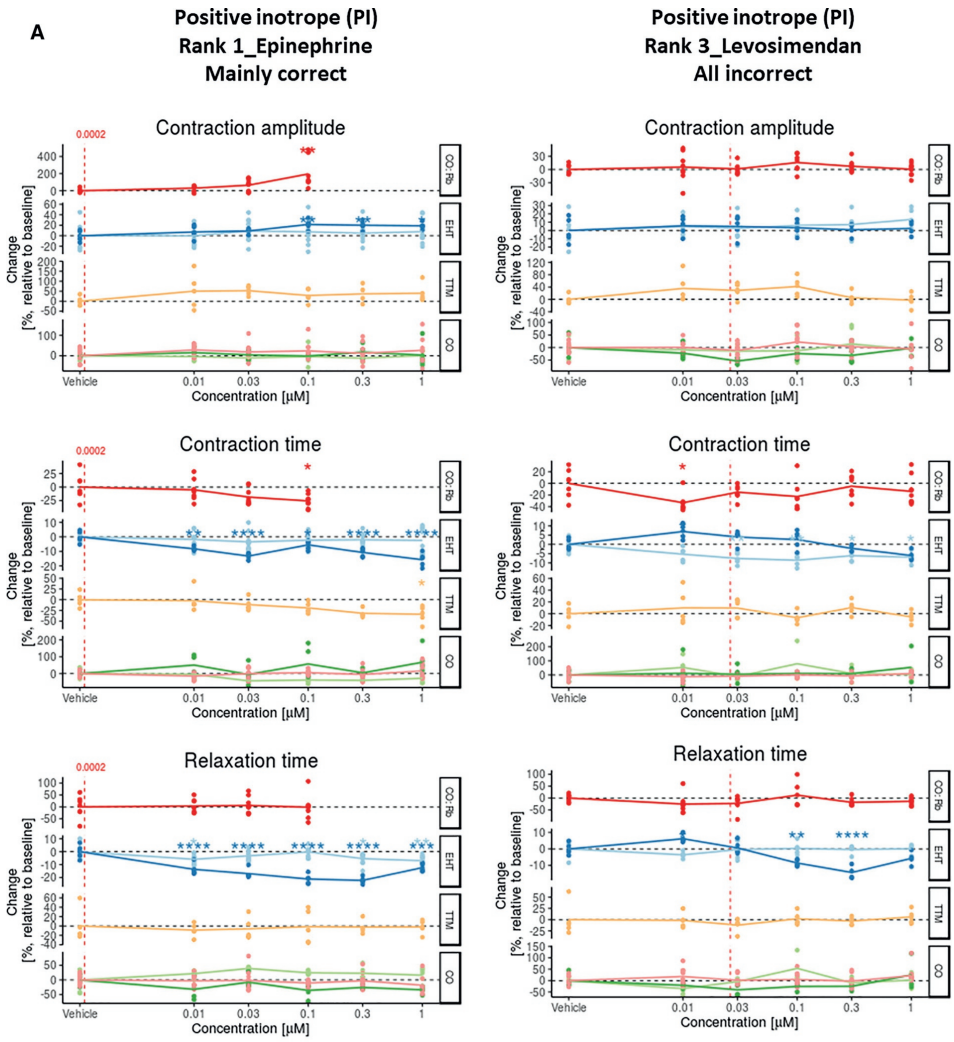

	Predicted correctly? Epinephrine	Predicted correctly? Levosimendan
CO: Rb: Rabbit CMs	Yes	No
EHT: R-PAT	Yes	No
EHT: ERC	No	No
TTM: Pluricyte	Yes (with Ca^{2+})	No
CO: R-PAT	No	No
CO: iCell2	Yes	No
CO: Pluricyte	No	No

into a heat map to reflect the percentage change for NIs (Figure 2A) and PIs (Figure 2B). In 6/7 correctly predicted cardio-active PIs, 1 or more contractile parameters (CA, CT, and/or RT) recorded from EHTs reached statistical significance at concentrations within, or close to, the FTPC range, whereas 2D platforms appeared to be less sensitive (Figure 2B). This is illustrated by epinephrine, where significant changes (p of ≤ 0.05, Dunnett's post-test) in CT and RT were detected within the FTPC range at a sensitivity of 10- to 100-fold greater than the 2D platforms, and a similar pattern was seen for forskolin (Figure 2B). These trends did not extend to NIs, presumably because on- or off-target cardiac toxicity associated with a proportion of compounds in this group will be occurring after longer incubation times and at higher concentrations than those used for therapeutic benefit, which is reflected in the FTPC.

Finally, we investigated which parameter was most informative (Figure 3). Where prediction was correct, we asked which parameter within these *in vitro* models reached significance at the lowest drug concentration. Pooled data from both PIs and NIs showed no clear distinction between CA, CT, and RT. However, segregation showed that CA was clearly most informative parameter for NIs. In contrast, CT was highly informative for PIs and particularly those with cAMP-mediated modes of action, with some contribution being derived from RT in hiPSC-CMs and CA in rabbit CMs.

Understanding why incorrect assignments were made and improving test platforms
The data above highlighted several deficiencies, including: (1) the discrimination of changes in contractility assessed from intermittent video measurements using a motion algorithm on 2D systems was lower than the continuous tension measurements on

Figure 1: Contraction analysis across the platform-cell combinations for PIs and NIs.

A, Contraction analysis across the platform-cell combinations for PIs. Examples are given to illustrate when some or all platform-cell combinations enable correct or incorrect predictions of the PIs, epinephrine, and levosimendan, respectively. The table indicates where decision making was guided by data from Ca^{2+} transients and/or voltage, with example data provided for epinephrine and verapamil in Supplementary Figures 4A and 4B. B, Contraction analysis across the platform-cell combinations for NIs. Examples are given to illustrate when some or all platform-cell combinations enable correct or incorrect predictions of the NIs, verapamil, and sunitinib, respectively. The table indicates where decision making was guided by data from Ca^{2+} transients and/or voltage, with example data provided for epinephrine and verapamil in Supplementary Figures 4A and 4B. C, Contraction analysis across the platform-cell combinations for NEs. Examples are given to illustrate when some or all platform-cell combinations enable correct or incorrect predictions of the NEs, acetylsalicylic acid, and captopril, respectively.

Red dotted line is free therapeutic plasma concentration (FTPC). Dunnett's stats versus vehicle control: *p < 0.05; **p < 0.01; ***p < 0.001; ****p < 0.0001. Abbreviations: CO, CellOPTIQ; EHT, engineered heart tissue; TTM, Triple Transient Measurement.

A

Drug	Rank	CellLine	parameter	Concentration 0.01	0.03	0.1	0.3	1	3	10	30	100
Verapamil	7		FTPC		0.05 µM							
		CO: Rb	CA	-54.95	-82.09	-80.27	NR	NR				
			CT	-7.87	-7.92	24.26	NR	NR				
			RT	15.17	23.28	60.89	NR	NR				
		EHT: ERC	CA	-8.17	-42.18	-89.19	-100	-100				
			CT	-1.06	-9.48	-25.36	NR	NR				
			RT	-10.05	-17.26	-16.33	NR	NR				
		EHT: R-PAT	CA	5.93	-26.48	-100	-100	NR				
			CT	3.79	-7.32	NR	NR	NR				
			RT	4.07	-6.23	NR	NR	NR	-	-	-	-
		TTM:	CA	-30.53	-50.11	-78.76	NR	NR	-	-	-	-
			CT	-11.49	-31.01	-68.09	NR	NR	-	-	-	-
			RT	-0.44	-8.95	-11.2	NR	NR	-	-	-	-
		CO: iCell2	CA	36.23	-7.03	8.1	-39.6	-100	-	-	-	-
			CT	103.13	84.97	4.58	-7.93	-100	-	-	-	-
			RT	31.3	4.47	47.12	-10.27	-100	-	-	-	-
		CO: Pluricyte	CA	30.6	-6	24.3	8.3	-100	-	-	-	-
			CT	3.43	18.5	-11.54	-41.46	-100	-	-	-	-
			RT	-35.77	-32.36	-50.72	-59.18	-100	-	-	-	-
		CO: R-PAT	CA	12.04	3.47	-11.34	-26.84	-98.03	-	-	-	-
			CT	-35.26	-16.5	-16.76	-36.58	-80.63	-	-	-	-
			RT	-5.87	1.28	14.88	-25.46	-87.94	-	-	-	-
Sunitinib	9		FTPC	0.003 µM								
		CO: Rb	CA	-	-	17.79	7.28	-31.96	-57.64	-77.7	-	-
			CT	-	-	4.17	-2.68	3.91	5.18	45.93	-	-
			RT	-	-	8.87	0.33	23.64	137.67	300.4	-	-
		TTM:	CA	-	-	42.31	27.59	15.24	-39.48	-20.73	-	-
			CT	-	-	9.95	13.19	-4.28	-17.53	-23.25	-	-
			RT	-	-	28.32	19.51	22.97	18.57	9.33	-	-
		CO: iCell2	CA	-	-	7.6	-16.86	-20.5	4.82	-24.76	-	-
			CT	-	-	-11.92	11.7	-43.4	-11.72	9.86	-	-
			RT	-	-	1.78	-2.26	62.3	5.38	-7.1	-	-
		CO: Pluricyte	CA	-	-	-13.02	4.46	3.08	17.57	-100	-	-
			CT	-	-	162.66	58.3	16.26	24.83	-100	-	-
			RT	-	-	-46.48	-1.14	-10.16	-19.22	-100	-	-
Citalopram	16		FTPC		0.05 µM							
		EHT: ERC	CA	-	-	-	-	-26.58	-65.22	-100	-100	-100
			CT	-	-	-	-	1.82	0.76	NR	NR	NR
			RT	-	-	-	-	5	7.72	NR	NR	NR
		EHT: R-PAT	CA	-	-	-	-	-1.52	-30.72	-100	NR	NR
			CT	-	-	-	-	6.49	-4.03	NR	NR	NR
			RT	-	-	-	-	4.96	-1.33	NR	NR	NR
		CO: R-PAT	CA	-	-	-	-	11.74	-13.54	-61.3	-100	-100
			CT	-	-	-	-	-11.44	-2.23	-19.46	-100	-100
			RT	-	-	-	-	6.18	-8.13	-30.71	-100	-100
Itraconazole	18		FTPC	0.00086 µM								
		EHT: ERC	CA	-	-	-9.9	-16.06	-36.58	-51.18	-100	-	-
			CT	-	-	6.88	6.19	11.31	8.49	NR	-	-
			RT	-	-	1.93	1.74	-10.18	-29.37	NR	-	-
		EHT: R-PAT	CA	-	-	5.93	-1.39	-15.86	-51.14	NR	-	-
			CT	-	-	13.55	4.63	4.61	12.2	NR	-	-
			RT	-	-	-2.65	-8.52	-19.46	-33.17	NR	-	-
		CO: R-PAT	CA	-	-	-32.83	-25.86	-16.36	-48.12	-100	-	-
			CT	-	-	8.5	25.46	6.66	-29.86	-100	-	-
			RT	-	-	-2.15	-2.14	-2.08	-62.62	-100	-	-
Sorafenib	19		FTPC		0.03 µM							
		EHT: ERC	CA	-	-	-15.06	-16.8	-22.49	-37.56	-56.3	-	-
			CT	-	-	-1.34	-2.42	3.62	6.27	4.68	-	-
			RT	-	-	3.4	2.78	-1.17	-14.39	-24.43	-	-
		EHT: R-PAT	CA	-	-	-1.68	-3.89	-11.75	-25.63	-50.4	-	-
			CT	-	-	3.22	1.8	8.7	6.42	13.89	-	-
			RT	-	-	0.22	1.31	-1.98	-6.48	1.55	-	-
		CO: R-PAT	CA	-	-	-12.8	-2.87	-10.56	-49.21	-100	-	-
			CT	-	-	4.36	28.21	10.03	-48.43	-100	-	-
			RT	-	-	-3.54	23.61	-12.26	-55.88	-100	-	-
Ivabradine	20		FTPC		0.01 - 0.1 µM							
		EHT: ERC	CA	-	-	-5.9	-7.34	-9.23	-19.14	-55.6	-	-
			CT	-	-	0.77	-0.27	-3.68	-8.35	-13.62	-	-
			RT	-	-	-1.61	-3.04	4.08	27.35	45.3	-	-
		EHT: R-PAT	CA	-	-	-6.21	-7.39	-2.05	8.83	-15.68	-	-
			CT	-	-	0.17	-7.87	-6.8	-13.46	-26.88	-	-
			RT	-	-	3.15	0.06	-1.13	-0.25	-2.34	-	-
Flecainide	22		FTPC			0.2 - 0.4 µM						
		EHT: ERC	CA	-	-	-8.14	-9.09	-24.62	-38.05	-74.5	-	-
			CT	-	-	3.26	-0.71	-4.9	-21.24	NR	-	-
			RT	-	-	0.83	1.07	18.08	42.22	NR	-	-
		EHT: R-PAT	CA	-	-	-5.47	-20	-6.8	-100	NR	-	-
			CT	-	-	-4.73	-15.53	-6.29	NR	NR	-	-
			RT	-	-	-5.29	-17.79	-25.78	NR	NR	-	-
Phentolamine	24		FTPC						2.25 µM			
		EHT: ERC	CA	-	-	-	-	-1.62	-23.21	-89.9	-100	-100
			CT	-	-	-	-	-8.02	-16.4	-30.49	NR	NR
			RT	-	-	-	-	25.36	39.86	52.53	NR	NR
		EHT: R-PAT	CA	-	-	-	-	-3.14	-28.82	NR	NR	NR
			CT	-	-	-	-	-4.82	-17.74	NR	NR	NR
			RT	-	-	-	-	-12.69	-27.78	NR	NR	NR
		CO: R-PAT	CA	-	-	-	-	-20.04	-27.6	-41.1	-100	-100
			CT	-	-	-	-	-7.2	-7.9	-22.32	-100	-100
			RT	-	-	-	-	41.8	-2.7	-23.44	-100	-100
Zimelidine	28		FTPC					0.78 µM				
		EHT: ERC	CA	-	-	-	-	5.12	-6.91	-37.4	-95.23	-100
			CT	-	-	-	-	-3.17	-8.58	-13.03	-24.92	NR
			RT	-	-	-	-	23.76	42.78	42.59	27.92	NR
		EHT: R-PAT	CA	-	-	-	-	18.37	-1.27	NR	NR	NR
			CT	-	-	-	-	-2.11	-15	NR	NR	NR
			RT	-	-	-	-	-7.02	-22.03	NR	NR	NR

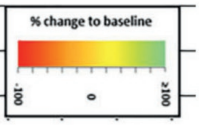

B

Drug	Rank	CellLine	parameter	Concentration (μM) 0.01	0.03	0.1	0.3	1	3	10	30	100
Epinephrine	1		FTPC	0.0002 - 0.05 μM								
		CO: Rb	CA	30.07	65.04	**196.24**	NR	NR				
			CT	-5.19	-18.51	**-25.74**	NR	NR				
			RT	3.81	5.91	-1.28	NR	NR				
		EHT: R-PAT	CA	7.09	9.12	**21.56**	**20.03**	**19.01**				
			CT	**-8.25**	**-13.22**	**-5.5**	**-10.7**	**-15.73**				
			RT	**-13.66**	**-16.98**	**-21.16**	**-22.2**	**-12.31**				
		TTM:	CA	50.36	52.81	28.71	36.91	39.83				
			CT	-2.29	-11.44	-18.99	-31.56	**-33.84**				
			RT	-8.72	-5.98	-1.49	-2.16	-1.96				
		CO: iCell2	CA	-3.6	-10.7	-3.9	-11.66	0.88				
			CT	-4.16	-42.92	-37.92	-39.86	-27.74				
			RT	21.74	39.32	24.58	23.08	16.28				
Forskolin	2		FTPC	0.012 - 0.024 μM								
		CO: Rb	CA	-	-	-12.35	13.09	-4.22	-15.54	7.04	-	-
			CT	-	-	-33.78	6.68	30.44	-5.28	8.26	-	-
			RT	-	-	7.1	9.92	36.35	45.43	34.6	-	-
		EHT: ERC	CA	-	-	-3.31	3.37	15.59	17.71	13.29	-	-
			CT	-	-	**-23.21**	**-30.5**	**-32.53**	**-30.3**	**-32.7**	-	-
			RT	-	-	**-11.15**	**-13**	**-18.03**	**-22.4**	**-23.2**	-	-
		EHT: R-PAT	CA	-	-	5.07	3.93	9.63	-0.39	-15.07	-	-
			CT	-	-	-2.05	**-7.33**	2.09	-0.56	-4.19	-	-
			RT	-	-	-3.69	**-17.1**	**-20.9**	**-21.8**	**-19**	-	-
		TTM:	CA	-	-	31.98	22.85	6.31	13.63	7.17	-	-
			CT	-	-	-26.83	-26.78	**-31.31**	**-37.4**	**-35.1**	-	-
			RT	-	-	11.15	-38.03	-37.12	-28.9	-33.23	-	-
Pimobendan	4		FTPC	0.005 - 0.01 μM								
		EHT: ERC	CA	-	-	-	-	-3.26	-7.67	5.58	13.42	13.29
			CT	-	-	-	-	-9.17	**-12.5**	**-11.2**	-8.21	**-11.4**
			RT	-	-	-	-	-3.72	3.43	5	13.03	13.55
Dobutamine	11		FTPC			0.07 - 1 μM						
		EHT: ERC	CA	-	-	5.01	3.75	**17.2**	**18.07**	12.27	-	-
			CT	-	-	-2.43	**-11.5**	**-26.23**	**-31.7**	**-37.2**	-	-
			RT	-	-	1.97	7.23	-4.42	-6.38	1.23	-	-
		EHT: R-PAT	CA	-	-	**17**	**28.48**	**37.5**	**43.62**	**31.95**	-	-
			CT	-	-	**-9.74**	**-12.9**	**-11.53**	**-12.3**	**-25.2**	-	-
			RT	-	-	**-20**	**-20.3**	**-18.29**	**-17.9**	**-21.6**	-	-
Milrinone	13		FTPC			0.1 - 0.15 μM						
		EHT: ERC	CA	-	-	-	-	2.32	1.61	-0.59	7.51	7.64
			CT	-	-	-	-	**-7.84**	**-8.45**	**-12.9**	**-15.57**	**-17.6**
			RT	-	-	-	-	2.96	0.11	0.33	-6.06	-1.51
		EHT: R-PAT	CA	-	-	-	-	-1.98	-2.27	4.87	18.46	NR
			CT	-	-	-	-	0.4	-5.11	-1.59	-10.85	NR
			RT	-	-	-	-	-0.07	-2.91	-3.65	**-8.98**	NR
Omecamtiv mecarbil	14		FTPC		0.05 - 0.42 μM							
		EHT: ERC	CA	3.03	5.86	11.22	**20.63**	**21.75**	-	-	-	-
			CT	0.66	0.04	3.8	18.9	37.51	-	-	-	-
			RT	2.88	1.98	-1.06	-5.53	-1.94	-	-	-	-
		EHT: R-PAT	CA	-12.48	0.75	17.48	**53.19**	NR	-	-	-	-
			CT	-2.22	2.07	**19.04**	**36.85**	NR	-	-	-	-
			RT	1.43	1.17	-9.2	**-25.8**	NR	-	-	-	-
Terbutaline	21		FTPC					1.3 μM				
		EHT: ERC	CA	-	-	4.46	9.04	**16.84**	**23.59**	**29.18**	-	-
			CT	-	-	**-22.01**	**-28.4**	**-29.62**	**-23.9**	**-22.3**	-	-
			RT	-	-	-14.96	-16.51	-17.06	-16.25	-1.97	-	-
		EHT: R-PAT	CA	-	-	7.94	1.9	14.3	**17.48**	NR	-	-
			CT	-	-	**-14.82**	**-21.3**	**-16.82**	**-24.2**	NR	-	-
			RT	-	-	**-24.73**	**-35.2**	**-30.03**	**-32.8**	NR	-	-

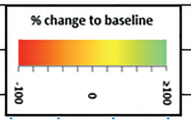

Figure 2: Sensitivity of platform-cell combinations for predicting PIs and NIs.

A, Sensitivity of platforms-cell combinations for predicting negative inotropes (NIs). Where NIs were correctly predicted, data are presented as percent change relative to baseline for any of the 3 contractility parameters (CA, contraction amplitude; CT, contraction time; RT, relaxation time). The bolded black text indicates where significance was reached using Dunnett's stats versus vehicle control and $p < 0.05$. Abbreviations: CO, CellOPTIQ; EHT, engineered heart tissue; FPTC, free plasma therapeutic concentration; NR, not recorded; TTM, Triple Transient Measurement. B, Sensitivity of platform-cell combinations for predicting positive inotrope (PIs). Where PIs were correctly predicted, data are presented as percent change relative to baseline for any of the 3 contractility parameters (CA, contraction amplitude; CT, contraction time; RT, relaxation time). The bolded black text indicates where significance was reached using Dunnett's stats versus vehicle control and $p < 0.05$.

3D systems, (2) detection of PIs was challenging, particularly to 2D platforms, and (3) chronic toxicants, such as doxorubicin, were poorly predicted after the acute (30 min) treatment duration.

We reasoned that medium composition may be a contributing factor in signal-to-noise ratio and poor detection of PIs. This was because, on the CO platform, switching from protein-containing (RPMI-B27) to serum-/protein-free medium increased the mean beat rate from 0.7 to ≥ 1.2 Hz (Supplementary Figure 5; $p \leq .0001$, Mann-Whitney). This was concurrent with increased spread of the data for CA, CT, and RT, wherein the standard deviations for RPMI-B27 versus serum-/protein-free medium were 12.1 versus 32.8, 14.5 versus 20.1, and 10.7 versus 26.9, respectively (Supplementary Figure 5). It has previously been reported in native heart muscle preparations that lower beating rate is associated with a positive force-frequency relationship (up to approximately 2 Hz) and stronger inotropic effects of most PIs[23]. Therefore, we retested PIs from the test set of drugs using CO:R-PAT, because this platform:cell combination proved poorly predictive (0/8) in the blinded study. In these revised testing conditions, 6/8 PIs showed reduced CT and/or RT (Figure 4).

We extended these studies to the 3D EHT platform, this time slowing spontaneous beating to < 0.5 Hz with 300 nM ivabradine, a pharmacological blocker of the "funny" If current[24]. Notably, these "slowed" EHTs could faithfully follow electrical pacing in increments from 0.5 to 2.5 Hz (Supplementary Figure 6). Whereas force-frequency relationships was negative above 1.5 Hz, it was positive between 0.5 and 1.5 Hz, evidenced by a 147% increase in force generation concurrent with significant shortening of CT and RT (Supplementary Figure 6). We therefore re-evaluated 6 of the PIs in the presence of 300 nM ivabradine with electrical pacing at 0.5, 0.7, 1.0, 1.5, and 2.0 Hz. These also included epinephrine, levosimendan, and pimobendan, which had been incorrectly predicted by EHT:R-PAT and/or EHT:ERC platform-cell combinations. Notably, for all 6 drugs, positive inotropy was evident via increases in CA but only at 0.5 and 0.7 Hz, and sometimes at 1 Hz, but never at 1.5 or 2 Hz (Figure 5). Consistent with this, shortening of CT was observed for all drugs acting via increased cAMP, with

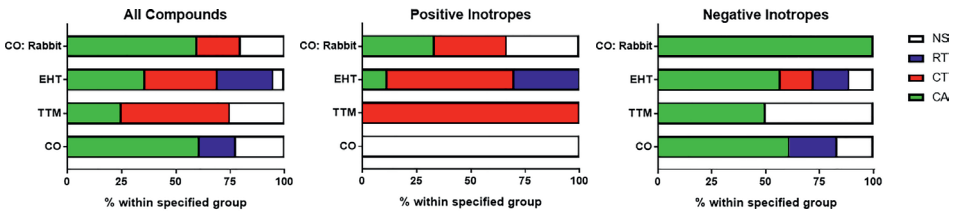

the largest changes often occurring at the lower pacing frequencies (Figure 5). Thus, in both 2D and 3D configurations, lower beating frequencies led to increased predictivity for PIs.

Finally, we considered NIs that had been incorrectly predicted (or not tested), including doxorubicin and sunitinib. Although 30 min exposure of hiPSC-CMs to these anticancer drugs altered electrophysiology, effects on contractility were predicted with variable accuracy (Table 1, web tool). We asked whether longer term exposure would affect contractility (Supplementary Figure 7). The CO:R-PAT platform-cell combination showed that exposure to the highest concentration of either drug for 24 h led to loss of contraction and cell death. Similarly, using the EHT:ERC platform-cell combination, exposure to doxorubicin ceased EHT contraction after 17.5 h, whereas exposure to 1 μM sunitinib led to a decline in CA over a 7-day period (Supplementary Figure 7). Thus, although short-term exposure to these NIs perturbed the electrophysiology of hiPSC-CMs, longer term exposure caused overt cytotoxicity and/or negative inotropy.

Discussion

Through blinded testing across multiple geographical sites, we evaluated the ability of 7 different platform-cell combinations to predict whether drugs of interest to the pharmaceutical industry were positive, negative, or neutral inotropes. We achieved this by examining contractility parameters (CA, CT, and RT), as well as using Ca^{2+} transients and/or electrophysiology to assist in decision making in some instances. Within the context of these *in vitro* models, we found that CA was the most informative parameter for NIs. Particularly after refinement involving slowing of beat rate to below 1 Hz (Figure 5, Supplementary Figure 6), CA was highly informative of PIs in the EHT system but far less so in the 2D systems. Although contraction- and relaxation-time provided confirmatory readouts for PIs in 3D EHTs, these parameters typically served as the primary source of predictivity in 2D (Figure 4), especially where the mode of action involved cAMP signaling.

Figure 3: Most informative contractility marker.

Parameters that led to the correct prediction of drug responses were assessed. Data show the breakdown by percentage for the parameters (CA, contraction amplitude; CT, contraction time; RT, relaxation time) that reached significance at the lowest concentration (Dunnett's stats vs vehicle control and $p < 0.05$). White boxes (NS, not significant) indicate where predictions were made due to a trend rather than reaching significance, and/or by guidance from Ca^{2+} and/or voltage data. Abbreviations: CO, CellOPTIQ; EHT, engineered heart tissue; TTM, Triple Transient Measurement.

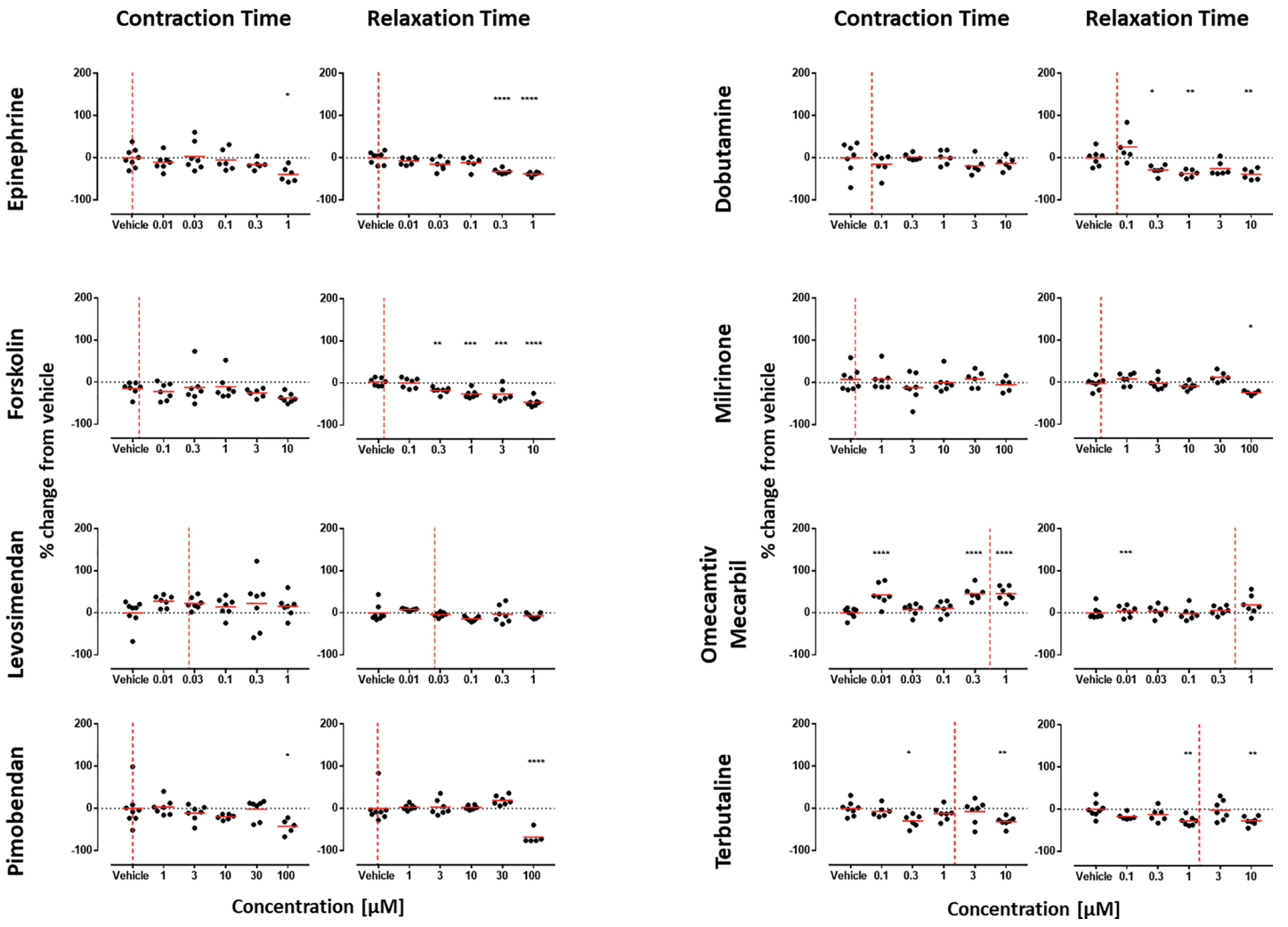
Contraction Time
Relaxation Time
Epinephrine
Forskolin
Levosimendan
Pimobendan
Dobutamine
Milrinone
Omecamtiv Mecarbil
Terbutaline
% change from vehicle
Concentration [µM]

We propose that an efficient way to predict the inotropic effect of drugs would be first to conduct acute (30 min) testing in hiPSC-CMs. Spontaneous beat rates should be < 1 Hz, which can be achieved by modifying the culture medium, using pharmacological blockage with ivabradine, and/or selecting hiPSC-CMs with slow intrinsic rates. In EHTs, this approach unveiled a clear positive force-frequency relationship. If no changes in inotropy are detected in the acute assay, then exposure times can be increased to ≥ 24 h to determine whether the drugs have a chronic effect. These timelines were suggested by GSK (ie, ≤ 30 min considered as acute; ≥ 24 h as chronic), which proved to be a useful approach because it allowed a predictive accuracy of 85% in 2D monolayers and 93% in 3D EHTs.

In reaching these refined conditions, we noted greater importance of the cell preparation protocol, testing conditions, methods of measuring contractility, and 2D versus 3D than the cell type used, which was not necessarily expected. There were differences in the purity/composition of the different cell types and in their baseline electrophysiological characteristics, which partly reflects their maturity state at single cell level (Supplementary Table 3). However, there was not an obvious correlation between these differences and predictivity. For example, initial testing of the same cell type (Pluricyte hiPSC-CMs) on 2 platforms (TTM and CO) gave different accuracies (78% vs 56%). The same was true for R-PAT hiPSC-CMs on the EHT and CO platforms (67% vs 44%).

Modifying both the culture environment (by including a protein source that caused a beat rate to be slowed, and signal-to-noise ratio and data variability to be reduced) and the drug exposure conditions (by including both acute chronic testing for ≤ min and ≥ 24 h, respectively) for the CO:R-PAT combination allowed the accuracy of prediction using this cell line to be increased to 85%. It is possible that further improvements could be made, whilst simultaneously shedding light on mechanism of action. For example, analysis of data during different stages of relaxation identified positive lusitropy for dobutamine (at 50% relaxation) and late relaxation deficit for ivabradine (at 80% relaxation). During the blinded phase, we also correctly predicted that drug rank 14 was omecamtiv mecarbil on account of the unusual response of increased CT (approximately

Figure 4: Refined culture conditions increase predictivity of PIs in 2D monolayers of hiPSC-CMs.

Contraction analysis was carried out on the 8 PIs from the drug test set using the CO:R-PAT platform-cell combination. Only CT and RT are shown because data in Figure 3 showed these to be the most informative parameters for PIs. Whereas testing in serum-/protein-free medium failed to identify any PIs correctly (web tool), the slowed beat rate and improved signal-to-noise ratio afforded by culture in RPMI-B27 allowed correct identification of 6/8 PIs by significant decreases in CT and/or RT. Red dotted line is free therapeutic plasma concentration. Dunnett's stats versus vehicle control: *p <0 .05; **p < 0.01; ***p < 0.001; ****p < 0.0001.

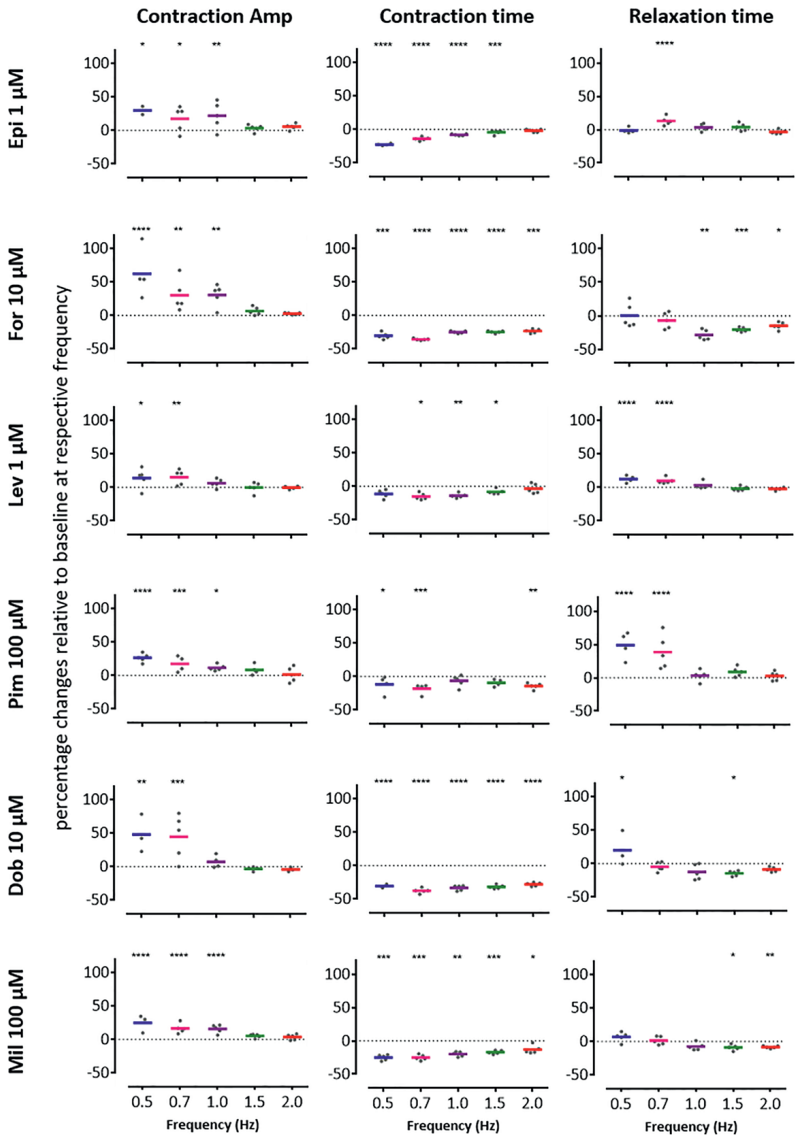

Figure 5: Slowed beat rate increases the predictivity of PIs) in 3D EHTs.

Contraction analysis was carried out using EHTs with 6 of the PIs from the drug test set: epinephrine (Epi), forskolin (For), levosimendan (Lev), pimobendan (Pim), dobutamine (Dob), and milrinone (Mil) which had been predicted with variable accuracy (web tool). In all cases, the drugs (applied as a high concentration bolus) increased contraction amplitude (CA) but only at

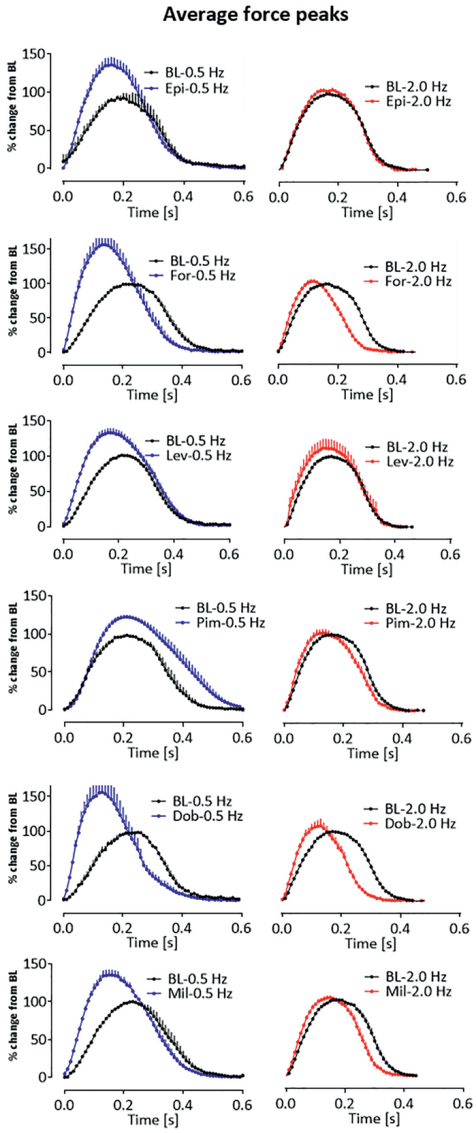

0.5 and 0.7 Hz, and sometimes at 1 Hz, with the largest effects seen in contraction time (CT) also often occurring at these frequencies. Scatter plots show percentage changes relative to baseline at respective frequency. Averaged peaks for force are shown for baseline (BL, black peaks) versus after treatment in EHTs paced at 0.5 Hz (blue peaks) or 2.0 Hz (red peaks). Dunnett's stats versus baseline at respective frequency: *$p < 0.05$; **$p < 0.01$; ***$p < 0.001$; ****$p < 0.0001$.

+40%) without convincing evidence for increased CA[25]. This shows the value of applying pharmacological knowledge to drug responses in hiPSC-CMs to derive mechanistic information out of multiparametric assessments, in this case combined evaluation of CA, CT, and RT in hiPSC-CMs configured as 3D EHTs, in this case combined evaluation of CA, CT, and RT in hiPSC-CMs configured as 3D EHTs.

Another consideration is the difference between single cells, continuous monolayers, and 3D engineered constructs. The single rabbit cardiomyocyte assay used near-physiological rates of stimulation (2 Hz) and subphysiological rates (1 Hz or lower) may have improved scope to detect PIs. In adult heart preparations, a common feature of PI interventions that raise intracellular Ca^{2+} is the occurrence of spontaneous diastolic SR Ca^{2+} release. This phenomenon is linked to negative inotropy and arrhythmic behavior in single cells and intact myocardium[26,27]. In this study, spontaneous diastolic Ca^{2+} release and associated diastolic shortening was observed in isolated rabbit myocytes in response to β-adrenoreceptor stimulation and drugs that raise cAMP directly (e.g. forskolin), but this phenomenon was not reported in any of the hiPSC-CMs platforms. This is consistent with the minimal involvement of the SR in excitation-contraction coupling typically seen in embryonic cardiomyocytes and hiPSC-CMs[28]; in this context, the PI effect from cAMP arises mainly from cAMP-mediated stimulation of L-type Ca^{2+} current.

Out of necessity, preparations of native adult CMs are dispersed and seeded as cultures of single cells. It is known that variance in cell density influences electrophysiological parameters[29], particularly within, and between, preparations of single cell preparations, including hiPSC-CMs[17]. Therefore, although the structural and function (eg, prevalent SR) maturity of adult native adult CMs from rabbit is an advantage over hiPSC-CMs, this is offset by the high level of heterogeneity of single cell preparations, which reduces the discrimination power. Although some of the differences will be due to the physiology of rabbit CMs relative to human CMs, we have also seen higher variability in human atrial trabeculae as compared with hiPSC-EHT; hence, there are separate challenges in using native cells. It is for these reasons we elected to use hiPSC-CMs within 2D or 3D syncytium, where individual cell-to-cell variability is averaged due to mechanical and electrical coupling. In addition, several studies have shown previously that the EHT format compared with standard 2D culture favors maturation in terms of MDP and upstroke velocity[30,31], structure[22], and metabolic preference[32].

Blinded analysis was done using serum-/protein-free medium, with the intention of avoiding protein-drug binding that might blunt the responses within the *in vitro* system. However, at least in the CO:R-PAT platform-cell combination, serum-/protein-free medium was a hindrance, leading to high spontaneous beat rates, and poor signal-to-noise ratio ratios. These issues were abrogated by using protein-containing medium (RPMI-B27), which enhanced the accuracy of predicting PIs on the CO:R-PAT platform from 0% to 75%. This indicates that, for this purpose, the benefits brought by the protein-containing medium outweigh the concerns of drug binding and batch-to-batch variations of protein ingredients. Nevertheless, voltage-sensitive dyes, such as FluoVolt, interact with proteins and reduce the signal-to-noise ratio, which make simultaneous recording of contraction and voltage challenging, although this may be

Table 1: Effects of compounds on cardiomyocyte contractility *in vitro*

Drugs were ranked by GSK personnel to provide a testing order, based on modes of action that were of interest to them. For each platform-cell combination, data listed represent mean maximum measurable percentage change relative to baseline for CA, CT, and RT. The concentration at which this effect occurred is listed but when it was different for CA, CT, and RT information is added after the relevant parameter. Green indicates the predicted effect matched the known effect on inotropy. Analysis platforms were CO (CellOPTIQEHT), EHT (engineered heart tissue) and TTM (Triple Transient Measurement). Cardiomyocyte types were rabbit adult cardiomyocytes (as comparator) or hiPSC lines: P-Cyte, (Pluricyte, Ncardia); iCell2 (Cellular Dynamics International); R-PAT (University of Nottingham); ERC18 (University of Hamburg).

Abbreviations: FPTC, free plasma therapeutic concentration; ACE, angiotensin converting enzyme; PDE, phosphodiesterase; SSR inhibitor, selective serotonin reuptake inhibitor; PI, positive inotrope; NI, negative inotrope; NE, no effect.

Compound	Rank	Mode of Action	Platform	Cell	CA	CT	RT	Test Range µM	Conc µM	FPTC µM	Known Effect	Blinded Assignment
Epinephrine	1	Nonselective α1-, β1-, and β2-adrenoceptor agonist	CO	Rabbit	+196	−26	+6 0.03 µM	0.01–1	0.1	0.0002–0.05	PI	PI
			TTM	P-Cyte	+53 0.03 µM	−34 1 µM	−9		0.01			PI
			CO	P-Cyte	+18 0.3 µM	+67 1 µM	−36		0.1			NE
			CO	iCell2	−12 0.3 µM	−43	+39		0.03			PI
			CO	R-PAT	+27 0.01 µM	+16	−18		1			NE
			EHT	R-PAT	+22	−16 1 µM	−22 0.3 µM		0.1			PI
			EHT	ERC18	+8	−6 1 µM	−7		0.01			NE

Compound	Rank	Mode of Action	Platform	Cell	CA	CT	RT	Test Range µM	Conc µM	FPTC µM	Known Effect	Blinded Assignment
Forskolin	2	Adenylyl cyclase stimulator	CO	Rabbit	−16	−34 0.1 µM	+45	0.1–10	3	0.012–0.024	PI	PI
			TTM	P-Cyte	+72 10 µM	−37 3 µM	−38		0.3			PI
			CO	P-Cyte	+31 1 µM	+55 3 µM	+47		0.3			NE
			CO	iCell2	−44	+64	+44		10			NI
			CO	R-PAT	−31 10 µM	−33	+20		0.1			NE
			EHT	R-PAT	+15 10 µM	−7	−22 3 µM		0.3			PI
			EHT	ERC18	+18 3 µM	−33	−23		10			PI
Levosimendan	3	Calcium sensitizer	CO	Rabbit	+16 0.1 µM	−33	−25	0.01–1	0.01	0.026–0.35	PI	NE
		PDE3 inhibitor	TTM	P-Cyte	+42 0.1 µM	+11 0.3 µM	−12		0.03			NE
		KATP channel agonist	CO	P-Cyte	−54	+54	−40		0.03			NE
			CO	iCell2	+14 0.3 µM	+80	+54		0.1			NE
			CO	R-PAT	+23 0.1 µM	−12	22 1 µM		0.01			NE
			EHT	R-PAT	+6	−7	−14 0.3 µM		0.01			NE
			EHT	ERC18	+13 1 µM	−9 0.1 µM	−4		0.01			NE
Pimobendan	4	Calcium sensitizer	CO	Rabbit	+132 1 µM	+72	+42	1–100	3	0.005–0.01	PI	NE
		PDE3 inhibitor	TTM	P-Cyte	+55	−31 10 µM	+73		30			NE
			CO	P-Cyte	−23 10 µM	+69	−19		3			NE
			CO	iCell2	+65	+69	−13 100 µM		1			NE
			CO	R-PAT	+18	+26 10 µM	+29		100			NE
			EHT	R-PAT	+12	−3.5	+12 100 µM		1			NE
			EHT	ERC18	+13 30 µM	−13	+14 100 µM		3			PI

Dobutamine	11	α1-, β1-, and β2-adrenoceptor agonist	CO	R-PAT	+39 3 μM	−16 10 μM	+29	0.1–10	0.3	0.07–1	PI	NE
			EHT	R-PAT	+44 3 μM	−25	−22		10			PI
			EHT	ERC18	+18 3 μM	−37 10 μM	+7		0.3			PI
Milrinone	13	PDE3 inhibitor	CO	R-PAT	−17	+16 3 μM	+15 100 μM	1–100	1	0.1–0.15	PI	NE
			EHT	R-PAT	+18	−11	−9		30			PI
			EHT	ERC18	+7	−18	−6 30 μM		100			PI
Omecamtiv mecarbil	14	Cardiac-specific myosin activator	CO	R-PAT	−47	+117	−34 0.01 μM	0.01–1	1	0.05–4.2	PI	NI
			EHT	R-PAT	+53	+37	−26		0.3			PI
			EHT	ERC18	+22	+38	−6 0.3 μM		1			PI
Terbutaline	21	β2-adrenoceptor agonist	CO	R-PAT	+28	−32 3 μM	−35 10 μM	0.1–10	0.3	1.3	PI	NE
			EHT	R-PAT	+17	−24	−35 0.3 μM		3			PI
			EHT	ERC18	+29 10 μM	−30	−17		1			PI
Verapamil	7	L-type calcium channel blocker, hERG blocker	CO	Rabbit	−82 0.03 μM	+24	+61	0.01–1	0.1	0.05	NI	NI
			TTM	P-Cyte	−79	−68	−11		0.1			NI
			CO	P-Cyte	(5/5)Q	(5/5)Q	(5/5)Q		1			NI
			CO	iCell2	(4/5)Q	+103 0.1 μM	(4/5)Q		1			NI
			CO	R-PAT	−98	−91	−88		1			NI
			EHT	R-PAT	(5/5)Q 0.1 μM	−7	−6		0.03			NI
			EHT	ERC18	(3/5)Q 0.3 μM	−25 0.1 μM	−17		0.1			NI

Compound	Rank	Mode of Action	Platform	Cell	CA	CT	RT	Test Range µM	Conc µM	FPTC µM	Known Effect	Blinded Assignment
Doxorubicin	8	Impairs Ca2+ transport mechanisms in SR	TTM	P-Cyte	−47	−46	+51	0.1–10	100	1–2	NI	NE
			CO	P-Cyte	−15	+70	+72		100			NE
			CO	iCell2	+65	−39	+57 30 µM		1			NE
			CO	R-PAT	−27 100 µM	+41 30 µM	−12		1			NE
Sunitinib	9	Multitargeted TK inhibitor	CO	Rabbit	−78	+46	+300	0.1–10	10	0.003	NI	NI
			TTM	P-Cyte	+42	−23 10 µM	+28		0.1			NI
			CO	P-Cyte	(5/5)Q	+163 0.1 µM	(5/5)Q		10			NI
			CO	iCell2	−25 10 µM	−43	+62		1			NI
			CO	R-PAT	−20	+34 0.1 µM	+33		10			NE
			EHT	R-PAT	+11	+6	+4 0.1 µM		0.3			NE
			EHT	ERC18	−8	+6	−8		3			NE
Citalopram	16	SSR inhibitor, hERG & L-type calcium channel blocker	CO	R-PAT	(10/10)Q	(10/10)Q	(10/10)Q	1–100	30	0.05	NI	NI
			EHT	R-PAT	(4/4)Q 10 µM	−6 3 µM	+5		1			NI
			EHT	ERC18	(5/5)Q 10 µM	+2 1 µM	+7		3			NI
Itraconazole	18	Triazole antifungal, mechanism unclear	CO	R-PAT	(5/5)Q	(5/5)Q	(5/5)Q	0.1–10	10	0.00086	NI	NI
			EHT	R-PAT	−51	+14 0.1 µM	−33		3			NI
			EHT	ERC18	(5/5)Q 10 µM	+11	−29 3 µM		1			NI

Sorafenib	19	Multitargeted TK inhibitor	CO	R-PAT	(10/10)Q	(10/10)Q	(10/10)Q	0.1–10	10	0.03	NI	NI
			EHT	R-PAT	−50	+14	+6 3 µM		10			NI
			EHT	ERC18	−56	+6 3 µM	−24		10			NI
Ivabradine	20	If inhibitor	CO	R-PAT	+46	+22	+24 0.3 µM	0.1–10	0.1	0.01–0.1	NI	NE
			EHT	R-PAT	−16	−27	+3 0.1 µM		10			NI
			EHT	ERC18	−56	14	+45		10			NI
Flecainide	22	Sodium channel blocker, hERG blocker	CO	R-PAT	+31	+26 10 µM	+29 1 µM	0.1–10	0.1	0.2–0.4	NI	NE
			EHT	R-PAT	(6/6)Q 3 µM	−16	−26 1 µM		0.3			NI
			EHT	ERC18	−74 10 µM	−21	+42		3			NI
Phentolamine	24	Nonselective α-adrenoceptor antagonist	CO	R-PAT	(5/5)Q	(5/5)Q	(5/5)Q	1–100	30	2.25	NI	NI
			EHT	R-PAT	5/5)Q 10 µM	−18	−28		3			NI
			EHT	ERC18	(5/5)Q	−30	+53		10			NI
Zimelidine	28	SSR inhibitor	EHT	R-PAT	18 1 µM	−15	−22	1–100	3	0.78	NI	NI
			EHT	ERC18	(5/5)Q 100 µM	−25 30 µM	+43		3			NI
Acetylsalicylic acid	5	Cyclooxygenase inhibitor	CO	Rabbit	+26	−21	−13	10–1000	100	0.3–2	NE	NE
			TTM	P-Cyte	+34	−8 1000 µM	+24 100 µM		10			NE
			CO	P-Cyte	−21 30 µM	−35	+20		10			NE
			CO	iCell2	−58 30 µM	−44	+47 1000 µM		10			NE
			CO	R-PAT	+23	−26 300 µM	+17 1000 µM		100			NE
			EHT	R-PAT	−14	+8 100 µM	+15		1000			NE
			EHT	ERC18	+8 300 µM	−8	−15		1000			NE

Compound	Rank	Mode of Action	Platform	Cell	CA	CT	RT	Test Range µM	Conc µM	FPTC µM	Known Effect	Blinded Assignment
Atenolol	6	β1 > β2 adrenoceptor antagonist	CO	Rabbit	+16	−13	+968 0.3 µM	0.1–10	1	1	NE	NE
			TTM	P-Cyte	+54	+8	−19 3 µM		1			NE
			CO	P-Cyte	−29	−71 10 µM	+69 3 µM		1			NE
			CO	iCell2	−42 0.1 µM	+58	−52		0.3			NE
			CO	R-PAT	−28 3 µM	+11	+11 10 µM		0.3			NE
			EHT	R-PAT	−25	+7 1 µM	+14		10			NE
			EHT	ERC18	+3	−13	−9 3 µM		10			NE
Captopril	10	ACE inhibitor	CO	Rabbit	−91	+72	+212	1–100	100	1–2	NE	NI
			TTM	P-Cyte	+136	−5	−14 10 µM		1			NE
			CO	P-Cyte	+24 30 µM	+132	−38		100			NE
			CO	iCell2	−27	+15 3 µM	−20 10 µM		1			NE
			CO	R-PAT	+18 3 µM	−26	−16 30 µM		1			NE
			EHT	R-PAT	−18	−7 100 µM	−9 10 µM		3			NE
			EHT	ERC18	+7	−10	−6 1 µM		3			NE
Glibenclamide	12	KATP channel antagonist	CO	Rabbit	+66 1 µM	−27 0.3 µM	+61	0.1–10	0.1	0.02–0.06	NE	NE
			CO	R-PAT	+36	−26 10 µM	+31		0.1			NE
			EHT	R-PAT	+3	+6	−12		1			NE
			EHT	ERC18	+6	+10	−5 3 µM		10			NE
Enalaprilat	15	ACE inhibitor	CO	R-PAT	+54	+20 10 µM	+34	1–100	100	0.12	NE	NE
			EHT	R-PAT	+33	+5 1 µM	−14		30			PI
			EHT	ERC18	+2 10 µM	−3	−4		100			NE

Clonidine	17	α2-adrenoceptor agonist	**CO**	**R-PAT**	−24	+26	−27	0.01–1	0.3	0.002–0.004	NE	**NE**
			EHT	**R-PAT**	+10	+11 0.1 μM	−12		0.3			**NE**
			EHT	**ERC18**	+5 0.3 μM	+5	+4		0.1			**NE**
Paracetamol	23	Prostaglandin synthesis inhibitor	**CO**	**R-PAT**	+19 100 μM	+26	+13 1000 μM	10–1000	30	50	NE	**NE**
			EHT	**R-PAT**	−19	−20	−9 100 μM		1000			**NE**
			EHT	**ERC18**	+3 100 μM	−9	+10		1000			**NE**
Tolbutamide	25	KATP channel antagonist, adenylyl cyclase stimulator	**CO**	**R-PAT**	+35	−16 10 μM	+45	1–100	100	20–30	NE	**NE**
			EHT	**R-PAT**	−12	+9	−8 10 μM		1			**NE**
			EHT	ERC18	+21	−3	−9		100			PI
Pravastatin	26	HMG CoA reductase inhibitor	**CO**	**R-PAT**	+53	+42	+12 1 μM	1–100	3	0.018	NE	**NE**
			EHT	**R-PAT**	−19	−15 30 μM	13 100 μM		3			**NE**
			EHT	ERC18	+19	+3 30 μM	−11 100 μM		10			PI
Sildenafil	27	PDE5 inhibitor	**CO**	**R-PAT**	+56	+39	+30 3 μM	0.3 – 30	10	0.02	NE	**NE**
			EHT	**R-PAT**	−10	−16	+13 3 μM		10			**NE**
			EHT	**ERC18**	+9	−4 10 μM	−6		1			**NE**

Table 2: Predictivity tables and scores

Collective data are presented for cross comparison between platform-cell combinations relating to the 9 drugs tested in common or all drugs evaluated. Green shading shows predictivity of > 75%, orange of 50%–74%, and red of < 50%. Predictivity is gauged as whether the assignment made by the investigators matched the assignment made by the commercial sponsor, GlaxoSmithKline, and the available literature described in Supplementary Table 1.

Platform:Cell Combination		Config.	Nine Drugs in Common				All Drugs Assessed			
			PI (%)	NI (%)	NE (%)	Total (%)	PI (%)	NI (%)	NE (%)	Total (%)
CellOPTIQ	Rabbit CMs	2D	2/4 (50)	2/2 (100)	2/3 (67)	6/9 (67)	2/4 (50)	2/2 (100)	3/4 (75)	7/10 (70)
TTM	Pluricyte hiPSC-CMs		2/4 (50)	2/2 (100)	3/3 (100)	7/9 (78)	2/4 (50)	2/3 (67)	3/3 (100)	7/10 (70)
CellOPTIQ	Pluricyte hiPSC-CMs		0/4 (0)	2/2 (100)	3/3 (100)	5/9 (56)	0/4 (0)	2/3 (67)	3/3 (100)	5/10 (50)
	iCell2 hiPSC-CMs		1/4 (25)	2/2 (100)	3/3 (100)	6/9 (67)	1/4 (25)	2/3 (67)	3/3 (100)	6/10 (60)
	R-PAT hiPSC-CMs		0/4 (0)	1/2 (50)	3/3 (100)	4/9 (44)	0/8 (0)	5/9 (56)	10/10 (100)	15/27 (56)
EHT	R-PAT hiPSC-CMs	3D	2/4 (50)	1/2 (50)	3/3 (100)	6/9 (67)	6/8 (75)	8/9 (89)	9/10 (90)	23/27 (85)
	ERC hiPSC-CMs		2/4 (50)	1/2 (50)	3/3 (100)	6/9 (67)	6/8 (75)	8/9 (89)	8/10 (80)	22/27 (81)

overcome by measuring extracellular voltage.

Treatment of hiPSC-CMs with doxorubicin for 30 min caused changes in electrophysiology (eg, triangulation, see web tool) and hence gave a distinctive response compared with NEs such as acetylsalicylic acid. Nevertheless, this acute exposure did not always cause changes in inotropy, which shows the importance of examining an appropriate concentration range and/or exposure times of drugs. Increasing exposure time to approximately 1–7 days unveiled doxorubicin and sunitinib as NIs, consistent with the extended timescale over which cardiac toxicity presents clinically and is in line with data from a previous study using TKI-inhibitor[33]. Interestingly, with 24 h of doxorubicin treatment, the CO:R-PAT platform-cell combination appeared to show a trend of positive inotropy from 1 to 30 μM (increased CA; decreased CT) but cell death at 10 μM. This aligns with reports indicating the effects of doxorubicin are complex in that transient positive inotropy is followed by robust negative inotropy at higher concentrations[34-36].

The levels of accuracy of up to 93% in predicting drug-induced changes in contractility in human hearts under these refined conditions are favorable relative to those from animal model[37,38]. They are also comparable with data using 3D cardiac microtissues containing hiPSC-CMs, cardiac endothelial cells, and cardiac fibroblasts, which correctly predicted 23 of 29 (85%) inotropes across a nonblinded panel of compounds[15]. These findings are encouraging, but it is not always straightforward to translate hiPSC-CM-related parameters of CA, CT, RT, and chronotropy (beat rate) to clinically relevant data. We have suggested that data derived from hiPSC-CMs on CA is informative for NIs in all cell-platforms combinations and for PIs in the 3D EHT platform. However, in the 2D systems, CT, and RT may be informative for PIs. We have considered different explanations for this observation. If 2D systems are less adept at showing an increase in CA, then decreases in CT (clinotropy; also expressed as an increase in dF/dt) or decreases in RT (lusitropy; also expressed as an increase in −dF/dt) become more important. By considering pF/dt values, which can change independently of the peak force, there is alignment with the effects seen *in vivo*, which are often expressed as a change in dP/dt_{max} or $-dP/dt_{min}$. An alternative explanation is that, although this is not automatically intuitive, it may be a quirk of hiPSC-CMs; as a model system, there are limitations and adaptations in thinking need to be made. Nevertheless, the robustness of this notion will need to be tested on a wider range of drugs to determine whether these *in vitro* parameters are relevant to *in vivo* cardiac physiology.

Effects on cardiac contractility per se may not indicate or predict a clinically relevant detrimental effect on the heart. For example, cardio-active L-type calcium channel blockers are used for treatment of hypertension. Additional "structural" endpoints, such as mitochondrial membrane permeability (Δψm), endoplasmic reticulum integrity, contractile filament expression/organization, ATP depletion, and cardiac troponin levels in hiPSC-CM-based assay platforms may add interpretive value to functional changes[20]. A limitation of our study was that some modes of action were not represented in the drug panel, such as the SERCA activator CDN1163[39,40], or the myosin inhibitor blebbistatin[41], and these would be interesting to include in blinded assays in the future.

In our study, we looked for trends or significant changes in the parameters measured, but did not apply a cut off on how much change was considered meaningful (e.g. > 15% change and statistical significance). Whether analysis can be modified in the future is for consideration but would need to be done with care. The NE drugs, enalaprilat, tolbutamide, and pravastatin caused changes of 19%–33% in CA on the EHT platform and were incorrectly predicted as PIs. However, these magnitudes of changes were similar or greater than those recorded for PIs, and so adding thresholds on CA would not have improved prediction and could have been detrimental. Relationship to FTPC was not a strong association either, with the maximum changes of the incorrectly predicted NEs varying from 3-fold below the FTPC (tolbutamide) to > 100-fold above (enalaprilat, pravastatin). This also underscores the importance of technical precision and inclusion of time controls in each single experiment, particularly in strategies employing cumulative concentration-response analyses which take time.

These observations likely reflect the complexity of drug-cell interactions, which means differential effects can occur dependent on the concentration and categorizing as PI, NI, and NE was difficult in some cases. Inotropic effects of high concentrations of sulphonylureas, such as tolbutamide, have been reported for *in vitro* systems[42]. Angiotensin converting enzyme (ACE) inhibitors, such as enalaprilat, lead to bradykinin accumulation and thereby lead to bradykinin B1 receptor activation, which elevates intracellular Ca^{2+} and causes a positive inotropic effect[43]. Similarly, phentolamine is a neutral inotrope at free plasma concentrations of approximately 2.5 µM in patients[44], but at concentrations above 10 µM phentolamine causes negative inotropy via modulation of fast sodium and L-type calcium channels[45,46]. This is consistent with our data, indicating that there are multiple pharmacological effects of this compound. For ivabradine the concentrations provided were much higher than the FTPC, which can lead to off-target effects of poorly selective drugs[47]. In some cases, such as zimelidine, the difficulty arose due to lack of robust *in vitro* data within the literature[48-50]. Care must therefore be used when (1) selecting test compounds by primary pharmacology and (2) using *in vitro* assay paradigms to predict *in vivo*, clinically relevant cardiotoxicity, either when used as a "screening assay" to rank compounds or as a reflex investigative assay, e.g. following detection of cardiotoxicity in animal toxicology studies.

Because PIs are cardio-active drugs, it might be expected that the FTPC aligns with responses from hiPSC-CMs. This was true for the EHT platform, where significant responses were within, or close to, the FTPC. However, both the pharmacologic or statistical sensitivity of 2D hiPSC-CM cultures and isolated single rabbit cardiomyocytes were considerably lower. Two explanations may account for these observations. First, the greater stability of CMs in 3D constructs permitted cumulative dosing of EHTs within the same well, which created tighter datasets than the 2D systems, where parallel dosing in separate well was required. Second, in contrast to 2D monolayers that evaluated hiPSC-CM movement in unloaded conditions, the EHT platform measures force of contraction under loaded conditions[52]. This facilitates maturation and Frank-Starling mechanisms for force generation are followed, leading to higher basal tone and cAMP signaling[42,52]), which are important modes of action of the PIs epinephrine, forskolin, and milrinone. Consistent with this, positive inotropy of milrinone was shown in "Biowire II" tissue engineered constructs, which also places hiPSC-CMs under loaded

conditions to facilitate maturation[53].

To measure whole heart function and its integration with neurohormonal or hemodynamic feedback, numerous assessment parameters are used, including P_{max}, dP/dt_{max} (max rate of change if pressure) and left ventricular ejection fraction[54]. Atenolol, a selective β1-adrenoceptor antagonist, requires intact sympathetic innervation and is an NI in the clinic but shows NE in hiPSC-CMs[55,56]. Similarly, the mode of action for clonidine is through presynaptic alpha-adrenoceptors on sympathetic neurons with the consequence of reduced sympathetic drive and its effect on heart function (reduced heart rate and force)[57,58], but these effects would not be detected in a "cardiomyocyte only" model. Predictive screening will also benefit from inclusion of auxiliary cell types, such as neural lineages to enable evaluation of drugs that work via the neurohormonal system.

Other issues that need to be considered for the future include throughput, user variability, cell availability, cost, and batch-to-batch variability. Although the TTM platform allowed simultaneous measurement of contraction, Ca^{2+} handling, and voltage, the low throughput meant that only 10 drugs were evaluated in 1 hiPSC-CM line. User variability has been noted in other studies. For example, variations in TdP predictability across different sites using identical instruments were reported in the CiPA study, and so could be a factor in the site to site differences we observed. Cost was another factor, wherein each drug assessed typically required 1.6 million (40 wells in a 96-well plate) and 5 million (5 EHTs) hiPSC-CMs, corresponding to up to approximately $3000 per drug at current prices. For these reasons, most of the assays in this report were done using hiPSC-CMs produced "in house," where cost for 1.6 or 5 million cells is approximately $16 or $50, respectively, albeit without the same level of quality control of commercial cells. Nevertheless, for both in house and commercial cells, batch-to-batch variation meant that the drug assays need to be repeated. These issues become more prominent when larger tissue engineered constructs are used. For example, "heart-in-a-jar" technologies, produce miniature 3D engineered electro-mechanically coupled cardiac organoid chamber that mimic pumping action similar to natural heart but require 10 million hiPSC-CM[59]. Thus, it is encouraging that scaled production of hiPSC-CMs is now becoming relatively routine and so costs should decrease in the near future.

Altogether, this study suggests that, even in their current status of technology evolution, hiPSC-CMs cultured in 2D and 3D may have value to predictive safety pharmacology. Given the high resource and costs involved with drug development, even modest improvements in the pipeline could have large socioeconomic and 3R benefits. More than 6000 putative medicines are in preclinical development, using millions of animals at an annual total cost of $11.3Bn, and so each percentile reduction equates to approximately $100 M. Similarly, reducing drug attrition in phase 1 clinical trials by 5% could reduce development costs by 5.5%–7.1%. Building on our work with further improvement and validation studies, conducted in a blinded manner, will facilitate uptake of hiPSC-CMs as a routine tool in safety pharmacology.

Funding

National Centre for the Replacement, Refinement & Reduction of Animals in Research (CRACK-IT: 35911-259146, NC/K000225/1); the British Heart Foundation (SP/15/9/31605, RG/15/6/31436, PG/14/59/31000, RG/14/1/30588, P47352/CRM); the German Research Foundation (DFG-Es-88/12-1, HA3423/5-1); European Research Council (ERC-AG-IndivuHeart, ERC-AdG STEMCARDIOVASC); Netherlands Science Foundation (NWO) under the Gravitation Grant "NOCI" Program (024.003.001); European Commission (FP7-Biodesign); German Centre for Cardiovascular Research (DZHK) and the German Ministry of Education and Research, the Freie und Hansestadt Hamburg; ZonMW (ZorgOnderzoek Nederland—Medische wetenschappen); MKMD (Meer Kennis met Minder Dieren) Applications of Innovations 2015–2016.

References

1. Catapult. (2018). State of the discovery nation 2018 and the role of the medicines discovery catapult. Available at: https://s3-eu-west-1.amazonaws.com/media.newmd.catapult/wp-content/uploads/2018/01/16220811/MDC10529-Thought-Leader_v10_Interactive_v1.pdf.

2. IFPMA. (2017). International Federation of Pharmaceutical Manufacturers and Associations. The Pharmaceutical Industry and Global Health Facts and Figure. Geneva, Switzerland. Available at: https://www.ifpma.org/wp-content/uploads/2017/02/IFPMA-Facts-And-Figures-2017.pdf.

3. Onakpoya I. J., Heneghan C. J., Aronson J. K. Post-marketing withdrawal of 462 medicinal products because of adverse drug reactions: A systematic review of the world literature. *BMC Med.* **14,** 10 (2016).

4. Fuentes A. V., Pineda M. D., Venkata K. Comprehension of top 200 prescribed drugs in the US as a resource for pharmacy teaching, training and practice. *Pharmacy* **6,** 43 (2018).

5. Shah R. R. Can pharmacogenetics help rescue drugs withdrawn from the market? *Pharmacogenomics* **7,** 889–908 (2006).

6. Food Drug Administration HHS. International Conference on Harmonisation; guidance on S7B nonclinical evaluation of the potential for delayed ventricular repolarization (QT interval prolongation) by human pharmaceuticals; availability. *Notice. Fed. Regist*. **70,** 61133–61134 (2005).

7. Food Drug Administration HHS. International Conference on Harmonisation; guidance on E14 clinical evaluation of QT/QTc interval prolongation and proarrhythmic potential for non-antiarrhythmic drugs; availability. *Notice. Fed. Regist.* **70,** 61134–61135 (2005).

8. Gintant G. An evaluation of hERG current assay performance: Translating preclinical safety studies to clinical QT prolongation. *Pharmacol. Ther.* **129,** 109–119 (2011).

9. Gintant G., Fermini B., Stockbridge N., Strauss D. The evolving roles of human iPSC-derived cardiomyocytes in drug safety and discovery. *Cell Stem Cell* **21,** 14–17 (2017).

10. Fermini B., Hancox J. C., Abi-Gerges N., Bridgland-Taylor M., Chaudhary K. W., Colatsky T., Correll K., Crumb W., Damiano B., Erdemli G., et al. A new perspective in the field of cardiac safety testing through the Comprehensive *in vitro* Proarrhythmia Assay paradigm. *J. Biomol. Screen*. **21,** 1–11 (2016).

11. Kanda Y., Yamazaki D., Osada T., Yoshinaga T., Sawada K. Development of torsadogenic risk assessment using human induced pluripotent stem cell-derived cardiomyocytes: Japan iPS cardiac safety assessment (JiCSA) update. *J. Pharmacol. Sci.* **138,** 233–239 (2018).

12. Sager P. T., Gintant G., Turner J. R., Pettit S., Stockbridge N. Rechanneling the cardiac proarrhythmia safety paradigm: A meeting report from the cardiac safety research consortium. *Am. Heart J.* **167,** 292–300 (2014).

13. Blinova K., Dang Q., Millard D., Smith G., Pierson J., Guo L., Brock M., Lu H. R., Kraushaar U., Zeng H., et al. International multisite study of human-induced pluripotent stem cell-derived cardiomyocytes for drug proarrhythmic potential assessment. *Cell Rep.* **24,** 3582–

3592 (2018).

14. Bot C. T., Juhasz K., Haeusermann F., Polonchuk L., Traebert M., Stoelzle-Feix S. Cross—Site comparison of excitation-contraction coupling using impedance and field potential recordings in hiPSC cardiomyocytes. *J. Pharmacol. Toxicol. Methods* **93,** 46–58 (2018).

15. Pointon A., Pilling J., Dorval T., Wang Y., Archer C., Pollard C. High-throughput imaging of cardiac microtissues for the assessment of cardiac contraction during drug. *Toxicol. Sci.* **155,** 444–457 (2017).

16. van Meer B. J., Krotenberg A., Sala L., Davis R. P., Eschenhagen T., Denning C., Tertoolen L. G. J., Mummery C. L. Simultaneous measurement of excitation-contraction coupling parameters identifies mechanisms underlying contractile responses of hiPSC-derived cardiomyocytes. *Nat. Commun.* **10,** 4325 (2019).

17. Mosqueira D., Mannhardt I., Bhagwan J. R., Lis-Slimak K., Katili P., Scott E., Hassan M., Prondzynski M., Harmer S. C., Tinker A., et al. CRISPR/Cas9 editing in human pluripotent stem cell-cardiomyocytes highlights arrhythmias, hypocontractility, and energy depletion as potential therapeutic targets for hypertrophic cardiomyopathy. *Eur. Heart J.* **39,** 3879–3892 (2018).

18. Smith J. G. W., Owen T., Bhagwan J. R., Mosqueira D., Scott E., Mannhardt I., Patel A., Barriales-Villa R., Monserrat L., Hansen A., et al. Isogenic pairs of hiPSC-CMs with hypertrophic cardiomyopathy/LVNC-associated ACTC1 E99K mutation unveil differential functional deficits. *Stem Cell Rep.* **11,** 1226–1243 (2018).

19. Breckwoldt K., Letuffe-Breniere D., Mannhardt I., Schulze T., Ulmer B., Werner T., Benzin A., Klampe B., Reinsch M. C., Laufer S., et al. Differentiation of cardiomyocytes and generation of human engineered heart tissue. *Nat. Protoc.* **12,** 1177–1197 (2017).

20. Sala L., van Meer B. J., Tertoolen L. G. J., Bakkers J., Bellin M., Davis R. P., Denning C., Dieben M. A. E., Eschenhagen T., Giacomelli E., et al. MUSCLEMOTION: A versatile open software tool to quantify cardiomyocyte and cardiac muscle contraction *in vitro* and *in vivo*. *Circ. Res.* **122,** e5–16 (2018).

21. Duncan G., Firth K., George V., Hoang M. D., Staniforth A., Smith G., Denning C. Drug-mediated shortening of action potentials in LQTS2 human induced pluripotent stem cell-derived cardiomyocytes. *Stem Cells Dev.* **26,** 1695–1705 (2017).

22. Mannhardt I., Breckwoldt K., Letuffe-Breniere D., Schaaf S., Schulz H., Neuber C., Benzin A., Werner T., Eder A., Schulze T., et al. Human engineered heart tissue: Analysis of contractile force. *Stem Cell Rep.* **7,** 29–42 (2016).

23. Butler L., Cros C., Oldman K. L., Harmer A. R., Pointon A., Pollard C. E., Abi-Gerges N. Enhanced characterization of contractility in cardiomyocytes during early drug safety assessment. *Toxicol. Sci.* **145,** 396–406 (2015).

24. Bois P., Bescond J., Renaudon B., Lenfant J. Mode of action of bradycardic agent, S 16257, on ionic currents of rabbit sinoatrial node cells. *Br. J. Pharmacol.* **118,** 1051–1057 (1996).

25. Malik F. I., Hartman J. J., Elias K. A., Morgan B. P., Rodriguez H., Brejc K., Anderson R. L., Sueoka S. H., Lee K. H., Finer J. T., et al. Cardiac myosin activation: A potential therapeutic approach for systolic heart failure. *Science* **331,** 1439–1443 (2011).

26. Allen D. G., Eisner D. A., Pirolo J. S.,

Smith G. L. The relationship between intracellular calcium and contraction in calcium-overloaded ferret papillary-muscles. *J. Physiol. Lond.* **364,** 169–182 (1985).

27. Hess P., Wier W. G. Excitation-contraction coupling in cardiac Purkinje-fibers—Effects of caffeine on the intracellular Ca-2+ transient, membrane currents, and contraction. *J. Gen. Physiol.* **83,** 417–433 (1984).

28. Knollmann B. C. Induced pluripotent stem cell-derived cardiomyocytes boutique science or valuable arrhythmia model? *Circ. Res.* **112,** 969–976 (2013).

29. Du D. T. M., Hellen N., Kane C., Terracciano C. Action potential morphology of human induced pluripotent stem cell-derived cardiomyocytes does not predict cardiac chamber specificity and is dependent on cell density. *Biophys. J.* **108,** 1–4 (2015).

30. Lemoine M. D., Mannhardt I., Breckwoldt K., Prondzynski M., Flenner F., Ulmer B., Hirt M. N., Neuber C., Horváth A., Kloth B., et al. Human iPSC-derived cardiomyocytes cultured in 3D engineered heart tissue show physiological upstroke velocity and sodium current density. *Sci. Rep.* **7,** 5464 (2017).

31. Lemoine M. D., Krause T., Koivumäki J. T., Prondzynski M., Schulze M. L., Girdauskas E., Willems S., Hansen A., Eschenhagen T., Christ T. Human induced pluripotent stem cell-derived engineered heart tissue as a sensitive test system for QT prolongation and arrhythmic triggers. *Circ. Arrhythm. Electrophysiol.* **11,** e006035 (2018).

32. Ulmer B. M., Stoehr A., Schulze M. L., Patel S., Gucek M., Mannhardt I., Funcke S., Murphy E., Eschenhagen T., Hansen A. Contractile work contributes to maturation of energy metabolism in hiPSC-derived cardiomyocytes. *Stem Cell Rep.* **10,** 834–847 (2018).

33. Jacob F., Yonis A. Y., Cuello F., Luther P., Schulze T., Eder A., Streichert T., Mannhardt I., Hirt M. N., Schaaf S., et al. Analysis of tyrosine kinase inhibitor-mediated decline in contractile force in rat engineered heart tissue. *PLoS One* **11,** e0145937 (2016).

34. Kim D. H., Akera T., Brody T. M. Inotropic actions of doxorubicin in isolated guinea-pig atria—Evidence for lack of involvement of Na+, K+-adenosine triphosphatase. *J. Pharmacol. Exp. Ther.* **214,** 368–374 (1980).

35. Vanboxtel C. J., Olson R. D., Boerth R. C., Oates J. A. Doxorubicin—Inotropic effects and inhibitory action on ouabain. *J. Pharmacol. Exp. Ther.* **207,** 277–283 (1978).

36. Wang Y. X., Korth M. Effects of doxorubicin on excitation-contraction coupling in guinea-pig ventricular myocardium. Circ. Res. 76, 645–653 (1995).

37. Lawrence C. L., Pollard C. E., Hammond T. G., Valentin J. P. *In vitro* models of proarrhythmia. *Br. J. Pharmacol.* **154,** 1516–1522 (2008).

38. Valentin J.-P., Bialecki R., Ewart L., Hammond T., Leishmann D., Lindgren S., Martinez V., Pollard C., Redfern W., Wallis R. A framework to assess the translation of safety pharmacology data to humans. *J. Pharmacol. Toxicol. Methods* **60,** 152–158 (2009).

39. Dahl R. A new target for Parkinson's disease: Small molecule SERCA activator CDN1163 ameliorates dyskinesia in 6-OHDA-lesioned rats. *Bioorg. Med. Chem.* **25,** 53–57 (2017).

40. Kang S., Dahl R., Hsieh W., Shin A.,

Zsebo K. M., Buettner C., Hajjar R. J., Lebeche D. Small molecular allosteric activator of the sarco/endoplasmic reticulum Ca^{2+}-ATPase (SERCA) attenuates diabetes and metabolic disorders. *J. Biol. Chem.* **291,** 5185–5198 (2016).

41. Kovacs M., Toth J., Hetenyi C., Malnasi-Csizmadia A., Sellers J. R. Mechanism of blebbistatin inhibition of myosin II. *J. Biol. Chem.* **279,** 35557–35563 (2004).

42. Huupponen R. Adverse cardiovascular effects of sulfonylurea drugs clinical-significance. Med. Toxicol. 2, 190–209 (1987).

43. Ignjatovic T., Tan F. L., Brovkovych V., Skidgel R. A., Erdos E. G. Activation of bradykinin B-1 receptor by ACE inhibitors. *Int. Immunopharmacol.* **2,** 1787–1793 (2002).

44. Wallis R., Gharanei M., Maddock H. Predictivity of *in vitro* non-clinical cardiac contractility assays for inotropic effects in humans—A literature search. *J. Pharmacol. Toxicol. Methods* **75,** 62–69 (2015).

45. Rosen M. R., Gelband H., Hoffman B. F. Effects of phentolamine on electrophysiologic properties of isolated canine purkinje fibers. *J. Pharmacol. Exp. Ther.* **179,** 586–593 (1971).

46. Sada H. Effect of phentolamine, alprenolol and prenylamine on maximum rate of rise of action potential in guinea-pig papillary-muscles. *Naunyn Schmiedebergs Arch. Pharmacol.* **304,** 191–201 (1978).

47. Choi H. Y., Bae K.-S., Cho S.-H., Ghim J.-L., Choe S., Jung J. A., Lim H.-S. Population plasma and urine pharmacokinetics of ivabradine and its active metabolite S18982 in healthy Korean volunteers. *J. Clin. Pharmacol.* **56,** 439–449 (2016).

48. Forsberg T., Lindbom L. O. . Cardiovascular effects of zimelidine and tricyclic anti-depressants in conscious rats. *Acta Pharmacol. Toxicol.* **53,** 223–229 (2009).

49. Lindbom L. O., Forsberg T. Cardiovascular effects of zimelidine and other antidepressant in conscious rats. *Acta Psychiatr. Scand. Suppl.* **63,** 380–384 (1981).

50. Naranjo C. A., Sellers E. M., Kaplan H. L., Hamilton C., Khouw V. Acute kinetic and dynamic interactions of zimelidine with ethanol. *Clin. Pharmacol. Ther.* **36,** 654–660 (1984).

51. Eder A., Vollert I., Hansen A., Eschenhagen T. Human engineered heart tissue as a model system for drug testing. *Adv. Drug Deliv. Rev.* **96,** 214–224 (2016).

52. Uzun A. U., Mannhardt I., Breckwoldt K., Horvath A., Johannsen S. S., Hansen A., Eschenhagen T., Christ T. Ca^{2+}-currents in human induced pluripotent stem cell-derived cardiomyocytes effects of two different culture conditions. *Front. Pharmacol.* **7,** 300 (2016).

53. Zhao Y., Rafatian N., Feric N. T., Cox B. J., Aschar-Sobbi R., Wang E. Y., Aggarwal P., Zhang B., Conant G., Ronaldson-Bouchard K., et al. A platform for generation of chamber-specific cardiac tissues and disease modeling. *Cell* **176,** 913–927.e18 (2019).

54. Guth B. D., Chiang A. Y., Doyle J., Engwall M. J., Guillon J.-M., Hoffmann P., Koerner J., Mittelstadt S., Ottinger S., Pierson J. B., et al. The evaluation of drug-induced changes in cardiac inotropy in dogs: Results from a HESI-sponsored consortium. *J. Pharmacol. Toxicol. Methods* **75,** 70–90 (2015).

55. Kaumann A. J., Blinks J. R. Stimulant and depressant effects of beta-adrenoceptor blocking-agents on isolated heart-muscle—A positive inotropic effect not mediated through adrenoceptors. *Naunyn Schmiedebergs Arch. Pharmacol.* **311,** 205–218 (1980).

56. Lemoine H., Schonell H., Kaumann A. J. Contribution of beta-1-adrenoceptors and beta-2-adrenoceptors of human atrium and ventricle to the effects of noradrenaline and adrenaline as assessed with (–)-atenolol. *Br. J. Pharmacol.* **95,** 55–66 (1988).

57. Jarrott B., Louis W. J., Summers R. J. Characteristics of clonidine-H-3 binding to an alpha-adrenoceptor in membranes from guinea-pig kidney. *Br. J. Pharmacol.* **65,** 663–670 (1979).

58. Kleiber N., Mathot R. A. A., Ahsman M. J., Wildschut E. D., Tibboel D., de Wildt S. N. Population pharmacokinetics of intravenous clonidine for sedation during paediatric extracorporeal membrane oxygenation and continuous venovenous hemofiltration. *Br. J. Clin. Pharmacol.* **83,** 1227–1239 (2017).

59. Li R. A., Keung W., Cashman T. J., Backeris P. C., Johnson B. V., Bardot E. S., Wong A. O. T., Chan P. K. W., Chan C. W. Y., Costa K. D. Bioengineering an electro-mechanically functional miniature ventricular heart chamber from human pluripotent stem cells. *Biomaterials* **163,** 116–127 (2018).

Supplementary information

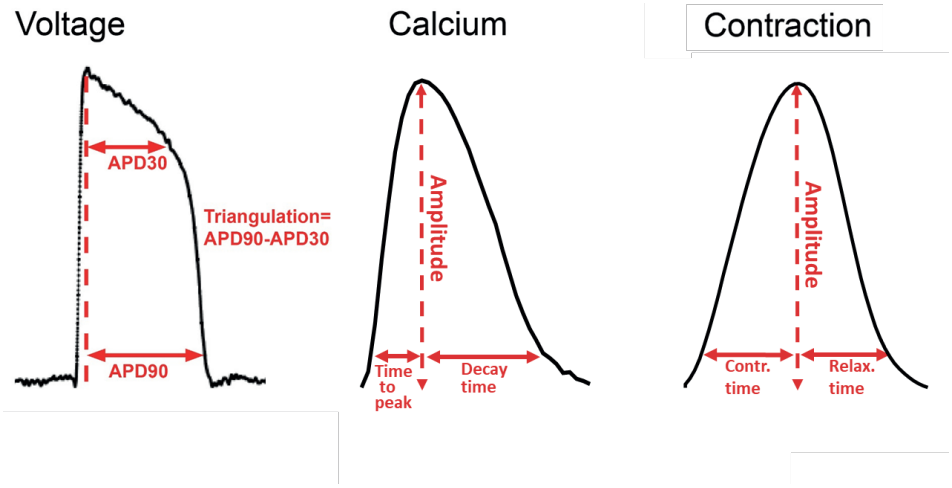

Supplementary Figure 1: Schematic description of the parameters used to quantify drug effect in hiPSC-CMs.

Data were calculated using the *MUSCLEMOTION* algorithm. APD, action potential duration.

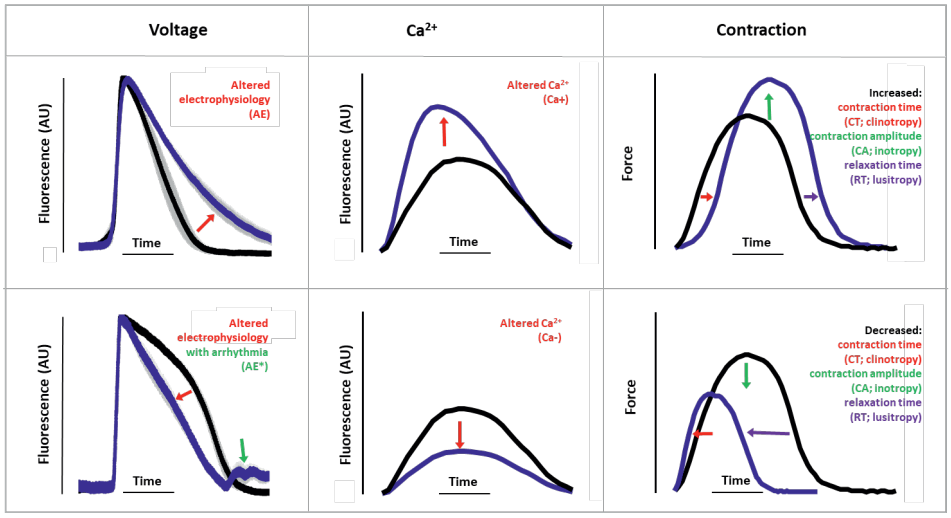

Supplementary Figure 2: Terminology used in evaluation of responses.

Black traces are baseline readings, while blue are after treatment. The colour of the arrows and text matches to indicate the type of change occurring.

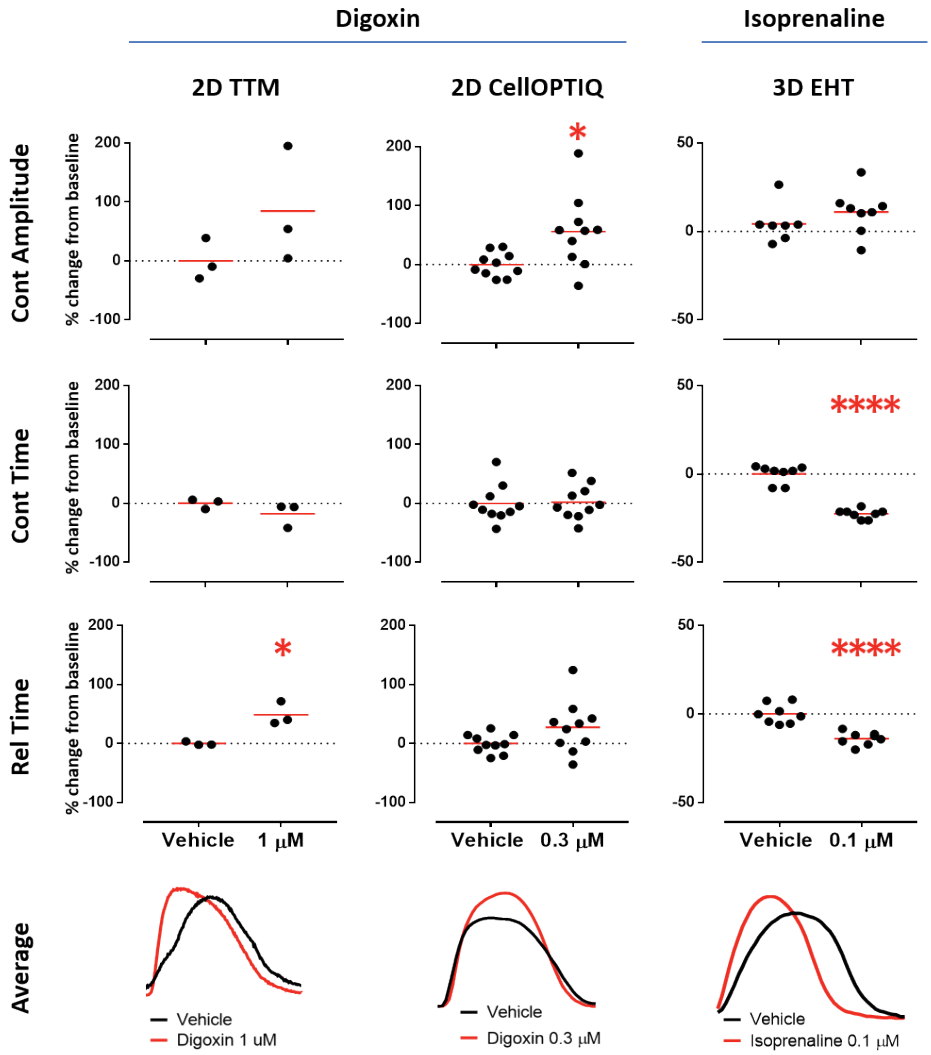

Supplementary Figure 3: Training sets to unify drug testing procedures.

Representative contractility data are shown for positive (digoxin, 2D; isoprenaline, 3D) and negative (nifedipine 2D, 3D) inotropes evaluated in hiPSC-CMs using the TTM (Triple Transient Measurement), CellOPTIQ® and EHT (engineered heart tissue) platforms. The percentage change in drug treated samples is relative to their respective vehicle control. Unpaired T-test. * p<0.05; ** p<0.01; *** p<0.001; **** p<0.0001.

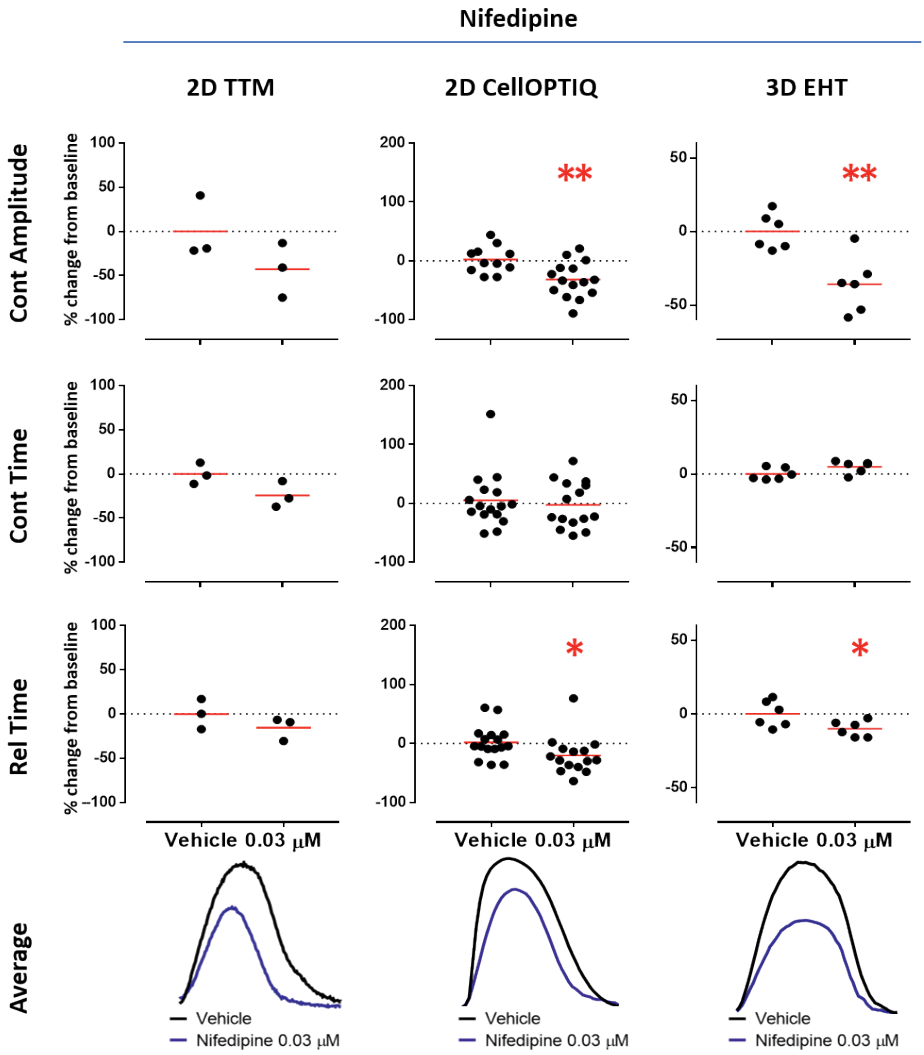
Nifedipine
2D TTM
2D CellOPTIQ
3D EHT
Cont Amplitude
Cont Time
Rel Time
Average
% change from baseline
**
*
Vehicle 0.03 μM
Vehicle
Nifedipine 0.03 μM

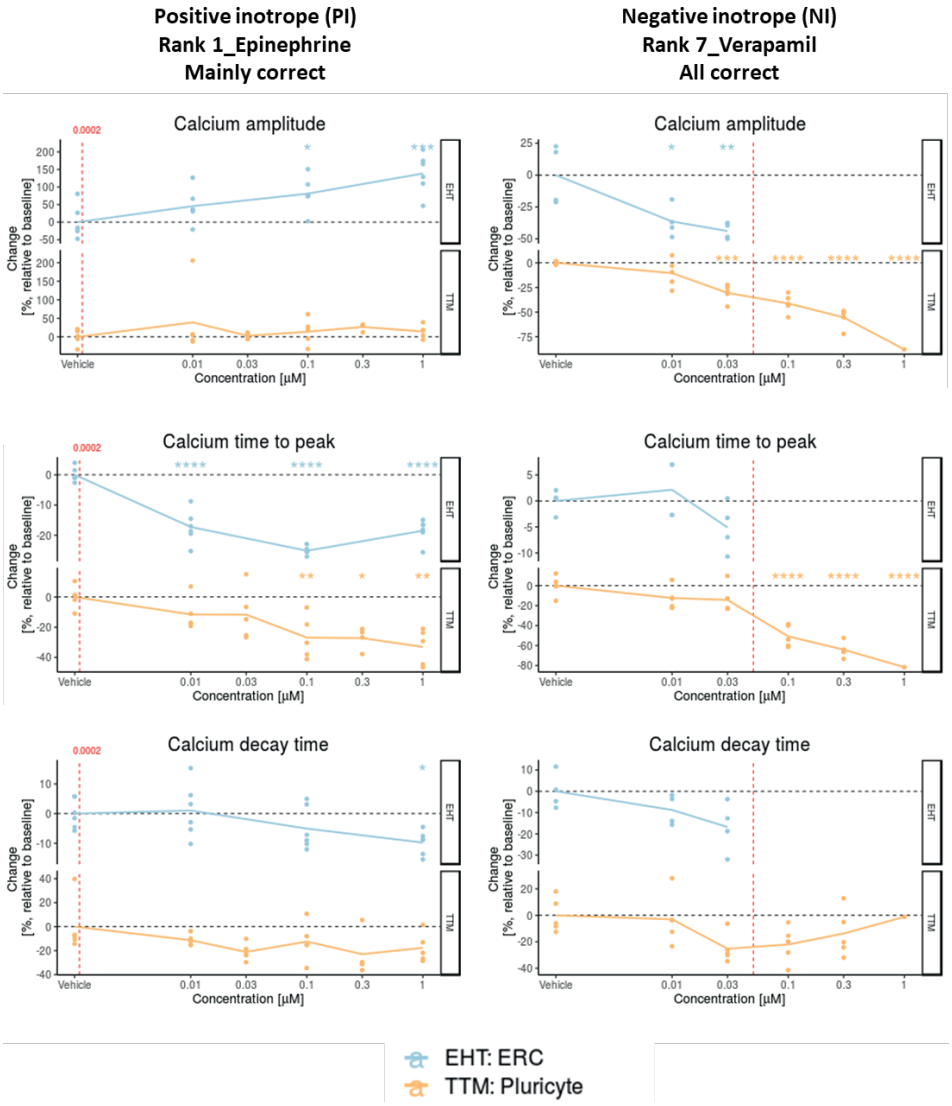

Supplementary Figure 4A: Role of Ca^{2+} analysis in prediction of inotropic response.

In some instances, Ca^{2+} transient analysis was used to guide prediction of whether a compound had a positive or negative inotropic effect. Red dotted line is free therapeutic plasma concentration (FTPC). Mainly correct: correct in most platform-cell combinations (Figure 1A), All correct: correct in all platform-cell combinations (Figure 1B). Dunnett's stats vs vehicle control: *, P<0.05; **, P<0.01; ***, P<0.001; ****, P<0.0001.

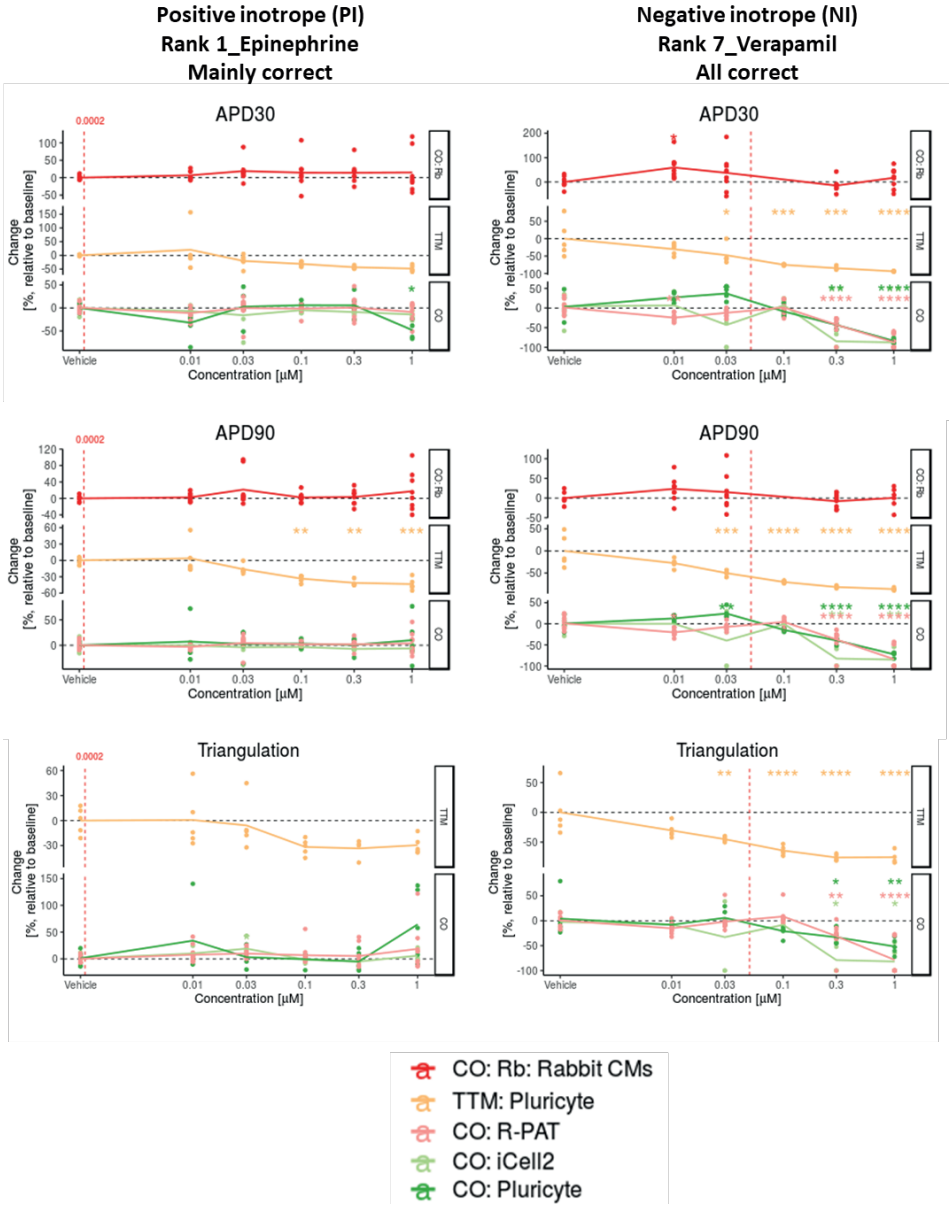

Supplementary Figure 4B: Role of voltage analysis in prediction of inotropic response.

In some instances, voltage transient analysis was used to guide prediction of whether a compound had a positive or negative inotropic effect. Red dotted line is free therapeutic plasma concentration (FTPC). Dunnett's stats vs vehicle control: *, P<0.05; **, P<0.01; ***, P<0.001; ****, P<0.0001.a

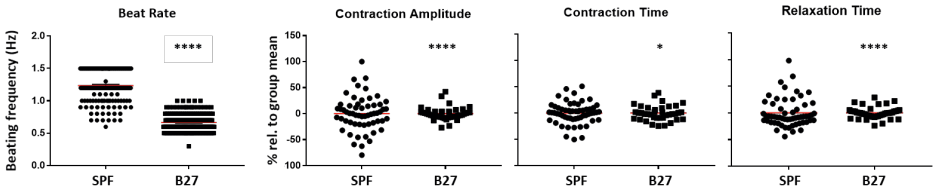

Supplementary Figure 5: Serum/protein-free medium increases spontaneous beating rates and data distribution.

Using the CO:R-PAT platform-cell combination, recordings were evaluated in hiPSC-CMs cultured as 2D monolayers in serum-/protein-free medium (SPF) versus the protein-containing medium, RPMI-B27 (B27). Culture in SPF significantly increased spontaneous beating rates (P≤ 0.0001, Mann Whitney), and increased variance of data distribution for CA, CT and RT (P≤ 0.0001, 0.05 and 0.0001, respectively; F-test for variance).

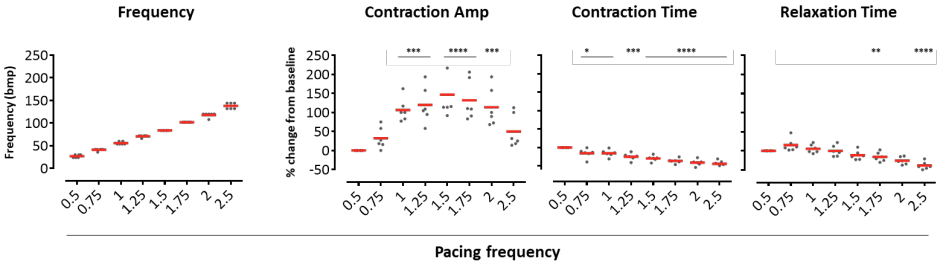

Supplementary Figure 6: Positive force frequency relationship in EHTs paced between 0.5 and 1.5 Hz.

Spontaneous beat rate of EHTs was reduced by 3 hour pre-treatment with 300 nM ivabradine, an If current inhibitor. Subsequent electrical pacing showed beating frequencies that followed the frequency of the stimulus. CA increased from 0.5 to 1.5 Hz but plateaued and declined at higher frequencies. These changes were reflected in the CT and RT data. Dunnett's stats vs vehicle control: *, P<0.05; **, P<0.01; ***, P<0.001; ****, P<0.0001.

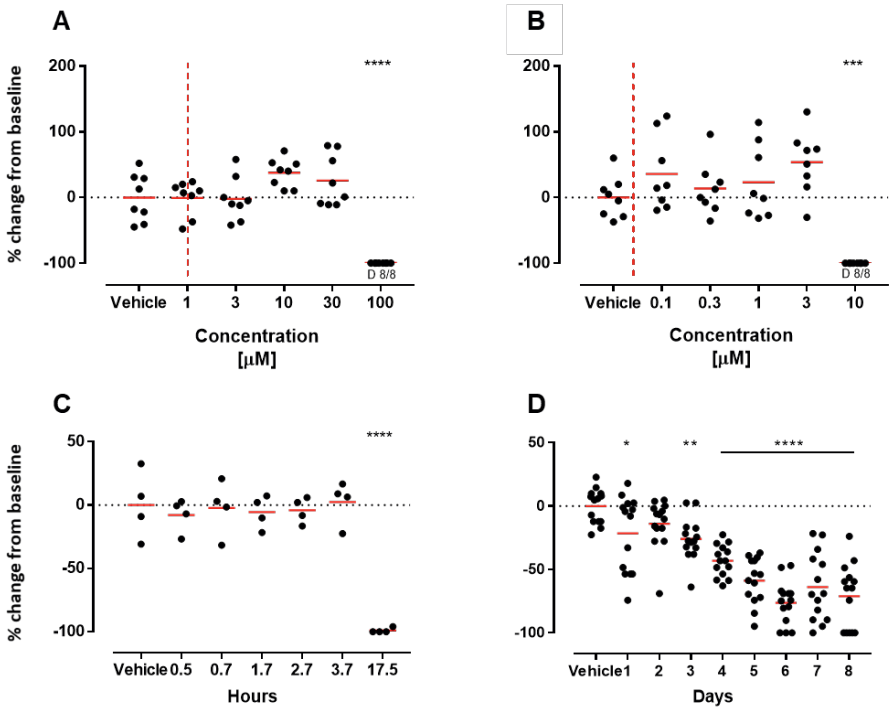

Supplementary Figure 7: Prolonged exposure detects NIs in 2D and 3D cultures of hiPSC-CMs.

Contraction amplitude (CA) was measured in the CO:R-PAT platform-cell combination exposed to various concentrations of doxorubicin (A) or sunitinib (B) for 24 hours, with the highest test concentration causing cell death. Red dotted line is free therapeutic plasma concentration (FTPC). The EHT:ERC platform-cell combination was exposed to 100 µM doxorubicin (C) or 1 µM sunitinib (D) for up to 17.5 hr (C) or up to 8 days (D). CA is shown normalized to time controls. Dunnett's stats vs vehicle control: *, P<0.05; **, P<0.01; ***, P<0.001; ****, P<0.0001.

Supplementary Table 1: Compound selection within the CRACK-IT study.

Eight training, non-blinded "Tier 1 (T1) training set" compounds with known positive or negative inotropic effects were selected to standardise the working practices across the platform-cell combinations within the study. Twenty eight "Tier 2 (T2) test set" compounds were chosen for the blinded phase of the study, of which 18 were positive inotropes (PI) or negative inotropes (NI) and span the main modes of action known to alter contractility responses of cardiomyocytes. The remainder were considered as no effect drugs (NE, no effect on cardiac contractility). A 5 x ½ log range was chosen based on the literature and/or free therapeutic plasma concentration (FTPC). Abbreviations: n.d, not defined; n.a, not applicable; PC, positive chronotropy; PI, positive inotropy; PCl, positive clinotropy; PL, positive lusitropy; NC, negative chronotropy; NI, negative inotropy; NCl, negative clinotropy; NL, negative lusitropy; inotropy is defined as change in peak force, clinotropy as change in time-to-peak force (generally from 20% above baseline to peak and "positive" being an abbreviation) and lusitropy as change in relaxation time (time from peak force generally to 80% relaxation and "positive" being an abbreviation); EC_{50}, half maximal effective concentration; IC_{50}, half maximal effective inhibitory concentration; GP, guinea pig; hERG, human eag-related gene; NCX, Na^+/Ca^{2+} exchanger; RR, blood pressure; RyR2, ryanodine receptor 2; SR, sarcoplasmic reticulum; * indicates lack of clarity in literature on inotropic effect; # in spontaneously contracting preparations.

Drug	Use	PI, NI, NE	Main mechanism of action	Expected cardiac effects in vivo	Expected effect on contractility in isolated cardiomyocytes/ heart muscles	Cellular mechanism of inotropic effect	Concentration range applied (μM)	FTPC (μM)	Refs
Isoprenaline	T1	PI	β1- and β2-adrenoceptor agonist	PI, PC	PI, PC#, PCl, PL EC_{50} 0.01 μM	Increase in cAMP, Ca^{2+} influx, SR Ca^{2+} uptake and SR load	0.0003-0.1	0.0095	(Reyes et al. 1993)
Digoxin	T1	PI	Na^+/K^+ ATPase inhibitor	PI, arrhythmias	PI+ PL (< 1 μM, slowly developing, $t_{1/2}$ conc.-dependent) NI + diast. shortening (>1 μM)	Na^+/K^+ inhibition, Ca^{2+} increase via NCX	0.01-10	0.00075-0.0015	(Lullmann and Ravens 1973)
Bay K 8644	T1	PI	L-type Ca^{2+} channel agonist	PI (indirect NC because of RR increase)	PI, NL	Increase in Ca^{2+} influx	0.03-3	n.d.	(Aass et al. 1988)

EMD 57033	T1	PI	Calcium sensitizer	PI	PI, NL, EC_{50} ~5 μM, diastolic shortening at high conc.	Myofilament sensitization to Ca^{2+}	0.01-30	16 μM	(Hajjar et al. 1997), (de Zeeuw et al. 2000)
Caffeine	T1	PI	Opener of RyR2 (at high concentration)	PI or NI o NE	Small PI and PL at 100 μM, transient large PI, NL at >10 mM	Opening of RyR2	100-10,000	20-40	(Chaban et al. 2017)
Nifedipine	T1	NI	L-type Ca^{2+} channel blocker (dihydropyridine)	Small NI (direct) overridden by adrenergic activation, PC (indirect)	NI, IC_{50} 0.1 μM	Decreased Ca^{2+} influx	0.003-0.3	0.02	(Angus et al. 2000)
Ryanodine	T1	NI	Inhibitor of RyR2	n.d.	NI, NCl, species dependent biphasic, IC_{50} ~0.01 μM	Decreased SR Ca^{2+} release	1-30	n.d.	(Sutko and Willerson 1980), (Fedorov et al. 2002)
Thapsigargin	T1	NI	Inhibitor of SR Ca^{2+} ATPase	n.d.	Heart muscle: NI ~50% at 500 μM, NL ~20% at 500 μM Isolated myocytes: ~90% NI at 0.1 μM	Decreased SR Ca^{2+} uptake and load	0.3-30	n.d.	(Kirby et al. 1992), (Baudet et al. 1993)
Epinephrine	T2	PI	Non-selective α1-, β1- and β2-adrenoceptor agonist	PI, PC	PI, PC#, PCl, PL EC_{50} 0.1 μM	Increase in cAMP, Ca^{2+} influx, SR Ca^{2+} uptake and SR load	0.01 - 1	0.0002-0.050	(Molenaar et al. 2007), (Wortsman et al. 1984)
Forskolin	T2	PI	Adenylyl cyclase stimulator	PI, PC	PI, PC#, PCl, PL EC_{50} 5-10 μM	Increase in cAMP, Ca^{2+} influx, SR Ca^{2+} uptake and SR load	0.1 - 10	0.012-0.024 (colforsin)	(Bristow et al. 1984), (Kikura et al. 2004)

Levosimendan	T2	PI	PDE3 inhibitor (IC_{50} 25 nM) Calcium sensitizer K_{ATP} channel agonist	PI, PC (more heart rate increase and RR decrease than dobutamine)	Small PI (~50%), PC#, PCl+PL (14%), EC_{50} ~0.1 µM	Increase in cAMP and myofilament sensitization to Ca^{2+}	0.01 - 1	0.026-0.35	(Boknik et al. 1997), (Hasenfuss et al. 1998), (Mebazaa et al. 2007), (Papp et al. 2012), (Orstavik et al. 2014), (Abi-Gerges et al. 2013), (Puttonen et al. 2008)
Pimobendan	T2	PI	Calcium sensitizer PDE inhibitor (partial)	PI, small PC	PI, small PC#, PL and NL at low/high conc., EC_{50} 34 µM	Increase in cAMP and myofilament sensitization to Ca^{2+}	1 - 100	0.005-0.01	(Honerjager et al. 1984), (Berger et al. 1985), (Chu et al. 1995)
Dobutamine	T2	PI	α1-, β1- and β2 adrenoceptor agonist	PI, PC, less HR-stimulation than epinephrine	PI, PC#, PCl, PL. EC_{50} 1-3 µM	Increase in cAMP, Ca^{2+} influx, SR Ca^{2+} uptake and SR load	0.1 - 10	0.07-1	(Ishihata et al. 1988), (Brown et al. 1987), (Mahoney et al. 2016)
Milrinone	T2	PI	PDE3 inhibitor	PI, PC (more heart rate increase and RR decrease than dobutamine)	Small PI, PC#, PCl, PL (smaller than ISO) EC_{50} 60 µM	Increase in cAMP, Ca^{2+} influx, SR Ca^{2+} uptake and SR load	1-100	0.1-0.15	(Brown et al. 1986), (Bailey et al. 1994)
Omecamtiv mecarbil	T2	PI	Cardiac specific myosin activator	PI, prolonged syst. ejection time, small decrease in heart rate	PI, NCl, NL, diastolic shortening (dog myocytes). EC_{50} 1 µM	Increased number of myosin heads binding to actin, no affection of Ca^{2+} transient	0.01 - 1	0.05 -0.42	(Cleland et al. 2011), (Planelles-Herrero et al. 2017), (Horvath et al. 2017), (Teerlink et al. 2011), (Liu et al. 2016)

Terbutaline	T2	PI	β2-adrenoceptor agonist	Small PI and PC	PI, PC#, PCl, PL. EC_{50} 3 μM	Increase in cAMP, Ca^{2+} influx, SR Ca^{2+} uptake and SR load	0.1 - 10	1.3	(Schafers et al. 1994), (Dyreborg et al. 2016)
Verapamil	T2	NI	L-type Ca^{2+} channel blocker, hERG blocker	NI (direct) partially masked by adrenergic activation (indirect), NC or none, ND (direct)	NI, IC_{50} 0.1 μM	Decreased Ca^{2+} influx	0.01 - 1	0.05	(Angus et al. 2000), (Giacomini et al. 1984)
Doxorubicin	T2	NI	Impairs Ca^{2+} transport mechanisms in sarcoplasmic reticulum	NI, time course of cardiotox dose-dependent	PI+NCl and reduced post-rest potentiation at 30 μM (GP), but strong NI at 1000 μM (GP, rat); rate-dependent	Complex, including increased mitochondrial ROS	0.1 - 10	1-2	(Temma et al. 1993), (Hofling and Bolte 1981), (Matsushita et al. 2000), (Danesi et al. 1999)
Sunitinib	T2	NI	Multi-targeted TK inhibitor	NI, NC at high doses, chronic cardiotox	NI, IC_{50} 10 μM	Complex	0.1 - 10	0.003	(Mooney et al. 2015), (Abi-Gerges et al. 2013), (Bello et al. 2006)
Citalopram	T2	NI	SSR inhibitor, hERG & L-type Ca^{2+} channel inhibitor	None (at therapeutic doses), higher risk of TdP	NI at 30 μM (-57% in hEHT, -38% in human atria)	Decrease in Ca^{2+} influx	1 - 100	0.05	(Witchel et al. 2002), (Mannhardt et al. 2017), (Rao 2007)
Itraconazole	T2	NI	Triazole antifungal, inhibitor of Na^{+} channels and mitochondrial voltage-dependent anion channel 1	NI	NI (-30% at 0.3 μM; rabbit heart)	Decreased Na^{+} influx (?)	0.1 - 10	0.00086 (higher in tissues)	(Head et al. 2015), (Qu et al. 2013), (Bellmann 2007)

Sorafenib	T2	NI	Multi-targeted kinase inhibitor	None or NI at high doses, delayed cardiotox	None (feline and canine CM, but cell death), NI (rat heart)	n.d.	0.1 - 10	0.03 (higher tissue levels)	(Henderson et al. 2013), (Duran et al. 2014), (Abi-Gerges et al. 2013), (Kim et al. 2013)
Ivabradine*	T2	NI	I_f inhibitor	NC (therapeutic)	None, NC at >10 µM (spontaneously beating preps), NIE (-13/-60% in guinea pig atria/PM, -38% human trabeculae at 100 µM); PI in mouse left atria and 30% of human trabeculae	Decrease in Ca^{2+} transient peak	0.1 - 10	0.01-0.1	(Perez et al. 1995), (Boldt et al. 2010), (Bois et al. 1996), (Mesirca et al. 2014), (Choi et al. 2016)
Flecainide	T2	NI	Na^+ channel blocker, hERG blocker	NI	NI, IC_{50} 0.3 µM	Decreased Na^+ influx (?)	0.1 - 10	0.2-0.4	(Abi-Gerges et al. 2013), (McQuinn et al. 1988)
Phentolamine	T2	NI	Non-selective α adrenoceptor antagonist, Na^+ and Ca^{2+} channel blocker at high conc.	PC (indirect)	NI, IC_{50} ~20 µM	Decreased Na^+ and Ca^{2+} influx	1-100	2.25	(Sada 1978), (Rosen et al. 1971)
Zimelidine*	T2	NI	SSR inhibitor	None (at ther. doses), QT and QRS widening at high doses	n.d.	n.d.	1 - 100	0.78	(Lindbom and Forsberg 1981), (Forsberg and Lindbom 1983), (Naranjo et al. 1984)
Acetylsalicylic acid	T2	NE	Cyclooxygenase inhibitor	None	None	n.a.	1 - 100	0.3-2	(Abi-Gerges et al. 2013)
Atenolol	T2	NE	β1>β2 adrenoceptor antagonist	NI, NC, ND	None (in absence of agonist) until 3000 µM (in contrast to e.g. propranolol)	n.a.	0.1 - 10	1	(Lemoine et al. 1988), (Kaumann and Blinks 1980)

Captopril	T2	NE	ACE inhibitor	None	None	n.a.	1-100	1-2	(Abi-Gerges et al. 2013), (Giudicelli et al. 1987)
Glibenclamide	T2	NE	K_{ATP} channel antagonist	None or PI in ischemia	None; PI in ischemia or presence of K_{ATP} opener; NI in adrenalectomized dogs, NE in isolated dog heart trabeculae	n.a.	0.1 - 10	0.02-0.06	(Satoh et al. 1990), (Murakami et al. 1992), (Pogatsa and Dubecz 1977), (Rydberg et al. 1997)
Enalaprilat	T2	NE	ACE inhibitor	None	None	n.a.	1 - 100	0.12	(Stage et al. 2017)
Clonidine	T2	NE	α2-adrenoceptor agonist	NI, NC	None	n.a.	0.01 - 1	0.002-0.004	(Jarrott et al. 1979), (Kleiber et al. 2017)
Paracetamol	T2	NE	Prostaglandin synthesis inhibitor	None	None	n.a.	10 - 1000	50	(Marks et al. 2012), (Kamali et al. 1993), (Brown et al. 1992)
Tolbutamide	T2	NE*	K_{ATP} channel antagonist, weak adenylyl cyclase stimulator	None or PI (dogs, men)	None (canine CM) or small PI (rabbit atria, rat heart), EC_{50} ~30 µM	Increase in cAMP (?)	1 - 100	20-30	(Levey et al. 1971), (Lasseter et al. 1972), (Abi-Gerges et al. 2013), (Whiting et al. 1981)
Pravastatin	T2	NE	HMG CoA reductase inhibitor	None	None	n.a.	1 - 100	0.018	(Costantine et al. 2016)
Sildenafil	T2	NE	PDE5 Inhibitor	None or PI+PC (indirect)	None	n.a.	0.3 - 30	0.02	(Sugiyama et al. 2001), (Walker et al. 1999)

Aass H, Skomedal T, Osnes JB. 1988. Increase of cyclic amp in subcellular fractions of rat heart muscle after beta-adrenergic stimulation: Prenalterol and isoprenaline caused different distribution of bound cyclic amp. J Mol Cell Cardiol. 20(9):847-860.

Abi-Gerges N, Pointon A, Pullen GF, Morton MJ, Oldman KL, Armstrong D, Valentin JP, Pollard CE. 2013. Preservation of cardiomyocytes from the adult heart. J Mol Cell Cardiol. 64:108-119.

Angus JA, Sarsero D, Fujiwara T, Molenaar P, Xi Q. 2000. Quantitative analysis of vascular to cardiac selectivity of l- and t-type voltage-operated calcium channel antagonists in human tissues. Clin Exp Pharmacol Physiol. 27(12):1019-1021.

Bailey JM, Levy JH, Kikura M, Szlam F, Hug CC, Jr. 1994. Pharmacokinetics of intravenous milrinone in patients undergoing cardiac surgery. Anesthesiology. 81(3):616-622.

Baudet S, Shaoulian R, Bers DM. 1993. Effects of thapsigargin and cyclopiazonic acid on twitch force and sarcoplasmic reticulum ca2+ content of rabbit ventricular muscle. Circ Res. 73(5):813-819.

Bellmann R. 2007. Clinical pharmacokinetics of systemically administered antimycotics. Curr Clin Pharmacol. 2(1):37-58.

Bello CL, Sherman L, Zhou J, Verkh L, Smeraglia J, Mount J, Klamerus KJ. 2006. Effect of food on the pharmacokinetics of sunitinib malate (su11248), a multi-targeted receptor tyrosine kinase inhibitor: Results from a phase i study in healthy subjects. Anticancer Drugs. 17(3):353-358.

Berger C, Meyer W, Scholz H, Starbatty J. 1985. Effects of the benzimidazole derivatives pimobendan and 2-(4-hydroxy-phenyl)-5-(5-methyl-3-oxo-4,5-dihydro-2h-6- pyridazinyl) benzimidazole . Hcl on phosphodiesterase activity and force of contraction in guinea-pig hearts. Arzneimittelforschung. 35(11):1668-1673.

Bois P, Bescond J, Renaudon B, Lenfant J. 1996. Mode of action of bradycardic agent, s 16257, on ionic currents of rabbit sinoatrial node cells. British journal of pharmacology. 118(4):1051-1057.

Boknik P, Neumann J, Kaspareit G, Schmitz W, Scholz H, Vahlensieck U, Zimmermann N. 1997. Mechanisms of the contractile effects of levosimendan in the mammalian heart. J Pharmacol Exp Ther. 280(1):277-283.

Boldt A, Gergs U, Ponicke K, Simm A, Silber RE, Neumann J. 2010. Inotropic effects of ivabradine in the mammalian heart. Pharmacology. 86(5-6):249-258.

Bristow MR, Ginsburg R, Strosberg A, Montgomery W, Minobe W. 1984. Pharmacology and inotropic potential of forskolin in the human heart. J Clin Invest. 74(1):212-223.

Brown L, Nabauer M, Erdmann E. 1986. The positive inotropic response to milrinone in isolated human and guinea pig myocardium. Naunyn-Schmiedeberg's archives of pharmacology. 334(2):196-201.

Brown L, Nabauer M, Erdmann E. 1987. Dobutamine: Positive inotropy by nonselective adrenoceptor agonism in isolated guinea pig and human myocardium. Naunyn Schmiedebergs Arch Pharmacol. 335(4):385-390.

Brown RD, Wilson JT, Kearns GL, Eichler VF, Johnson VA, Bertrand KM. 1992. Single-dose pharmacokinetics of ibuprofen and acetaminophen in febrile children. Journal of clinical pharmacology. 32(3):231-241.

Chaban R, Kornberger A, Branski N, Buschmann K, Stumpf N, Beiras-Fernandez A, Vahl CF. 2017. In-vitro examination of the positive inotropic effect of caffeine and taurine, the two most frequent active ingredients of energy drinks. BMC cardiovascular disorders. 17(1):220.

Choi HY, Bae KS, Cho SH, Ghim JL, Choe S, Jung JA, Lim HS. 2016. Population plasma and urine pharmacokinetics of ivabradine and its active metabolite s18982 in healthy korean volunteers. Journal of clinical pharmacology. 56(4):439-449.

Chu KM, Shieh SM, Hu OY. 1995. Pharmacokinetics and pharmacodynamics of enantiomers of pimobendan in patients with dilated cardiomyopathy and congestive heart failure after single and repeated oral dosing. Clin Pharmacol Ther. 57(6):610-621.

Cleland JG, Teerlink JR, Senior R, Nifontov EM, Mc Murray JJ, Lang CC, Tsyrlin VA, Greenberg BH, Mayet J, Francis DP et al. 2011. The effects of the cardiac myosin activator, omecamtiv mecarbil, on cardiac function in systolic heart failure: A double-blind, placebo-controlled, crossover, dose-ranging phase 2 trial. Lancet. 378(9792):676-683.

Costantine MM, Cleary K, Hebert MF, Ahmed MS, Brown LM, Ren Z, Easterling TR, Haas DM, Haneline LS, Caritis SN et al. 2016. Safety and pharmacokinetics of pravastatin used for the prevention of preeclampsia in high-risk pregnant women: A pilot randomized controlled trial. Am J Obstet Gynecol. 214(6):720 e721-720 e717.

Danesi R, Conte PF, Del Tacca M. 1999. Pharmacokinetic optimisation of treatment schedules for anthracyclines and paclitaxel in patients with cancer. Clinical pharmacokinetics. 37(3):195-211.

de Zeeuw S, Trines SA, Krams R, Duncker DJ, Verdouw PD. 2000. *In vivo* evidence that emd 57033 restores myocardial responsiveness to intracoronary ca(2+) in stunned myocardium. European journal of pharmacology. 403(1-2):99-109.

Duran JM, Makarewich CA, Trappanese D, Gross P, Husain S, Dunn J, Lal H, Sharp TE, Starosta T, Vagnozzi RJ et al. 2014. Sorafenib cardiotoxicity increases mortality after myocardial infarction. Circ Res. 114(11):1700-1712.

Dyreborg A, Krogh N, Backer V, Rzeppa S, Hemmersbach P, Hostrup M. 2016. Pharmacokinetics of oral and inhaled terbutaline after exercise in trained men. Front Pharmacol. 7:150.

Fedorov VV, Sharifov OF, Piatakova OP, Beloshapko GG, Iushmanova AV, Rozenshtraukh LV. 2002. [effects of ryanodine receptors block on spontaneous initiation of atrial fibrillation in the intact canine heart]. Kardiologiia. 42(2):59-71.

Forsberg T, Lindbom LO. 1983. Cardiovascular effects of zimelidine and tricyclic antidepressants in conscious rats. Acta Pharmacol Toxicol (Copenh). 53(3):223-229.

Giacomini KM, Massoud N, Wong FM, Giacomini JC. 1984. Decreased binding of verapamil to plasma proteins in patients with liver disease. J Cardiovasc Pharmacol. 6(5):924-928.

Giudicelli JF, Richer C, Mattei A. 1987. Pharmacokinetics and biological effects of captopril and hydrochlorothiazide after acute and chronic administration either alone or in combination in hypertensive patients. British journal of clinical pharmacology. 23 Suppl 1:51S-63S.

Hajjar RJ, DiSalvo TG, Schmidt U, Thaiyananthan G, Semigran MJ, Dec GW, Gwathmey JK. 1997. Clinical correlates of the myocardial force-frequency relationship in patients with end-stage heart failure. The Journal of heart and lung transplantation : the official publication of the International Society for Heart Transplantation. 16(11):1157-1167.

Hasenfuss G, Pieske B, Castell M, Kretschmann B, Maier LS, Just H. 1998. Influence of the novel inotropic agent levosimendan on isometric tension and calcium cycling in failing human myocardium. Circulation. 98(20):2141-2147.

Head SA, Shi W, Zhao L, Gorshkov K, Pasunooti K, Chen Y, Deng Z, Li RJ, Shim JS, Tan W et al. 2015. Antifungal drug itraconazole targets vdac1 to modulate the ampk/mtor signaling

axis in endothelial cells. Proc Natl Acad Sci U S A. 112(52):E7276-7285.
Henderson KA, Borders RB, Ross JB, Huwar TB, Travis CO, Wood BJ, Ma ZXJ, Hong SP, Vinci TM, Roche BM. 2013. Effects of tyrosine kinase inhibitors on rat isolated heart function and protein biomarkers indicative of toxicity. Journal of Pharmacological and Toxicological Methods. 68(1):150-159.
Hofling B, Bolte HD. 1981. Acute negative inotropic effect of adriamycin (doxorubicin). Naunyn-Schmiedeberg's archives of pharmacology. 317(3):252-256.
Honerjager P, Heiss A, Schafer-Korting M, Schonsteiner G, Reiter M. 1984. Ud-cg 115--a cardiotonic pyridazinone which elevates cyclic amp and prolongs the action potential in guinea-pig papillary muscle. Naunyn-Schmiedeberg's archives of pharmacology. 325(3):259-269.
Horvath B, Szentandrassy N, Veress R, Almassy J, Magyar J, Banyasz T, Toth A, Papp Z, Nanasi PP. 2017. Frequency-dependent effects of omecamtiv mecarbil on cell shortening of isolated canine ventricular cardiomyocytes. Naunyn Schmiedebergs Arch Pharmacol. 390(12):1239-1246.
Ishihata A, Kushida H, Endoh M. 1988. Enantiomers of dobutamine increase the force of contraction via beta adrenoceptors, but antagonize competitively the positive inotropic effect mediated by alpha-1 adrenoceptors in the rabbit ventricular myocardium. J Pharmacol Exp Ther. 246(3):1080-1087.
Jarrott B, Louis WJ, Summers RJ. 1979. The characteristics of [3h]-clonidine binding to an alpha-adrenoceptor in membranes from guinea-pig kidney. British journal of pharmacology. 65(4):663-670.
Kamali F, Thomas SH, Ferner RE. 1993. Paracetamol elimination in patients with non-insulin dependent diabetes mellitus. British journal of clinical pharmacology. 35(1):58-61.
Kaumann AJ, Blinks JR. 1980. Stimulant and depressant effects of beta-adrenoceptor blocking agents on isolated heart muscle. A positive inotropic effect not mediated through andrenoceptors. Naunyn-Schmiedeberg's archives of pharmacology. 311(3):205-218.
Kikura M, Takada T, Sato S. 2004. Age- and sex-specific incidence, risk, and latency period of a perioperative acute thromboembolism syndrome (pats). Thromb Haemost. 91(4):725-732.
Kim A, Dombi E, Tepas K, Fox E, Martin S, Wolters P, Balis FM, Jayaprakash N, Turkbey B, Muradyan N et al. 2013. Phase i trial and pharmacokinetic study of sorafenib in children with neurofibromatosis type i and plexiform neurofibromas. Pediatric blood & cancer. 60(3):396-401.
Kirby MS, Sagara Y, Gaa S, Inesi G, Lederer WJ, Rogers TB. 1992. Thapsigargin inhibits contraction and ca2+ transient in cardiac cells by specific inhibition of the sarcoplasmic reticulum ca2+ pump. J Biol Chem. 267(18):12545-12551.
Kleiber N, Mathot RAA, Ahsman MJ, Wildschut ED, Tibboel D, de Wildt SN. 2017. Population pharmacokinetics of intravenous clonidine for sedation during paediatric extracorporeal membrane oxygenation and continuous venovenous hemofiltration. British journal of clinical pharmacology. 83(6):1227-1239.
Lasseter KC, Levey GS, Palmer RF, McCarthy JS. 1972. The effect of sulfonylurea drugs on rabbit myocardial contractility, canine purkinje fiber automaticity, and adenyl cyclase activity from rabbit and human hearts. The Journal of clinical investigation. 51(9):2429-2434.
Lemoine H, Schonell H, Kaumann AJ. 1988. Contribution of beta 1- and beta 2-adrenoceptors of human atrium and ventricle to the effects of noradrenaline and adrenaline as assessed with (-)-atenolol. British journal of pharmacology. 95(1):55-66.
Levey GS, Palmer RF, Lasseter KC, McCarthy J. 1971. Effect of tolbutamide on adenyl cyclase in rabbit and human heart and contractility of isolated rabbit atria. J Clin Endocrinol Metab. 33(2):371-374.
Lindbom LO, Forsberg T. 1981. Cardiovascular effects of zimelidine and other antidepressant in conscious rats. Acta Psychiatr Scand Suppl. 290:380-384.
Liu LC, Dorhout B, van der Meer P, Teerlink JR, Voors AA. 2016. Omecamtiv mecarbil: A new cardiac myosin activator for the treatment of heart failure. Expert Opin Investig Drugs. 25(1):117-127.
Lullmann H, Ravens U. 1973. The time courses of the changes in contractile force and in transmembfane potentials induced by cardiac glycosides in guinea-pig papillary muscle. Br J Pharmacol. 49(3):377-390.
Mahoney L, Shah G, Crook D, Rojas-Anaya H, Rabe H. 2016. A literature review of the pharmacokinetics and pharmacodynamics of dobutamine in neonates. Pediatr Cardiol. 37(1):14-23.
Mannhardt I, Eder A, Dumotier B, Prondzynski M, Kramer E, Traebert M, Sohren KD, Flenner F, Stathopoulou K, Lemoine MD et al. 2017. Blinded contractility analysis in hipsc-cardiomyocytes in engineered heart tissue format: Comparison with human atrial trabeculae. Toxicological sciences : an official journal of the Society of Toxicology. 158(1):164-175.
Marks L, Borland S, Philp K, Ewart L, Lainee P, Skinner M, Kirk S, Valentin JP. 2012. The role of the anaesthetised guinea-pig in the preclinical cardiac safety evaluation of drug candidate compounds. Toxicol Appl Pharmacol. 263(2):171-183.
Matsushita T, Okamato M, Toyama J, Kodama I, Ito S, Fukutomi T, Suzuki S, Itoh M. 2000. Adriamycin causes dual inotropic effects through complex modulation of myocardial ca2+ handling. Jpn Circ J. 64(1):65-71.
McQuinn RL, Pentikainen PJ, Chang SF, Conard GJ. 1988. Pharmacokinetics of flecainide in patients with cirrhosis of the liver. Clinical pharmacology and therapeutics. 44(5):566-572.
Mebazaa A, Nieminen MS, Packer M, Cohen-Solal A, Kleber FX, Pocock SJ, Thakkar R, Padley RJ, Poder P, Kivikko M et al. 2007. Levosimendan vs dobutamine for patients with acute decompensated heart failure: The survive randomized trial. JAMA : the journal of the American Medical Association. 297(17):1883-1891.
Mesirca P, Alig J, Torrente AG, Muller JC, Marger L, Rollin A, Marquilly C, Vincent A, Dubel S, Bidaud I et al. 2014. Cardiac arrhythmia induced by genetic silencing of 'funny' (f) channels is rescued by girk4 inactivation. Nat Commun. 5:4664.
Molenaar P, Savarimuthu SM, Sarsero D, Chen L, Semmler AB, Carle A, Yang I, Bartel S, Vetter D, Beyerdorfer I et al. 2007. (-)-adrenaline elicits positive inotropic, lusitropic, and biochemical effects through beta2 -adrenoceptors in human atrial myocardium from nonfailing and failing hearts, consistent with gs coupling but not with gi coupling. Naunyn Schmiedebergs Arch Pharmacol. 375(1):11-28.
Mooney L, Skinner M, Coker SJ, Currie S. 2015. Effects of acute and chronic sunitinib treatment on cardiac function and calcium/calmodulin-dependent protein kinase ii. British journal of pharmacology. 172(17):4342-4354.
Murakami M, Furukawa Y, Karasawa Y, Ren LM, Takayama S, Chiba S. 1992. Inhibition by glibenclamide of negative chronotropic and inotropic responses to pinacidil, acetylcho

line, and adenosine in the isolated dog heart. Journal of cardiovascular pharmacology. 19(4):618-624.
Naranjo CA, Sellers EM, Kaplan HL, Hamilton C, Khouw V. 1984. Acute kinetic and dynamic interactions of zimelidine with ethanol. Clinical pharmacology and therapeutics. 36(5):654-660.
Orstavik O, Ata SH, Riise J, Dahl CP, Andersen GO, Levy FO, Skomedal T, Osnes JB, Qvigstad E. 2014. Inhibition of phosphodiesterase-3 by levosimendan is sufficient to account for its inotropic effect in failing human heart. Br J Pharmacol. 171(23):5169-5181.
Papp Z, Edes I, Fruhwald S, De Hert SG, Salmenpera M, Leppikangas H, Mebazaa A, Landoni G, Grossini E, Caimmi P et al. 2012. Levosimendan: Molecular mechanisms and clinical implications: Consensus of experts on the mechanisms of action of levosimendan. Int J Cardiol. 159(2):82-87.
Perez O, Gay P, Franqueza L, Carron R, Valenzuela C, Delpon E, Tamargo J. 1995. Effects of the two enantiomers, s-16257-2 and s-16260-2, of a new bradycardic agent on guinea-pig isolated cardiac preparations. British journal of pharmacology. 115(5):787-794.
Planelles-Herrero VJ, Hartman JJ, Robert-Paganin J, Malik FI, Houdusse A. 2017. Mechanistic and structural basis for activation of cardiac myosin force production by omecamtiv mecarbil. Nat Commun. 8(1):190.
Pogatsa G, Dubecz E. 1977. The direct effect of hypoglycaemic sulphonylureas on myocardial contractile force and arterial blood pressure. Diabetologia. 13(5):515-519.
Puttonen J, Kantele S, Ruck A, Ramela M, Hakkinen S, Kivikko M, Pentikainen PJ. 2008. Pharmacokinetics of intravenous levosimendan and its metabolites in subjects with hepatic impairment. Journal of Clinical Pharmacology. 48(4):445-454.
Qu Y, Fang M, Gao B, Amouzadeh HR, Li N, Narayanan P, Acton P, Lawrence J, Vargas HM. 2013. Itraconazole decreases left ventricular contractility in isolated rabbit heart: Mechanism of action. Toxicol Appl Pharmacol. 268(2):113-122.
Rao N. 2007. The clinical pharmacokinetics of escitalopram. Clinical pharmacokinetics. 46(4):281-290.
Reyes G, Schwartz PH, Newth CJ, Eldadah MK. 1993. The pharmacokinetics of isoproterenol in critically ill pediatric patients. Journal of clinical pharmacology. 33(1):29-34.
Rosen MR, Gelband H, Hoffman BF. 1971. Effects of phentolamine on electrophysiologic properties of isolated canine purkinje fibers. The Journal of pharmacology and experimental therapeutics. 179(3):586-593.
Rydberg T, Jonsson A, Karlsson MO, Melander A. 1997. Concentration-effect relations of glibenclamide and its active metabolites in man: Modelling of pharmacokinetics and pharmacodynamics. British journal of clinical pharmacology. 43(4):373-381.
Sada H. 1978. Effect of phentolamine, alprenolol and prenylamine on maximum rate of rise of action potential in guinea-pig papillary muscles. Naunyn-Schmiedeberg's archives of pharmacology. 304(3):191-201.
Satoh E, Yanagisawa T, Taira N. 1990. Specific antagonism by glibenclamide of negative inotropic effects of potassium channel openers in canine atrial muscle. Jpn J Pharmacol. 54(2):133-141.
Schafers RF, Adler S, Daul A, Zeitler G, Vogelsang M, Zerkowski HR, Brodde OE. 1994. Positive inotropic effects of the beta 2-adrenoceptor agonist terbutaline in the human heart: Effects of long-term beta 1-adrenoceptor antagonist treatment. J Am Coll Cardiol. 23(5):1224-1233.
Stage C, Jurgens G, Guski LS, Thomsen R, Bjerre D, Ferrero-Miliani L, Lyauk YK, Rasmussen HB, Dalhoff K, Consortium I. 2017. The pharmacokinetics of enalapril in relation to ces1 genotype in healthy danish volunteers. Basic Clin Pharmacol Toxicol. 121(6):487-492.
Sugiyama A, Satoh Y, Shiina H, Takahara A, Yoneyama M, Hashimoto K. 2001. Cardiac electrophysiologic and hemodynamic effects of sildenafil, a pde5 inhibitor, in anesthetized dogs. Journal of cardiovascular pharmacology. 38(6):940-946.
Sutko JL, Willerson JT. 1980. Ryanodine alteration of the contractile state of rat ventricular myocardium. Comparison with dog, cat, and rabbit ventricular tissues. Circ Res. 46(3):332-343.
Teerlink JR, Clarke CP, Saikali KG, Lee JH, Chen MM, Escandon RD, Elliott L, Bee R, Habibzadeh MR, Goldman JH et al. 2011. Dose-dependent augmentation of cardiac systolic function with the selective cardiac myosin activator, omecamtiv mecarbil: A first-in-man study. Lancet. 378(9792):667-675.
Temma K, Akera T, Chugun A, Kondo H, Hagane K, Hirano S. 1993. Comparison of cardiac actions of doxorubicin, pirarubicin and aclarubicin in isolated guinea-pig heart. European journal of pharmacology. 234(2-3):173-181.
Walker DK, Ackland MJ, James GC, Muirhead GJ, Rance DJ, Wastall P, Wright PA. 1999. Pharmacokinetics and metabolism of sildenafil in mouse, rat, rabbit, dog and man. Xenobiotica. 29(3):297-310.
Whiting B, Williams RL, Lorenzi M, Varady JC, Robins DS. 1981. Effect of naproxen on glucose metabolism and tolbutamide kinetics and dynamics in maturity onset diabetics. British journal of clinical pharmacology. 11(3):295-302.
Witchel HJ, Pabbathi VK, Hofmann G, Paul AA, Hancox JC. 2002. Inhibitory actions of the selective serotonin re-uptake inhibitor citalopram on herg and ventricular l-type calcium currents. FEBS letters. 512(1-3):59-66.
Wortsman J, Frank S, Cryer PE. 1984. Adrenomedullary response to maximal stress in humans. Am J Med. 77(5):779-784.

Supplementary Table 2: Comparison and unification of standard operating procedures for TTM, CO and EHT platforms.

In house means the conditions or assays used for hiPSC-CMs derived from in house hiPSC lines using in house differentiation methods. Commercial means use of Pluricyte and/or iCell2 hPSC-CMs that were purchased from Ncardia and Cellular Dynamics International, respectively.

	Protocol	Triple Transient Measurement (TTM)	CellOPTIQ® (CO)	Engineered Heart Tissues (EHTs)
Starting conditions	Format	96-well plate		1 million hiPSC-CMs / EHT
	Age	Thawing + 5-7 days	Thawing + 5-7 days (commercial) Differentiation time + 10 days (in house)	Differentiation time + 14-30 days
	Culture medium	Manufacturer instructions	Manufacturer instructions (commercial) Standard culture medium (in house)	Standard culture medium (in house)
	Quality control	Response to 100 nM digoxin; 30 nM nifedipine	Response to 30 nM nifedipine Cell purity >90% by a-actinin (in house) Spontaneous beat rate ≤1.5 Hz (in house)	Response to 100 nM isoprenaline and 30 nM nifedipine. Cell purity >70% by cTnT (for in house hiPSC-CMs). Minimum force: 0.1 mN
Experimental set-up	Medium	Commercial medium (serum free)	As for TTM (commercial) 1.8 mM Ca^{2+} (serum/protein free) (in house)	0.6-1 mM Ca^{2+}-modified Tyrode's soultion/DMEM (serum/protein free)
	Cell loading	ANINNE-6 plus, Rhod 3 AM and CellMask Deep Red	FluoVolt™	Lentiviral mediated expression of GCaMP6f in EHTs (transduction during EHT fabrication)
	Recording: Baselines	Paced at 1.2 Hz; 7 sec/area	Paced at 1.2-1.7 Hz; 10 sec/area	Paced at 1.5x basal rate (0.7-2.3 Hz); 10 sec/EHT
	Recording: Conc-response curves	Replicates: 5 wells/compound and 3 areas/well + time matched vehicle controls	Replicates: 5 wells/compound + time matched vehicle controls	Replicates: 6 EHTs/compound + time matched vehicle controls
		Solvent: max 0.1% DMSO; Treatment duration: 30 mins		
		Single concentration/well		Cumulative concentrations/EHT
		Paced at 1.2 Hz; 7 sec/area	Paced at 1.2-1.7 Hz; 10 sec/well	Paced at 1.5x basal rate (0.7-2.3 Hz); 10 sec/EHT
	Analysis	Analysis performed offline		Analysis performed online and offline
Follow-up	Recovery	n/a		Rest and recreation for ≥2 days in standard medium
	Additional testing	n/a		Baseline at 1.8 mM Ca^{2+}-Tyrode/DMEM (spontaneous; 20 sec/EHT), compare to prior baseline to evaluate permanent damage
	Repeat testing	No repeated use of cells		

Supplementary Table 3. Characterisation of the cell populations used relating to cardiomyocyte purity, subtype and electrophysiology

* Data taken from Cellular Dynamics International website (https://fujifilmcdi.com/products-services/icell-products/icell-cardiomyocytes2/) and/or PMID: 21890694.

‡ Ratio APD90/50, wherein a value of >1.7 predicts atrial-, 1.4-1.7 pacemaker- and <1.4 ventricular-like subtypes, as defined in PMID: 17895862.

§ Measured as (APD30–40)/(APD70–80) and assigned as described in PMID: 21890694.

Denoted: A, predicted as atrial-like; P, predicted as pacemaker-like; V, predicted as ventricular-like.

† Values given for ventricular-like cells, with subtype assignment made based on morphology of patch clamp electrophysiology waveform.

¤ Standard QC-criteria for every Pluricyte® Cardiomyocyte batch.

¥ Data from PMID: 28492526; 29925535 and/or 30416051.

Φ There have been conflicting views on the value of using single cell patch clamp as a predictor of cardiac subtypes. Depending on seeding density and other variables, the AP morphology of hiPSC-CMs may have any shape including those resembling chamber-specific subtypes (PMID: 25564842).

n.d. is not done (or not known / disclosed); IHC is immunohistochemistry; Replicates: N = biological, n = technical; All ± is SEM.

Cell Line Characterization							Assay Baseline Characterization					
			Single cell Patch Clamp									
Cell Line	**Differentiation method**	**Purity (marker[s] used)**	**Subtypes A:P:V%[Φ]**	**APD90**	**MDP**	**Spontaneous beat rate (Hz)**	**Platform**	**Cell line**	**Contraction duration**	**Contraction time**	**Relaxation time**	**Beat rate**
Pluricyte	Small molecules, no genetic modification or selection. Day of differentiation n.d.	>70% cTnT[+], of which >70% MLC2v[+¤]	n.d.	170±50; n=12	-75±5; n=12	0.5±0.2	TTM	Pluricyte	364±10 ms (N=3, n=50)	208±7 ms (N=3, n=50)	156±5 ms (N=3, n=50)	1.2 Hz (paced)
							CellOPTIQ	Pluricyte	658±6 ms (N=3, n=60)	213±6 ms (N=3, n=60)	445±7 ms (N=3, n=60)	1.2 Hz (paced)
iCell[2]	n.d.	>90% a-actinin[+]; n.d. for MLC2v[+¤]	24:22:54%; N=59[§]	415±22; n=32*[†]	-76±22; n=32[*†]	0.6±0.1; n=32[*†]		iCell[2]	414±3 ms (N=3, n=60)	146±4 ms (N=3, n=60)	267±4 ms (N=3, n=60)	1.5-1.7 Hz (paced)
R-PAT	Small molecules and growth factors, no genetic modification or selection. Day 22-35 of differentiation	>80% a-actinin[+] and/or cTnT[+]; >80% MLC2v[+¤]	4:18:78%; N=5, n=49[‡]	224±14; N=5, n=49	-62±1; N=5, n=49	n/a; triggered		R-PAT	423±4 ms (N=3, n=60)	152±2 ms (N=3, n=60)	276±4 ms (N=3, n=60)	1.2-1.5 Hz (paced
							EHT	R-PAT	499±11, N=144	183±4 ms, N=144	294±3 ms, N=144	1.0 Hz (paced)
ERC	Small molecule & growth factor based 3D[¥]. Day 22-35 of differentiation	>80% cTnT[+]; by IHC: MLC2v, high; MLC2a, low[¥]	n.d.	302±20 ms, N=11[¥]	-78±3.5 mV, N=5[¥]	n/a; triggered 1 Hz[¥]		ERC	313±2 ms, N=134	166±1 ms, N=134	148±1 ms, N=134	1.4 Hz (paced)

Abstract

Organ-on-Chips (OoCs) are micro-fabricated devices which are used to culture cells in order to mimic functional units of human organs. The devices are designed to simulate the physiological environment of tissues *in vivo*. Cells in some types of OoCs can be stimulated *in situ* by electrical and/or mechanical actuators. These actuations can mimic physiological conditions in real tissue and may include fluid or air flow, or cyclic stretch and strain as they occur in the lung and heart. These conditions similarly affect cultured cells and may influence their ability to respond appropriately to physiological or pathological stimuli. To date, most focus has been on devices specifically designed to culture just one functional unit of a specific organ: lung alveoli, kidney nephrons or blood vessels, for example. In contrast, the modular Cytostretch membrane platform described here allows OoCs to be customized to different OoC applications. The platform utilizes silicon-based micro-fabrication techniques that allow low-cost, high-volume manufacturing. We describe the platform concept and its modules developed to date. Membrane variants include membranes with (i) through-membrane pores that allow biological signaling molecules to pass between two different tissue compartments, (ii) a stretchable micro-electrode array for electrical monitoring and stimulation, (iii) micro-patterning to promote cell alignment, and (iv) strain gauges to measure changes in substrate stress. This paper presents the fabrication and the proof of functionality for each module of the Cytostretch membrane. The assessment of each additional module demonstrate that a wide range of OoCs can be achieved.

Chapter 7

Cytostretch, an Organ-on-Chip platform

Modified after Micromachines 7, 120 (2016)

Nikolas Gaio, Berend van Meer, William Quirós Solano, Lambert Bergers, Anja van de Stolpe, Christine Mummery, Pasqualina Sarro and Ronald Dekker

Introduction

Research and development (R&D) expenditure by the pharmaceutical industry has increased exponentially since the 1970s and has become a large share of their overall cost structure. However, this has not led to an increase in the number of drugs entering the market, explaining in part why average development costs per drug have risen to an estimated $2.6 billion[1]. The consequence is an urgent need for new technologies to identify and validate reliable new human therapeutic targets, and for more effective drug development[2].

In current preclinical drug R&D, cell cultures and animal models are often used to predict responses to drug compounds in humans. However, these models do not always capture human physiology and pathology sufficiently to be used as good surrogates[3]. One alternative under investigation is the use of primary human cells or stem cell line–derived cells in culture but it is clear that to be true substitutes, other aspects of their (patho) physiology *in situ* need to be considered. This may include cell and tissue geometries, electrical activity and substrate mechanics.

Organ-on-Chips (OoCs) are models which take these considerations into account by combining sophisticated chip technology with biology. This enables human responses

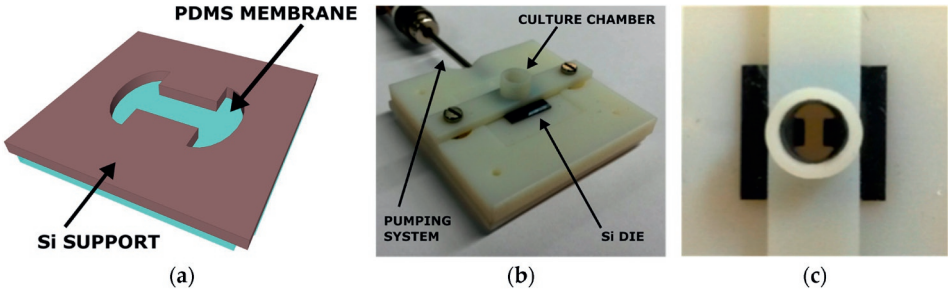

Figure 1: Cytostretch.

(a) Back view of the 3D sketch of the Cytostretch; (b) Example of a 3D-printed holder for the Cytostretch, including a cell culture chamber on top of the die and a pumping system to inflate the membrane; (c) Top view of the device mounted in the holder.

to be recapitulated *in vitro* more accurately than in other systems described so far[2,3]. OoCs are micro-fabricated devices comprised of microfluidic parts, e.g. channels and chambers in plastic foils, and a stretchable or porous membrane, on which cells are cultured. OoCs make it possible to culture complex tissue structures at a small scale[4]. The cultured cells, often different cell types, are allowed to interact *in vitro* to create a tissue model of functional units of an organ. These may, for example, be nephrons of the kidney, alveoli of the lungs, or the blood-brain barrier of the vascular system. Growth, proliferation, differentiation, maturation and controlled interactions between different cell types in the model are facilitated in the controlled environment of the OoC chip device[4].

Most OoCs are fabricated using polydimethylsiloxane (PDMS). This material has several advantages: low cost, easy patterning via soft lithography, biocompatibility, optical transparency and permeability to gasses[5,6]. Often, OoCs are fabricated by sealing three-dimensional (3D) PDMS structures patterned through replica molding processes, also known as soft lithography[6]. This technique allows simple and rapid modeling of new OoC devices and is therefore particularly useful in rapid testing of new designs[2]. However, soft lithography is based on labor-intensive procedures that reduce device throughput and yield, a hurdle to large-scale fabrication. This conflicts with the need for low-cost OoCs for cell culture which is conventionally based on the extensive use of

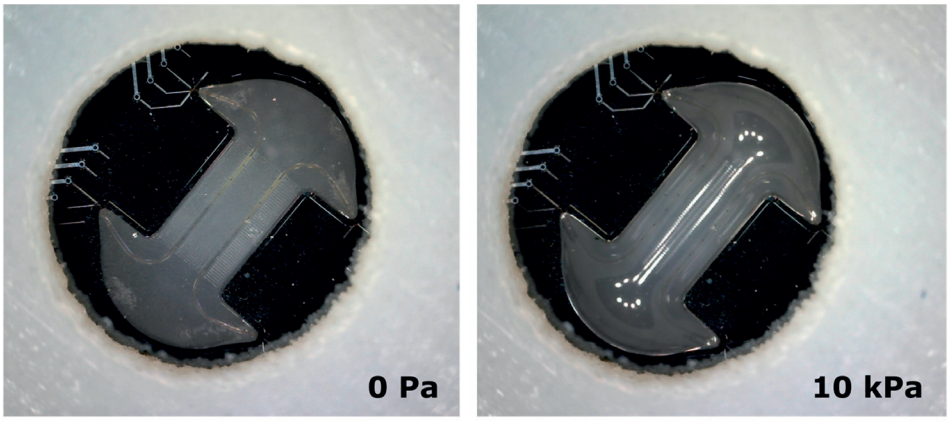

Figure 2: Cytostretch membrane.

(a) Cytostretch (with MEA module embedded) at relaxed state; (b) The Cytostretch device during inflation by applying an air pressure of 10 kPa on the back of the membrane.

disposables.

Research to date has focused on the development of devices that represent a single functional unit of an organ. There are thus well-described OoCs for liver[7], kidney[8], lung[9] and gut[10], among multiple other organs[2]. Some developments realized multiple functionalities in one OoC. For example, Booth et al.[11] presented a blood-brain barrier model composed of a microfluidic system, a filter membrane, which supports and separates multiple cell cultures, and two electrodes, which characterize the membrane impedance. Furthermore, Huh et al.[9] presented a microfluidic device with a stretchable cell-culture substrate embedded in a microfluidic channel to apply hemodynamic shear stress and mechanical strain to a lung cell culture. However, due to the fabrication techniques used for these OoCs, including other functionalities requires a complete redesign of the system and complicates the fabrication. Moreover, these systems are usually not compatible with previously developed silicon-based sensors such as thermal, optical, pH and electrical sensors[2,3]. Eliminating these drawbacks would greatly facilitate progress in OoC development.

Here, we report a novel customizable membrane platform, also called Cytostretch, based on conventional cleanroom-compatible micro-fabrication processes allowing wafer-scale fabrication and integration of silicon-based electronics. This enables large-quantity fabrication of a stretchable membrane with different features, e.g. micropores, micro-grooves, electrodes, so that it may be incorporated in different OoCs for different cell culture applications. The platform builds on the technology originally developed for a heart-on-chip model by Pakazad et al.[12]. The basic element of the Cytostretch membrane platform consists of a freestanding PDMS membrane, shaped as a dog-

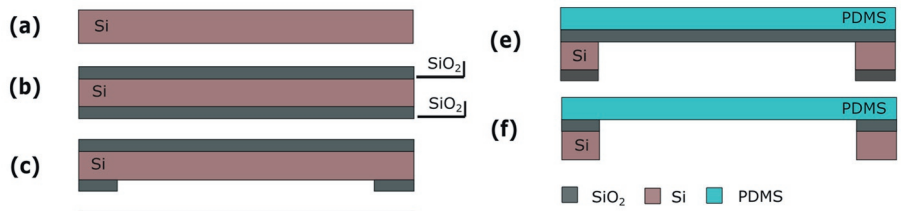

Figure 3: Process flow for the product platform.

(a) Si wafer; (b) PECVD SiO_2 deposition; (c) Back SiO_2 patterning; (d) PDMS deposition; (e) DRIE Si etching; (f) Wet SiO_2 etching. Figures are not to scale.

bone and fabricated on a silicon chip, as shown in Figure 1a. This chip was attached to a plastic cylinder or 3D-printed holder to contain cell culture medium, as shown in Figure 1b,c, thus enabling cell research. We envision that by adding different features to the membrane, adapting the shape and dimensions, and incorporating it into different microfluidic devices, it could be used for different OoCs. The features could be added through fabrication modules, which could be readily added or removed from the processing without affecting the fabrication complexity. In this way it is possible to customize the membrane to realize specific, more complex functionalities in OoCs while still yielding numerous devices.

In this paper we present the Cytostretch modules developed to date. The main goal of this paper is to show the potential of this approach by proving the functionality of each module. These are individually described by presenting their integration in the Cytostretch membrane and their characterization in a particular OoC application.

Cytostretch membrane product platform

The Cytostretch PDMS membrane is the carrier for the other technology modules. PDMS membranes have two main advantages as substrates for stem cell culture. Firstly, substrate stiffness can be tuned by altering the ratio between the elastomer and cross-linker[13], this can modulate cell morphology, function, and fate[14]. Previous work suggests that matching the substrate elasticity with *in vivo* tissue elasticity can induce and direct stem cell differentiation[13]. For example, soft substrates promote neuronal differentiation, while substrates with bone-like stiffness promote osteogenic differentiation[13].

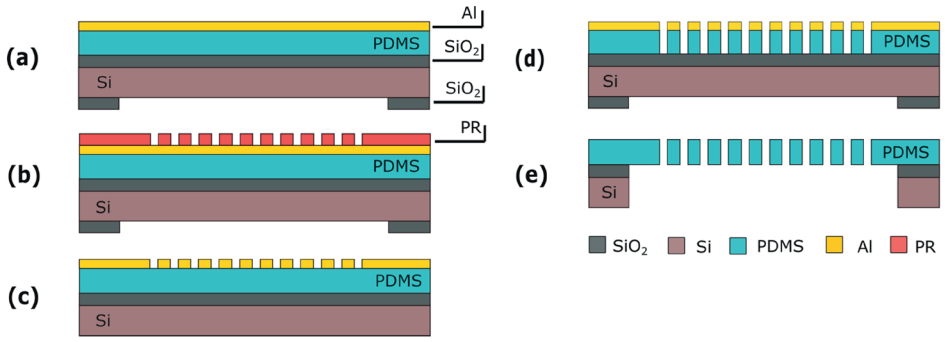

Figure 4: Process flow for the through-membrane micro-pore array.

(a) Al sputtering; (b) PR spinning and patterning; (c) Al patterning; (d) PDMS patterning; (e) Membrane releasing. Figures are not to scale.

Secondly, the elasticity of PDMS allows the membrane to be inflated and deflated statically and cyclically, using a pneumatic system, this exerts physical forces on cells cultured on the membrane. Hemodynamic shear stress or physical forces have, for example, been reported to affect the developmental fate of human pluripotent stem cells (hPSC) in culture[13,15] and stress induced by mechanical deformation might reveal disease-related functional changes. For example, cell spreading, growth and morphology can be promoted by cyclically stretching the culture substrate[16,17].

Figure 2 shows Cytostretch membrane in a relaxed state (a) without air pressure and (b) bi-axially expanded with air pressure (10 kPa) applied. In this situation cells can only be cultured on the side of the membrane that is covered with culture fluid, and not on the air-exposed side. The Cytostretch membrane has been previously stretched with pressure values up to 40 kPa, with correspondent vertical displacements of 500 µm[12].

Fabrication

Silicon (Si) wafers are used as a starting substrate for the fabrication of the Cytostretch membrane platform. Processing starts with the deposition of 2 and 6 µm of silicon oxide (SiO_2) by plasma-enhanced chemical vapor deposited (PECVD) on the front and back of the wafer, respectively (Figure 3b). The SiO_2 layer on the back is patterned by dry-etching in order to define the membrane area (Figure 3c). Subsequently, a 15-µm-thick PDMS layer is spun onto the front of the wafer at 3500 rpm for 30 s and cured for

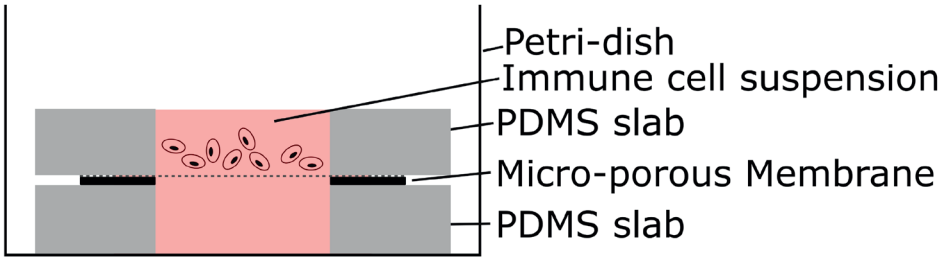

Figure 5: Schematic of setup for simple migration experiment.

30 m at 90 °C (Figure 3d). Finally, the membrane is released by removing the Si and the SiO_2 layers from underneath the membrane using deep reactive ion etching (DRIE) and buffered hydrofluoric acid (BHF), respectively (Figure 3f).

Through-membrane micro-pores

A Cytostretch membrane with through-membrane micro-pores of defined size may be useful for applications where a cell layer or 3D tissue needs to be supported while allowing the exchange of biological signals through the membrane from one chamber of a microfluidics device to a second chamber. An example of such signaling is immune cell migration from blood vessels to a wound in the skin[18,19]. Conventionally, commercially available low-porosity non-stretchable thin foils (t~10–20 µm) are used. However, a highly porous support is preferred in this type of application so that the membrane is optimally permeable for the signal.

Stretchability might be useful for investigating the role of mechanical load in skin scarring[20]. The utility of a Cytostretch membrane with defined pore size is illustrated in Section 3.3 by the migration of THP-1 monocytes (an immune cell-line) in a chemotactic essay.

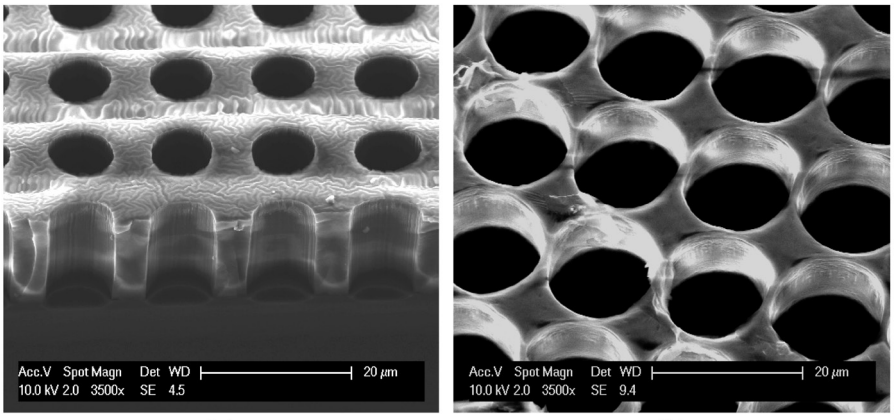

(a) (b)

Figure 6: SEM images of microporous PDMS membranes.

(a) 15-µm-thick membrane with through-membrane pores 8 µm in diameter; (b) 9-µm-thick membrane with through-membrane pores 14 µm in diameter.

Fabrication

This module consists of an array of through-membrane micro-pores patterned in the PDMS layer. To include the pores, this module is inserted into the fabrication flow immediately after PDMS spinning and curing (Figure 3d). An aluminum (Al) layer is sputtered on the PDMS at room temperature (Figure 4a). The Al is masked with 4 µm of photoresist (PR) (AZ ECI 3027) and dry-etched (Figure 4b,c). The lithography and etching processes used are optimized to circumvent issues caused by the difference between the expansion coefficients of the PDMS and the PR. Besides serving as a hard mask, the Al layer reduces the effects of the differences in expansion coefficients by acting as a buffer layer between PDMS and PR. Next, the pore array is dry-etched in the PDMS layer (Figure 4d) and the Al hard-etch mask is removed by wet-etching. The fabrication ends by releasing the membrane as before (Figure 4e).

Characterization

The resulting through-membrane micro-pores were characterized after fabrication using scanning electron microscopy (SEM). THP-1 cells, cultured in RPMI-1640 medium, were used for the immune cell migration experiment. A basic test similar to a standard Boyden chamber experiment[21] was performed (Figure 5). The membrane was placed between two PDMS slab with a center hole of 5 mm to create two fluid chambers. The bottom chamber was filled with culture medium, which was enriched with monocyte chemoattractant protein 1 (MCP-1) while the immune cells were seeded in the top

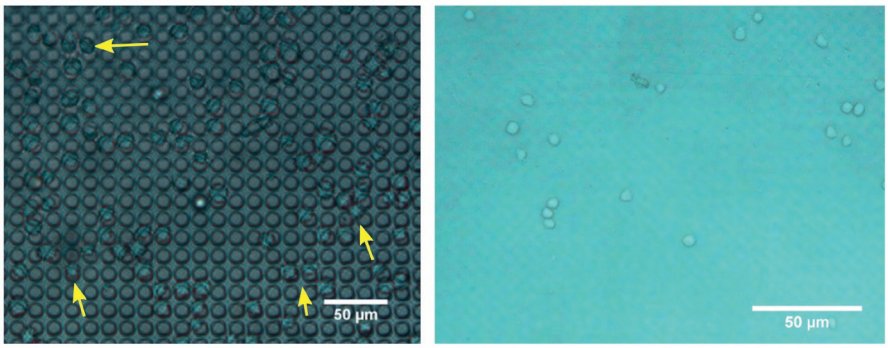

(a) (b)

Figure 7: Phase contrast images of migration experiment.

(a) The top of the micro-porous membrane 5 min after seeding shows immune cells resting on pores; (b) The volume below the membrane 3.5 h after seeding shows immune cells floating.

chamber. The MCP-1 provided a strong stimulus to attract monocytes. Images of the membrane and the volume below were recorded with a Leica inverted phase microscope, 20× objective, at 5 min and 3.5 h after seeding the membrane.

Results and Discussion

Pores 8–14 µm in diameter (and 15 µm pitch) were etched in the Cytostretch membrane. The SEM pictures of a membrane patterned with pores with an 8 µm diameter and a 14 µm diameter are shown in Figure 6a,b, respectively. For the migration experiment, membranes with 8 µm pores were used. After 5 min, cells were observed on top of the membranes, settling on/near the pores (Figure 7a). At that time, cells were not observed on the bottom of the membrane. After 3.5 h, however, the immune cells were visible in the fluid below the membrane (Figure 7b) and had virtually disappeared from the top of the membrane. This shows that the membrane does not restrict migration to the opposite side.

Micro-Electrode Array

The activity of electrically active cells, such as heart, muscle and neural cells, can be recorded on microelectrode arrays (MEAs). Changes in this electrical response due to drugs have shown to be predictive for their pharmacological safety profile[22]. MEAs can also be used to stimulate electrogenic cells, and modulate their behavior by means of

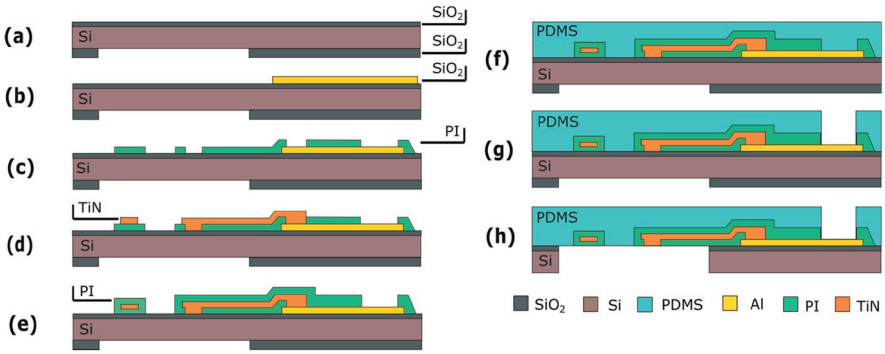

Figure 8: Process flow for the MEA module.

(a) Substrate; (b) Al deposition and patterning; (c) First layer of polyimide (or, alternatively, parylene) is spun and patterned; (d) TiN deposition and patterning; (e) Second layer of polyimide (or, alternatively, parylene) is spun and patterned; (f) PDMS deposition; (g) PDMS patterning; (h) Membrane releasing. Figures are not to scale.

contacts are etched through the PDMS layer on the front of the wafer (Figure 8g), using an Al layer as a hard mask as done in the previous module. The process flow again ends with the release of the membrane as previously described (Figure 8h).

Characterization

The Cytostretch membrane equipped with the MEA was characterized after microfabrication using SEM. At the current stage the MEA has only been tested for recording the electrical activities of cells. To investigate the electrical recording capabilities of the electrodes, hPSC-CMs were plated onto Cytostretch with the MEA module. First, the devices were sterilized in ethanol and coated with Matrigel (Invitrogen, Carlsbad, CA, USA). Next, the cells were plated and cultured on the device for 36 h in a CO_2 incubator at 37 °C. The readout of the field potential of the hPSC-CMs is performed with a Multi Channel System (MCS) USB-MEA-System. Cytostretch interfaces with this system through a printed circuit board as presented in[12,25].

Results and Discussion

SEM images of the Cytostretch device including both the MEA and the micro-groove modules are shown in Figure 9a,b. Twelve electrodes with a minimum geometric surface area (GSA) of 50 μm^2 can be fabricated, although, for this application, electrodes

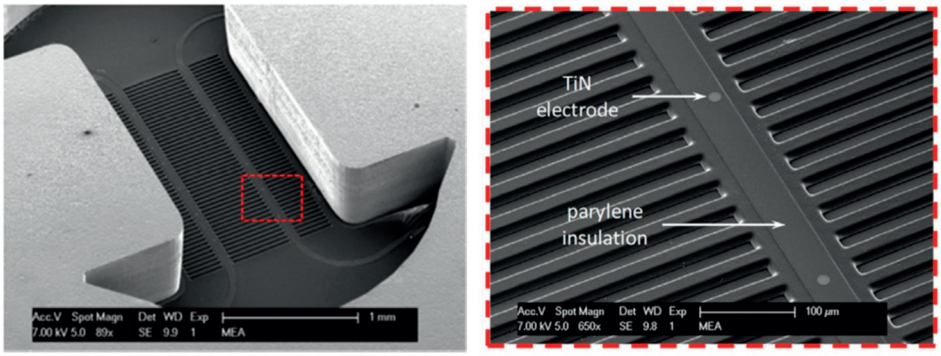

(a) (b)

Figure 9: SEM image of the Cytostretch chip.

(a) SEM image of the Cytostretch chip from the back; (b) Close-up of the area highlighted in (a) depicting transversal micro-grooves, the exposed TiN electrodes and parylene insulation of the metal tracks. Adapted from[25].

electrical impulses[23]. Furthermore, electrical stimulation might play a role in the cardiac differentiation of human embryonic stem cells[24].

A stretchable electrode-containing Cytostretch membrane can be inserted into culture devices[12,25]. The stretchable membrane consists of an array of 12 titanium nitride (TiN) electrodes embedded in the PDMS membrane. In order to demonstrate the functionality of the module, the Cytostretch membrane was tested by recording the electrical activity of human pluripotent stem cell–derived cardiomyocytes (hPSC-CMs) plated on the Cytostretch membrane.

Fabrication

This module is fabricated before the PDMS deposition (Figure 3d). The processing starts by depositing and patterning 500 nm of Al on the front side of the wafer (Figure 8b). This metal layer is used for the contact pads and the electrical interconnects outside the membrane area. Next, the metal lines extending from the contact pads to the electrodes are fabricated. These consist of a 100-nm-thick layer of sputtered TiN, sandwiched between two layers of polymide or, alternatively, parylene (Figure 8e).

Next, PDMS is spin-coated and cured (Figure 8f), and metal openings to the electrical

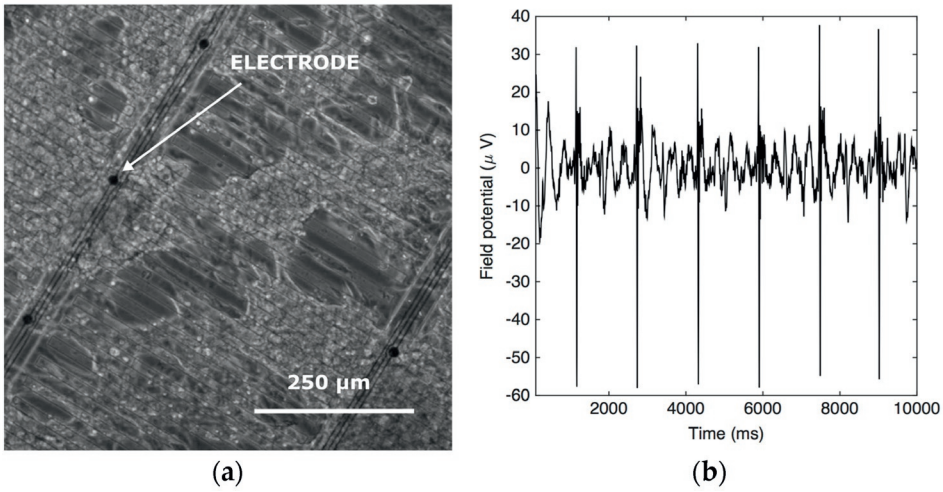

Figure 10: MEA measurements of hPSC-CMs.

(a) Optical images of induced pluripotent stem cell derived cardiomyocytes on the Cytostretch device; (b) The field potential recording from one of the electrodes.

with a 110 µm² GSA were chosen. The maximum number of electrodes included in the Cytostretch membrane is defined by the width of the interconnect tracks in the dog-bone-shaped membrane, as presented by Pakazad et al.[12,25]. The hPSC-CMs plated on the Cytostretch started beating spontaneously within three days, demonstrating their viability and functionality. Figure 10a shows the Cytostretch with hPSC-CMs after three days of culture.

The recorded signal shows the electric field potential of the hPSC-CMs on top of the electrode. The signal was filtered with Matlab using a band pass filter (2–200 Hz) and a cut-off filter (50 Hz) to remove motion artifacts. The spikes in the electric field potential seen in Figure 10b correspond to the depolarization phase of the action potential[25]. Typical recorded signals are in the order of 100 µV. The signal has a relatively low signal-to-noise ratio (SNR) compared to other works[26,27], due to the high electrochemical impedance of the flat and subcellular electrodes included in the Cytostretch device[12,25]. The impedance can be improved by coating the electrodes with porous coating such as carbon nanotubes as shown previously[28].

Micro-Grooves

Organ tissues *in situ* are highly organized, layered structures that incorporate multiple cell types to simulate complex organ-specific functions, including organ repair by cell renewal, vascularization and inflammatory responses. Both macroscopic and

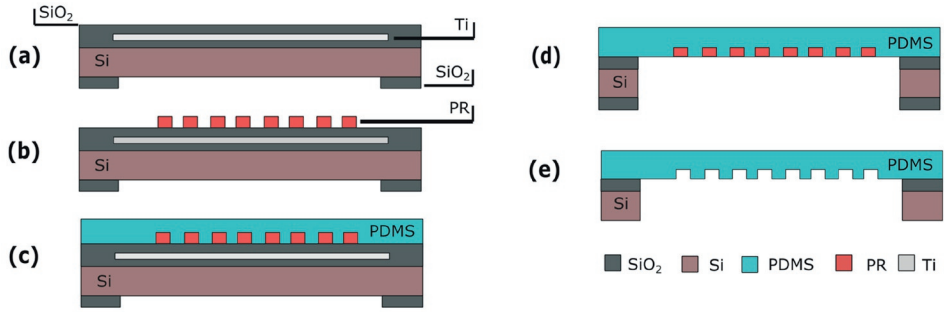

Figure 11: Process flow for the micro-groove module.

(a) Substrate with Ti mask embedded in the front-side SiO_2 layer; (b) PR spinning and patterning; (c) PDMS patterning; (d) Membrane releasing; (e) PR stripping. Figures are not to scale.

microscopic organization of cells takes place so that, for example, stem cells of the intestine orient themselves in the intact tissue and smooth muscle cells within the intestine that generate the peristaltic contraction, co-integrate appropriately. In striated muscle, anisotropic orientation of cells is crucial, since it determines the direction in which the muscle shortens. Feinberg et al. showed anisotropic cardiac myocyte alignment by micro-contact printing of an extracellular matrix (ECM) protein[29]. However, this manual technique is not suitable for micro-fabrication and is cumbersome in a cell lab.

The Cytostretch membrane can be patterned to create micro-grooves to control the orientation of cells in the culture. This module was employed to provide topological cues to hPSC-CMs and assess their anisotropic alignment after seven days in culture.

Fabrication

The micro-grooves are fabricated on the same side of the Cytostretch membrane as the MEA electrodes are deposited to determine electrical activity in organized (cardiac) tissues. The micro-groove module is therefore fabricated before spinning on the PDMS. This module requires a layer of titanium (Ti) embedded in the SiO_2 substrate (Figure 11a). This masks the PR from UV light generated during final DRIE etching, preventing unwanted PR cross-linking. After substrate fabrication (Figure 11a), 4-µm-thick PR is spin-coated and patterned (Figure 11b). The PR will serve as a mold for the micro-pattern formation in the PDMS membrane. Next, PDMS is spun onto the wafer and

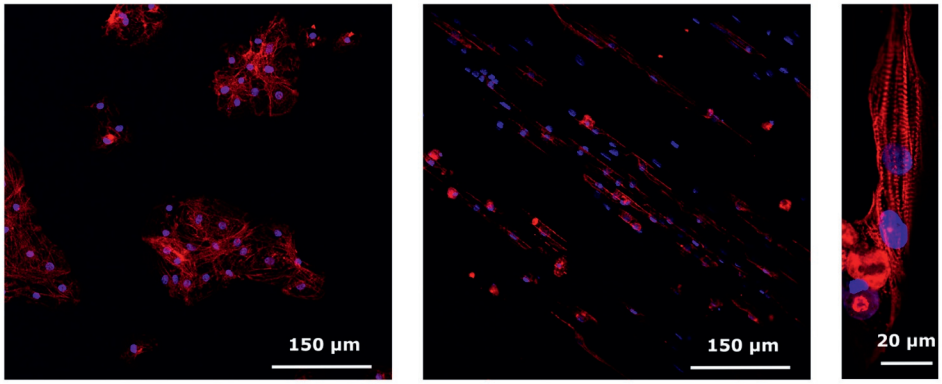

Figure 12: Confocal images of hPSC-CMs stained for anti-alpha-actinin (red) and DAPI (blue) to reveal the sarcomeric structure and cell nucleus.

(a) hPSC-CM on plain PDMS; (b,c) hPSC-CM on micro-patterned PDMS.

cured (Figure 11c) and the membrane is released (Figure 11d). After etching the oxide and Ti UV block layer, the PR mold is dissolved in acetone.

Characterization

The micro-grooves were characterized using SEM. In order to assess the degree of alignment, the micro-patterned PDMS was UV-treated and coated with Matrigel (Invitrogen). Commercially available human induced pluripotent stem cell (hiPSC)-derived cardiomyocytes (Pluriomics, Galileiweg, The Netherlands) were thawed and after seven days replated onto the micro-grooved PDMS. Cells were cultured in Pluriomics Cardiomyocyte Medium.

After seven days in culture on the micro-patterned substrate, the cells were fixed with 2% paraformaldehyde and stained with an anti-alpha-actinin antibody, anti-troponin-I antibody and DAPI (4',6-diamidino-2-phenylindole) to reveal the sarcomeric structures and cell nucleus.

Results and Discussion

A SEM picture of the micro-grooves embedded in the Cytostretch membrane is shown in Figure 9a,b. With this fabrication technique, the width and the height of the micro-grooves are determined by the lithography step shown in Figure 11b. The width can range from 0.5 µm to hundreds of µm, while the depth of the grooves can range from 1 to 12 µm. hPSC-CMs plated on standard culture substrates such as culture plastic or glass coverslips show a more isotropically orientated sarcomeric organization compared to cardiomyocytes *in vivo*, which is thought in part to be regulated by

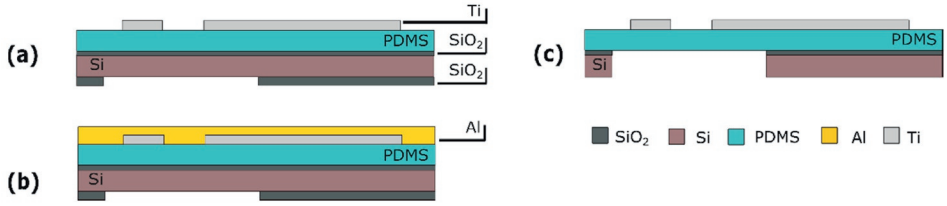

Figure 13: Process flow for the strain gauges.

(a) Ti deposition and patterning; (b) Al deposition; (c) membrane releasing and Al etching. The figures are not to scale.

their shape[30]. hPSC-CMs are less mature than adult myocardium and this is evident in several of their physiological properties, among which cardiomyocyte elongation: adult cardiomyocytes have a length-to-width ratio of 5–9.5 to 1 whereas hPSC-CMs are limited to a ratio of 3 to 1[31].

Compared to hPSC-CMs cultured on plain PDMS-coated coverslips (Figure 12a), the topological cues of the micro-patterned PDMS increase the aspect ratio of hPSC-CMs and induce a more rectangular shape, possibly by limiting cell width. Figure 12b,c show, respectively, a large-field view of the cell culture grown on the micro-grooves and a representative hPSC-CM cultured on micro-grooved PDMS with an aspect ratio of 7:1, indicating a more physiological cardiomyocyte elongation.

Strain Gauges

To date, most OoCs have used static optical techniques (immunofluorescence end-point detection, microscope cell imaging) to measure the deformation of PDMS membranes during inflation[32]. In a previous work we presented a novel Cytostretch membrane module that integrates sensing structures into the membrane to quantify the strain applied to heart or muscle cells[33], or exerted by them during contraction. Ti strain gauges were integrated in the Cytostretch PDMS membrane, and characterized by measuring the resistance change as a result of the applied strain.

Fabrication

A 100-nm-thick layer of titanium (Ti) is deposited by sputter coating onto the PDMS

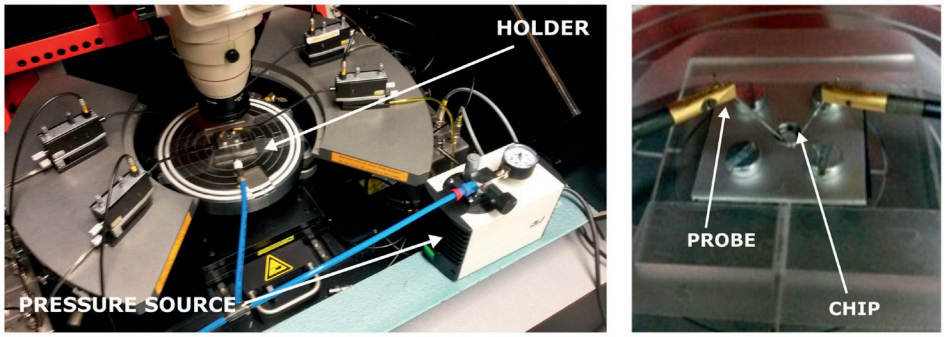

(a) (b)

Figure 14: Measurement setup for strain gauge measurement.

Measurement setup (a) and custom-made holder (b) used to measure the resistance change of the Ti strain gauges in the Cytostretch membrane platform.

layer at room temperature to avoid cracking of subsequent layers. The Ti layer is patterned to form strain gauges with different geometries by dry etching with 3-µm-thick positive PR as the masking layer (Figure 13a). To protect the strain gauges during release etch from the back, the front of the wafer is temporarily covered with a 200-nm-thick layer of Al (Figure 13b). After the membrane is released, the Al layer is selectively removed in a solution of acetic, phosphoric and hydrofluoric acid without damaging the strain gauges (Figure 13c).

Characterization

The strain gauges were characterized in a custom-made setup to test their resistance under mechanical strain. The setup consists of a probe station, a custom-made holder for the Cytostretch and a pressure source (Figure 14a,b). To verify the change in resistance of the gauge when the membrane is deformed, the probe station is configured to continuously record the I–V characteristics of the devices. The deformation of the membrane is induced by applying a positive pressure to the membrane through the cavity formed by the silicon and the bottom of the holder. The pressure change is monitored using a standard manometer capable of measuring pressures down to 100 Pa.

Results and Discussion

Figure 15a shows a Ti strain gauge fabricated on the edge of the Cytostretch PDMS membrane. When the membranes are stretched by applying a controllable pressure up to 1 kPa, the relative resistance change is approximately 5% (Figure 15b). This can be related to the strain in the membrane obtained analytically, as observed in the secondary axis[32]. As mentioned in Section 2 strain can be used to induce specific stem cell fate. Hence, the membrane acts as the tunable substrate for cell culture and the strain gauges make it possible to continuously monitor the strain applied to the Cytostretch membrane. The characterization of the device demonstrates the feasibility of sensor integration in the Cytostretch membrane platform.

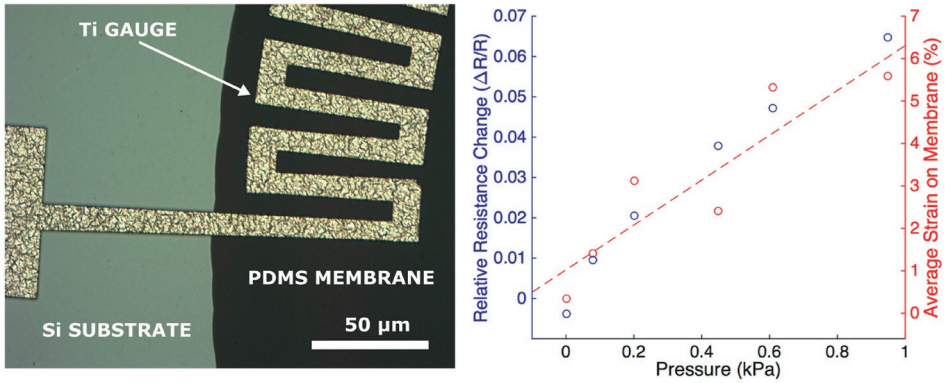

(a) (b)

Conclusions

Although OoCs in combination with appropriate cells and microenvironments are promising tools for disease modeling, drug efficacy and toxicity tests, their low technological readiness is a hurdle for commercialization, large-scale production and fabrication compatibility with silicon-based sensors. Here, a modular and customizable membrane platform for OoCs is presented. The membranes are designed and fabricated with conventional integrated circuit (IC) and microelectromechanical systems (MEMS) technologies, to enable high-yield, low-cost volume production and the integration of standard silicon-based sensors and actuators.

The platform consists of a micro-fabricated PDMS membrane, with four different technology membrane variants that can be independently inserted in the main fabrication flow without affecting other features to add functionality depending on the requirements of a particular application. The membrane variants have been described in detail and their fabrication process has been discussed. Moreover, the functionality of each membrane has been demonstrated in a typical OoC application.

The first technology module is used to etch an array of through-membrane pores in order to create a PDMS membrane with pores of a defined size that enables signal exchange through the membrane. The membrane was tested by studying the migration of immune cells through the pores. The second module consists of an integrated stretchable micro-electrode array. The electrode array was tested by measuring the electric field potential of cardiomyocytes cultured on the device's membrane under cyclic stretch. The third technology module adds micro-grooves, molded in the PDMS membrane. The grooves are used to align cells and improve the orientation and sarcomeric organization of hPSC-CMs cultured on the membrane. The last module adds strain gauges that are used as a feedback sensor in order to enable real-time measurement of the membrane strain.

Figure 15: Strain gauge results.

(a) Optical image from the front side showing a close-up of the Ti gauges at the interface between the silicon substrate and the PDMS membrane. As presented in[33], the strain gauges were fabricated on circular membranes; (b) Relative resistance change of a strain gauge (primary Y axis) and the average strain on the membrane (secondary Y-axis) as function of pressure.

The modular character of the Cytostretch membrane platform makes it highly suitable for realizing various functions in OoCs when integrated with appropriate microfluidics. New technology modules will be developed in the near future to present more features and functions, all allowing large-scale OoC membrane manufacture. This could provide new opportunities for the field of OoCs.

Acknowledgments

The authors would like to thank the Institute for human Organ and Disease Model technologies (hDMT). Moreover, the authors would like to thank and Saeed Pakazad for his contribution to the design and manufacturing of the Cytostretch platform as a part of his PhD project. Nikolas Gaio was financed by Electronic Components and Systems for European Leadership (ECSEL) "InForMed" (No. 2014-2-662155). Lambert Bergers and Anja van de Stolpe were financed by the Dutch Government through ZonMw (MKMD project No. 40-42600-98-010). Berend van Meer and Christine Mummery were financed by an European Research Council-Advanced Grant (ERC-AdG) (ERCAdG 323182 STEMCARDIOVASC). William Quirós Solano was financed by Instituto Tecnológico de Costa Rica.

References

1. Gassmann, O., Reepmeyer, G., von Zedtwitz, M. Trends and drivers for growth in the pharmaceutical industry. *Leading Pharmaceutical Innovation* (2008).

2. Beißner, N., Lorenz, T., Reichl S. Organ on chip. *Microsystems for Pharmatechnology* (2016).

3. Van der Meer A. D., van den Berg, A. Organs-on-chips: Breaking the *in vitro* impasse. *Integr. Biol.* **4,** 461–470 (2012).

4. Van de Stolpe, A., den Toonder, J. Workshop meeting report Organs-on-Chips: Human disease models. *Lab Chip* **13,** 3449–3470 (2013).

5. Jo, B.H., van Lerberghe, L.M., Motsegood, K.M., Beebe, D.J. Three-dimensional micro-channel fabrication in polydimethylsiloxane (PDMS) elastomer. *J. Microelectromech. Syst.* **9,** 76–81 (2000).

6. Toepke, M.W., Beebe, D.J. PDMS absorption of small molecules and consequences in microfluidic applications. *Lab Chip* **6,** 1484–1486 (2006).

7. Bale, S.S., Vernetti, L., Senutovitch, N., Jindal, R., Hegde, M., Gough, A., McCarty, W.J., Bakan, A., Bhushan, A., Shun, T.Y., et al. *In vitro* platforms for evaluating liver toxicity. *Exp. Biol. Med.* **239,** 1180–1191 (2014).

8. Jang, K.J., Mehr, A.P., Hamilton, G.A., McPartlin, L.A., Chung, S., Suh, K.Y., Ingber, D.E. Human kidney proximal tubule-on-a-chip for drug transport and nephrotoxicity assessment. *Integr. Biol.* **5,** 1119–1129 (2013).

9. Huh, D., Matthews, B.D., Mammoto, A., Montoya-Zavala, M., Hsin, H.Y., Ingber, D.E. Reconstituting organ-level lung functions on a chip. *Science* **328,** 1662–1668 (2010).

10. Kim, H.J., Huh, D., Hamilton, G., Ingber, D.E. Human gut-on-a-chip inhabited by microbial flora that experiences intestinal peristalsis-like motions and flow. *Lab Chip* **12,** 2165–2174 (2012).

11. Booth, R., Hanseup, K. Characterization of a microfluidic *in vitro* model of the blood-brain barrier (μBBB). *Lab Chip* **12,** 1784–1792 (2012).

12. Pakazad, S.K., Savov, A., van de Stolpe, A., Dekker, R. A novel stretchable micro-electrode array (SMEA) design for directional stretching of cells. J. *Micromech. Microeng.* **24,** 3 (2014).

13. Teixeira, A.I., Ilkhanizadeh, S., Wigenius, J.A., Duckworth, J.K., Inganäs, O., Hermanson, O. The promotion of neuronal maturation on soft substrates. *Biomaterials* **30,** 4567–4572 (2009).

14. Park, J., Kim, P., Helen, W., Engler, A.J., Levchenko, A., Kim, D.H. Control of stem cell fate and function by engineering physical microenvironments. *Integr. Biol.* **4,** 1008–1018 (2012).

15. Discher, D.E., Mooney, D.J., Zandstra, P.W. Growth factors, matrices, and forces combine and control stem cells. *Science* **324,** 1673–1677 (2009).

16. Cui, Y., Hameed, F.M., Yang, B., Lee, K., Pan, C.Q., Park, S., Sheetz, M. Cyclic stretching of soft substrates induces spreading and growth. *Nat. Commun.* **6,** 6333 (2015).

17. Huang, Y., Nam-Trung, N., Khoi, S.L., Peter, P.F.L., Maohan, S., Min, W., Leyla, K., Benoit, L. Multiarray cell stretching platform for high-magnification real-time imaging. *Nanomedicine* **8,** 543–553 (2013).

18. Broek, L.J., Limandjaja, G.C., Niessen,

F.B., Gibbs, S. Human hypertrophic and keloid scar models: Principles, limitations and future challenges from a tissue engineering perspective. *Exp. Dermatol.* **23,** 382–386 (2014).

19. Bergers, L., Waaijman, T., de Gruijl, T., van de Stolpe, A., Dekker, R., Gibbs, S. Skin-on-chip: Integrating skin-tissue and microsystems engineering. In *Proceedings of the 2015 4th TERMIS World Congress*, Boston, MA, USA, 8–12 September 2015, pp. 8–9.

20. Ogawa, R., Okai, K., Tokumura, F., Mori, K., Ohmori, Y., Huang, C., Hyakusoku, H., Akaishi, S. The relationship between skin stretching/contraction and pathologic scarring: The important role of mechanical forces in keloid generation. *Wound Repair Regen.* **20,** 149–157 (2012).

21. Boyden, S. The chemotactin effect of mixtures of antibody and antigen on polymorphonuclear leukocytes. *J. Exp. Med.* **115,** 453–466 (1962).

22. Braam, S.R., Tertoolen, L., van de Stolpe, A., Meyer, T., Passier, R., Mummery, C.L. Prediction of drug-induced cardiotoxicity using human embryonic stem cell-derived cardiomyocytes. *Stem Cell Res.* **4,** 107–116 (2010).

23. Wang, K., Fishman, H.A., Dai, H., Harris, J.S. Neural stimulation with a carbon nanotube microelectrode array. *Nano Lett.* **6,** 2043–2048 (2006).

24. Ogawa, R., Okai, K., Tokumura, F., Mori, K., Ohmori, Y., Huang, C., Hyakusoku, H., Akaishi, S., Kitamura, N., Kawano, M., et al. Electrical stimulation modulates fate determination of differentiating embryonic stem cells. *Stem Cells* **25,** 562–570 (2007).

25. Khoshfetrat, P.S. Stretchable Micro-Electrode Arrays for Electrophysiology. Ph.D. Thesis, Delft University of Technology, Delft, The Netherlands (2015).

26. Gerwig, R., Fuchsberger, K., Schroeppel, B., Link, G.S., Heusel, G., Kraushaar, U., Schuhmann, W., Stett, A., Stelzle, M. PEDOT-CNT composite microelectrodes for recording and electrostimulation applications: Fabrication, morphology, and electrical properties. *Front. Neuroeng.* **5,** 8 (2012).

27. Gabay, T., Ben-David, M., Kalifa, I., Sorkin, R., Ze'ev, R.A., Ben-Jacob, E., Hanein, Y. Electro-chemical and biological properties of carbon nanotube based multi-electrode arrays. *Nanotechnology* **18,** 035201 (2007).

28. Gaio, N., van Meer, B., Silvestri, C., Pakazad, S., Vollebregt, S., Mummery, C.L., Dekker, R. Upside-down carbon nanotube (CNT) micro-electrode array (MEA). In *Proceedings of the 2015 IEEE on SENSORS*, Busan, Korea, 1–4 (2015).

29. Feinberg, A.W., Feigel, A., Shevkoplyas, S.S., Sheehy, S., Whitesides, G.M., Parker, K.K. Muscular thin films for building actuators and powering devices. *Science* **317,** 1366–1370 (2007).

30. Bray, M.A., Sheehy, S.P., Parker, K.K. Sarcomere alignment is regulated by myocyte shape. *Cell Motil. Cytoskelet.* **65,** 641–651 (2008).

31. Denning, C., Borgdorff, V., Crutchley, J., Firth, K.S., George, V., Kalra, S., Kondrashov, A., Hoang, M.D., Mosqueira, D., Patel, A., et al. Cardiomyocytes from human pluripotent stem cells: From laboratory curiosity to industrial biomedical platform. *Biochim. Biophys. Acta* **1863,** 1728–1748 (2015).

32. Schomburg, W.K. *Introduction to Microsystem Design*; Springer: Berlin/ Heidelberg, Germany (2011).

33. Quiros-Solano, W.F., Pandraud, G.,

Sarro, P.M. Wafer-level fabrication of strain gauges on PDMS membranes for low-pressure sensing. *In Proceedings of the 2015 IEEE on SENSORS*, Busan, Korea, 1–4 (2015).

Abstract

The polymer polydimethylsiloxane (PDMS) is widely used to build microfluidic devices compatible with cell culture. Whilst convenient in manufacture, PDMS has the disadvantage that it can absorb small molecules such as drugs. In microfluidic devices like "Organs-on-Chip", designed to examine cell behavior and test the effects of drugs, this might impact drug bioavailability. Here we developed an assay to compare the absorption of a test set of four cardiac drugs by PDMS based on measuring the residual non-absorbed compound by High Pressure Liquid Chromatography (HPLC). We showed that absorption was variable and time dependent and not determined exclusively by hydrophobicity as claimed previously. We demonstrated that two commercially available lipophilic coatings and the presence of cells affected absorption. The use of lipophilic coatings may be useful in preventing small molecule absorption by PDMS.

Chapter 8

Small molecule absorption by PDMS in the context of drug response bioassays

Modified after Biochemical and Biophysical Research Communications 482, 323-328 (2017)

Berend van Meer, Henk de Vries, Karl Firth, Jasper van Weerd, Leon Tertoolen, Marcel Karperien, Pascal Jonkheijm, Chris Denning, Ad IJzerman, Christine Mummery

Introduction

Differences in physiology can compromise the ability of animal models to predict drug responses in humans accurately. As a result, inappropriate drugs may enter clinical trials or useful drugs discarded unnecessarily early in development. One of the most common adverse drug effects is still cardiotoxicity despite use of ion channel ("HERG") assays to predict arrhythmic risk, illustrating the urgent need for improvement in human cardiac models[1]. In this context, the Food and Drug Association (FDA) recently initiated the Comprehensive *In Vitro* Proarrhythmia Assay (CiPA) (cipaproject.org), to assess cardiac drug safety using cardiomyocytes from human pluripotent stem cells. Among the models being examined are several incorporating cardiomyocytes into polymer-based devices or microtissues[2–4] rather than conventional tissue culture substrates like glass and plastic, which are orders of magnitude harder and less elastic than cells would normally encounter in tissue. Resulting stress can influence cell behavior profoundly and thus drug responses[5–7]. Soft polymer substrates like polydimethylsiloxane (PDMS) are preferred by bioengineers because they can be used to fabricate microfluidic channels, flexible membranes and provide topological cues to recapitulate blood vessels, mechanical tissue strain and induce cell orientation[8–10]. Furthermore, sensors that measure electrical activity, metabolic behavior, ion transport and force of contraction can be integrated as readouts[2,11]. PDMS-based Organ-on-Chip devices can also be used for live cell imaging and are compatible with immunoassays, disease phenotyping and drug testing[12,13]. Soft polymer-based microfluidic assays have long been used for multiple biological purposes[14] but PDMS most commonly because of its biocompatibility, transparency, ease of microfabrication, molding properties and tunable substrate mechanics[15]. Its elasticity has made it particularly useful in mimicking tissues that undergo cyclic stretch and strain in the body, such as the lungs or heart[2,8,11]. One of its drawbacks, however, is its absorption of compounds added to culture medium in bioassays, most particularly, hydrophobic small molecules like many drugs[16–18]. This reduces the available drug dose, shifts the dose response curve and thus limits the predictive value of assays.

There have been few direct comparisons of absorption of different compounds by PDMS with other (more inert) substrates and how cell culture affects absorption has not been investigated. Toepke et al. examined the absorption of hydrophobic small molecules qualitatively with a fluorescence assay but this was not quantitative[17]. Wang et al. did assess final compound concentration quantitatively over time and determined a threshold that distinguished compounds with negligible absorption from those where it was significant, based on the log P value[18], a measure of hydrophobicity. It was claimed that all compounds with a log P value greater than 2.67 would show high absorption by PDMS substrates. In addition, they tested whether glass and titanium dioxide coatings reduced compound binding. These coatings have been reported to be biocompatible[16], but the presence of cells on compound absorption or coating degradation has not been investigated. Parylene coating has also been reported[19], but it compromises important properties of PDMS, such as its elasticity and gas permeability.

Here, we determined small molecule absorption by PDMS-coated culture wells versus standard culture plastic for four drugs that affect the heart, our primary research

area[20,21] for which there is interest in knowing their toxic threshold: verapamil, bepridil, Bay K 8644 and nifedipine. Toxic thresholds can only be determined accurately if the compound availability to cells is known. We therefore investigated whether cell density affected absorption and tested the ability of two commercial coatings (available on request) to reduce absorption, without affecting biocompatibility or cell plating[22]. Finally, we combined a commercial coating with cell culture to investigate the combined effect on the free drug concentration over time of incubation.

Experimental

Preparation of plates

Standard tissue culture grade polystyrene (TCPS) 96-well CELLSTAR® multiplates (Greiner Bio-One, Germany) were used. For PDMS absorption experiments, bottoms of wells were coated with 20 µL PDMS Sylgard 184 (Dow Corning, Auburn, MI), 1:10 weight ratio curing agent to elastomer. LipoCoat Cellbinder (LipoCoat, Enschede, The Netherlands) was used to coat oxygen plasma treated PDMS-coated 96-wells plates (PDMS Sylgard 184, Dow Corning, Auburn, MI).

Experimental procedure and sample retrieval

Verapamil, nifedipine (Sigma Aldrich, Saint Louis, MO), bepridil and Bay K 8644 (Tocris, United Kingdom) were diluted in dimethylsulfoxide (DMSO; Sigma Aldrich) to obtain 1 mM stock. This was diluted 1:1,000 in Dulbecco's Phosphate Buffered Saline without calcium and magnesium (DPBS) or in Tyrode's buffer when cells were present, to a working concentration of 1 µM. All solutions were prepared in disposable glass vials. 250 µL of the working solution was pipetted into the TCPS or PDMS wells and incubated for 0.5, 1, 2 or 3 hours before being gently mixed with a pipette and transferred to a glass vial which was sealed immediately. In addition, 250 µL of the working solution was pipetted into a glass vial for every sample group at the start of the experiment to provide baseline values (concentration at time zero). Time points were chosen to allow <10% change in absorption at the final time point for all compounds. Experiments were in duplicate. Cell culture experiments were at 37°C; other experiments were at room temperature.

HPLC

Drug concentrations were determined by HPLC using a solvent delivery system from Gilson (Middleton, WI) equipped with a Gilson auto injector. A VI/VIZ detector (Applied Biosystems 759A; Thermo Fisher Scientific, Waltham, MA) was used, monitoring the UV absorption maximum of the compounds under investigation. A Discovery® column (125 x 4.6 mm; Supelco, Bellefonte, PA) was applied, with a stationary phase of C18, 5µM particles. As mobile phase, MeCN was used at 40-65% (depending on the compound), 5 mM SDS and 0.1% TFA. Flow speed was 0.8 ml/min and the injection volume 100 µl. Recording and processing of data was performed using ADchom software (Leiden University, the Netherlands). In every experiment a calibration curve was included to validate the system and the linearity of the compound UV absorption response. Measurements were performed in duplicate or triplicate, as indicated. Averages from individual experiments are shown in the graphs. Since replicates showed little spread, n=2 was standard for non-biological assays.

Cell culture
Human Embryonic Kidney 293T (HEK293T) cells were maintained in Dulbecco's Modified Eagle Medium (DMEM) supplemented with 2 mM L-glutamine, 10 mM non-essential amino acids (NEAA), 25 U/ml penicillin, 25 µg/ml streptomycin (Thermo Fisher Scientific), and 10% fetal calf serum (FCS) (Sigma Aldrich). Culture medium was refreshed every 3-4 days. For experiments, cells were dissociated from standard 6 well tissue culture plates (Greiner Bio-One, Germany) with 0.1% trypsin and plated in 96-well plates at three densities: 9×10^3, 37×10^3 and 117×10^3 cells per well (0.3 cm^2) corresponding to low, medium and high surface coverage, respectively.

Cell staining
Cells were briefly washed with PBS before fixation with 2% neutral paraformaldehyde for 30 min at room temperature. Next, cells were permeabilized for 8 min with 0.1% Triton X-100 (Sigma Aldrich) in PBS then preincubated with 4% FCS in PBS for 1 hour to block non-specific binding. Cells were incubated with PBS plus Alexa Fluor 488 Phalloidin (1:40; Invitrogen) and 4% FCS for 30 min. Finally, cells were incubated with PBS plus DAPI Nucleic Acid Stain (1:1000; Invitrogen) before glass coverslips were mounted on top of the PDMS with ProlongGold (Thermo Fisher Scientific). Between every step, cells were washed with PBS and prior to Phalloidin with PBS plus 0.05% Tween 20 (Merck, Germany).

Results

HPLC was used to measure the free drug concentrations in PBS. Four compounds that affect cardiac behaviour and of interest to validate in cardiotoxicity models *in vitro* were incubated for 0.5, 1, 2 and 3 hours on TCPS wells with PDMS as the base and compared to the absorption by standard TCPS wells after 3 hours (Figure 1). Absorption by TCPS, measured as loss of compound from solution, was negligible or low but detectable for Bay K 8644, verapamil and nifedipine and somewhat higher for bepridil. PDMS however absorbed compounds much more variably: verapamil and nifedipine were absorbed 20 to 50% more than by TCPS after 3 hours whilst for Bay 8644 there was no difference between TCPS and PDMS. Bepridil was strikingly reduced more than 80% by PDMS after 3 hours. To exclude compound degradation or absorption of the compounds by glass storage vials, Bay K 8644 and bepridil solutions were kept in glass containers for 3 hours and compared with the starting concentrations (Figure S1). No differences were observed. All compounds reached steady state (<10% concentration change) both on PDMS and TCPS.

To investigate whether compound hydrophobicity, molecular weight or topological polar surface area was correlated with the absorption by PDMS, the final free drug concentration was plotted as described previously[18]. The log P values of the compounds used here were 4.03 (Bay K 8644[23]), 8.0 (bepridil[24]) and 3.79 (verapamil[25]) and ± 3 (nifedipine; provided by the manufacturer), but there was no correlation between these values and our measures of absorption (Figure 2A). Similarly, no correlation was found between the measures of absorption and the molecular weight (Figure 2B). The correlation between topological polar surface area and compound absorption by PDMS

was linear (R^2: 7.61). We also examined the effect of several mixtures of PDMS with variable elasticity on absorption[26] but all showed similar high reduction in free bepridil concentration after 3 hours (data not shown) so we did not pursue this further.

Next, we coated the PDMS surface with Cellbinder, a lipid-based coating with cell binding properties[22]. To facilitate cell attachment on otherwise zwitterionic, non-fouling and cell repellent surfaces, positive surface charge had been introduced in the Cellbinder coating to promote cell adhesion. Two Cellbinder coatings were compared: Cellbinder and Cellbinder+, which has greater stability. After 3 hour incubation, bepridil retained higher free drug concentration, indicating less absorption, on both coatings compared to uncoated PDMS (Figure 2D and 2E). No difference was found between the two.

Apart from direct substrate effects, culture of cells could also influence free compound availability since cells may either absorb compounds or block absorption sites on the substrate. We therefore investigated whether HEK293T (kidney cell) culture density on PDMS substrates affected loss of compounds from solution. Again, low and high binders (Bay K 8644 and bepridil, respectively) were incubated at 37°C (Figure 2F and 2G). Bay K 8644 was reduced as cell density increased from 9×10^3 to 37×10^3 and 117×10^3 cells, respectively, after 0.5 hour and 3 hours of incubation. A similar effect was seen for bepridil after 0.5 hour although at 3 hours, no differences in free concentration were evident between the three cell densities, all being equally low.

HEK293T cells were also cultured on TCPS, PDMS, and PDMS with Cellbinder coating to investigate both biocompatibility and cell binding properties (Figure 3). Cell spreading on PDMS was less than on TCPS and cells remained rounded with reduced visible cytoskeleton and nuclei closer together. When cultured on PDMS coated with Cellbinder, more focal adhesion points of the cytoskeleton were seen, indicating improved attachment and less stress.

Finally, different densities of HEK293T cells were cultured on Cellbinder and Cellbinder+-coated PDMS substrates and subsequently incubated with Bay K 8644 and bepridil to investigate the effect on free drug concentration (Figure 4). For Bay K 8644, both coatings showed increased absorption at the highest cell density after 0.5 and 3 hours, as also shown for uncoated PDMS plus HEK293T cell culture. For bepridil, there was a difference between the low and high cell density on the Cellbinder coating after 0.5 hours, but this was not sustained at 3 hours.

By analyzing the values found for free drug concentrations of Bay K 8644 and bepridil incubation after 3 hours on different substrates with and without HEK293T cell culture (medium density) we compared the effect of the substrate conditions on the final free drug concentrations. Figure 4C shows a decrease in Bay K 8644 concentration on PDMS with HEK293T culture, while there was no difference between PDMS, coated PDMS and coated PDMS with HEK293T culture. However, the loss of bepridil concentration on coated substrates was reduced compared to the uncoated substrates; there was no effect of the absence or presence of cell cultures.

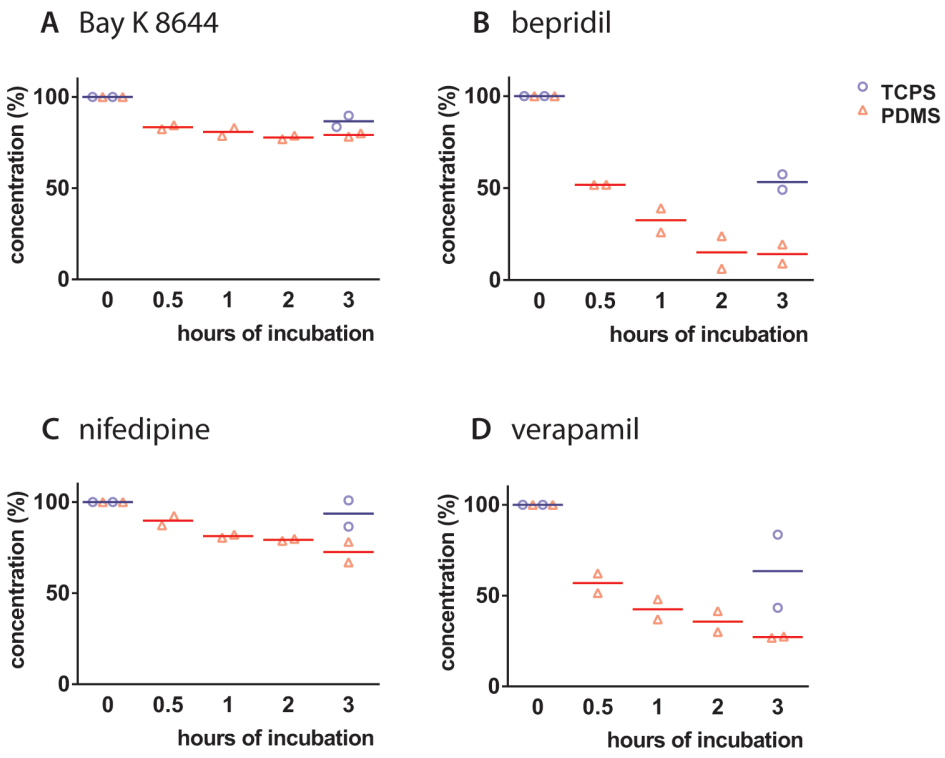

Figure 1: Free drug concentration lifetime for incubation on TCPS and PDMS.

Free drug concentration after 0.5, 1, 2 and 3 hours incubation on PDMS and 3 hours on TCPS of A) Bay K 8644, B) bepridil, C) nifedipine and D) verapamil. Averages from two independent experiments are shown.

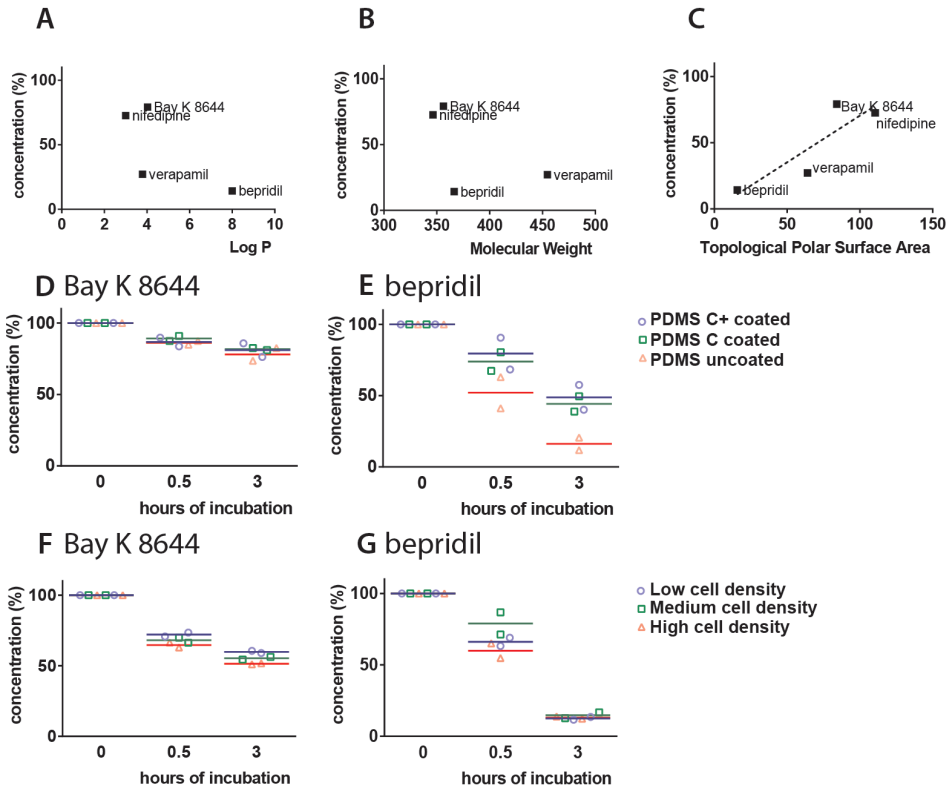

Figure 2: Properties and/or conditions that influence free drug concentration lifetime on PDMS.

A) Plot of the final free drug concentration of Bay K 8644, bepridil, nifedipine and verapamil after 3 hours of incubation on PDMS set out against their hydrophobicity (log P). B) Plot of the final free drug concentration of Bay K 8644, bepridil, nifedipine and verapamil after 3 hours incubation on PDMS versus their molecular weight. C) Plot of the final free drug concentration of Bay K 8644, bepridil, nifedipine and verapamil after 3 hours of incubation on PDMS versus their topological polar surface area and fitted with a linear best fit (dotted line, R square: 7.61). D) and E) plots of the free drug concentration of Bay K 8644 and bepridil, respectively, after 0, 0.5 and 3 hours of incubation on PDMS coated with Cellbinder+, Cellbinder and without coating. F) and G) plots of the free drug concentration of Bay K 8644 and bepridil, respectively, after 0, 0.5 and 3 hours of incubation at low, medium and high plating cell densities on PDMS substrates. Averages from two independent experiments are shown.

Discussion

Cell culture devices made from PDMS are widely used in multiple formats but may bind molecules selectively from the medium, reducing their effective availability to cells. The study here showed that several cardio-active compounds differed in their absorption by TCPS-wells with PDMS base versus standard TCPS-wells. The presence of PDMS significantly affected the free concentration of compounds. Bepridil was most highly absorbed by TCPS with PDMS base after 3 hours, followed by verapamil. Nifedipine and Bay K 8644 retained the highest free drug levels after the longest incubation time. No relationship was found between the reduction after incubation on TCPS with PDMS base and that on standard TCPS: for example, Bay K 8644 was reduced equally on both substrates whilst verapamil was reduced >50% on PDMS but not on TCPS. After 3 hours of incubation, all compounds reached steady state (<10% concentration change) on PDMS, indicating saturation of the substrate. We estimated that the total reduction of bepridil concentration would be ±85 % with a surface area of 0.3 cm^2 and volume of 250 µL, indicating a free concentration of 150 nM instead of 1 µM after 3 hours incubation. Typically, in a microfluidic chamber, the volume-to-surface ratio would be lower. For example, a PDMS microfluidic channel might normally have dimensions 50 x 5 mm length x width and 200 µm height, equivalent to 5.20 cm^2 surface and 50 µL volume. Since the volume-to-surface ratio increases more than 86 times, the reduction in free compound concentration could be expected to increase similarly, highlighting the importance of this issue.

According to the log P threshold of 2.67 based on five compounds predicted by Wang et al., small molecules would be absorbed by PDMS and all compounds we examined should have shown high absorption but this was not the case. More importantly, we were unable to find a clear correlation between absorption and log P, suggesting that hydrophobicity is not the (single) parameter determining compound absorption by PDMS as proposed by Wang et al. Molecular weight of the compounds was also not correlated with the absorption by PDMS, nor did a combination of the log P value and molecular weight. We conclude that hydrophobicity and molecular weight are not the (only) parameters determining small molecule drug binding as previously suggested. Topological polar surface area indicated a linear relationship with absorption, but this should be confirmed by measurements with more compounds.

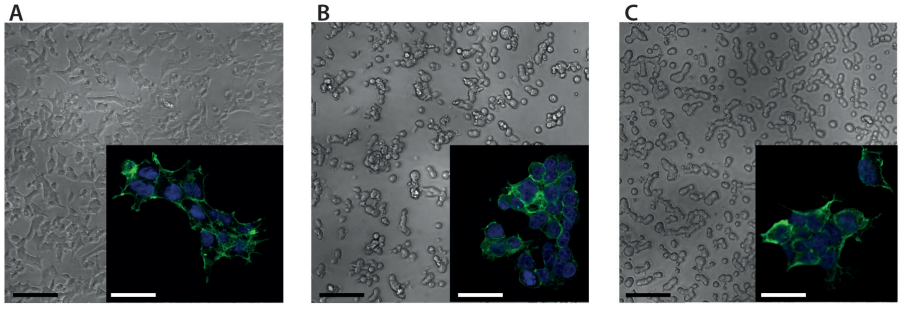

Ways to reduce compound absorption by PDMS specifically are of great interest. Two variants of a commercially available coating for PDMS were tested. These differed in chemical stability according to the manufacturer: Cellbinder+ is stable when exposed to air, whilst the regular variant of Cellbinder must be kept hydrated. The coatings are lipid-based and designed to mimic natural cell membrane interface. These types of materials are resistant to surface accumulation of proteins and can also act as barriers, preventing passage of molecules through the layer[22]. Both coatings had similar blocking properties with respect to the absorption by PDMS. They reduced the high absorption of bepridil by PDMS of >80% after 3 hours to approximately 50%. Also, absorption of Bay K 8644 was reduced compared to uncoated surfaces, although only slightly.

HEK293T cells were used as a model to investigate the biocompatibility of the coating and also whether cells confounded absorption. HEK293 cells express endogenous calcium and sodium channels[27,28], although these calcium channels are insensitive to the calcium channel specific Bay K 8644[28]. The binding of bepridil was expected to be higher since it is non-selective compound and known to block both calcium and sodium channels[29]. However, after incubation of 3 hours on PDMS plated with HEK293T cells, the free concentration of Bay K 8644 was highly reduced compared to incubation on PDMS only. The effect of compound absorption by cells is more pronounced than their potential to block compound absorption by the substrate, showing greater reduced free compound concentration at the high cell density compared to the low cell density. In contrast, the absorption of bepridil was not affected by the presence of cells. Since the absorption of bepridil by PDMS is very high, any reduction caused by the introduction of the HEK293T cells might be masked by the dominant substrate effect.

For PDMS coatings to be of practical use in cell culture assays they should be biocompatible and support cell attachment. Uncoated PDMS is biocompatible, but cells only attach following surface treatments such as the exposure to an oxygen plasma or ultra violet light[30,31]. However, these treatments would destroy organic molecules like Cellbinder. An ideal coating would facilitate similar or better cell adherence than regular PDMS, without surface pre-treatment. Although most focal adhesion points were evident in HEK293T cells cultured on TCPS and the cytoskeleton showed greater cell spreading, Cellbinder-coated PDMS also supported adequate cell adherence, demonstrating its potential utility through both biocompatibility and cell adherence although adherence was lower than on TCPS.

Figure 3: Commercial coating for PDMS to reduce drug binding and cell plating.

Representative images of HEK293T, brightfield and fluorescent staining of the cytoskeleton (green) and nuclei (blue), on A) TCPS, B) PDMS and C) Cellbinder coated PDMS. White bars indicate 25 µm, black bars indicate 350 µm.

Cellbinder-coated PDMS to which HEK293T cells were attached showed reduced compound absorption, both for Bay K 8644 and bepridil. The reduction in Bay K 8644 reached steady state within 0.5 hour and the free concentration remained high for at least 3 hours compared to uncoated PDMS with HEK293T cells. For both compounds, no differences were found between coated PDMS with and without cells, indicating that the coatings remained intact during cell culture and stable over longer periods of cell culture.

Overall, the study clearly showed the importance of determining the residual compound in the incubation fluid at the end of cellular dose response bioassays as part of dose response validation.

Acknowledgements

HEK293T cells were kindly provided by Milena Bellin (LUMC).

Funding

Work in the Mummery lab is supported by the European Research Council [grant number ERCAdG 323182 STEMCARDIOVASC]. NC3Rs CRACK-IT [grant number 35911-259146] supported work in both the Mummery and Denning labs.

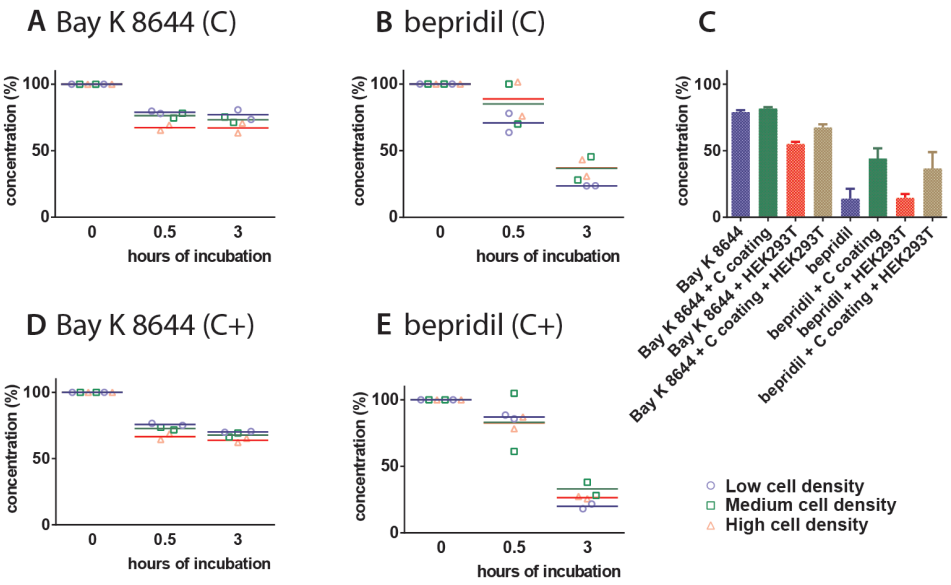

Figure 4: Effect of cell density on coated PDMS.

A), B), D) and E) show plots of the free drug concentration of Bay K 8644 and bepridil after 0, 0.5 and 3 hours of incubation at low, medium and high cell plating densities on PDMS coated with Cellbinder+ (C+) and Cellbinder (C). C) Summary of the effect of the final free drug concentration of Bay K 8644 and bepridil after 3 hours of incubation on PDMS, Cellbinder coated PDMS, PDMS plus HEK293T cell culture and Cellbinder coated PDMS plus HEK293T cell culture. Averages from two independent experiments are shown.

References

1. Laverty, H. G. *et al.* How can we improve our understanding of cardiovascular safety liabilities to develop safer medicines? *Br. J. Pharmacol.* **163,** 675–693 (2011).

2. Gaio, N. *et al.* Cytostretch, an Organ-on-Chip Platform. *Micromachines* **7,** 120 (2016).

3. Mannhardt, I. *et al.* Human Engineered Heart Tissue: Analysis of Contractile Force. *Stem Cell Reports* **7,** 29–42 (2016).

4. Passier, R., Orlova, V. & Mummery, C. Complex Tissue and Disease Modeling using hiPSCs. *Cell Stem Cell* **18,** 309–321 (2016).

5. Yeung, T. *et al.* Effects of substrate stiffness on cell morphology, cytoskeletal structure, and adhesion. *Cell Motil. Cytoskeleton* **60,** 24–34 (2005).

6. Murphy, W. L., McDevitt, T. C. & Engler, A. J. Materials as stem cell regulators. *Nat. Mater.* **13,** 547–557 (2014).

7. Engler, A. J. *et al.* Embryonic cardiomyocytes beat best on a matrix with heart-like elasticity: scar-like rigidity inhibits beating. *J. Cell Sci.* **121,** 3794–3802 (2008).

8. Huh, D. *et al.* Reconstituting organ-level lung functions on a chip. *Science* **328,** 1662–8 (2010).

9. Feinberg, A. W. *et al.* Muscular thin films for building actuators and powering devices. *Science* **317,** 1366–70 (2007).

10. Meer, A. D. van der, Orlova, V. V., Dijke, P. ten, Berg, A. van den & Mummery, C. L. Three-dimensional co-cultures of human endothelial cells and embryonic stem cell-derived pericytes inside a microfluidic device. *Lab Chip* **13,** 3562–3568 (2013).

11. Khoshfetrat Pakazad, S. *et al.* A stretchable Micro-Electrode Array for *in vitro* electrophysiology. in *2011 IEEE 24th International Conference on Micro Electro Mechanical Systems* 829–832 (IEEE, 2011). doi:10.1109/MEMSYS.2011.5734553

12. Huh, D., Torisawa, Y., Hamilton, G. a, Kim, H. J. & Ingber, D. E. Microengineered physiological biomimicry: organs-on-chips. *Lab Chip* **12,** 2156–64 (2012).

13. Esch, E. W., Bahinski, A. & Huh, D. Organs-on-chips at the frontiers of drug discovery. *Nat. Rev. Drug Discov.* **14,** 248–260 (2015).

14. Whitesides, G. M. The origins and the future of microfluidics. *Nature* **442,** 368–73 (2006).

15. Jo, B. H., Van Lerberghe, L. M., Motsegood, K. M. & Beebe, D. J. Three-dimensional micro-channel fabrication in polydimethylsiloxane (PDMS) elastomer. *J. Microelectromechanical Syst.* **9,** 76–81 (2000).

16. Gomez-Sjoberg, R., Leyrat, A. A., Houseman, B. T., Shokat, K. & Quake, S. R. Biocompatibility and reduced drug absorption of sol-gel-treated poly(dimethyl siloxane) for microfluidic cell culture applications. *Anal. Chem.* **82,** 8954–60 (2010).

17. Toepke, M. W. & Beebe, D. J. PDMS absorption of small molecules and consequences in microfluidic applications. *Lab Chip* **6,** 1484–1486 (2006).

18. Wang, J. D., Douville, N. J., Takayama, S. & Elsayed, M. Quantitative analysis of molecular absorption into PDMS microfluidic channels. *Ann. Biomed. Eng.* **40,** 1862–1873 (2012).

19. Sasaki, H., Onoe, H., Osaki, T., Kawano, R. & Takeuchi, S. Sensors and Actuators B : Chemical Parylene-coating in PDMS microfluidic channels prevents the absorption of fluorescent dyes. *Sensors Actuators B. Chem.* **150,** 478–482 (2010).

20. Braam, S. R. *et al.* Prediction of drug-induced cardiotoxicity using

human embryonic stem cell-derived cardiomyocytes. *Stem Cell Res.* **4,** 107–16 (2010).

21. van Meer, B. J., Tertoolen, L. G. J. & Mummery, C. L. Concise Review: Measuring Physiological Responses of Human Pluripotent Stem Cell Derived Cardiomyocytes to Drugs and Disease. *Stem Cells* **34,** 2008–2015 (2016).

22. van Weerd, J., Karperien, M. & Jonkheijm, P. Supported Lipid Bilayers for the Generation of Dynamic Cell-Material Interfaces. *Adv. Healthc. Mater.* **4,** 2743–2779 (2015).

23. Mason, R. P., Moring, J. & Herbette, L. G. A molecular model involving the membrane bilayer in the binding of lipid soluble drugs to their receptors in heart and brain. *Int. J. Radiat. Appl. Instrumentation. Part B. Nucl. Med. Biol.* **17,** 13–33 (1990).

24. Nawada, T. *et al.* Mechanism of inhibition of the sodium current by bepridil in guinea-pig isolated ventricular cells. *Br. J. Pharmacol.* **116,** 1775–80 (1995).

25. Hansch, C., Leo, A. & Hoekman, D. *Exploring QSAR: Hydrophobic, Electronic, and Steric Constants*. (American Chemistry Society, 1995).

26. Palchesko, R. N., Zhang, L., Sun, Y. & Feinberg, A. W. Development of Polydimethylsiloxane Substrates with Tunable Elastic Modulus to Study Cell Mechanobiology in Muscle and Nerve. *PLoS One* **7,** e51499 (2012).

27. He, B. & Soderlund, D. M. Human embryonic kidney (HEK293) cells express endogenous voltage-gated sodium currents and Nav1.7 sodium channels. *Neurosci. Lett.* **469,** 268–272 (2010).

28. Berjukow, S. *et al.* Endogenous calcium channels in human embryonic kidney (HEK293) cells. *Br. J. Pharmacol.* **118,** 748–54 (1996).

29. Yatani, A., Brown, A. M. & Schwartz, A. Bepridil block of cardiac calcium and sodium channels. *J. Pharmacol. Exp. Ther.* **237,** 9–17 (1986).

30. Heidi Au, H. T., Cui, B., Chu, Z. E., Veres, T. & Radisic, M. Cell culture chips for simultaneous application of topographical and electrical cues enhance phenotype of cardiomyocytes. *Lab Chip* **9,** 564–575 (2009).

31. Fuard, D., Tzvetkova-Chevolleau, T., Decossas, S., Tracqui, P. & Schiavone, P. Optimization of poly-di-methyl-siloxane (PDMS) substrates for studying cellular adhesion and motility. *Microelectron. Eng.* **85,** 1289–1293 (2008).

Supplementary information

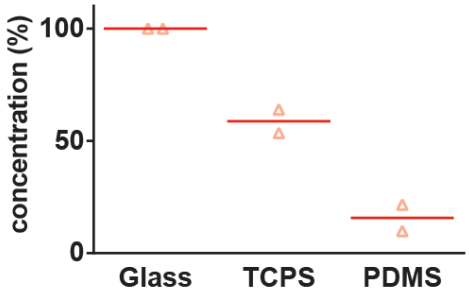

Supplementary Figure 1: Compound stability in glass.

Final free drug concentration of bepridil after 3 hours of incubation in sealed glass containers compared to incubation in TCPS and PDMS well plates. Averages from two independent experiments are shown.

Abstract

Over the past 15 years, human pluripotent stem cell derived cardiomyocytes (hPSC-CMs) have been extensively explored as a new model to study human responses to cardiac drugs and disease. To become a fully-fledged alternative to current animal or non-cardiac *in vitro* models, hPSC-CM based micro physiological systems (MPSs) need to (i) exhibit a mature (postnatal or adult) cardiac phenotype – at least for the features of interest in each particular study – and (ii) output clinically or mechanistically interpretable data. These two critical requirements would allow these models to be designated as accurate *in vitro* models of native human myocardium.

In this thesis several tools were developed towards fulfilling these requirements. First of all, a new measurement method to quantify cardiac contractility from bench to bedside was introduced. Whilst challenging to develop, the method is straightforward in use, was validated across a wide range of contractile models and made widely available for use in standard laboratory settings. To gain mechanistic insight into the complete excitation-contraction (EC) coupling cascade, a non-invasive optical measurement method was also developed to quantify the action potential, calcium flux and contraction of hPSC-CMs simultaneously in response to drugs and disease. In addition to the measurement technique as such, new analysis methods based on statistics and known cardiac physiology were developed that can automatically identify the mechanism of action of cardioactive drugs. The application of the system was further demonstrated in a blinded, multi-centre evaluation of drug-induced contractility changes. Next, aiming to further improve maturation of hPSC derived models using non-chemical cues, a modular Organ-on-Chip (OoC) device was developed in which a wide range of features could be built to enable for example cyclic stretch and cardiomyocyte anisotropic alignment. Finally, looking critically at polydimethylsiloxane (PDMS), the current standard material used to make many MPSs, its absorption of cardioactive drugs and compounds was investigated and solutions to mitigate this problem were explored. In this final chapter the results presented in this thesis and future perspectives are discussed.

Chapter 9

General discussion and future perspectives

Mimicking human cardiac function with hPSC-CMs

Although hPSC-CMs are promising models for cardiotoxicology screening, drug development and disease research, their limited maturity remains a hurdle to full use. As summarized in Chapter 2, many of their functional and structural properties remain underdeveloped *in vitro*. It is not unsurprising, therefore, that there are many efforts ongoing worldwide to address this and improve this maturation state[1–4]. It is not believed that there is an intrinsic block to maturation of hPSC-CMs since in the right microenvironment *in vivo* after transplantation to the heart (of animals) maturation appears to take place[5,6]. Sensitive measurement tools however, might be the most immediate solution to mitigate poor maturity at least in part (e.g. low force of contraction might be detectable with more sensitive quantification methods) but more fundamental limitations are encountered when cardiac mechanisms present in adult cardiomyocytes are not fully developed in hPSC-CMs[7]. For example, this might be the reason for the lack of cAMP-related effect in the PDE3 inhibitors tested in Chapter 5 and 6. Apart from the cellular immaturity, the interaction of cardiomyocytes with different cell types in the *in vivo* microenvironment is important to take into consideration. For example, the absence of sympathetic nervous system is a very likely reason explaining why no effect was found in hPSC-CMs in response to atenolol (Chapter 5 and 6)[8]. In addition, the mechanical environment of cardiomyocytes is important. The OoC device 'Cytostretch' developed in Chapter 6 can be used to investigate whether an environment that resembles the mechanical properties of the heart more closely by including for example cyclic strain and topological cues for alignment will improve hPSC-CM maturation. While the dimensions of certain features currently used in the device might be suboptimal[9] or perhaps irrelevant[10], it was demonstrated that the fabrication of the modular device is feasible. In fact, this flexible design can be used easily and adapted to exploit important maturation cues reported[11]. In addition, electrical stimulation has recently been shown to mature hPSC-CMs significantly[3] and can be applied via the integrated electrodes. Furthermore, the PDMS on the device can be tuned to have viscoelastic properties that mimic the walls of the heart which is reported to influence cardiomyocyte function[12] and might improve hPSC-CM maturation although this has not yet been formally shown[13].

The cellular composition of the adult myocardium is not limited to cardiomyocytes. In fact, only around 30% of all cells are myocytes, while the other 70% is a combination of cardiac endothelial cells, cardiac fibroblasts and vascular stromal cells[14]. Incorporating these different cardiac cellular subtypes is likely to increase the predictive power of hPSC-CMs since it can capture indirect effects of other cells on cardiomyocytes (e.g. endothelial cells that are reported to play a major role in trastuzumab-induced cardiotoxicity[15]) but also because the correct (cardiac) cellular niche has been reported to play a role in maturing the myocytes themselves[16,17]. In most work reported in this thesis, these carefully controlled and composed multicellular cardiac cultures were not used although it is most likely that even with the highly efficient differentiation protocols used, all cardiomyocyte batches not specifically purified contained an (undefined) non-myocyte population. This was the case for both in-house differentiated hPSC-CMs but also for the commercially available Pluricyte hPSC-CMs also used in this thesis. Although more expensive, the benefit of commercial cells in general should not

be underestimated. Large batches of frozen cells allow multiple experiments at defined moments after thaw using a single differentiated population, thus decreasing assay-to-assay variation. Moreover, the quality control (QC) incorporated in the production process of commercial suppliers ensures high reproducibility and less batch-to-batch variation. Freezing methods for hPSC-CMs are becoming more widely available and using this for large batches of in-house differentiated cell populations does provide researchers (particularly as in this thesis, with complex downstream experimental set-ups) with more flexibility. It is thus an approach to decreasing inter-experiment variation without extra expense. However, the QC in most laboratories still largely relies to fluorescence-activated cell analysis or sorting to define the cellular composition of a differentiated population of cells. This could and should where possible be extended to functional readouts. MUSCLEMOTION in combination with a simple imaging tool such as a smartphone or in-incubator microscope might be used to implement such QC for contractility of hPSC-CMs in addition to the protein expression profile (Chapter 3).

Apart from batch-to-batch variability, hPSC line-to-line variability is important to take into account when designing and executing assays for drugs and disease. Even when hPSC-CMs are cultured and measured in similar conditions, they still show variability in functional parameters such as action potential duration 90%[18]. This line-to-line variation emphasizes the importance of using isogenic controls wherever possible when studying human induced pluripotent stem cell (hiPSC) derived from patients as models for disease phenotype. Alternatively, a set of well-described cardioactive drugs could be tested in each experiment as reference data for that particular line. Especially when testing drugs (blinded identity for operator) reference compounds offer a solution by comparing results of each line to their line-specific response to the reference compounds.

As hPSC-CM based models continue to advance and more closely resemble adult myocardium, their accuracy and predictivity is also expected to increase. However, even the best human models will inherently be a simplification of the reality making it important to select and use the right model for each given task. Nevertheless, even the output of fully matured human models is not easily translated to clinic relevance; the models often require a completely different measurement approach than used in patients and drug and compound metabolism, bioavailability and breakdown may strongly depend on the intact human body. The aspects addressed in this thesis mainly concern standardizing measurement methods.

Measuring cardiac function in hPSC-CMs based models

Measurement methods determining physical features of hPSC-CMs are typically used to gain insight in the state of maturation or drug- and disease-induced effects. The phenotypic changes of hPSC-CMs associated with these conditions are essentially reflected in (a combination of) a wide range of parameters related to the structure, action potential, calcium handling and -storage, contraction or metabolism. The level at which these changes take place can differ and can range from changes in gene and protein expression and protein trafficking to purely mechanical and electrical alterations. Ultimately, the most salient feature of cardiomyocytes is their cyclic

contraction and to quantify this MUSCLEMOTION was developed in Chapter 3. However, MUSCLEMOTION is a relative measure of contractility and is not able to quantify the force of contraction which gives more insight in the contractile power and is measured in more complex setups[2,19]. Although absolute values of force of contraction are valuable, care has to be taken in comparing the force generated by hPSC-CM in different setups since they might be subjected to different load. MUSCLEMOTION, but also the Triple Transient Measurement (TTM) system developed in Chapter 5 are all optical systems. While this often circumvents the need for complex substrates, making its applicability versatile, and reduces the invasiveness of the measurement method on the cell, the use of fluorescent sensors can increase experimental variation due to bleaching, loading differences and internalization of the sensor in cellular sub-compartments such as the mitochondria. In part, this problem could be mitigated by using ratiometric fluorescence sensors in the TTM system, but this would require more fluorescent channels to be multiplexed and would decrease the effective sampling frequency. Furthermore, even though less invasive than for example patch-clamp electrophysiology, these sensors should not be considered "non-invasive" for the cells. First of all, light – especially high power light at small wavelengths – induces reactive oxygen species in the cell culture media[20]. Secondly, the sensors themselves affect cellular behavior. For example, calcium sensitive dyes might have a buffering effect since calcium ions bind to and sequester the dye molecules which reduces the contractility depending on the concentration used. However, the kinetics of contraction and relaxation have been reported not to change[21].

The parameter that is theoretically the most limiting in the measurement is the voltage sensitive signal and more specifically the upstroke time (T_{rise}) which is related to the maximum upstroke (V_{max}) in classical electrophysiology. This potential limitation is due to the minimum sampling frequency for assessing the action potential which is calculated to be around 8.8 kHz (Chapter 2) in adult cardiomyocytes; this is more than 26 times higher than the 333 Hz used in the TTM system. However, hPSC-CMs have a lower V_{max} which makes the measurements of V_{max} at 333 Hz sufficient at their current maturation state. Extracellular field potential recordings as used in Cytostretch are easily made at sampling frequencies >10 kHz using the embedded electrodes. Compared to the TTM system and MUCLEMOTION, the advantage of integrating the culture environment and measurement tools is a reduction in readout apparatus complexity, ease-of-use and the potential for continuous monitoring. However, this comes at the expense of a higher price per data point, less flexibility in cellular configuration of the model and fixed predefined readouts. The choice for PDMS as material to develop these chips is also arguable. While the advantages of PDMS for Organ-on-Chip devices are evident (e.g. rapid prototyping, transparent, biocompatible, stretchable, tunable mechanic properties) the material absorbs many small molecules – and thus drugs – in high amounts (Chapter 7). This problem was mitigated to some extent by lipophobic coatings (also used for contact lenses) but is still lacking an off-the-shelf solution applicable in every lab. It was shown that the index for hydrophobicity (LogP) does not explain the level of absorption as is reported previously[22]. However, the inverse topological polar surface area seems to be a predictive measure.

Where possible, hPSC-CM features should be quantified in ways that are clinically

interpretable. MUSCLEMOTION was used both *in vitro* and *in vivo*, but head-to-head comparison of the results is still impossible due to the difference in cellular configuration and load, for example. The TTM system provides insight in the cellular physiology but is not easy comparable with the whole heart. In fact, most of our understanding of cardiac physiology at the cellular level derives from animal studies. It is often difficult to find studies performed on (adult or even fetal) human cardiomyocytes to examine interspecies differences.

Importantly, measurement tools developed in this thesis should be automated where possible. Apart from reducing the need for operator time and skills, this will further remove unintentional bias from the operator. For example, selecting measurement areas in the TTM system is now done by the operator while automation could have these randomly selected. Apart from the measurement method, automated analyses, such as the algorithm developed in Chapter 5 to identify mechanism of action in hPSC-CM drug responses, will eliminate bias in the interpretation of results. Automation can lead to unbiased, reproducible measurements with the potential to scale up. These are important requirements to make accurate human avatars for drug and disease research.

hPSC based models as human avatars

Together with advanced artificial intelligence computational modelling[23], hPSC based models and OoCs are likely to revolutionize the way pharma predicts, tests and screens potential drug candidates. As hPSC based MPSs (hPSC-MPSs) will increasingly capture the complete human complexity including unknown pathways or mechanisms, they could be used to check and validate predictions made by *in silico* models. Since this approach is fundamentally different from the current high-throughput *in vitro* method for identifying drug candidates applied in most cases, it is important to adopt the future hPSC-MPSs (or MPSs derived from other cell sources) to the new scenario instead of trying to replace the old. In practice, this means that the need for high-throughput MPSs or OoCs might be less important than often implied[24]. In turn, this allows for a higher price per data point and thus more complex models. Apart from pharma, academic research groups are likely to adopt hPSC-MPSs, especially if models emerge that have outputs that can be related to human physiology or clinical data directly. If MPS based assays can be made more widely available to non-expert laboratories and researchers they could be used as an 'plug-and-play' assay in the experimental palette. A portfolio of different devices is required since it is unlikely there will be one chip fit for all purposes. While emerging commercial OoC companies are instrumental in promoting this approach, the lack of flexibility in some commercial products is not beneficial for biological research where every organ may have unique requirements. Moreover, it is not likely that every hPSC based model needs an actual microfluidic chip, making MPS more favorable as a term over OoC. The emerging companies are however of great importance since they are the first to produce large batches of chips which is a step in reducing the lack of reproducibility found typically in in-house fabricated devices. Especially since relatively high variation is inherent to the field of biology, the technological part of the MPS should be made as reproducible as possible. The need for a wide portfolio of devices and models imposes difficulties on standardization and harmonization in the field. If anywhere these are most likely to be introduced in

regulatory settings such as safety and toxicology testing.

The field would be best focused on developing MPS of critical organs in combination with essential human-specific processes such as the immune and inflammatory system (triggers to many diseases) in environments that provide the correct chemical and/or mechanical cues to organize the cells as in native tissue. This process of organization is a trade-off between directed bioengineering and developmental self-assembly which will require close collaboration and communication between engineers and biologists to find the right balance for each MPS. To develop disease specific MPS of these critical organs, data banks with well-documented hiPSC lines are essential and emerging at acceptable cost and these can be used to identify and predict disease severity based on genetic background. In addition, using CRISPR/CAS9 it is becoming increasingly possible to introduce a large number of different mutations efficiently in a single hiPSC cell line to investigate the mutation-specific effects of, for example, long QT syndrome where multiple mutations are described for same disease[25].

Future perspectives

Use of hPSC derived cells as models of disease, for drug discovery and the identification of toxic responses in organs and tissues is coming of age but is widely expected to become "adult" in the near future due to further integration of biology and engineering which will enable complex, biologically mature and patient-specific MPS. As costs to produce hiPSC lines from patients and their subsequent differentiation beginning to decrease and cell banks with associated patient information come online worldwide, it seems increasingly likely that stem cell-based models might become personalized or semi-personalized using hPSC of genetically similar subpopulations. What we have now are readily accessible options for scaled production of well-defined differentiated stem cells that allow high throughput bioassay screens on hundreds of well-plates with each

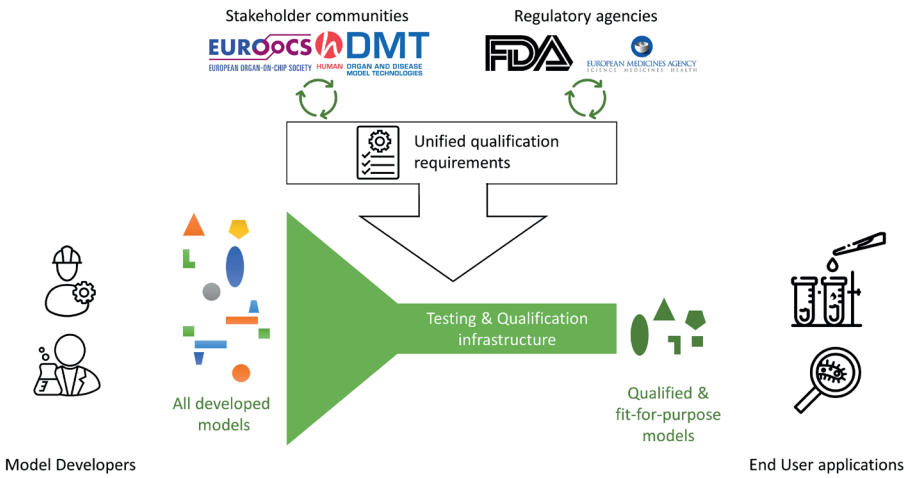

well containing an identical cell population. What we (academics and pharma) would increasingly like to have though, is to have these well-plates filled with differentiated stem cells from hundreds of different individuals or patients. This would make the technology personalized. More research is clearly required to develop reproducible and fit-for-purpose MPS with readouts that are clinically relevant and give insight in human physiology but at the same time are scaled down to reduce the cost of each data point. This would make it feasible for pharma to carry screens on large compound libraries across whole populations rather than just a few individuals. This could best be done using advanced robotic or liquid handling systems based and several of the quantitative bioassay assays developed in this thesis could be implemented in these pipelines.

Coming-of-age of the field will also require infrastructure suitable to bridge the gap from academia to end user applications. Such infrastructure should be technological (e.g. standardized platform technology, reproducible fabrication, automation software) but also biological (e.g. large batched of hPSC derivates, large biobanks for population screenings, testing facilities) and even mathematical (e.g. *in vitro* to *in vivo* relationship modelling). Such multidisciplinary infrastructure needs to be built and supported by a large network of developers, end users and other stakeholders in close collaboration with each other. A possible model for this is shown in Figure 1. This shows a infrastructure design to take the technology forward such that it can be implemented by regulatory bodies as alternatives to current technologies which often miss human (patho)physiological relevance.

Figure 1: Organ-on-Chip infrastructure is needed to bridge the gap from model developers to end user applications.

This infrastructure should be able to select, test and qualify models making them directly suitable for End Users. Importantly, the qualification requirements should be defined in close collaboration with both stakeholder communities and regulatory agencies to ensure wide support but also take steps towards incorporation of such models in the drug approval process. Image credits (Noun Project): engineer by Esaú Aguilera, Scientist by parkjisun, Job Description by SBTS, testing by priyanka, bacteria observation by Egorova Valentina.

References

1. Giacomelli, E. *et al.* Three-dimensional cardiac microtissues composed of cardiomyocytes and endothelial cells co-differentiated from human pluripotent stem cells. *Development* dev.143438 (2017).

2. Birket, M. J. *et al.* Contractile Defect Caused by Mutation in MYBPC3 Revealed under Conditions Optimized for Human PSC-Cardiomyocyte Function. *Cell Rep.* **13,** 733–745 (2015).

3. Ronaldson-Bouchard, K. *et al.* Advanced maturation of human cardiac tissue grown from pluripotent stem cells. *Nature* **556,** 239–243 (2018).

4. Lemoine, M. D. *et al.* Human iPSC-derived cardiomyocytes cultured in 3D engineered heart tissue show physiological upstroke velocity and sodium current density. *Sci. Rep.* **7,** 5464 (2017).

5. van Laake, L. W. *et al.* Human embryonic stem cell-derived cardiomyocytes survive and mature in the mouse heart and transiently improve function after myocardial infarction. *Stem Cell Res.* **1,** 9–24 (2007).

6. Dai, W. *et al.* Survival and maturation of human embryonic stem cell-derived cardiomyocytes in rat hearts. *J. Mol. Cell. Cardiol.* **43,** 504–516 (2007).

7. Mannhardt, I. *et al.* Blinded contractility analysis in hipsc-cardiomyocytes in engineered heart tissue format: Comparison with human atrial trabeculae. *Toxicol. Sci.* **158,** 164–175 (2017).

8. Schäfer, M., Frischkopf, K., Taimor, G., Piper, H. M. & Schlüter, K.-D. Hypertrophic effect of selective β_1-adrenoceptor stimulation on ventricular cardiomyocytes from adult rat. *Am. J. Physiol. Physiol.* **279,** C495–C503 (2000).

9. Li, J. *et al.* Human Pluripotent Stem Cell-Derived Cardiac Tissue-like Constructs for Repairing the Infarcted Myocardium. *Stem Cell Reports* **9,** 1546–1559 (2017).

10. Han, J., Wu, Q., Xia, Y., Wagner, M. B. & Xu, C. Cell alignment induced by anisotropic electrospun fibrous scaffolds alone has limited effect on cardiomyocyte maturation. *Stem Cell Res.* **16,** 740–750 (2016).

11. Jiang, Y., Park, P., Hong, S.-M. & Ban, K. Maturation of Cardiomyocytes Derived from Human Pluripotent Stem Cells: Current Strategies and Limitations. *Mol. Cells* **41,** 0–0 (2018).

12. McCain, M. L., Yuan, H., Pasqualini, F. S., Campbell, P. H. & Parker, K. K. Matrix elasticity regulates the optimal cardiac myocyte shape for contractility. *Am. J. Physiol. Heart Circ. Physiol.* **306,** H1525-39 (2014).

13. Besser, R. R. *et al.* Engineered microenvironments for maturation of stem cell derived cardiac myocytes. *Theranostics* **8,** 124–140 (2018).

14. Pinto, A. R. *et al.* Revisiting cardiac cellular composition. *Circ. Res.* **118,** 400–409 (2016).

15. Sandoo, A., Kitas, G. D. & Carmichael, A. R. Endothelial dysfunction as a determinant of trastuzumabmediated cardiotoxicity in patients with breast cancer. *Anticancer Res.* **34,** 1147–1151 (2014).

16. Giacomelli, E. *et al.* Three-dimensional cardiac microtissues composed of cardiomyocytes and endothelial cells co-differentiated from human pluripotent stem cells. *Development* dev.143438 (2017).

17. Ravenscroft, S. M., Pointon, A., Williams, A. W., Cross, M. J. & Sidaway, J. E. Cardiac non-myocyte cells show enhanced pharmacological function suggestive of contractile maturity in stem cell derived cardiomyocyte microtissues. *Toxicol. Sci.* **152,** 99–112 (2016).

18. Sala, L., Bellin, M. & Mummery, C. L. Integrating cardiomyocytes from human pluripotent stem cells in safety pharmacology: has the time come? *Br. J. Pharmacol.* 1–17 (2016).

19. Mannhardt, I. *et al.* Human Engineered Heart Tissue: Analysis of Contractile Force. *Stem Cell Reports* **7,** 29–42 (2016).

20. Grzelak, A., Rychlik, B. & Bartosz, G. Light-dependent generation of reactive oxygen species in cell culture media. *Free Radic. Biol. Med.* **30,** 1418–1425 (2001).

21. Pointon, A. *et al.* Assessment of cardiomyocyte contraction in human-induced pluripotent stem cell-derived cardiomyocytes. *Toxicol. Sci.* **144,** 227–237 (2015).

22. Wang, J. D., Douville, N. J., Takayama, S. & Elsayed, M. Quantitative analysis of molecular absorption into PDMS microfluidic channels. *Ann. Biomed. Eng.* **40,** 1862–1873 (2012).

23. Kumar, N., Hendriks, B. S., Janes, K. A., de Graaf, D. & Lauffenburger, D. A. Applying computational modeling to drug discovery and development. *Drug Discov. Today* **11,** 806–811 (2006).

24. Probst, C., Schneider, S. & Loskill, P. High-throughput Organ-on-a-chip systems: Current status and remaining challenges. *Curr. Opin. Biomed. Eng.* **6,** 33–41 (2018).

25. Brandão, K. O., Tabel, V. A., Atsma, D. E., Mummery, C. L. & Davis, R. P. Human pluripotent stem cell models of cardiac disease: from mechanisms to therapies. *Dis. Model. Mech.* **10,** 1039–1059 (2017).

Summary

Studying diseases or the effect of new drugs on the human body is challenging, not least because of the lack of proper testing models that recapitulate human physiology. Most research is done using animal models but these often show differences with humans in disease manifestation and responses to drugs. For example, drugs that had no effect on the hearts of animals later turned out to cause lethal arrhythmias in some humans. This – and the ethical issues around animal testing – is why, as in this thesis, there is increasing interest on making human heart models based on pluripotent stem cells (hPSCs). Aside from the heart, hPSCs can form all other cell types of the human body. hPSCs are normally only present in early embryos but can be isolated in culture as 'embryonic stem cells'. Since 2006, however, they can also be created artificially by genetic reprogramming of cells from the adult body. These hPSCs are referred to as 'human induced pluripotent stem cells' (hiPSCs). Many protocols are now available to direct 'differentiation' of hPSC to different types of tissue and organ specific cells, including lung, retina, blood vessel, brain and heart cells. This now means small numbers of cells can be collected from a patient (e.g. from blood, urine or skin), reprogrammed to hiPSCs, and then differentiated to heart muscle cells (cardiomyocytes). Since the genetics of the patient are maintained during reprogramming, the phenotype of a genetic disease affecting cardiac function can also be captured. The focus of this thesis has been developing methods to measure these cardiac phenotypes robustly and with sufficient complexity to reflects drug responses and disease of the heart.

Arguably, the heart is the most important organ of the human body and is thus a life-threatening target of toxic compounds and disease. Side effects of drugs designed to treat cancer (e.g. doxorubicin) often lead to impaired cardiac function. Using cardiomyocytes derived from hPSCs (hPSC-CMs) pharmaceutical companies are expected to be able to identify and possibly mitigate cardiotoxicity in early stages of their drug development pipeline.

To study the effect of drugs but also to investigate disease phenotypes, it is not only important to have hPSC-CMs but also the measurement tools used to evaluate cell behaviour. In this thesis, different tools to study the function of hPSC-CMs were developed, validated and tested. Firstly, the state-of-the-art on measurement methods in current use were reviewed (Chapter 1 & 2). We noted that quantification of cardiomyocyte contractility was mainly being done in research groups dedicated to physiology using complex measurement tools. This inspired us to develop MUSCLEMOTION, an open source software tool that enabled every biologist to quantify contractility simply using standard laboratory equipment (Chapter 3 & 4). Moreover, we found that we could quantify cardiac contractility not only *in vitro*, but

also *in vivo* in zebrafish and human echography recordings.

Cardiomyocyte contraction is not a simple process but the result of changes in the level of free intracellular calcium ions which is in turn regulated by changes in the electrical potential of the cell membrane. This process is called the excitation-contraction coupling (EC coupling) and cardioactive drugs typically induce changes in different stages of this process resulting in an increase or decrease of contraction force and/or beat rate. In Chapter 5, we developed for the first time a measurement method that provides insight in the different stages of the EC coupling. The microscope we built is capable of quantifying the electrical activity, calcium flux and contraction of muscle cells simultaneously. In addition, using a prediction algorithm based on previously published knowledge we could not only detected drug-induced changes in EC coupling but also identify mechanisms of action of these drugs. In other words, we could not only identify the resulting changes in contraction force and/or beat rate but also the mechanism that was targeted by those drugs. In Chapter 6 we validated the use of hPSC-CMs in combination with complex measurement systems through a blinded, multi-center study. We found that overall, hPSC-CMs were similarly predictive – if not better – than isolated rabbit cardiomyocytes for the compounds tested. Nevertheless, hPSC-CMs were not 100% accurate compared to clinical data and one important underlying reason for the discrepancy is that hPSC-CMs are typically immature, resembling fetal cardiomyocytes rather than muscle cells from the adult heart.

Further advance in methods to induce cardiomyocyte maturation is an important research area. While approaches such as development of multi cell type 3D tissues are among the biological routes to enable maturation, microengineering of a more physiologically relevant environment may achieve the same goal. These engineered microenvironments containing cells are often called micro physiological systems or Organs-on-Chips (OoCs). They can also accommodate sensors and actuators. In Chapter 7, a chip containing such a micro environment was developed and tested. This OoC device was modular to accommodate different cell types (e.g. heart, skin) and include different sensors (e.g. electrodes, force transducers). One of the key components in this device and used widely in the field is poly-dimethylsiloxane (PDMS) even though it is known to absorb compounds. We quantified this in detail for cardiac relevant drugs in Chapter 8 and investigated methods to mitigate this problem. Importantly, we found that it was not hydrophobicity as generally claimed but topological polar surface area that seemed to predicted compound absorption in PDMS.

Finally, Chapter 9 the results of these thesis and future perspectives are discussed.

Our results supported the notion that hPSC models will become human avatars and accurate measurement models able to recapitulate essential human-specific processes. Evidence suggests that it will also be possible to include inflammatory triggers of disease and the immune system. Nevertheless, for application in the drug development pipeline, disease modelling or personalized medicine, validation and development of robust, reproducible, scalable technology will be key.

Nederlandse samenvatting

Het bestuderen van het effect van ziektes of nieuwe medicijnen op het menselijk lichaam is uitdagend, niet in de laatste plaats vanwege het gebrek aan betrouwbare testmodellen die de menselijke fysiologie goed na bootsen. Dergelijk onderzoek wordt momenteel meestal uitgevoerd op dieren, maar de effecten van dezelfde medicijnen of ziektes zijn vaak anders bij dieren dan bij mensen. Zo zijn er bijvoorbeeld medicijnen bekend die geen effect hadden op het hart van dieren terwijl zij bij sommige mensen dodelijke hartritmestoornissen bleken te veroorzaken. Naast de ethische bezwaren rondom dierproeven, is dat de reden dat er een groeiende interesse is in het maken van menselijke hartmodellen gemaakt van pluripotente stamcellen (hPSCs). Behalve cellen van het hart, kunnen hPSCs zich ook tot alle andere celtypen van het menselijk lichaam ontwikkelen. hPSCs zijn normaal gesproken alleen maar aanwezig tijdens de ontwikkeling van jonge embryo's, maar deze kunnen geïsoleerd worden uit een embryo en in het laboratorium kunstmatig in kweek worden gehouden als 'embryonale stamcellen' (hESCs). Sinds 2006 is het echter mogelijk om hPSCs te creëren in het laboratorium door het genetisch herprogrammeren van cellen afkomstig uit een volwassen lichaam. Deze hPSCs worden humane geïnduceerde pluripotente stamcellen (hiPSC) genoemd. Er zijn vandaag de dag veel protocollen beschikbaar om de 'differentiatie' van hPSCs naar verschillende orgaan-specifieke celtypen te sturen, waaronder cellen voor longen, netvlies, bloedvaten, hersenen en het hart. Dit betekent dat er nu een klein aantal cellen bij een patiënt kan worden afgenomen (bijvoorbeeld uit bloed, urine of de huid), welke "ge-herprogrammeerd" kunnen worden naar hiPSCs en vervolgens gedifferentieerd kunnen worden naar hartspiercellen (cardiomyocyten). Aangezien de genen van de patiënt aanwezig en onveranderd blijven tijdens de herprogrammering, zijn uitingen van een genetische hartafwijking zichtbaar in de gedifferentieerde hartspiercellen. Het doel van dit proefschrift is geweest om methodes te ontwikkelen om deze uitingen van de hartspiercellen betrouwbaar te meten met genoeg complexiteit om subtiele reacties van de cellen te zien op toegediende medicijnen of erfelijke hartziekten.

Het hart is misschien wel het allerbelangrijkste orgaan van het menselijk lichaam en is dus een levensbedreigend doelorgaan voor giftige stoffen en ziektes. Zo leiden bijwerkingen van medicijnen die voorgeschreven worden voor het behandelen van kanker (bijvoorbeeld doxorubicine) regelmatig tot schade aan het hart. Door gebruik te maken van cardiomyocyten gedifferentieerd uit hPSCs (hPSC-CMs) kunnen farmaceutische bedrijven naar verwachting de bijwerkingen op het hart in een vroeg stadium van medicijnontwikkeling opsporen en voorkomen.

Om het effect van medicijnen of uitingen van ziektes te bestuderen, is het niet alleen belangrijk om hPSC-CMs te hebben, maar ook de meetsystemen om het gedrag van

de cellen te analyseren. In dit proefschrift zijn verschillende systemen ontwikkeld, gevalideerd en getest om de functionele eigenschappen van hPSC-CMs te bestuderen. Om te beginnen zijn de meest recente en beste meetmethodes die op dit moment in gebruik zijn besproken (Hoofdstuk 1 & 2). We merkten op dat het kwantificeren van de samentrekking van cardiomyocyten met name werd gedaan in onderzoeksgroepen die volledig gericht waren op het gebruik van complexe meetsystemen voor hartspiercelfysiologie. Dit inspireerde ons om MUSCLEMOTION te ontwikkelen, een open-source software applicatie die elke bioloog in staat stelt de samentrekking te kwantificeren met het gebruik van standaard laboratorium apparatuur (Hoofdstuk 3 & 4). We ontdekten zelfs dat we in staat waren om niet alleen samentrekking in het laboratorium te meten maar ook in het lichaam van zowel zebravissen als mensen, met gebruik van echocardiogram.

Het samentrekken van hartspiercellen is niet een simpel proces, maar het resultaat van veranderingen op het niveau van vrije calcium ionen in de cel, wat op haar beurt weer wordt gereguleerd door veranderingen in het elektrische potentiaal van het celmembraan. Dit proces heet de excitatie-contractie koppeling (EC koppeling) en medicijnen met een effect op het hart veroorzaken vaak veranderingen in verschillende stadia van dit proces, hetgeen zorgt voor een verhoging of verlaging van de contractiekracht en/of hartslag. De meetmethode die we in Hoofdstuk 5 hebben ontwikkeld was de eerste die met slechts één meting meer inzicht gaf in de verschillende stadia van de EC koppeling. De microscoop die we hebben gemaakt is in staat om de elektrische activiteit, de veranderingen in calcium ionen en de samentrekking van de hartspiercellen tegelijkertijd te kwantificeren. Door een voorspellingsalgoritme te gebruiken dat we ontwikkelden op basis van eerder gepubliceerde kennis konden we niet alleen verschillen in de hartspiercellen detecteren die veroorzaakt werden door medicijnen, maar konden we ook het mechanisme achter de verandering identificeren. In andere woorden, we konden niet alleen een verschil oppikken in contractiekracht of hartritme, maar ook het mechanisme dat werd beïnvloed door de medicijnen. In Hoofdstuk 6 hebben we dit systeem getest, vergeleken met andere complexe hPSC-CM meetsystemen en gevalideerd in een geblindeerde, multicenter studie. Over het geheel genomen konden we concluderen dat, voor de medicijnen die werden getest, hPSC-CMs even goed – zo niet beter – voorspellend waren voor wat er in mensen gebeurde vergeleken met geïsoleerde konijn cardiomyocyten. Desalniettemin waren hPSC-CMs niet 100% accuraat vergeleken met de klinische data, bijvoorbeeld omdat we bij sommige medicijnen geen verandering in contractie zagen terwijl dat bij een patiënt wel gebeurt. Een belangrijke reden daarvoor is dat de hPSC-CMs nog 'onvolwassen' zijn en zich meer als foetale cardiomyocyten gedragen dan volwassen hartspiercellen

uit een volgroeid individu.

Het verbeteren van methodes om de cardiomyocyten meer volwassen te maken is een belangrijk aandachtspunt in dit onderzoeksveld. Puur biologische routes, zoals het ontwikkelen van 3D weefsels bestaande uit meerdere celtypen, zijn veelbelovend voor het verder volwassen maken van de cellen. Aan de andere kant kunnen kunstmatige routes, zoals van het fabriceren van een micro-omgeving die lijkt op die van het volwassen hart, wellicht leiden tot vergelijkbaar resultaat. Deze kunstmatige micro-omgevingen, die gevuld zijn met cellen, worden micro-fysiologische systemen of Organen-op-Chips (OoCs) genoemd. Ze kunnen ook sensoren en actuatoren bevatten. In Hoofdstuk 7 hebben we een chip met een fysiologische micro-omgeving ontwikkeld en getest. Deze OoC is modulair en kan verschillende celtypen ondersteunen (bijvoorbeeld hart en huid) en er kunnen verschillende sensoren ingebouwd worden (bijvoorbeeld elektrodes en krachtmeters). Een van de belangrijke materialen die gebruikt werd in deze chip en veelvuldig gebruikt wordt in het veld is poly-dimethylsiloxaan (PDMS) terwijl het berucht is vanwege het absorberen van moleculen (zoals medicijnen). Dit hebben we in detail gekwantificeerd in Hoofdstuk 8 voor medicijnen die relevant zijn voor het hart en daarbij methodes onderzocht om de absorptie te verminderen. Terwijl hydrofobiciteit in het algemeen wordt gezien als de reden voor deze absorptie was een belangrijke ontdekking dat niet deze eigenschap maar de topologische polaire oppervlakte de absorptie van verschillende medicijnen leek te voorspellen.

Tot slot hebben we in Hoofdstuk 9 de resultaten van dit proefschrift en toekomstperspectieven beschreven. Onze resultaten versterken het idee dat hPSC modellen menselijke miniaturen worden die met behulp van accurate meetmethodes in staat zijn om essentiële processen na te bootsen die specifiek zijn voor de mens. Er is meer en meer bewijs dat suggereert dat het ook mogelijk wordt om ontstekingsreacties of ziektes van het immuunsysteem te includeren in deze modellen. Niettemin, om een volwassen toepassing te worden in het medicijnontwikkelingstraject, alsmede voor het bestuderen van ziektes of voor gebruik in gepersonaliseerde therapieontwikkeling, is validatie essentieel – net als de ontwikkeling van betrouwbare, reproduceerbare, schaalbare technologie.

Curriculum vitae

Berend van Meer was born on August 2, 1988 (Bloemendaal, the Netherlands). After graduating from secondary school in 2006 (Stedelijk Gymnasium Haarlem) he started a bachelor in Electrical Engineering at Delft University of Technology. During his bachelor he became interested in the field of Organs-on-Chips and did a six month internship under supervision of Prof. Dr. Ronald Dekker at Royal Philips N.V. in collaboration with Dr. Stefan Braam and Prof. Dr. Christine Mummery in the Leiden University Medical Centre (LUMC) with the aim to develop a cardiac muscular thin film using human stem cell derived cardiomyocytes. He graduated with an A+ result for his bachelor thesis and was awarded the IEEE Benelux Computer Society "Best High Tech Start-up Business Plan".

During his bachelor, Berend was co-founder of the Lisa Waller Hayes Foundation (LWH Foundation, now: Living With Hope), a non-profit organization that fights pancreatic cancer by raising awareness and funds for research. In 2011, he co-founded Technological Innovations in Medicine (TIM), a start-up company aimed to improve patient care with technological solutions, which led to the spin-out OSAsense, a home use screening tool to detect sleep apnea.

During his master Electrical Engineering – Microelectronics track, started in 2011, he focused mainly on biosensors, nanoelectronics and microfabrication, but also did a Strategic Marketing internship at Royal KPN N.V. where he developed a roadmap for emerging technologies of interest to the company. Berend graduated with an A+ result for his Master thesis where he developed a Skin-on-Chip model under supervision of Prof. Dr. Ronald Dekker at the Delft Institute of Microsystems and Microelectronics in collaboration with Prof. Dr. Sue Gibbs at the Vrije Universiteit Medical Centre.

Next, he started his PhD research in 2014 under supervision of Prof. dr. Christine Mummery and Dr. Leon Tertoolen in the department of Anatomy and Embryology at the LUMC. During his PhD research he was awarded two travel awards (Safety Pharmacology Society and Keystone) and a EIT Health PhD Transition Fellowships (€ 10,000). He has been selected and invited for several talks at scientific conferences and at two TEDx events. In 2020, he received the Hugo van Poelgeest Award for advancing research in animal alternatives for drug testing and disease modelling.

Since 2019, Berend has focused on bringing Organ-on-Chip technology closer to the societal application and is currently employed both at the LUMC and the University of Twente. He works on setting up academic centers of expertise that facilitate biological qualification and open technology platforms to Organ-on-Chip researchers and start-

up companies. In addition, he is coordinating several research projects in the group of Prof. Dr. Christine Mummery.

Berend lives in Haarlem, together with Mariëtte Kooren and their son Tijl.

List of publications

Blinded, Multicenter Evaluation of Drug-induced Changes in Contractility Using Human-induced Pluripotent Stem Cell-derived Cardiomyocytes

Berend J van Meer*, Umber Saleem*, Puspita A Katili, Nurul A N Mohd Yusof, Ingra Mannhardt, Ana Krotenberg Garcia, Leon Tertoolen, Tessa de Korte, Maria LH Vlaming, Karen McGlynn, Jessica Nebel, Anthony Bahinski, Kate Harris, Eric Rossman, Xiaoping Xu, Francis L Burton, Godfrey L Smith, Peter Clements, Christine L Mummery, Thomas Eschenhagen, Arne Hansen, Chris Denning

* Contributed equally
Published in Toxicological Sciences (2020), doi: 10.1093/toxsci/kfaa058

Simultaneous measurement of excitation-contraction coupling parameters identifies mechanisms underlying contractile responses of hiPSC-derived cardiomyocytes

Berend J. van Meer, Ana Krotenberg, Luca Sala, Richard Davis, Thomas Eschenhagen, Chris Denning, Leon G.J. Tertoolen, Christine L. Mummery

Published in Nature Communications (2019), doi: 10.1038/s41467-019-12354-8

Quantification of Muscle Contraction In Vitro and In Vivo Using MUSCLEMOTION Software: From Stem Cell-Derived Cardiomyocytes to Zebrafish and Human Hearts

Berend J. van Meer*, Luca Sala*, Leon G. J. Tertoolen, Godfrey L. Smith, Francis L. Burton, Christine L. Mummery

* Contributed equally
Published in Current Protocols in Human Genetics (2018), doi: 10.1002/cphg.67

MUSCLEMOTION: A Versatile Open Software Tool to Quantify Cardiomyocyte and Cardiac Muscle Contraction In Vitro and In Vivo

Berend J van Meer*, Luca Sala*, Leon T Tertoolen, Jeroen Bakkers, Milena Bellin, Richard P Davis, Chris N Denning, Michel A Dieben, Thomas Eschenhagen, Elisa Giacomelli, Catarina Grandela, Arne Hansen, Eduard Holman, Monique R Jongbloed, Sarah M Kamel, Charlotte D Koopman, Quentin Lachaud, Ingra Mannhardt, Mervyn P Mol, Diogo Mosqueira, Valeria V Orlova, Robert Passier, Marcelo C Ribeiro, Umber Saleem, Godfrey Smith, Francis LL Burton, Christine L Mummery

* Contributed equally
Published in Circulation Research (2018), doi: 10.1161/CIRCRESAHA.117.312067

Small molecule absorption by PDMS in the context of drug response bioassays

BJ van Meer, H. de Vries, K.S.A Firth, J. van Weerd, L.G.J. Tertoolen, H.B.J. Karperien, P. Jonkheijm, C. Denning, A.P. IJzerman, CL Mummery

Published in Biochemical and Biophysical Research Communications (2016) , doi: 10.1016/j.bbrc.2016.11.062

Cytostretch, an Organ-on-Chip Platform

Nikolas Gaio, Berend van Meer, William Quirós Solano, Lambert Bergers, Anja van de Stolpe, Christine Mummery, Pasqualina M. Sarro and Ronald Dekker

Published in Micromachines (2016), doi: 10.3390/mi7070120

Concise Review: Measuring physiological responses of human pluripotent stem cell derived cardiomyocytes to drugs and disease.

BJ van Meer, LG Tertoolen, CL Mummery

Published in Stem Cells (2016), doi: 10.1002/stem.2403

Dankwoord

Deze thesis was er nooit geweest zonder steun en hulp van velen.

Christine, het is een voorrecht om jou als promotor en vooral ook als mentor te hebben: jouw liefde voor wetenschap is aanstekelijk, jouw toewijding indrukwekkend en voor jouw vertrouwen in mij als techneut in een biologie-lab blijf ik eeuwig dankbaar. Je hebt mij leren denken en schrijven als een wetenschapper, mij vrijheid gegeven om mezelf te ontwikkelen en dat doe je nog steeds.

Leon, jij hebt me niet alleen veel theorie geleerd, maar ook hoe een complex idee in de praktijk kan worden gebracht. Waanzinnig veel dank voor het samen maanden mogen sleutelen aan 'onze' microscoop (jouw geesteskind), algoritmes, image intensifiers; zonder jou was ik nergens geweest en het was sowieso een stuk minder leuk geweest.

Luca, I miss you: we make a great team, Batman! Ana, I miss you too: we were so in sync that our SOP was timed per minute while discussing life. Anneloes, Joshua, Vera, Oleh, Elisa, Ruben, Marc, Vivi, Giulia, Loukia, Amy, Mervyn, Marga, Tessa, Christiaan, Catarina, Claire, Karina, Paul, Bas, Jeroen, Marga, Christiaan, Daniël, Bert, Lisa, Connie, Dennis, and all the others in the lab: thank you for your help and great times! Atie, dank voor alle hulp en soms samen zeuren. Dorien, moeder van hartspiercellen, dank dat je altijd klaarstaat. Robert, Stefan, Valeria, Susana, Richard, Christian, Monique, Milena, many thanks for tons of help, discussions and collaborations.

Crack It consortium, Chris, thank you for letting young researchers feel part of the team.

Leonie, het is leuk dat onze interesses dicht bij elkaar liggen en ons dagelijks werk toch zo anders is. Ik leer veel van je. Kay, jij geeft me al jaren een andere blik op de wereld: het kijken naar zinloze esthetiek en het vertellen van verhalen. En tegelijkertijd interesseer jij je tot in kleinste details van mijn onderzoek. Ik ben trots jullie als paranimfen te hebben.

Charlotte & Rutger-Jan, Anne & Reinout, Leonie & Bertolt, Julia, Alette, Bente, Lucie, Floor, Just, Bénine, Jet, Wiebe Berend en Huib, jullie zijn bronnen van inspiratie en zeer welkome afleiding, dank!

Lieve ouders, door jullie stabiliteit, eindeloze vertrouwen en ellenlange (inhoudelijke) discussies, heb ik me altijd vrij gevoeld om keuzes te maken die ik wilde. Zonder die dingen was ik nooit aan dit boekwerk begonnen.

Lieve Mariëtte, jij maakt elke dag vrolijk. Samen met Tijl. Je helpt me de frustratie te vergeten en de successen te vieren. Dank voor het accepteren van alle nerderigheid en in die geest: het kwantificeren van jouw emoties was toch het leukste van al dit onderzoek.